NASA CONTRACTOR REPORT

NASA CR-1885

ANALYSIS OF TRANSIENT, LINEAR WAVE PROPAGATION IN SHELLS BY THE FINITE DIFFERENCE METHOD

by Thomas L. Geers and Lawrence H. Sobel

Prepared by
LOCKHEED MISSILES & SPACE COMPANY
Palo Alto, Calif. 94304
for Langley Research Center

NATIONAL AERONAUTICS AND SPACE ADMINISTRATION • WASHINGTON, D. C. • DECEMBER 1971

1. Report No.	2. Government Accession No.	3. Recipient's Catalog No.
NASA CR-1885		

4. Title and Subtitle	5. Report Date
ANALYSIS OF TRANSIENT; LINEAR WAVE PROPAGATION IN SHELLS BY THE FINITE DIFFERENCE METHOD	December 1971
	6. Performing Organization Code

7. Author(s)	8. Performing Organization Report No.
Thomas L. Geers and Lawrence H. Sobel	

9. Performing Organization Name and Address	10. Work Unit No.
Lockheed Missiles & Space Company Lockheed Palo Alto Research Lab. Palo Alto, Calif. 94304	134-14-04-01
	11. Contract or Grant No. NAS 1-9111

12. Sponsoring Agency Name and Address	13. Type of Report and Period Covered
National Aeronautics and Space Administration Washington, D.C. 20546	Contractor Report
	14. Sponsoring Agency Code

15. Supplementary Notes

16. Abstract

This report contains: (1) analytical and numerical studies pertaining to the limits of applicability of the finite difference method in the solution of transient, linear wave propagation problems in shells, (2) a recommended computational procedure for the use of the method, and (3) a numerical investigation of the response of a cylindrical shell with cutouts to both longitudinal and radial transient excitations. It is found that the only inherent limitation of the finite difference method is its inability to reproduce accurately response discontinuities. This is not a serious limitation, in view of natural constraints imposed by the extension of Saint Verant's principle to wave propagation problems. It is also found that the short wave length limitations of thin shell (Bernoulli-Euler) theory create significant convergence difficulties in computed responses to certain types of transverse excitations. These difficulties may often be overcome, however, through proper selection of finite difference mesh dimensions and temporal or spatial smoothing of the excitation. Finally, it is found that cutouts produce moderate changes in early- and intermediate-time response of a cylindrical shell to axisymmetric pulse-loads applied at one end. The cutouts may, however, facilitate the undesirable late-time transfer of load-injected extensional energy into non-axisymmetric flexural response.

17. Key Words (Suggested by Author(s))	18. Distribution Statement
Wave propagation in shells Wave propagation by finite differences	Unclassified – Unlimited

19. Security Classif. (of this report)	20. Security Classif. (of this page)	21. No. of Pages	22. Price*
Unclassified	Unclassified	191	$3.00

*For sale by the National Technical Information Service, Springfield, Virginia 22151

FOREWORD

The research described in the present report was performed under Contract NAS 1-9111 with the NASA/Langley Research Center, Hampton, Virginia, with Dr. J. P. Raney as Contract Monitor. A companion volume, LMSC LS 69-6, contains the results of a search of the literature on linear transient wave propagation in elastic bars, plates and shells covering the period 1964 through early 1969.

The authors wish to thank Dr. J. P. Raney, Miss B. J. Durling and Mr. J. T. Howlett of the NASA/Langley Research Center for providing modal superposition solutions to certain problems investigated herein. They also wish to thank Dr. D. A. Evensen of TRW Systems, Redondo Beach, Calif., for his cooperation in coordinating the analytical and experimental cutout studies.

The authors also express their appreciation to Mr. P. S. Jensen of Lockheed and Mr. Wilson Silsby, recently at Lockheed but now at the Jet Propulsion Laboratories, Pasadena, Calif., for introducing important modifications into the STAR code. Last, but certainly not least, the authors express their gratitude to Mrs. Gloria Sherrard and Miss Jessie Vosti of Lockheed for their patience and perseverance in the skillful preparation of this report.

TABLE OF CONTENTS

Chapter 1. INTRODUCTION Page 1-1

1.1 Response Variables 1-2

1.2 Equations of Shell Theory 1-4

1.3 Various Numerical Methods of Solution 1-7

1.4 The STAR Code: Description and Application 1-8

Chapter 2. NUMERICAL STUDY OF CONVERGENCE Page 2-1

2.1 Displacement, Velocity and Acceleration Response to In-Plane Excitation 2-2

2.1.1 $(\vec{\alpha}, \tilde{t})$ - Excitations 2-2

2.1.2 $(\tilde{\alpha}, \vec{t})$ - Excitations 2-3

2.1.3 $(\vec{\alpha}, \vec{t})$ - Excitations 2-4

2.1.4 Conclusions 2-5

2.2 Displacement, Velocity and Acceleration Response to Transverse Excitation 2-6

2.2.1 $(\vec{\alpha}, \tilde{t})$ - Excitation 2-6

2.2.2 $(\tilde{\alpha}, \vec{t})$ - Excitation 2-8

2.2.3 $(\vec{\alpha}, \vec{t})$ - Excitations 2-8

2.2.4 Smoothed Excitations 2-10

2.2.5 Conclusions 2-11

2.3 Stress/Strain Response to In-Plane Excitation 2-12

2.3.1 $(\vec{\alpha}, \tilde{t})$ -, $(\tilde{\alpha}, \vec{t})$ -, and $(\vec{\alpha}, \vec{t})$ - Excitations 2-12

2.3.2 Conclusions 2-13

2.3.3 Comparison with Experimental Data 2-13

2.4 Stress/Strain Response to Transverse Excitation 2-16

2.4.1 $(\vec{\alpha}, \tilde{t})$ -, $(\tilde{\alpha}, \vec{t})$ -, and $(\vec{\alpha}, \vec{t})$ - Excitations 2-16

2.4.2 Smoothed Excitations 2-17

2.4.3 Conclusions 2-18

ANALYSIS OF TRANSIENT, LINEAR WAVE PROPAGATION IN SHELLS BY THE FINITE DIFFERENCE METHOD

By Thomas L. Geers and Lawrence H. Sobel
Lockheed Missiles & Space Company
Palo Alto, California

Chapter 1

INTRODUCTION

The finite difference method has been used for many years in the solution of differential equations, including those of shell theory. Because the method involves the transformation of differential equations for continuous variables into difference equations for discrete variables, a question of primary interest is the following: At what mesh size (if any) do the finite difference equations accurately reproduce the solutions of interest to the differential equations? This report addresses itself to that question as it pertains to transient, linear wave propagation in shells.

The motivation behind this study was to provide a sufficiently firm understanding of the title subject that detailed comparisons could be made between the finite difference method and other numerical methods of analysis. As the study progressed, it became possible to make preliminary comparisons; while these appear at appropriate points in the report, the comprehensive comparison study is left for future work.

The report is divided into five chapters. This chapter contains an outline of the considerations underlying the study and descriptions of the shell equations and the finite difference code used. The second chapter contains numerical results and discussion for a variety of wave propagation problems; this serves to establish the accuracy and practical limitations of the method. The third chapter presents the results of analytical investigations that explain certain behavior observed in the computations of Chapter 2 as well as some characteristics of computations by other methods. The fourth chapter deals with a problem of special interest, viz., the scattering of transient longitudinal and flexural waves in a cylindrical shell by cutouts. Chapter 5 completes the report with a statement of major conclusions and recommendations for future study.

1.1 RESPONSE VARIABLES

It is of course important at the outset to identify the response variables that are to be used as a basis for judging the accuracy of finite difference computations. To do this, we indicate two uses to which such computations are often put. First, transient shell response computations may be used as excitation inputs to small structural systems that are attached to the shell, in order to predict failure or survival of these systems. Second, transient shell responses may be used to predict failure or survival of the shell itself.

In connection with the first use, let us examine briefly the response of a damped, single-degree-of-freedom oscillator excited at its spring-dashpot attachment point. The response quantity on which the failure or survival of such a system most directly depends is the relative displacement across the spring-dashpot pair. Thus we write the governing equation for the oscillator in the form (Ref. 1)

$$\ddot{y} + 2\zeta\omega_o\dot{y} + \omega_o^2 y = -\ddot{x}_o \tag{1}$$

where y is relative displacement, x_o is attachment point displacement, ω_o and ζ are the oscillator's fixed-base undamped natural frequency and critical damping ratio, respectively ($\zeta \ll 1$ in the vast majority of cases), and a dot denotes single differentiation in time. If we now introduce the Fourier transform (Ref. 2)

$$\bar{f}(\omega) = \int_{-\infty}^{\infty} f(t)e^{-j\omega t}dt \tag{2}$$

the relative displacement response for quiescent initial conditions is given by

$$y(t) = \frac{1}{2\pi}\int_{-\infty}^{\infty} \frac{\omega^2\bar{x}_o(\omega)e^{j\omega t}}{\omega_o^2 + 2j\zeta\omega_o\omega - \omega^2}\,d\omega \tag{3}$$

Let us now consider three frequency regions in the (positive) frequency domain: (1) the region $0 \le \omega \le \omega_1$, where $\omega_1^2 \ll \omega_o^2$, (2) the region $\omega_1 \le \omega \le \omega_2$, where $\omega_2^2 \gg \omega_o^2$ and (3) the region $\omega_2 \le \omega \le \infty$. We write from Eq. 3, then, since $x_o(t)$ is real,

$$y(t) = -\frac{1}{2\pi\omega_o^2}\int_0^{\omega_1}\left[\frac{\bar{a}_o(\omega)e^{j\omega t}}{1-(\omega/\omega_o)^2+2j\zeta\omega/\omega_o}+\frac{\bar{a}_o^*(\omega)e^{-j\omega t}}{1-(\omega/\omega_o)^2-2j\zeta\omega/\omega_o}\right]d\omega$$

$$-\frac{1}{2\pi\omega_o}\int_{\omega_1}^{\omega_2}\left[\frac{\bar{v}_o(\omega)e^{j\omega t}}{2\zeta-j(1+\omega_o/\omega)(1-\omega/\omega_o)}+\frac{\bar{v}_o^*(\omega)e^{-j\omega t}}{2\zeta+j(1+\omega_o/\omega)(1-\omega/\omega_o)}\right]d\omega \qquad (4)$$

$$-\frac{1}{2\pi}\int_{\omega_2}^{\infty}\left[\frac{\bar{x}_o(\omega)e^{j\omega t}}{1-(\omega_o/\omega)^2-2j\zeta\omega_o/\omega}+\frac{\bar{x}_o^*(\omega)e^{-j\omega t}}{1-(\omega_o/\omega)^2+2j\zeta\omega_o/\omega}\right]d\omega$$

where an asterisk denotes complex conjugate and where $v_o(t)$ and $a_o(t)$ are the velocity and acceleration of the attachment point, respectively. Examination of the three integrals on the right side of Eq. 4 leads us to conclude that $y(t)$ varies roughly as $a_o(t)$, $v_o(t)$ and $x_o(t)$ for low-frequency ($\omega^2 \ll \omega_o^2$), intermediate-frequency ($\omega \sim \omega_o$), and high-frequency ($\omega^2 \gg \omega_o^2$) input motions, respectively.

From the above development, we conclude that, based on the highest natural frequency of a small attached system, we need not be concerned with intermediate- and high-frequency shell acceleration components or with high-frequency shell velocity components at the system's attachment point. This is fortunate, since, as we will observe in Chapter 2, high-frequency inaccuracies appear in computed acceleration histories before they appear in the corresponding velocity histories; high-frequency inaccuracies rarely appear in computed displacement histories.

In connection with the second use, that of predicting failure or survival of the shell itself, it is clear that the quantities of interest are either stresses or strains. These quantities are significant only to the extent that they combine in such a say so as to reach a failure criterion, and, in almost all problems, a few of them greatly exceed the others in magnitude. Hence, judgements regarding the accuracy of stress/strain computations should be based more upon considerations regarding peak values of significant stresses/strains and times of occurrence of the peak values than upon response details.

In accordance with the preceding discussion, conclusions regarding the accuracy of finite difference computations will be based upon displacement, velocity, acceleration, and stress/strain responses. It will generally be assumed that if a series of finite difference computations appropriate to a sequence of decreasing mesh sizes exhibit convergence with respect to the response quantities of interest, then the converged solutions constitute accurate reproductions of the true solutions of the governing differential equations. This assumption will be supported in many cases through comparisons with other types of solutions to specific problems and through analytical studies of convergence.

1.2 EQUATIONS OF SHELL THEORY

The finite difference computations of this report are based on the linear elastic equations for thin shells. There exist various equations of this type (see, e.g., Refs. 3-6); all of the varieties have the common characteristic that they admit errors of order h/a in the pertinent energy expressions, where h is a characteristic shell thickness and a is a characteristic radius of curvature. On this basis, then, they may all be considered equivalent. The finite difference code employed herein, the STAR code, is based in particular on the equations of Ref. 6. Although these equations are thoroughly discussed in Ref. 6, it is helpful for discussion purposes to specialize here to the case of the circular cylindrical shell. For this case, the pertinent strain-displacement relations are

$$\epsilon_\alpha(z) = \epsilon_{\alpha e} + \epsilon_{\alpha f}(z) = \frac{\partial u}{\partial \alpha} - z\,\frac{\partial^2 w}{\partial \alpha^2}$$

$$\epsilon_\beta(z) = \epsilon_{\beta e} + \epsilon_{\beta f}(z) = \frac{1}{a}\frac{\partial v}{\partial \beta} - \frac{w}{a} - \frac{z}{a^2}\left(\frac{\partial^2 w}{\partial \beta^2} + \frac{\partial v}{\partial \beta}\right) \qquad (5)$$

$$\epsilon_{\alpha\beta}(z) = \epsilon_{\alpha\beta e} + \epsilon_{\alpha\beta f}(z) = \frac{1}{a}\frac{\partial u}{\partial \beta} + \frac{\partial v}{\partial \alpha} - 2\,\frac{z}{a}\left(\frac{\partial^2 w}{\partial \alpha \partial \beta} + \frac{1}{2}\frac{\partial v}{\partial \alpha}\right)$$

where e and f denote extensional and flexural strains, respectively,* and the pertinent constitutive equations are

$$\sigma_\alpha = \frac{E}{1-\nu^2}(\epsilon_\alpha + \nu\epsilon_\beta)$$

$$\sigma_\beta = \frac{E}{1-\nu^2}(\epsilon_\beta + \nu\epsilon_\alpha) \qquad (6)$$

$$\tau_{\alpha\beta} = \frac{E}{2(1+\nu)}\epsilon_{\alpha\beta}$$

The notation for Eqs. 5 and 6 is defined in the following figure.

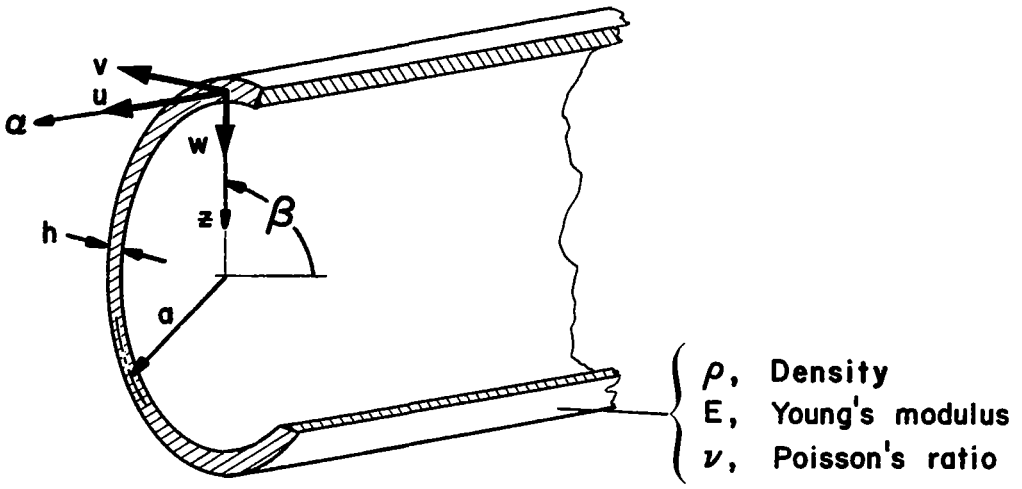

The introduction of Eqs. 5 and 6 into the appropriate strain and kinetic energy expressions, and the subsequent application of Hamilton's principle (see, e.g., Ref. 7) yield the so-called Euler equations, or the equations of motion for the shell

*Since the flexural terms correspond to the Bernoulli-Euler theory for the flexural deformation of beams, a theory which leads to equations of this type is sometimes referred to as a Bernoulli-Euler theory.

$$\frac{1}{c^2}\frac{\partial^2 u}{\partial t^2} - \frac{\partial^2 u}{\partial \alpha^2} - \frac{1}{2a^2}(1-\nu)\frac{\partial^2 u}{\partial \beta^2} - \frac{1}{2a}(1+\nu)\frac{\partial^2 v}{\partial \alpha \partial \beta} + \frac{\nu}{a}\frac{\partial w}{\partial \alpha} = \frac{p_\alpha(\alpha,\beta,t)}{\rho c^2 h}$$

$$\frac{1}{c^2}\frac{\partial^2 v}{\partial t^2} - \frac{1}{2a}(1+\nu)\frac{\partial^2 u}{\partial \alpha \partial \beta} - \frac{1}{a^2}\frac{\partial^2 v}{\partial \beta^2} - \frac{1}{2}(1-\nu)\frac{\partial^2 v}{\partial \alpha^2} + \frac{1}{a^2}\frac{\partial w}{\partial \beta}$$

$$- \frac{h^2}{12a^2}\left[\frac{1}{a^2}\frac{\partial^2 v}{\partial \beta^2} + \frac{1}{2}(1-\nu)\frac{\partial^2 v}{\partial \alpha^2} + \frac{\partial}{\partial \beta}(\nabla^2 v)\right] = \frac{p_\beta(\alpha,\beta,t)}{\rho c^2 h} \qquad (7)$$

$$\frac{1}{c^2}\frac{\partial^2 w}{\partial t^2} - \frac{\nu}{a}\frac{\partial u}{\partial \alpha} - \frac{1}{a^2}\frac{\partial v}{\partial \beta} + \frac{w}{a^2} + \frac{h^2}{12}\left[\nabla^4 w + \frac{1}{a^2}\frac{\partial}{\partial \beta}(\nabla^2 v)\right] = \frac{p_z(\alpha,\beta,t)}{\rho c^2 h}$$

where $\nabla^2(\ ) \equiv \left[\frac{\partial^2}{\partial \alpha^2} + \frac{1}{a^2}\frac{\partial^2}{\partial \beta^2}\right](\ )$, $\nabla^4(\ ) = \nabla^2[\nabla^2(\ )]$, $c = [E/\rho(1-\nu^2)]^{1/2}$

is the plate velocity for the shell material, and p_α, p_β, and p_z are surface tractions in the α- , β- , and z-directions, respectively. The initial and boundary conditions that are necessary for the complete description of a problem will not be given here (see, e.g., Ref. 7).

If an excitation is such that flexural effects are negligible in the response of the shell, then all terms multiplied by $h^2/12a^2$ in Eqs. 7 may be dropped. This yields the equations of motion for the so-called membrane shell. If an excitation is such that flexural wave lengths on the order of the shell thickness are present in the shell response, then thin shell (Bernoulli-Euler) theory is no longer adequate. One might then employ the equations of improved theory, which take into account the effects of transverse shear deformation and rotatory inertia. These equations may be obtained in a manner similar to that used to obtain Eqs. 7 (see, e.g., Ref. 8). For our purposes, it is only necessary to note that, while the extensional strain expressions for this theory are those of Eqs. 5, the flexural strain expressions are

$$\epsilon_{\alpha f}(z) = z\,\frac{\partial \varphi}{\partial \alpha}$$

$$\epsilon_{\beta f}(z) = \frac{z}{a}\,\frac{\partial \psi}{\partial \beta} \tag{8}$$

$$\epsilon_{\alpha\beta f}(z) = z\left(\frac{1}{a}\,\frac{\partial \varphi}{\partial \beta} + \frac{\partial \psi}{\partial \alpha}\right)$$

where the shell rotations φ and ψ become $-\partial w/\partial\alpha$ and $-(1/a)(\partial w/\partial\beta + v)$, respectively, in the limit of long structural wave lengths.*

1.3 VARIOUS NUMERICAL METHODS OF SOLUTION

Because linear dynamic shell equations are generally far too complicated to yield to direct solution in closed form, numerical methods of solution have been extensively employed. The most common of these have been the finite difference method, the finite element method, the method of modal superposition and the method of characteristics.

The finite difference and finite element methods both impose a gridwork on the shell, replace the continuous shell with a discrete model, and solve a set of algebraic equations. The two methods differ in that the finite difference method discretizes the governing partial differential equations for the continuous shell, while the finite element method discretizes the shell itself, representing it as an assemblage of plate or shell elements, each of which is described by a finite number of dependent variables. Temporal variation is generally treated in both methods with step-by-step numerical integration techniques.

The method of modal superposition first solves the eigenvalue problem associated with the homogeneous equations of motion in conjunction with the

*Since the flexural terms correspond to the Timoshenko theory for the flexural deformation of beams, a shell theory which includes the effects of transverse shear deformation and rotatory inertia is sometimes referred to as a Timoshenko theory.

governing boundary conditions.* The resulting shell modes are then used to construct the forced motion of the shell by linear superposition. The method of characteristics requires hyperbolic shell equations (Eqs. 7 are of the parabolic type with regard to flexural motion) and therefore makes use of improved (Timoshenko) shell theory. The shell equations are then recast in terms of the appropriate characteristics and solved numerically.

All of the above methods share a common failing, namely, the use of a finite number of response variables to represent continuous functions. Their success depends, therefore, upon the rate of convergence of their numerical solutions with respect to finite increases in the number of response variables (degrees-of-freedom) and the efficiency with which they effect the necessary computations for a given number of response variables. Generally speaking, the finite difference and finite element methods are numerically the most efficient for a given number of response variables; the method of modal superposition is less efficient, but often requires a smaller number of response variables and provides modal information that need only be generated once for multiple response computations; the method of characteristics is the least efficient method, but, because it embodies the essential characteristics of wave propagation behavior, it can accurately treat short wave length response, including response discontinuities. Thus, a decision as to which method should be used to solve a particular problem can only be based on the nature of the problem itself. (For a comprehensive assessment of current shell analysis capability, see Ref. 9.)

1.4 THE STAR CODE: DESCRIPTION AND APPLICATION

The STAR (Shell Transient Asymmetric Response) computer program can be used for the two-dimensional, nonlinear, transient response analysis of inelastic shells with unreinforced cutouts. A detailed discussion of the code is given in the User's Manual for STAR (Ref. 10). Improvements made in the code as part of the present study are described in Appendix A.

*For complicated geometries, the homogeneous equations of motion are usually solved with finite difference or finite element methods.

The STAR code is based on the general thin shell equations of Ref. 6, which include nonlinear geometric terms, and on a set of constitutive equations for a temperature-dependent, work-hardening material. Lines of principal curvature are used for the curvilinear coordinates (α,β) of the middle surface of the shell. (See Appendix A for notation and sign conventions.) The basic solution procedure employed by the code is as follows. The governing partial differential equations of motion are reduced to a set of time-dependent ordinary differential equations by the application of two-dimensional finite difference approximations for derivatives with respect to the shell's middle surface coordinates α and β. An explicit (central) finite difference numerical integration scheme is then employed for the solution of the ordinary differential equations.

Solutions obtained with the explicit scheme are numerically stable if the time step Δt is not greater than some critical value, Δt_{cr}. In the present study, Δt_{cr} is computed from (Ref. 11)

$$\Delta t_{cr} = \frac{2}{\omega_{max}} \tag{9}$$

where ω_{max} is the highest natural frequency for the discrete system obtained from the finite difference representation of the shell equations. Expressions for ω_{max} appropriate to uncoupled extensional and bending vibrations of a flat plate are given in Section 3.1. From those expressions and the above equation, we obtain the following critical time steps Δt^{E}_{cr} and Δt^{F}_{cr} corresponding to extensional and flexural plate vibrations, respectively:

$$\Delta t^{E}_{cr} = \left[\left(\frac{c}{\Delta\alpha}\right)^2 + \left(\frac{c_s}{a\Delta\beta}\right)^2\right]^{-\frac{1}{2}} \quad , \quad (\Delta\alpha < a\Delta\beta)$$

$$\Delta t^{F}_{cr} = \frac{\sqrt{3}}{hc}\left[\frac{1}{\Delta\alpha^2} + \frac{1}{(a\Delta\beta)^2}\right]^{-1} \tag{10}$$

where $c^2 = E/\rho(1-\nu^2)$, $c_s^2 = E/2(1+\nu)\rho$, $a = a(\alpha)$ is the shell radius, and $\Delta\alpha$ and $\Delta\beta$ are the mesh widths for the meridional and circumferential coordinates, respectively.* ($\Delta\beta = \infty$ for axisymmetric problems.) For all cases considered herein, Δt is less than the smaller of Δt^E_{cr} and Δt^F_{cr}. All numerical results thus obtained are numerically stable.

The mesh widths $\Delta\alpha$ and $\Delta\beta$ were selected in accordance with the following consideration. Let λ denote a characteristic structural wave length appropriate to nondispersive, axisymmetric wave propagation in the shell. Then, for problems with in-plane excitations, $\Delta\alpha$ was selected in accordance with the criterion $\Delta\alpha/\lambda \ll 1$. It was found that this criterion consistently gave good results, so it served as the basis for all problems characterized by predominantly in-plane excitations.

For problems with transverse loadings, $\Delta\alpha$ was selected in accordance with the criterion that $\Delta\alpha/h \sim 1$, where h is the shell thickness. A more sophisticated method for choosing $\Delta\alpha$ evolved during the course of the present study. This method is discussed in Chapter 3. In the solution of asymmetric problems, the mesh aspect ratio ($\Delta\alpha/a\Delta\beta$) was selected to be on the order of unity.

One of the major considerations used in the selection and execution of the problems of the next chapter was that the computation time for a single problem should be less than five minutes. The following approximate expression was used to estimate computation times on the Univac 1108 for both axisymmetric and asymmetric response problems:

$$\text{COMPUTATION TIME IN MINUTES} = n_\alpha n_\beta n_t/4000 \tag{11}$$

where n_α and n_β are the number of mesh points in the α and β directions, respectively, and n_t is the number of time points.

It should be emphasized that the scope of the STAR code (see Ref. 10) is appreciably broader than that required for the class of problems considered herein, namely, the linear, isothermal, transient response of constant-thickness, elastic, isotropic cylindrical and conical shells. Hence, run times for the STAR code will generally be higher than those for computer programs that are specifically developed for this class of problems.

*If $a\Delta\beta < \Delta\alpha$, $\Delta\alpha$ and $a\Delta\beta$ are interchanged in the first of Eqs. 10.

Chapter 2

NUMERICAL STUDY OF CONVERGENCE

In this chapter, we investigate numerically the convergence of finite difference transient wave propagation computations. Because we are primarily interested in propagation along the meridional coordinate, most of the cases involve axisymmetric response, although problems with gentle asymmetry are also included.

To facilitate our study, let us define four excitation classifications. The first classification is $(\tilde{\alpha}, \tilde{t})$, which includes excitations that are broad in the meridional dimension α and gradual in the temporal dimension t.* The second classification is $(\vec{\alpha}, \tilde{t})$, which consists of excitations that are narrow in α but gradual in t. The third is $(\tilde{\alpha}, \vec{t})$, which includes excitations that are broad in α but abrupt in t. The final classification is $(\vec{\alpha}, \vec{t})$, which consists of excitations that are narrow in α and abrupt in t. All non-axisymmetric excitations to be considered are broad in the circumferential dimension β.

In order to describe more precisely these classifications, we define a "spatially broad" excitation as one that contains no spatial discontinuities on an unbounded domain or one whose characteristic spatial dimension considerably exceeds the shell thickness; we define a "temporally gradual" excitation as one that produces no temporal discontinuities in the velocity response of the shell or one whose characteristic temporal dimension considerably exceeds the transit time of an extensional wave through the shell thickness. The terms "spatially narrow" and "temporally abrupt" are, of course, just the opposite of the above definitions. Because the imposition of boundary conditions is equivalent to the application of line loads to a shell, any disturbance reaching a shell boundary gives rise to an excitation that is spatially narrow in the direction normal to the boundary. Also, specification of an initial velocity condition constitutes the application of a temporally abrupt excitation.

The principal results of this chapter are summarized in Table 1 on page 2-19.

*Actually, excitations in this classification will not be specifically considered. This is because the studies pertaining to the other classifications demonstrate that $(\tilde{\alpha}, \tilde{t})$- excitations present no convergence problems.

2.1 DISPLACEMENT, VELOCITY AND ACCELERATION RESPONSE TO IN-PLANE EXCITATION

In this section, we examine convergence of the kinematic quantities appropriate to in-plane or, more specifically, longitudinal excitation of cylindrical shells.

2.1.1 $(\vec{\alpha}, \tilde{t})$ - Excitations

The first example involves an $(\vec{\alpha}, \tilde{t})$ - excitation in the form of a specified bell-shaped end-displacement whose temporal width is approximately equal to $a/2c$*. Thus, as discussed in Appendix B, $(k_\epsilon a)^2 \gg 1$, where k_ϵ is the wave number characteristic of the longitudinal strain, and a bell-shaped displacement wave propagates with negligible dispersion down the shell at the plate velocity c.

Fig. 1 shows displacement, velocity and acceleration histories at $\alpha/L = \frac{1}{2}$**. We see that, because of the nature of the excitation, taking a time derivative roughly halves the characteristic wave length $\lambda = 2\pi/k$. Thus, the coarse finite difference mesh is satisfactory for displacement computations but is marginal for velocity computations and unsatisfactory for acceleration computations. Fig. 2 shows displacement, velocity and acceleration snapshots at $ct/a = 0.533$. Because of the non-dispersive propagation, each response snapshot is essentially a laterally displaced mirror image of the corresponding history. This description holds at later times also, as indicated in Fig. 3, which shows snapshots at $ct/a = 2.132$. Comparing Figs. 2 and 3, we detect, for a fixed mesh width, a gradual deterioration in accuracy as time increases.

The second example also involves an $(\vec{\alpha}, \tilde{t})$ - excitation in the form of a specified bell-shaped end-displacement. In this case, however, $k_\epsilon a \sim 1$, and the wave suffers significant dispersion as it propagates down the shell (see Appendix B). Fig. 4 shows displacement, velocity and

---

*All the examples discussed in this chapter are described in detail in Table 2.

**Because, from Appendix B, $\dot{w} \approx - \nu(c/a)u$, a radial response quantity is smoother than the corresponding longitudinal response quantity. Furthermore, radial response is much smaller than the corresponding longitudinal response for longitudinal excitation. Thus, only longitudinal response quantities are shown.

acceleration histories at $\alpha/L = 0.24^{*}$. Basing the mesh width to characteristic wave length ratio, $\Delta\alpha/\lambda$, on response appropriate to non-dispersive propagation, we see that the convergence behavior of the finite difference computations in the example is similar but slightly superior to that observed in Fig. 1. This judgement is further supported by the response snapshots shown in Figs. 5 and 6. From Figs. 1-6, therefore, we conclude that the convergence of finite difference computations of displacement, velocity and acceleration response appropriate to in-plane $(\vec{\alpha}, \tilde{t})$ - excitation is satisfactory if $\Delta\alpha/\lambda \lesssim 1/20$.

The two preceding examples pertain to $(\vec{\alpha}, \tilde{t})$ - excitations that are temporally quite gradual and possess relatively well defined characteristic temporal wave lengths. Let us now consider an example in which the excitation is significantly less gradual and possesses no readily identifiable temporal wave length, viz., the ramp loading case described as Example 3 in Table 2. This excitation constitutes somewhat of an extreme test for in-plane $(\vec{\alpha}, \tilde{t})$ - excitations in that it produces a discontinuity in longitudinal shell acceleration. Fig. 7 presents displacement, velocity and acceleration histories at $\alpha/a = 1$. We observe that, because of the discontinuity in longitudinal shell acceleration, convergence of the finite difference computations for that quantity are only marginal; computations of the other kinematic quantities are satisfactorily convergent. This observation also applies to Fig. 8, which shows displacement, velocity and acceleration snapshots at $ct/a = 2$. Both of these figures display oscillations in the computed acceleration records that are characterized by non-dimensional spatial and temporal wavelengths of approximately $\pi\Delta\alpha/a$. This phenomenon is analogous to the familiar Gibbs' phenomenon in Fourier series solutions.

2.1.2 $(\tilde{\alpha}, \vec{t})$ - Excitations

The next example (Example 4) involves an $(\tilde{\alpha}, \vec{t})$ - excitation in the form of a longitudinal impulsive loading that gives rise to the initial

---

*Because $k_e a \sim 1$, the radial response quantities are comparable in magnitude to the longitudinal response quantities. The former are at least as smooth as the latter, however, so that again it is sufficient to display only the longitudinal response quantities.

velocity distribution described in Table 2. As discussed in Appendix B, $(k_\epsilon a)^2 \gg 1$, so that this example constitutes an essentially non-dispersive wave propagation problem. Fig. 9 shows displacement, velocity and acceleration histories at a distance $\alpha/L = 0.21$ to the right of the plane of loading anti-symmetry. We observe that, for a given $\Delta\alpha/\lambda$ - ratio, convergence behavior is about the same for this $(\tilde{\alpha}, \vec{t})$ - excitation as it is for the $(\vec{\alpha}, \tilde{t})$ - excitation of Example 1. In order to assure ourselves that satisfactory convergence for all kinematic quantities can indeed be attained, we examine Fig. 10, which presents displacement, velocity and acceleration snapshots at $ct/a = 0.2132$ and 0.8528.

The fifth example also deals with an $(\tilde{\alpha}, \vec{t})$ - excitation in the form of a longitudinal impulsive loading which produces an initial velocity condition. In this case, however, $k_\epsilon a \sim 1$ (Appendix B), so that the wave propagated along the shell suffers significant dispersion. Fig. 11 presents longitudinal displacement, velocity and acceleration histories at a distance $\alpha/L = 0.12$ to the right of the plane of loading anti-symmetry. The figure indicates that convergence is satisfactory for all quantities when $\Delta\alpha/\lambda \ll 1$. This is supported by Fig. 12, which shows displacement, velocity and acceleration snapshots at $ct/a = 1.91$ and 5.73. At the earlier time, dispersion effects have not yet become significant, so that the non-dispersive curves shown in the figure constitute accurate representations of the true response. This is no longer the case, however, at $ct/a = 5.73$.

As Example 6, we examine an $(\tilde{\alpha}, \vec{t})$ - excitation which gives rise to discontinuities in longitudinal acceleration, i.e., we consider the saw-tooth impulse loading described in Table 2. Displacement, velocity and acceleration histories at $\alpha/a = 2$ and snapshots at $ct/a = 2$ are shown in Figs. 13 and 14, respectively; these display the same marginal (at best) convergence in the acceleration computations that was observed in the $(\vec{\alpha}, \tilde{t})$ - excitation example of Figs. 7 and 8.

2.1.3 $(\vec{\alpha}, \vec{t})$ - Excitations

The seventh example deals with an $(\vec{\alpha}, \vec{t})$ - excitation, viz., a step end-velocity excitation. Because of the discontinuity in longitudinal shell velocity, the finite difference computations for that quantity, as

shown in Figs. 15 and 16, are only marginally convergent. Furthermore, because the acceleration can only be defined in terms of a generalized function (viz., the Dirac delta-function) at the wave front, computations of that quantity by the finite difference method (or, in fact, by other numerical methods) are unsatisfactory.

The final example of this section (Example 8) involves a non-axisymmetric $(\vec{\alpha}, \vec{t})$ - excitation in the form of a step end-velocity distributed as cos β for $-\frac{\pi}{2} \leq \beta \leq \pi/2$. Figure 17 shows displacement, velocity and acceleration snapshots at $ct/a = 2$, $\beta = 0$ and 90°. Comparing this figure with Fig. 15, we observe that, for $a_{\Delta\beta}/\lambda_{\beta} \ll 1$, the presence of gentle asymmetry has no effect on general convergence behavior. The gentle but distinct asymmetry is illustrated in Fig. 18, which shows kinematic response snapshots at $ct/a = 2$ and $\alpha/a = 1$.

2.1.4 Conclusions

From Figs. 1-18, we draw the following conclusions regarding thin shell finite difference computation of shell response to in-plane excitation. First, we conclude that computations of kinematic response quantities appropriate to $(\vec{\alpha}, \tilde{t})$ -, $(\tilde{\alpha}, \vec{t})$ -, and therefore $(\tilde{\alpha}, \tilde{t})$ - excitations are satisfactorily convergent as long as the ratio of each spatial mesh dimension to the shortest corresponding characteristic spatial wave length of the response is much less than unity. The value of the ratio required is determined by the length of time for which solutions are desired: the longer the time, the smaller the ratio must be. Second, we conclude that if an excitation produces a discontinuity in a response quantity, the finite difference computation of that quantity will be at best only marginally convergent due to the appearance of a type of Gibbs' phenomenon. Third, we conclude that the finite difference method cannot be used to compute the acceleration response of a shell subjected to an in-plane $(\vec{\alpha}, \vec{t})$ - excitation. As a final note: It is fitting that finite difference computations of shell response appropriate to $(\vec{\alpha}, \tilde{t})$ - excitations possess about the same convergence behavior as those appropriate to $(\tilde{\alpha}, \vec{t})$ - excitations. Finite difference computations of an $(\tilde{\alpha}, \vec{t})$ - generated wave that is reflected from a shell boundary are therefore as accurate after reflection as they are before reflection. This is because the reflection of an $(\tilde{\alpha}, \vec{t})$ - generated wave by a shell boundary directly

corresponds to the superposition of two waves: the $(\tilde{\alpha}, \vec{t})$ - generated wave propagating in the absence of a boundary and an $(\vec{\alpha}, \tilde{t})$ - generated wave produced at the boundary through the enforcement of the boundary condition.

2.2 DISPLACEMENT, VELOCITY AND ACCELERATION RESPONSE TO TRANSVERSE EXCITATION

The propagation of waves generated by transverse excitations is characterized by severe dispersion. We are therefore denied here the simple spatial wave length descriptions embodied in many of the preceding examples. Thus we deal immediately with transverse excitations that introduce no well-defined characteristic temporal or spatial wave lengths, but which are mathematically simple.

2.2.1 $(\vec{\alpha}, \tilde{t})$ - Excitation

The first example of this section, Example 9, involves the $(\vec{\alpha}, \tilde{t})$ - excitation of a clamped-clamped cylindrical shell by a uniform, radial step-pressure. That this problem constitutes a simple $(\vec{\alpha}, \tilde{t})$ flexural wave propagation problem is shown by the following argument. Consider an infinite shell excited over its entire length by the uniform step-pressure; its response is given by $w(\alpha,\beta,t) = w_\infty(t) = (P_o a^2/\rho h c^2)\,(1 - \cos ct/a)$, where P_o is the magnitude of the pressure step. Now consider an identical infinite shell excited axisymmetrically at $\alpha = 0$ and $\alpha = L$ by the prescribed radial displacements $w(0,\beta,t) = w(L,\beta,t) = - w_\infty(t)$. Since the combination of these two problems yields the problem of Example 9, and since the uniformly excited infinite shell problem embodies no flexural wave effects, Example 9 does constitute a simple $(\vec{\alpha}, \tilde{t})$ flexural wave propagation problem.

Fig. 19 shows displacement, velocity, and acceleration histories at $\alpha/L = \frac{1}{2}$ for Example 9.* We see that, while displacement and velocity convergence may be termed satisfactory, convergence of the acceleration computations is, at best, marginal. This convergence difficulty is analogous

*Longitudinal responses computed at other stations along the shell proved to be smaller and generally smoother than the corresponding radial responses.

to that of the previous section, which was associated with a discontinuity at the extensional wave front. As implied in Section 1.3, we cannot associate the propagation of a wave front with the elementary (Bernoulli-Euler) flexural equations. To do this, we employ improved (Timoshenko) theory that introduces an extensional wave front travelling at velocity $c = [E/\rho(1-\nu^2)]^{1/2}$ and a shear wave front travelling at velocity $c_s = [\varkappa E/2\rho(1+\nu)]^{1/2}$, where $\varkappa$ is the shear factor ($0.8 \lesssim \varkappa \lesssim 1.0$). On this basis, we see that the high-frequency oscillations in the $\Delta\alpha/h = 1$ acceleration history of Fig. 19 appear to begin with the arrival of two acceleration discontinuities (one from each end) that travel at c_s and simultaneously reach the shell's mid-station at $ct/a \approx 2$ (see, e.g., Ref. 13). A short time later, the acceleration history smooths out, only to be disrupted again upon the second arrival at $ct/a \approx 6$ of the acceleration discontinuities, which have been reflected from the ends of the shell. This interpretation is supported by the $\Delta\alpha/h = 1$ curves of Figs. 20 and 21, which show displacement, velocity and acceleration snapshots at $ct/a = 1.2$ and 4.8, respectively. The analogy between this behavior and that of the previous subsection is more completely established by comparison of Figs. 19 and 7.

While the $\Delta\alpha/h = 1$ computations appear to predict with some degree of accuracy the arrival of an acceleration discontinuity, the computations for other values of $\Delta\alpha/h$ either ignore its arrival or, in the case of the $\Delta\alpha/h = \frac{1}{2}$ computations, predict the arrival of a flexural wave with a velocity even greater than the dilatational velocity. This is in contrast to the case involving in-plane excitation, where changes in the value of $\Delta\alpha/h$ produce no such radical changes in the computed responses (see Fig. 7). We conclude, therefore, that the less than satisfactory convergence of the finite difference acceleration computations is due to the inability of elementary bending theory to treat properly the short wave length components contained in the acceleration response. The use of a finite differnce code based on improved theory should materially inprove this situation, even though the problem of dealing numerically with a response discontinuity would still be present.*

*The modal superposition acceleration snapshots of Figs. 20 and 21, which are computed from 180 modal responses appropriate to improved shell theory (Ref. 15), cannot be accurate in the vicinity of the acceleration discontinuity either; this problem will be discussed in greater detail later.

2.2.2 $(\tilde{\alpha}, \vec{t})$ - Excitation

The next example, Example 10, involves the $(\tilde{\alpha}, \vec{t})$ - excitation of the clamped-clamped cylindrical shell of Example 9 by an axisymmetric, triangular radial impulse. Fig. 22 shows displacement, velocity and acceleration histories at $\alpha/L = \frac{1}{2}$*. As in the previous example, convergence of the displacement and velocity computations is satisfactory, whereas convergence of the acceleration computations is, at best, marginal. This is also reflected in Figs. 23 and 24, which show displacement, velocity and acceleration snapshots at $ct/a = 1.2$ and 4.8, respectively. We observe from the latter that the lack of convergence in the acceleration computations persists even at rather late times. The problem is alleviated somewhat if the discontinuity in the spatial derivative of the initial velocity distribution is reduced. This is demonstrated in Fig. 25, which presents displacement, velocity and acceleration histories at $\alpha/L = \frac{1}{2}$ for the shell of Example 10 excited by an axisymmetric triangular radial impulse whose base is twice as wide as that appropriate to Fig. 22.

2.2.3 $(\vec{\alpha}, \vec{t})$ - Excitations

We now proceed to an example (Example 11) that involves an $(\vec{\alpha}, \vec{t})$ - excitation in the form of a uniform radial impulse applied to the clamped-clamped cylindrical shell of Example 9. It is easily seen that the displacement and velocity responses of this example are identical to the velocity and acceleration responses, respectively, of Example 9 (Figs. 19-21). Hence the discussion of the lack of convergence in the acceleration computations of Example 9 directly applies to the velocity computations of this example. We show the displacement and velocity responses as well as an acceleration history and two acceleration snapshots for this example in Figs. 26-28; these figures demonstrate that convergence of the finite difference acceleration computations is clearly unsatisfactory. The improved theory modal superposition computations are also suspect, in view of the discontinuity in the shell's velocity response.

---

*Again, longitudinal responses computed at other stations along the shell proved to be smaller and generally smoother than the corresponding radial responses.

In order to assess the effects of variations in $(\vec{\alpha}, \vec{t})$ - excitations, we consider as Example 12 the problem of the previous example with the clamped supports changed to free supports. Displacement, velocity and acceleration histories at $\alpha/L = 1/4$ are shown in Fig. 29 to demonstrate the smoothness of the longitudinal responses in relation to the corresponding radial responses. For these boundary conditions, longitudinal response is comparable in magnitude to radial response, a situation that does not occur in the case of clamped boundaries. Fig. 30 shows radial displacement, velocity and acceleration histories at $\alpha/L = 1/2$; comparing these results with those of Fig. 26, we see that the change in boundary conditions has no effect on the convergence behavior of the finite difference computations. This is also demonstrated in Figs. 31 and 32, which show displacement, velocity and acceleration snapshots at $ct/a = 1.2$ and $ct/a = 4.8$, respectively.

As Example 13, we examine the non-axisymmetric response of a clamped-clamped cylindrical shell to an $(\vec{\alpha}, \vec{t})$ - excitation in the form of a longitudinally uniform radial impulse that is distributed as $\cos \beta$ over the region $-\pi/2 \leq \beta \leq \pi/2$. In order to evaluate better the effects of gentle asymmetry, displacement, velocity and acceleration histories at $\alpha/L = 0.50$ are shown in Fig. 33 for the associated axisymmetric problem involving a uniform radial impulse. The less than satisfactory convergence of the velocity and acceleration computations is again apparent. Fig. 34 shows displacement, velocity and acceleration histories for the cosine radial impulse problem at $\alpha/L = 0.50$ and $\beta = 0$. The differences between these results and those of Fig. 33 are minor. Fig. 35, which shows corresponding histories at $\alpha/L = 0.50$ and $\beta = 90^{\circ}$, demonstrates that the convergence behavior of the axisymmetric and $\beta = 0$ results also characterizes the results at points on the shell that are not directly excited. The gentle but distinct asymmetry of the cosine impulse problem is illustrated in Fig. 36, which shows displacement, velocity and acceleration snapshots at $ct/a = 0.78$ and $\alpha/L = 0.50$. The $\Delta\alpha/h = 0.92$ and 1.73 results agree well at this early time; from Figs. 34 and 35, however, we see that these results begin to diverge a short time later. Finally, Figs. 37 and 38 show displacement, velocity and acceleration snapshots at $ct/a = 0.78$ for the uniform impulse problem and at $ct/a = 0.78$, $\beta = 0$ for the cosine impulse problem, respectively. As with Figs. 33 and 34, these computations display virtually

identical behavior. We conclude from Figs. 33-38, therefore, that finite difference response computations for gently non-axisymmetric excitations display the same convergence behavior as those for corresponding axisymmetric excitations.

2.2.4 Smoothed Excitations

The three preceding examples have demonstrated that, because of the limitations of the elementary bending theory on which they are based and because of their inability to treat properly response discontinuities, convergence of the finite difference computations of velocity and acceleration responses to $(\vec{\alpha}, \vec{t})$ - excitations are less than satisfactory. It is of interest, then, to examine two methods for modifying the excitation so as to ameliorate this situation.

The first method consists of smoothing the excitation temporally, e.g., converting the impulsive loading of Example 12 into a pressure loading of small, but finite, duration. Such a conversion is shown as Example 14 in Table 2. Displacement, velocity and acceleration histories appropriate to the load duration $ct_w/a = 0.82$ are shown in Fig. 39. This duration is much less than the period $c\tilde{T}/a = 2\pi$ of the sinusoidal response appropriate to the associated problem of an impulsively excited infinite shell. Hence the displacement response of Fig. 39 agrees quite well with that of Fig. 30, once the former is moved to the left a distance $ct_s/a = 0.41$ to allow for the finite duration of the triangular pressure loading. Convergence of the velocity and acceleration computations of Fig. 39 is much better than that of Fig. 30, however; we observe that smoothing even allows us to use the very fine mesh $\Delta\alpha/h = \frac{1}{2}$ without introducing the high-frequency oscillations encountered in $\Delta\alpha/h = 1$ acceleration computation of Fig. 30. Still further improvement in convergence behavior is achieved if the width of the triangular pressure loading is increased to $ct_w/a = 1.64$, as shown in Fig. 40. If the time shift $ct_s/a = 0.82$ is introduced into these results, even this temporally rather broad excitation constitutes a reasonable approximation to the impulsive excitation of Example 12.

The effects of temporal smoothing are even more clearly demonstrated in Fig. 41, which shows velocity and acceleration snapshots at $ct/a = 1.2$ for the shell of Example 12. Shown are 1) response snapshots for a uniform

impulse loading as computed with the modal superposition method based on improved theory, and 2) response snapshots for a spatially uniform triangular pressure loading of width $ct_w/a = 0.40$ as computed with the finite difference method based on elementary theory.* From this figure and Fig. 31, we see that there is much better agreement between the finite difference responses appropriate to the triangular pressure loading and the modal superposition solutions than between the latter and the finite difference solutions appropriate to the impulse loading.

The second method for improving the convergence of finite difference computations of velocity and acceleration responses to $(\vec{\alpha}, \vec{t})$ - excitations consists of smoothing the excitations spatially. For example, we might convert the uniform impulsive loading of Example 12 into an axisymmetric impulsive loading which constitutes a truncated Fourier series expansion $(\sin m\pi\alpha/L)$ of the longitudinally uniform loading, as shown as Example 15 in Fig. 42. Displacement, velocity, and acceleration histories at $\alpha/L = \frac{1}{2}$ for $m_{max} = 5$ are shown in Fig. 43; we observe that convergence is satisfactory for all three responses. Similar histories for $m_{max} = 11$ are shown in Fig. 44; here we must make velocity and acceleration computations with $\Delta\alpha/h = 1/2$ to demonstrate satisfactory convergence. Fig. 45 shows comparable histories for $m_{max} = 23$; at this point we find that the convergence of the displacement, velocity and acceleration computations is satisfactory, marginal and unsatisfactory, respectively. Thus, for $m_{max} = 23$, we have essentially the same convergence situation as that shown in Fig. 30 for the uniform impulsive loading.

2.2.5 Conclusions

From Figs. 19-45, we draw the following conclusions regarding thin shell finite difference computation of shell response to transverse excitation. First, we conclude that computations of displacement and velocity response appropriate to $(\vec{\alpha}, \tilde{t})$ -, $(\tilde{\alpha}, \vec{t})$ -, and therefore $(\tilde{\alpha}, \tilde{t})$ - excitations are satisfactorily convergent as long as the ratio of each spatial mesh

*A time shift of $ct_s/a = 0.20$ has been introduced into the finite difference results to position the peak of the triangular pressure loading at $t = 0$.

dimension to the shortest corresponding characteristic spatial wave length of the response is appreciably less than unity.* The convergence of transverse acceleration computations, however, is only marginal for $(\vec{\alpha}, \tilde{t})$ - and $(\tilde{\alpha}, \vec{t})$ - excitations, especially when discontinuities are involved. Second we conclude that the convergence of finite difference computations of transverse displacement, velocity, and acceleration response to $(\vec{\alpha}, \vec{t})$ - excitations is satisfactory, marginal, and unsatisfactory, respectively. This difficulty may be substantially overcome, however, by either temporal or spatial smoothing of the excitation. Third, we conclude that the convergence difficulties observed derive from two sources: the presence of discontinuities in certain responses, and the failure of thin (Bernoulli-Euler) shell theory to account properly for short structural wave length response components that contribute significantly to the total response.

2.3 STRESS/STRAIN RESPONSE TO IN-PLANE EXCITATION

We examine here the convergence of finite difference computations of stress/strain response to predominantly in-plane excitation of cylindrical and conical shells.

2.3.1 $(\vec{\alpha}, \tilde{t})$ -, $(\tilde{\alpha}, \vec{t})$ -, and $(\vec{\alpha}, \vec{t})$ - Excitations

We first consider the $(\vec{\alpha}, \tilde{t})$ - excitation problem of Example 2, whose kinematic shell responses were studied in Section 2.1. We skip Example 1 of that section because, for the virtually non-dispersive propagation that it displays, the essentially membrane stress and strain responses are almost directly proportional to the longitudinal velocity response of the shell, which has already been studied. Since Example 2 involves dispersive propagation, however, it is of interest to examine longitudinal membrane stress response for this case. Fig. 46 shows membrane stress responses at $\alpha/L = 0.24$, $ct/a = 5.73$ and $ct/a = 17.2$, respectively; convergence is seen to be satisfactory for $\Delta\alpha/\lambda_\sigma \ll 1$, where λ_σ is the stress characteristic wave length for dispersion-free propagation.

*Although we have not observed in this Section any gradual deterioration in accuracy with increasing time, the emergence of this problem in certain computations of the previous Section suggest that it may occur in computations for transverse excitations also. Fortunately, the problem is readily detected by means of multiple computations with various mesh dimensions.

The next example is the $(\vec{\alpha}, \tilde{t})$ - excitation problem of Example 3. Membrane stress responses at $\alpha/a = 1$ and $ct/a = 2$ for this example are shown in Fig. 47. Because of the absence of discontinuities, convergence of the finite difference computations is entirely satisfactory.

For the reason given above in connection with Example 1, we skip Example 4 and proceed to the $(\tilde{\alpha}, \vec{t})$ - excitation problem of Example 5. In Fig. 48, which shows longitudinal strain responses at $\alpha/L = 0.62$, $ct/a = 1.91$, and $ct/a = 5.73$, we find again that convergence of the finite difference computations is satisfactory for $\Delta\alpha/\lambda_\sigma \ll 1$.

Since the $(\tilde{\alpha}, \vec{t})$ - excitation of Example 6 (the saw tooth impulse) produces no discontinuities in stress/strain response, convergence of the corresponding finite difference computations is satisfactory, as it was for the $(\vec{\alpha}, \tilde{t})$ - excitation of Example 3 (see Fig. 47). Thus, we omit detailed examination of the stress/strain responses for this loading and proceed to the $(\vec{\alpha}, \vec{t})$ - excitation of Example 7. Because this excitation does produce discontinuities in longitudinal membrane stress/strain response, convergence of the finite difference computations of such response is, as indicated in Fig. 49, only marginal. The same is true for the corresponding non-axisymmetric case of Example 8, as indicated in Fig. 50.

2.3.2 Conclusions

From Figs. 46-50, we draw two conclusions. First, we conclude that finite difference computations of stress/strain response to predominantly in-plane excitation converge satisfactorily for cases involving $(\vec{\alpha}, \tilde{t})$ -, $(\tilde{\alpha}, \vec{t})$ -, and therefore $(\tilde{\alpha}, \tilde{t})$ - excitations, as long as the ratio at each spatial mesh dimension to the shortest corresponding characteristic spatial wave length of the response is much less than unity. Second, we conclude that the convergence of these same computations appropriate to in-plane $(\vec{\alpha}, \vec{t})$- excitations is only marginal as a result of the discontinuities present.

2.3.3 Comparison with Experimental Data

We now direct our attention to the comparison of finite difference computations of strain response with corresponding experimental data. The

first set of data, which derive from the excitation of very long cylindrical shells at one end by the imposition of axisymmetric, 20 μsec long, box-shaped longitudinal velocities, is described as Example 16 in Table 2. Strain histories for Specimen T-1 are shown in Fig. 51 at $\alpha = 3$ inches and 7.5 inches. We observe that, while the computations of peak strain and wave arrival time are accurate, the late time behavior of the experimentally measured longitudinal strain histories is not accurately predicted by the computed histories. Similar histories for Specimens T-13 and T-14 are shown in Figs. 52 and 53; we observe that the computations of peak strain are also accurate for these shells, but that computed arrival times and pulse shapes are not completely satisfactory. Disagreement between computed and measured pulse shapes should not be given too much weight, however, because the velocity excitations at the ends of the shells were never actually measured; the box-velocity excitation is only an assumed input based on less refined measurements.

Experiments in which the excitations were quite carefully measured are reported in Ref. 17. These experiments, which are described as Example 17 in Table 2, involve the axisymmetric longitudinal excitation of a hollow cone that is struck at the closed end by steel balls of various diameters. The excitations are given as longitudinal strain histories measured by a quartz crystal located at the impacted end of the cone. These inputs can be accurately described as

$$\epsilon_I(t) = \begin{cases} \epsilon_o \sin^2 \dfrac{\pi t}{\tau} & , \quad 0 \le t \le \tau \\ 0 & , \quad \text{otherwise} \end{cases} \tag{1}$$

Since this is hardly a complete specification of boundary conditions at the impacted end of the cone, some analysis is necessary.

The meridional stress resultant for an axisymmetrically excited conical shell can be written in the form

$$N_\alpha = \frac{Eh}{1-\nu^2}\left[\frac{\partial u}{\partial \alpha} + \frac{\nu}{a}\left(u \sin \varphi - w \cos \varphi\right)\right] \tag{2}$$

At the impacted end of the "shell" of Fig. 54, it seems reasonable to take $\partial w/\partial\alpha = 0$, so that, at that point, $\varepsilon_I = \frac{\partial}{\partial(\alpha \cos \varphi)} (u_{\text{longitudinal}})$ $= \partial u/\partial\alpha + \tan \varphi \, \partial w/\partial\alpha = \partial u/\partial\alpha$. It also seems reasonable to take u_{radial} $= -u \sin \varphi + w \cos \varphi$ equal to zero at the impacted end, which makes the term containing Poisson's ratio vanish. Unfortunately, the STAR code cannot handle mixed end conditions like $u \sin \varphi - w \cos \varphi = 0$, so that we now introduce an approximation. Since, for this "shell", $\varphi = 0.175 = \ll \pi/2$, we write from Eq. 2

$$N_\alpha \approx \frac{Eh}{1-\nu^2} \left(\frac{\partial u}{\partial \alpha} - \nu \frac{w}{a} \right) \tag{3}$$

which is the equivalent cylindrical shell aproximation. To make the Poisson's ratio term vanish, then, we take $w = 0$. Our boundary conditions at the impacted end of the hollow cone are therefore taken as

$$\begin{aligned} N_\alpha(\alpha_1, t) &= \frac{Eh}{1-\nu^2} \, \varepsilon_I(t) \\ w(\alpha_1, t) &= 0 \\ \frac{\partial w}{\partial \alpha}(\alpha_1, t) &= 0 \end{aligned} \tag{4}$$

Figure 54 shows STAR code computations of meridional membrane strain responses along with the experimental results. The very satisfactory performance of the thin shell equations used in the STAR code is surprising until we note that, except for the excitation of Fig. 54d, the structural wave lengths characterizing the primarily longitudinal shell response considerably exceed the 1/4 inch "shell" thickness. However, even in the case of Fig. 54d, for which the spatial width of the pulse is only about four times the mesh spacing, agreement between the computed and experimental results is satisfactory. Figure 54e shows extended results which include bending effects as well as wave reflection effects from the other end of the hollow cone. From this figure, we conclude first (Gage 2 results) that the STAR code accurately accounts for bending effects in the hollow cone, and second (Gage 3 results) that the free edge boundary condition

assumed at the far end of the cone is not a very successful simulation of the experimental boundary conditions, which were "not definitively established" by the experimentalists.

2.4 STRESS/STRAIN RESPONSE TO TRANSVERSE EXCITATION

We now investigate the convergence of finite difference computations of stress/strain response in cylindrical shells to predominantly transverse excitations.

2.4.1 $(\vec{\alpha}, \tilde{t})$ -, $(\tilde{\alpha}, \vec{t})$ -, and $(\vec{\alpha}, \vec{t})$ - Excitations

Our first example is Example 9, whose kinematic responses to a transverse $(\vec{\alpha}, \tilde{t})$ - excitation were the first studied in Section 2.2. Figure 55 shows longitudinal strain histories at $\alpha/L = 0$ and $\frac{1}{2}$.* We find that convergence of the membrane strain computations is uniformly satisfactory. Although we must use the rather fine mesh $\Delta\alpha/h = \frac{1}{2}$ to obtain generally acceptable convergence of the flexural strain computations, and although the computations appropriate to this mesh predict the arrival of a disturbance that travels faster than even the dilatational velocity, convergence of the finite difference computations of flexural strain may still be termed satisfactory. This judgement is supported by Fig. 56, which shows longitudinal strain snapshots at $ct/a = 1.2$ and 4.8.

The next example is the $(\tilde{\alpha}, \vec{t})$ - excitation problem of Example 10. Longitudinal strain responses at $\alpha/L = \frac{1}{2}$, $ct/a = 1.2$ and $ct/a = 4.8$ are shown in Fig. 57. We conclude, on the same basis as that used in connection with Figs. 55 and 56, that convergence of the finite difference membrane and flexural strain computations is satisfactory.

We now proceed to the $(\vec{\alpha}, \vec{t})$ - excitation problem of Example 11. Longitudinal strain responses of the shell to this uniform impulse loading are shown in Fig. 58. Convergence of the finite difference computations for

*In this and subsequent examples, circumferential strain response is so smooth that convergence of the finite difference computations of this quantity is uniformly satisfactory.

flexural strain response is seen to be uniformly unsatisfactory. The use of $\Delta\alpha/h$ - ratios smaller than unity offers no solution; the resulting response computations are even more wildly oscillatory and predict the existence of disturbances which propagate at velocities exceeding even the dilatational velocity. Since improved theory predicts the propagation of no discontinuities in longitudinal strain response for $(\vec{\alpha}, \vec{\tau})$ - excitations, this convergence problem can only be associated with the short wave length limitations of elementary bending theory.

It is interesting to note in Fig. 58 that (especially the results for $ct/a = 1.2$) the thin shell finite difference computations seem reasonably accurate in regions well behind the shear wave front (see the discussion of Example 9 in Section 2.2). This is in agreement with the results of other investigators (see, e.g., Ref. 18). As we would expect from Section 2.2, the convergence behavior of the finite difference computations is unchanged by a variation of boundary conditions. For example, changing the clamped boundary conditions of Example 11 to free support boundary conditions (Example 12) produces no improvement in the unsatisfactory convergence of the finite difference flexural strain computations.

We conclude this subsection with a brief examination of nonaxisymmetric longitudinal strain response appropriate to the $(\vec{\alpha}, \vec{\tau})$ - excitation problem of Example 13. Fig. 59 shows longitudinal strain histories at $\alpha/L = 0.50$ for the associated axisymmetric problem appropriate to a uniform impulse and for the cosine impulse problem at $\beta = 0$ and $\beta = 90^{\circ}$. We observe the unsatisfactory convergence of the flexural strain computations in all cases, noting especially the dramatically premature arrival of a computed flexural wave for $\Delta\alpha/h = 0.60$. Thus, we again find that finite difference response computations for gently non-axisymmetric problems display the same convergence behavior as that appropriate to the corresponding axisymmetric problems.

2.4.2 Smoothed Excitations

In view of the unsatisfactory convergence behavior just observed, let us now apply the temporal and spatial excitation smoothing techniques discussed previously in Section 2.2. We first consider the case of

Example 14, i.e., the application of a uniform triangular pressure pulse. Longitudinal strain histories for a load duration $ct/a = 0.82$ and longitudinal strain snapshots for a load duration of $ct/a = 0.40$, along with corresponding results for the impulse loading, are shown in Fig. 60. We see that convergence of the finite difference computations is substantially achieved for the $ct/a = 0.82$ triangular pressure loading, and that the $ct/a = 0.40$ finite difference computations lie closer than those for the impulse loading tc the impulse loading response computed with improved shell theory. Similar improvement in convergence is effected with spatial smoothing, as shown in Fig. 61. This figure, which pertains to truncated longitudinal Fourier series expansions of a uniform impulsive loading (Example 15), shows longitudinal strain histories at $\alpha/L = \frac{1}{2}$. We see that convergence is satisfactory for $m_{max} = 5$ and 11, but is only marginal for $m_{max} = 23$.

2.4.3 Conclusions

From Figs. 55-61, we draw the following conclusions regarding finite difference computation of stress/strain response to transverse excitation. First, we conclude that computations appropriate to $(\vec{\alpha}, \tilde{t})$ -, $(\tilde{\alpha}, \vec{t})$ -, and therefore $(\tilde{\alpha}, \tilde{t})$ - excitations are satisfactorily convergent providing that the ratio of each spatial mesh dimension to the shortest corresponding characteristic spatial wave length of the response is appreciably less than unity. Second, we conclude the computations appropriate to $(\vec{\alpha}, \vec{t})$ - excitations are unsatisfactory, a difficulty which may be partially overcome, however, by either temporal or spatial smoothing of the excitation. Third, we conclude that the unsatisfactory convergence encountered is caused by the failure of thin shell theory to account properly for short structural wave length response components that contribute significantly to total response.

2.5 SUMMARY

The conclusions of Subsections 2.1.4, 2.2.5, 2.3.2 and 2.4.3 are summarized and generalized in Table 1. It is important to recognize that this table does not indicate at what mesh dimensions convergence will be achieved, but indicates only the convergence behavior to be expected as the mesh dimensions are reduced.

Table 1. Convergence Behavior of Finite Difference Computations Based on Thin Shell Theory

Type of Excitation (all $\tilde{\beta}$)

Response Quantity	$(\tilde{\alpha}, \tilde{t})$	$(\vec{\alpha}, \tilde{t}), (\tilde{\alpha}, \vec{t})$	$(\vec{\alpha}, \vec{t})$
$u, v, w, \dot{v}, \dot{w}, \ddot{v}$ $\epsilon_{\beta e}, \epsilon_{\alpha f}, \epsilon_{\beta f}, \epsilon_{\alpha\beta e}, \epsilon_{\alpha\beta f}$	satisfactory[1]	satisfactory[1]	satisfactory[1]
$\dot{u}, \ddot{w}$ $\epsilon_{\alpha e}$	satisfactory[1]	satisfactory[1]	marginal[2]
$\ddot{u}$	satisfactory[1]	marginal to[1,2] satisfactory	unsatisfactory[2]

IN-PLANE EXCITATIONS

Type of Excitation (all $\tilde{\beta}$)

Response Quantity	$(\tilde{\alpha}, \tilde{t})$	$(\vec{\alpha}, \tilde{t}), (\tilde{\alpha}, \vec{t})$	$(\vec{\alpha}, \vec{t})$
$u, v, w, \dot{u}, \dot{v}, \ddot{u}, \ddot{v}$ $\epsilon_{\alpha e}, \epsilon_{\beta e}, \epsilon_{\beta f}, \epsilon_{\alpha\beta e}, \epsilon_{\alpha\beta f}$	satisfactory[1]	satisfactory[1]	satisfactory[1]
$\dot{w}$	satisfactory[1]	satisfactory[1]	marginal to[2,3] unsatisfactory
$\epsilon_{\alpha f}$	satisfactory[1]	satisfactory[1]	unsatisfactory[3]
$\ddot{w}$	satisfactory[1]	marginal to[2,3] unsatisfactory	unsatisfactory[2]

TRANSVERSE EXCITATIONS

[1]Convergence occurs as $\Delta\alpha$ and $a\Delta\beta$ become appreciably smaller than the shortest corresponding characteristic spatial wave length of the response of interest

[2]Less than satisfactory convergence is due to the presence of response discontinuities

[3]Less than satisfactory convergence is due to the short flexural wave length limitations of thin shell theory

Table 2. Numerical Examples

Ex.	Figures	Shell No.	Shell Parameters				Excitation		Ref.
			L/a	a/h	ν	B.C.'s*	Prescribe Shape	Spatial or Temporal Width	
1	1-3	1	2.5	25	0.3	C-C	$u(0,t)$ 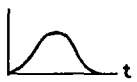	$0.533\ \frac{a}{c}$	12
2	4-6,46	2	20	100	0.3	C-C	$u(0,t)$	$3.82\ \frac{a}{c}$	12
3	7,8,47	3	∞	10	1/3	C	$N_\alpha(0,t)$ 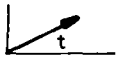		14
4	9,10	1					$\dot{u}(\alpha,0)$ 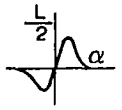	0.25a	12
5	11,12, 48	2					$\dot{u}(\alpha,0)$	4a	12, 15
6	13,14	3					$\dot{u}(\alpha,0)$ 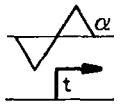	2a	
7	15,16, 49	3					$\dot{u}(0,t)$ 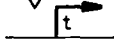		13, 14
8	17,18, 50	3					$\dot{u}(0,\beta,t)$ 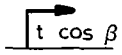	$-\frac{\pi}{2} \le \beta \le \frac{\pi}{2}$	
9	19-21, 55,56	4	2.4	20	0.25	C-C	$p(\alpha,t)$ 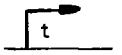		15
10	22-25, 57	4					$\dot{w}(\alpha,0)$ 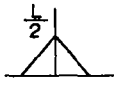	0.8a,1.6a	
11	26-28, 58	4					$p(\alpha,0)$		15
12	29-32	5	2.4	20	0.25	F-F	$p(\alpha,0)$ 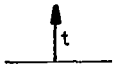		15
13	33-38, 59	6	1.65	17	0.286	C-C	$p(\alpha,\beta,0)$ 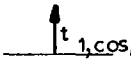	$\begin{matrix}-\pi \\ -\pi/2\end{matrix}\Big\} \le \beta \le \begin{Bmatrix}\pi \\ \pi/2\end{Bmatrix}$	
14	39-41, 60	5					$p(\alpha,t)$ 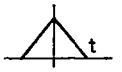	$0.82\ \frac{a}{c}, 1.64\ \frac{a}{c}, 0.40\ \frac{a}{c}$	
15	42-45, 61	5					$\dot{w}(\alpha,0) = \sum_{m=1,3}^{m_{max}} \frac{4}{\pi m} \sin\frac{m\pi\alpha}{L}$	$m_{max} = 5,11,23$	
16	51,52, 53	7	very long	19,7.5, 3.5	0.333	F-F	$\dot{u}(0,t)$ 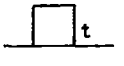	20 μ-sec	16
17	54	8	Fig. 54		0.333	Fig.54	$\epsilon(0,t)$ 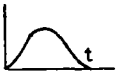	50,22,11, and 5 μ-sec	17

*C: clamped
F: freely-supported

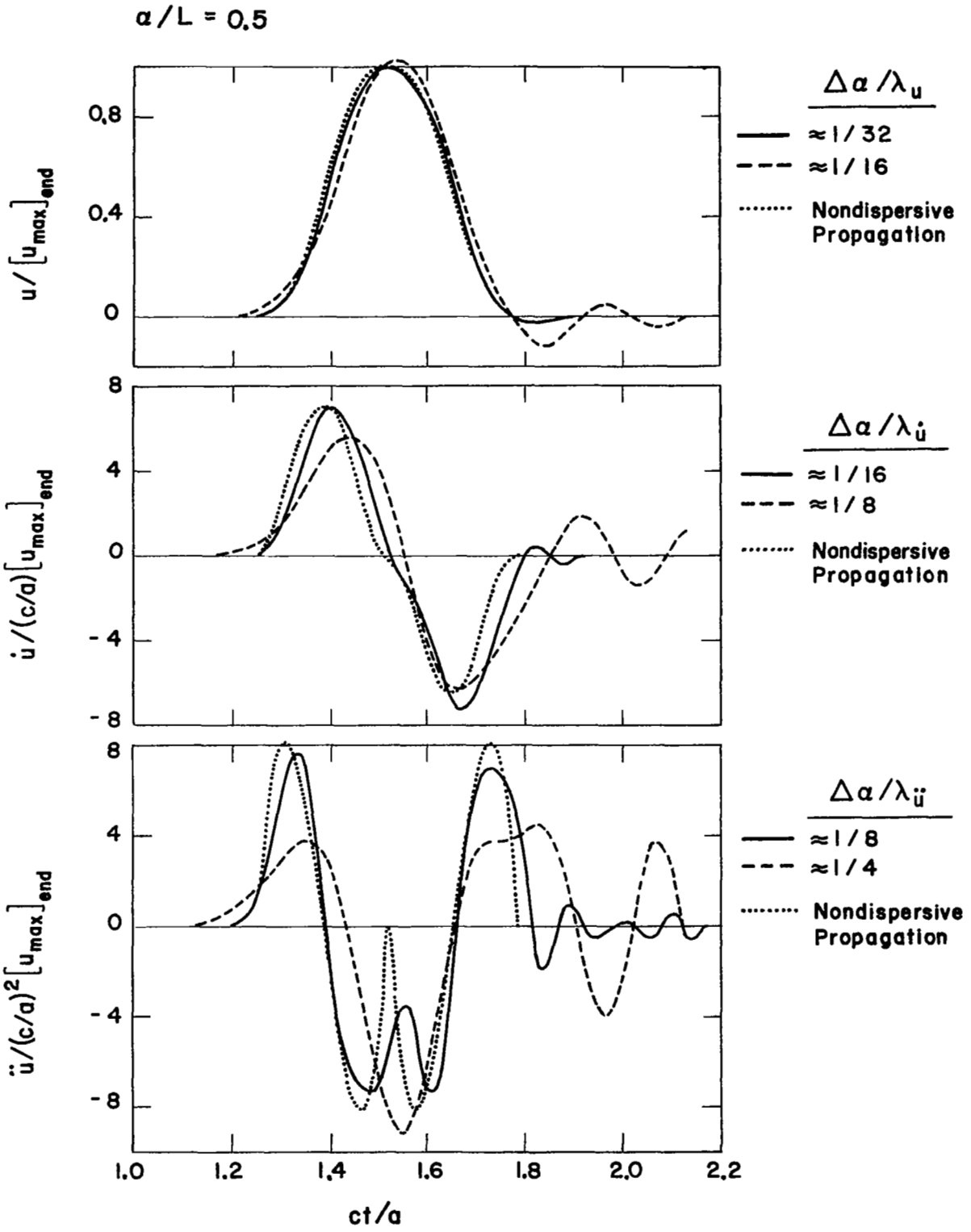

Figure 1. Kinematic Response Histories for Example 1

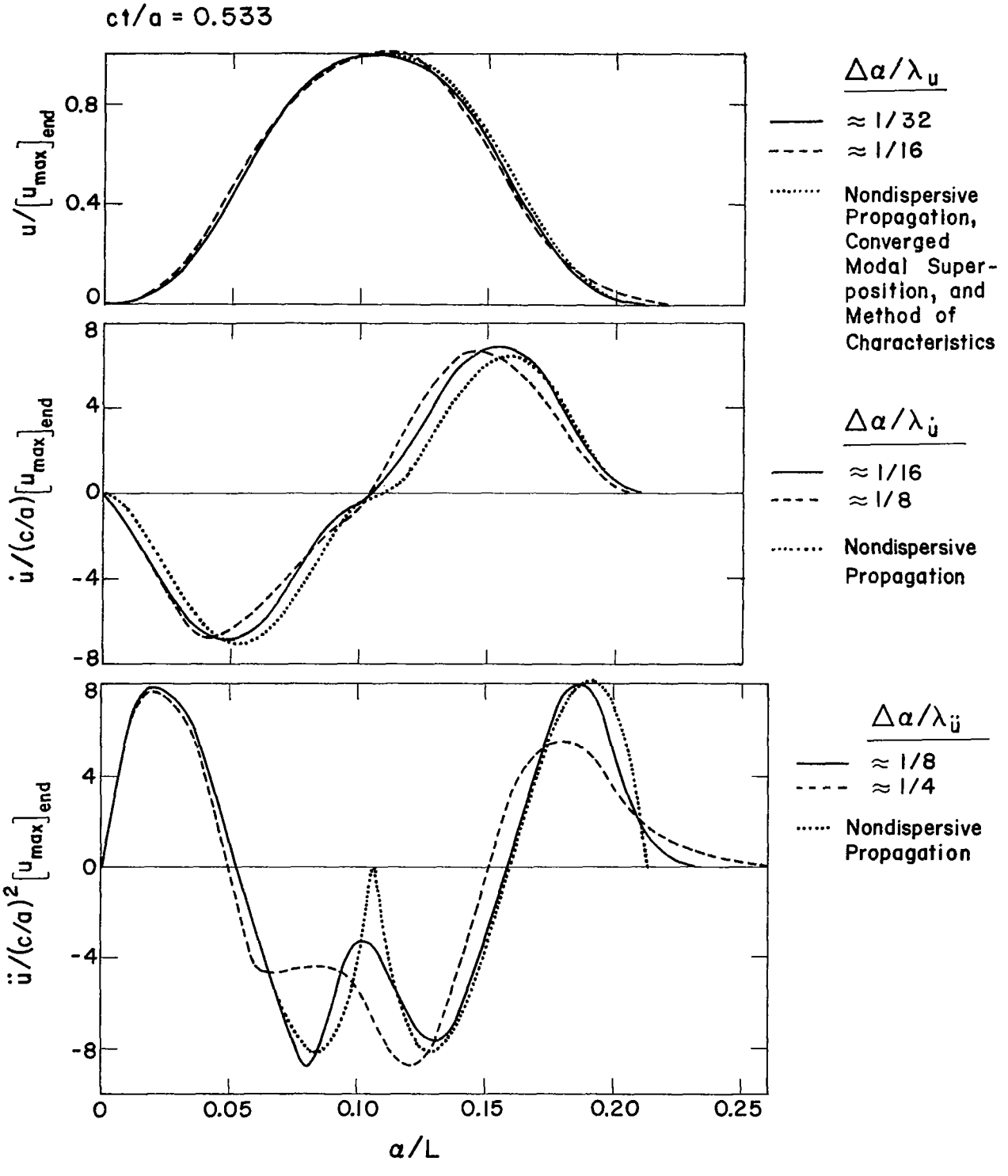

Figure 2. Kinematic Response Snapshots for Example 1

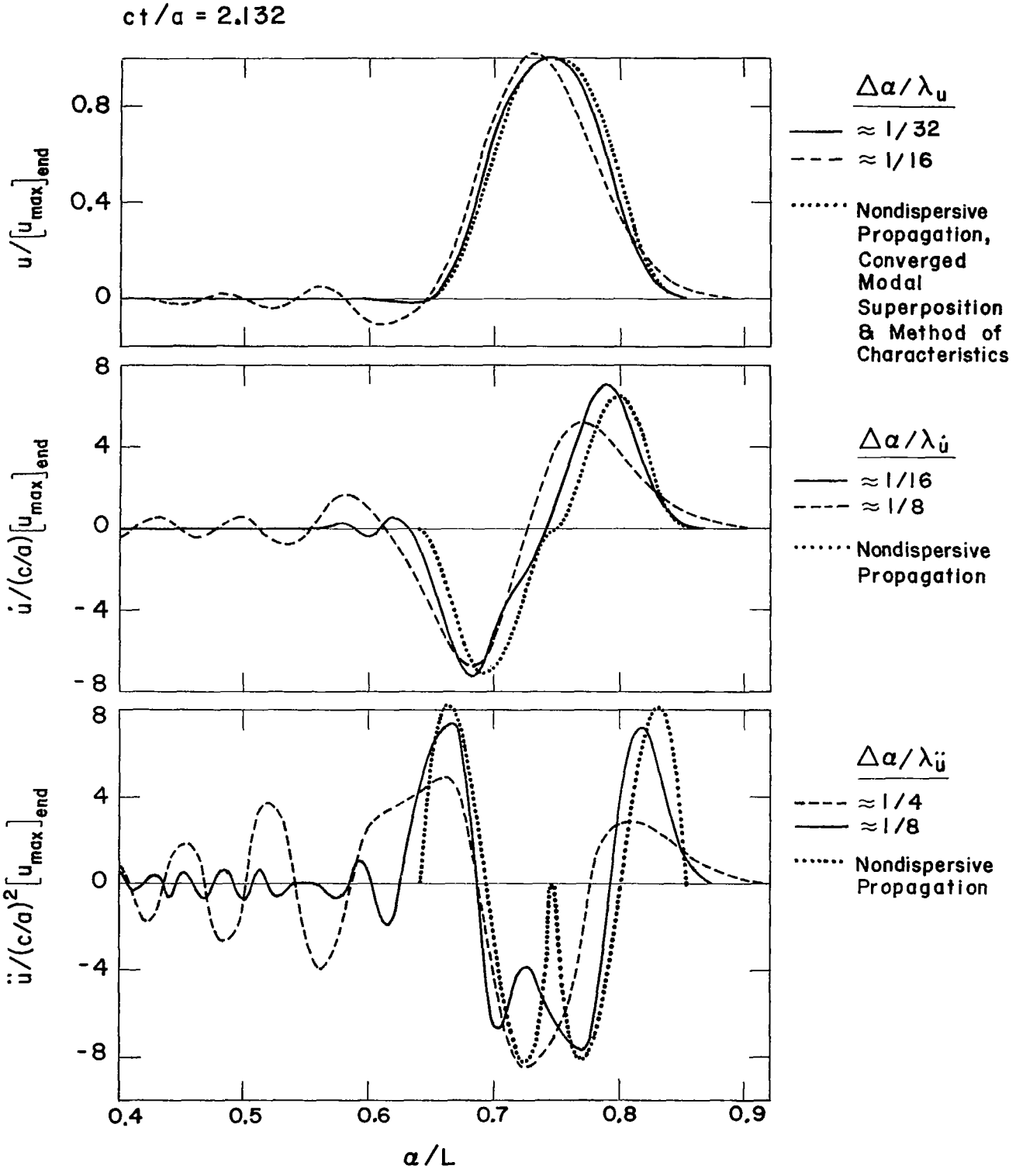

Figure 3. Kinematic Response Snapshots for Example 1

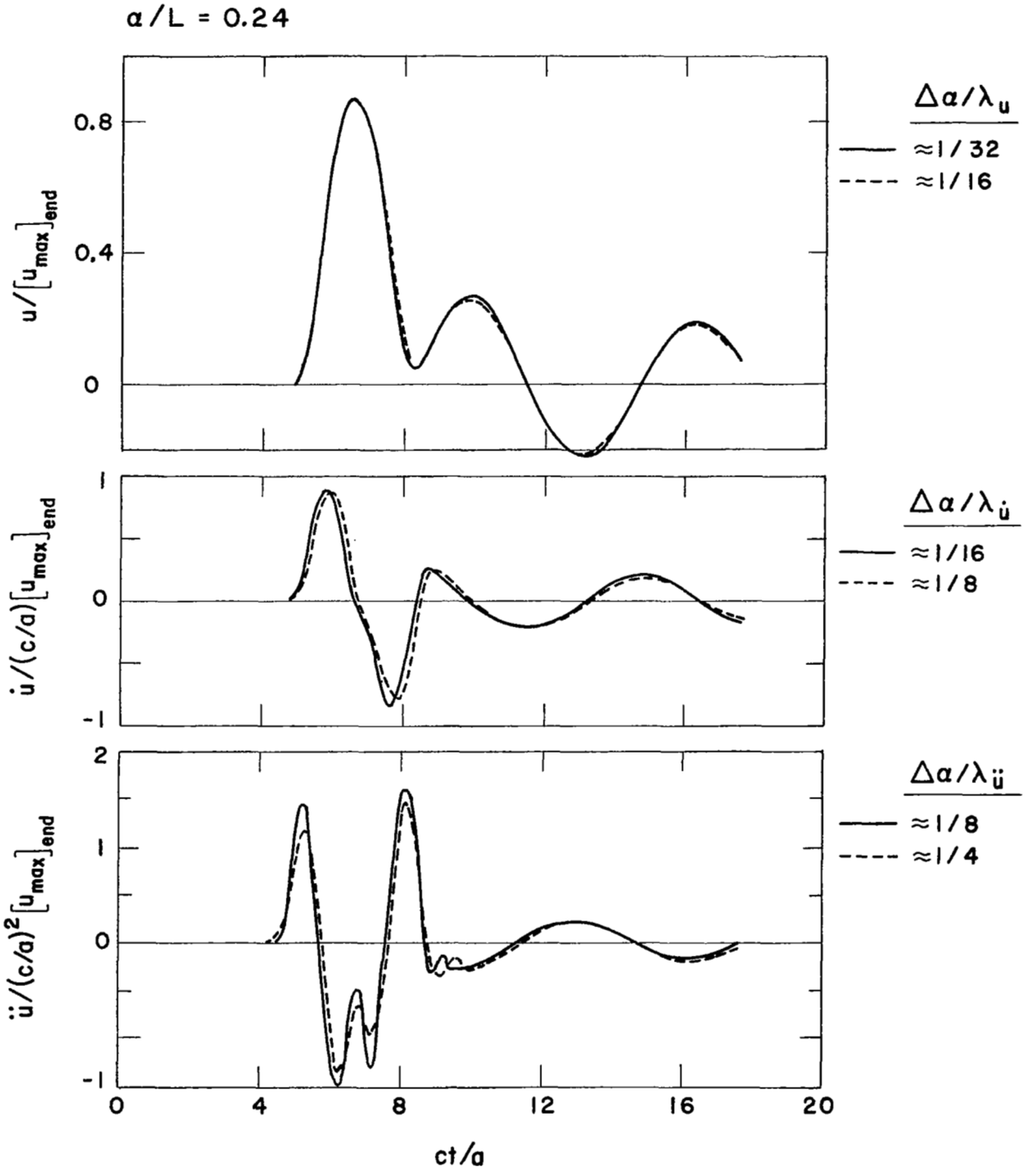

Figure 4. Kinematic Response Histories for Example 2

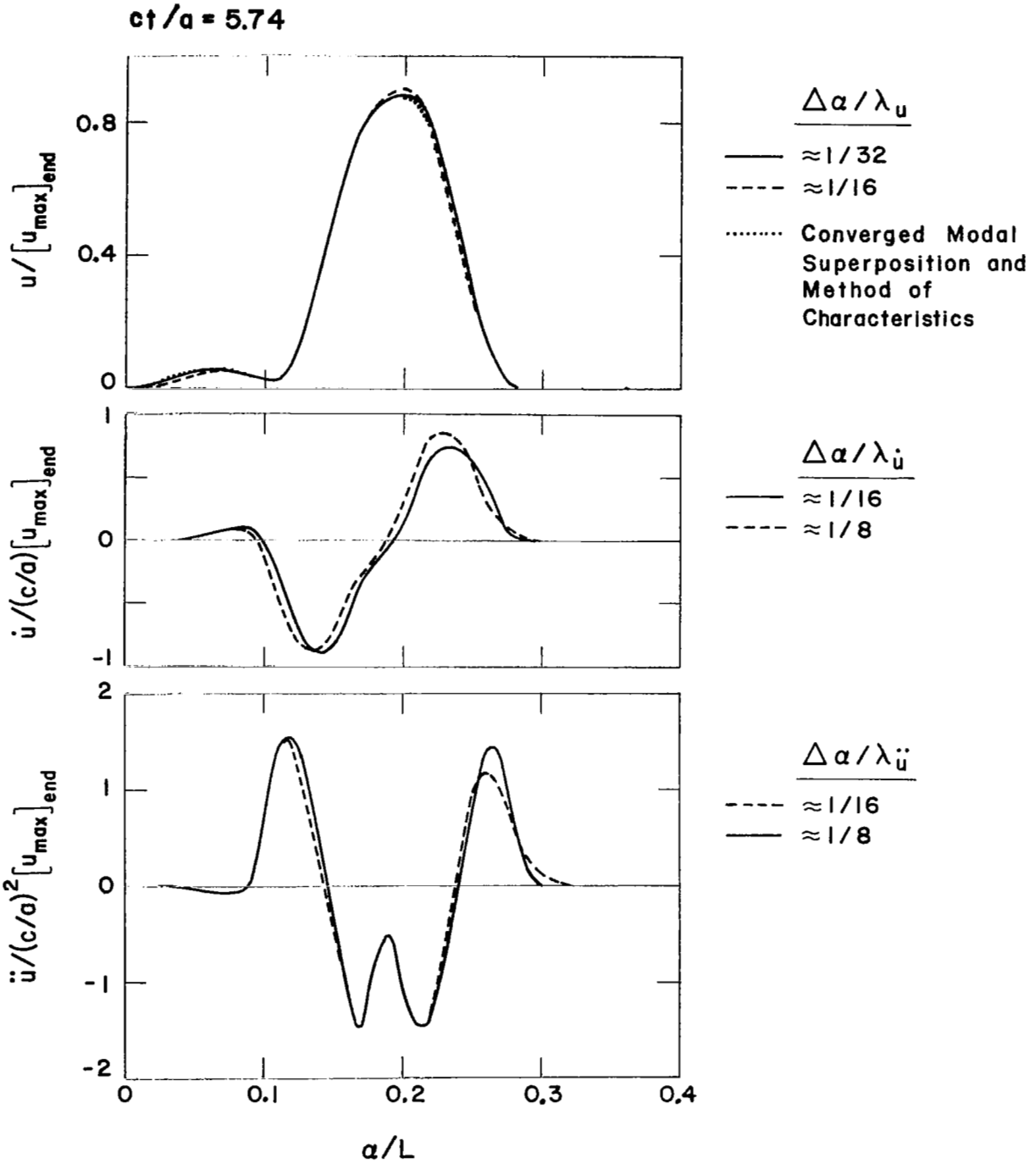

Figure 5. Kinematic Response Snapshots for Example 2

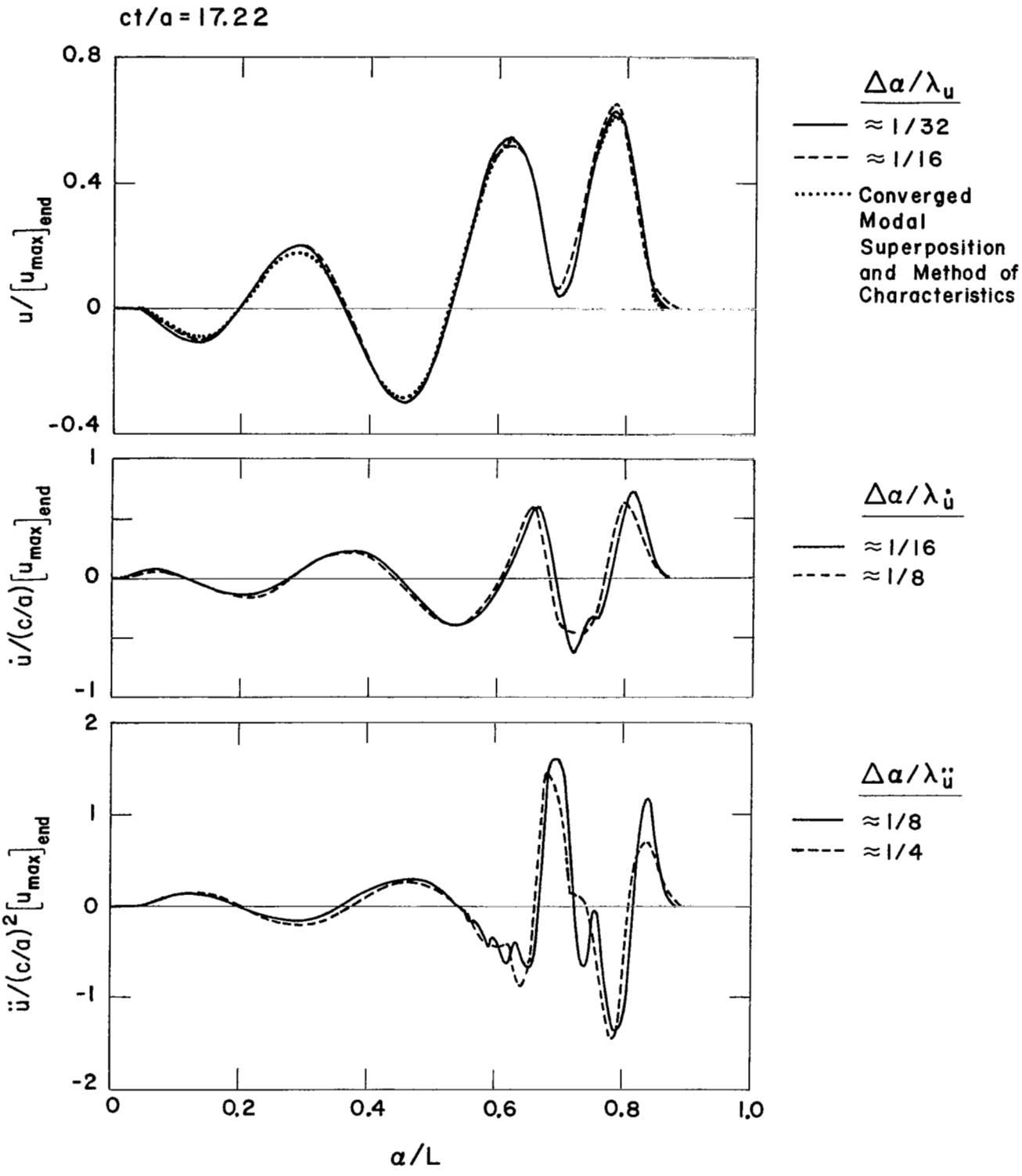

Figure 6. Kinematic Response Snapshots for Example 2

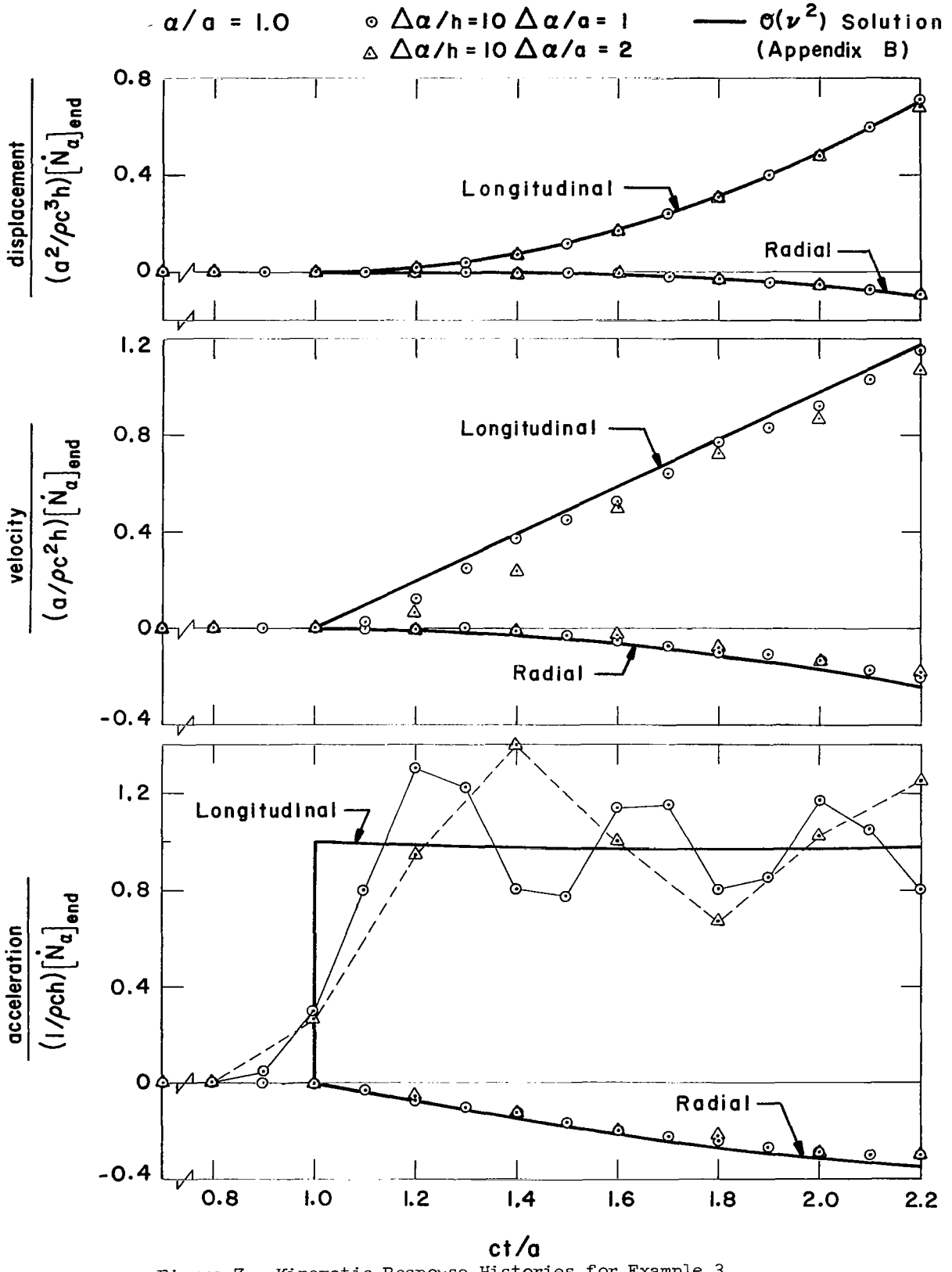

Figure 7. Kinematic Response Histories for Example 3

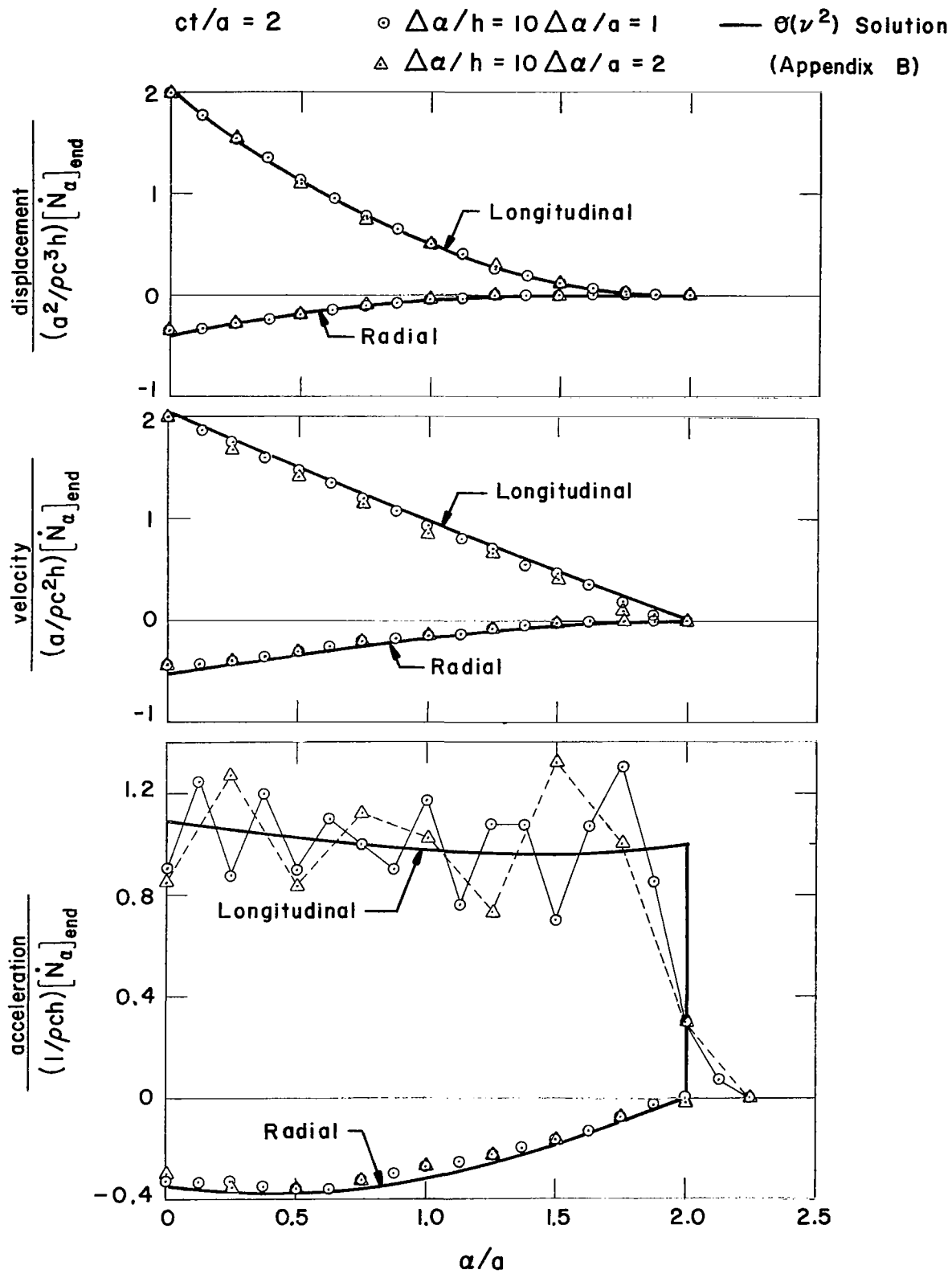

Figure 8. Kinematic Response Snapshots for Example 3

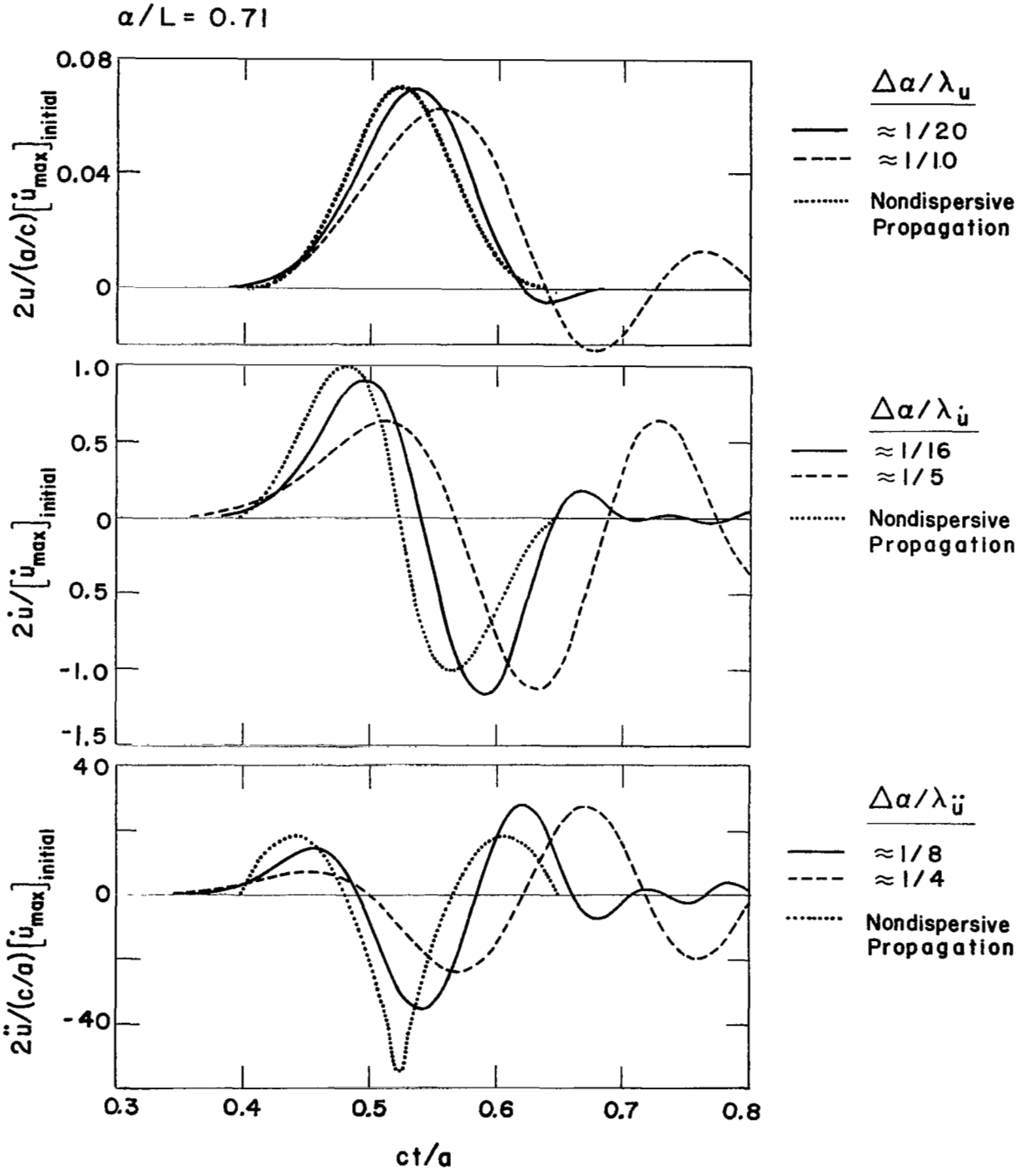

Figure 9. Kinematic Response Histories for Example 4

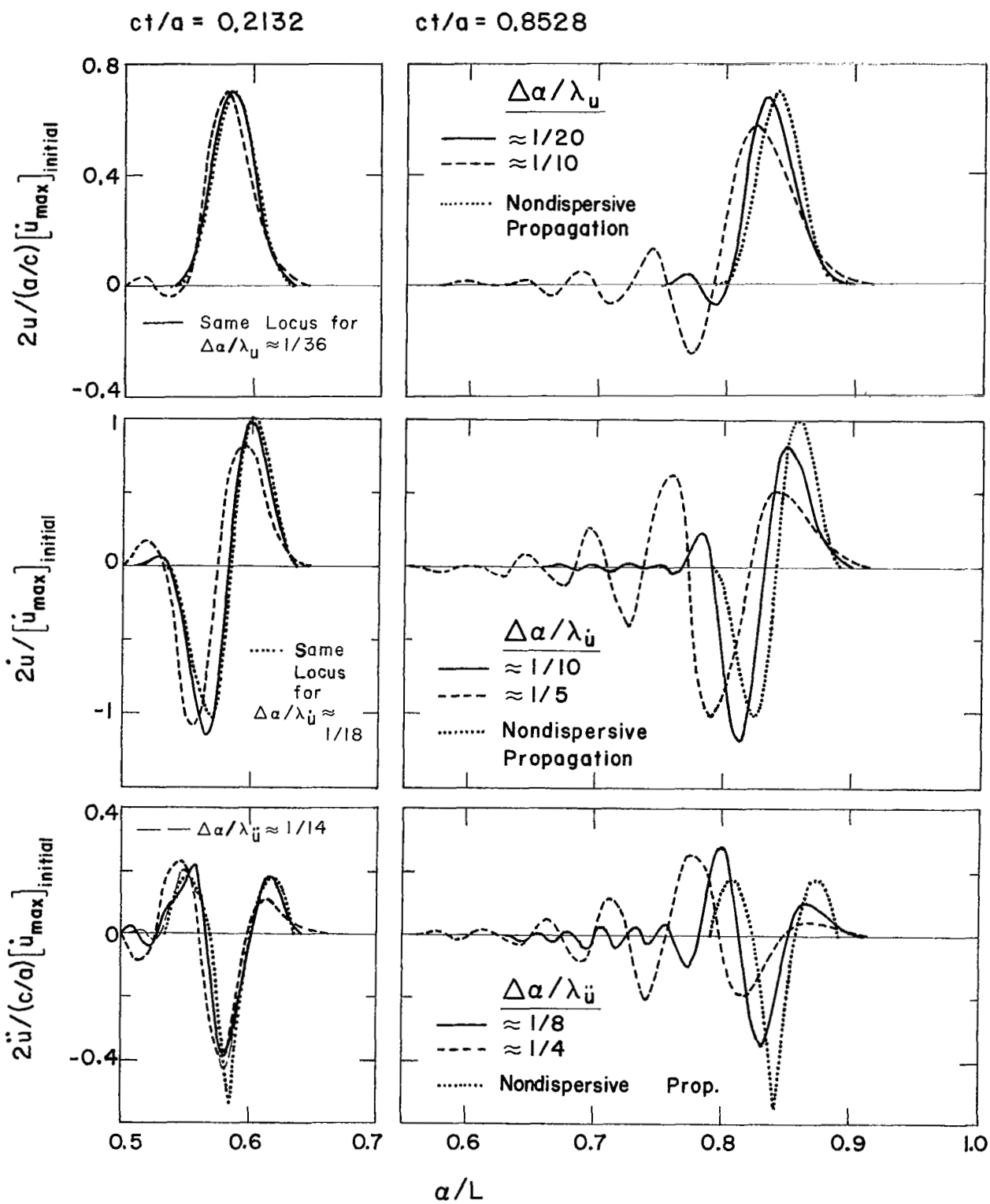

Figure 10. Kinematic Response Snapshots for Example 4

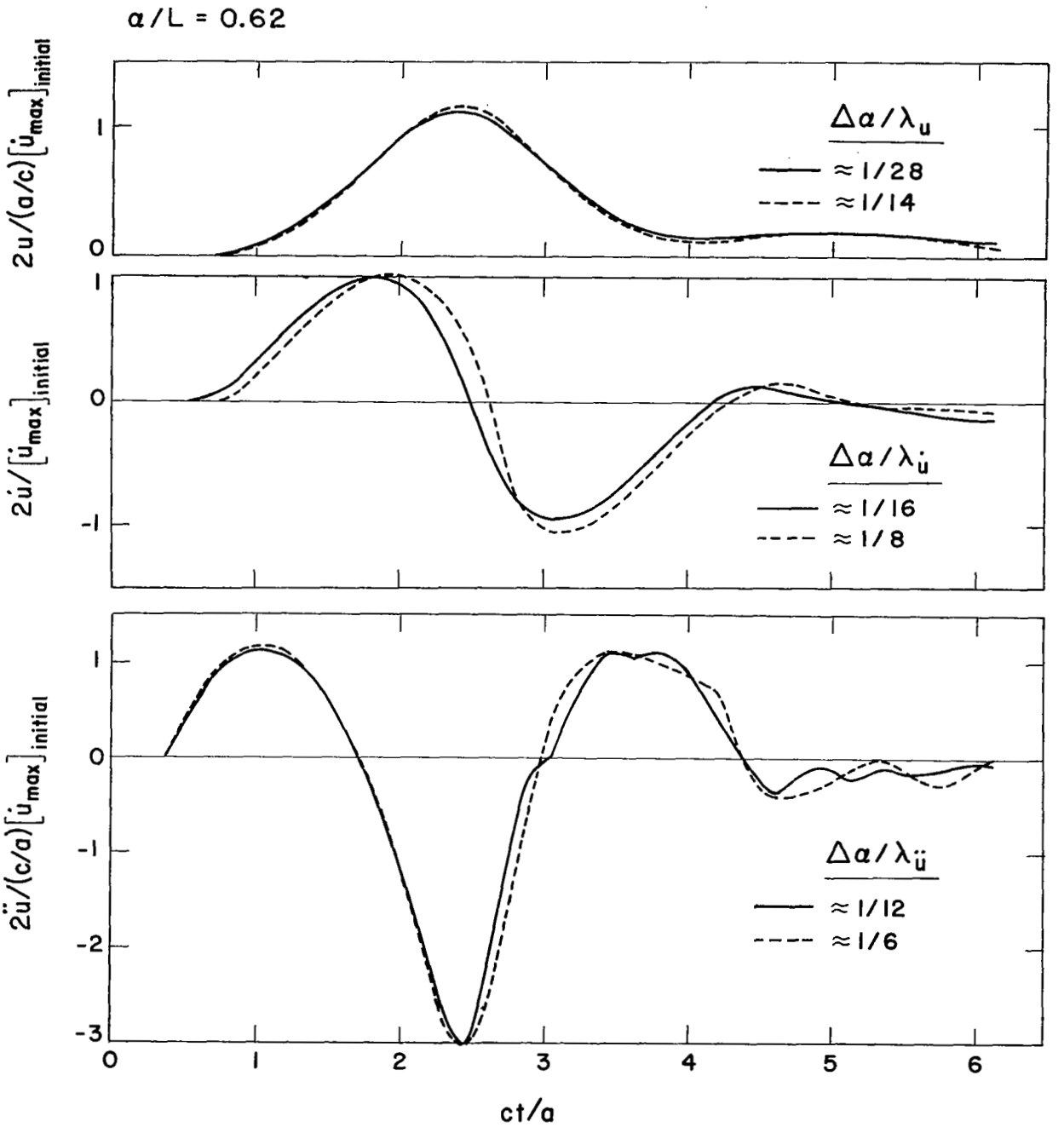

Figure 11. Kinematic Response Histories for Example 5

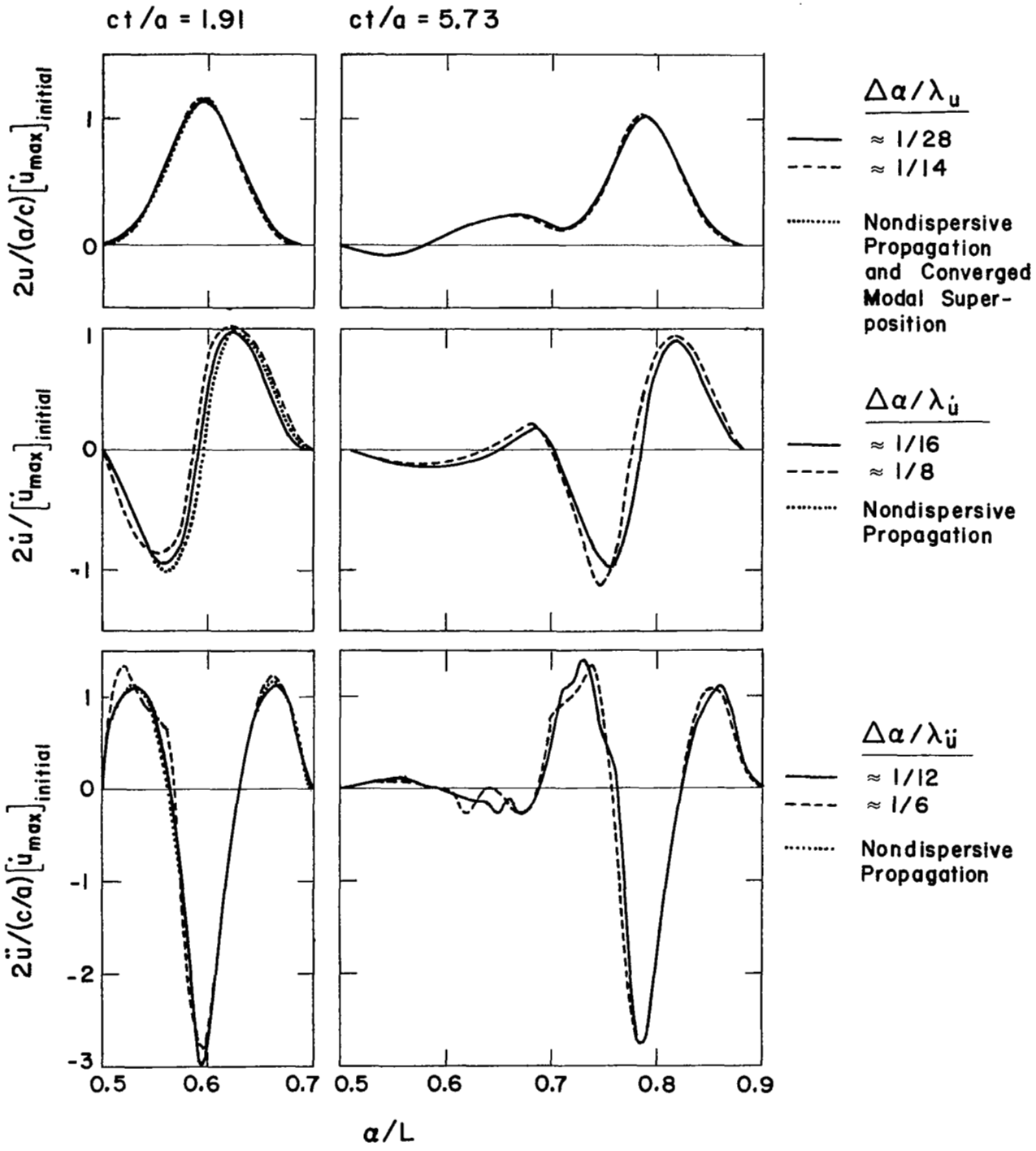

Figure 12. Kinematic Response Snapshots for Example 5

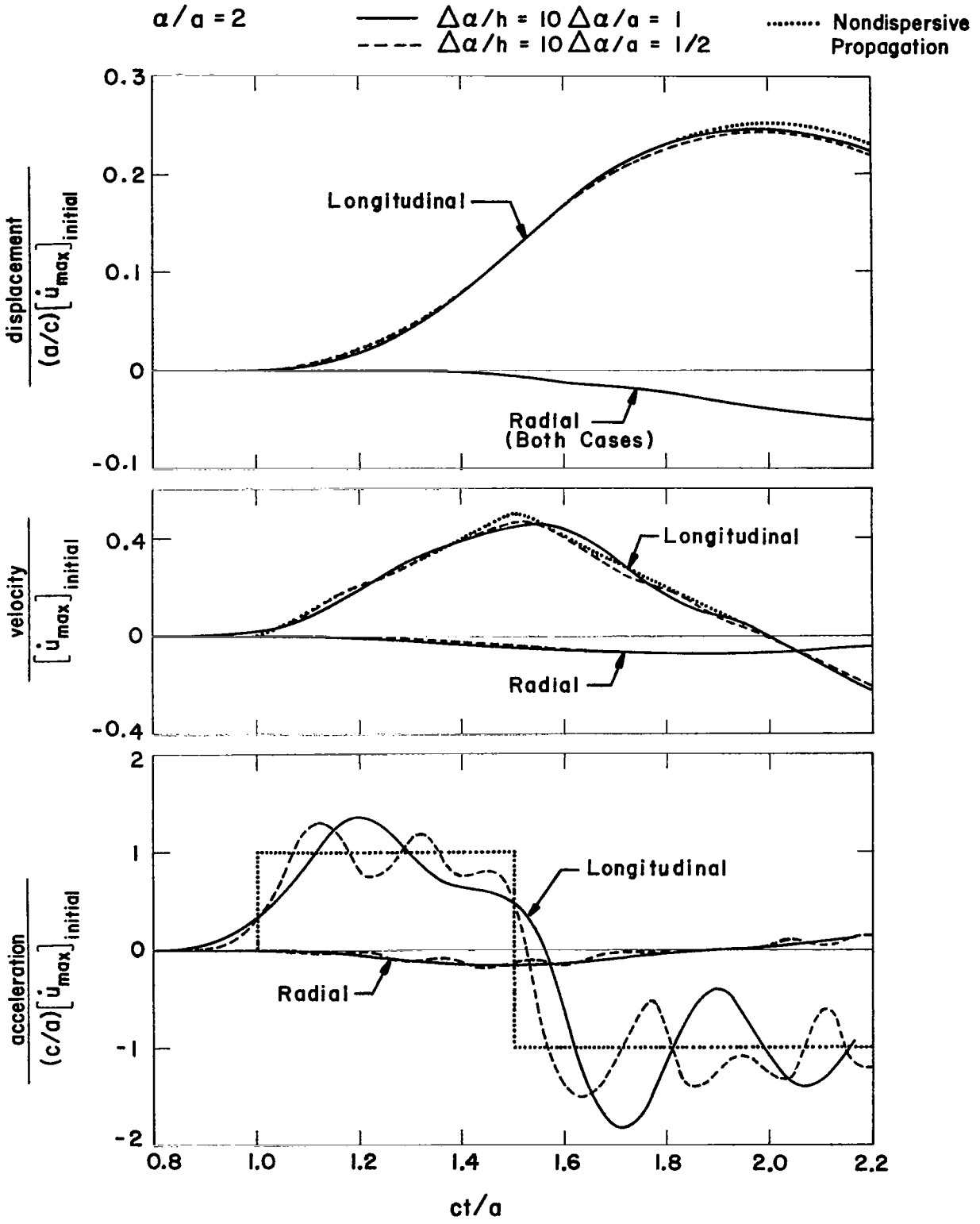

Figure 13. Kinematic Response Histories for Example 6

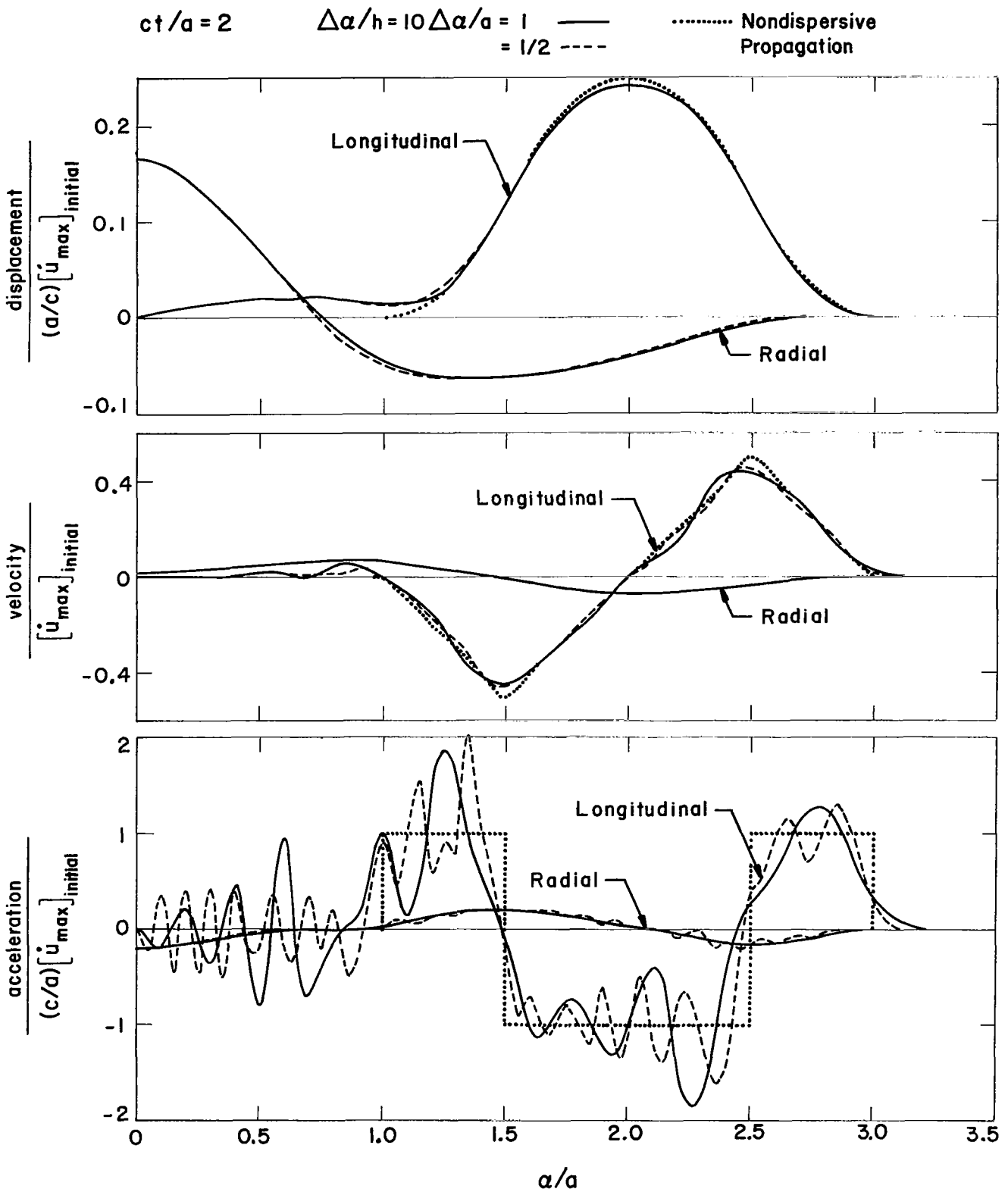

Figure 14. Kinematic Response Snapshots for Example 6

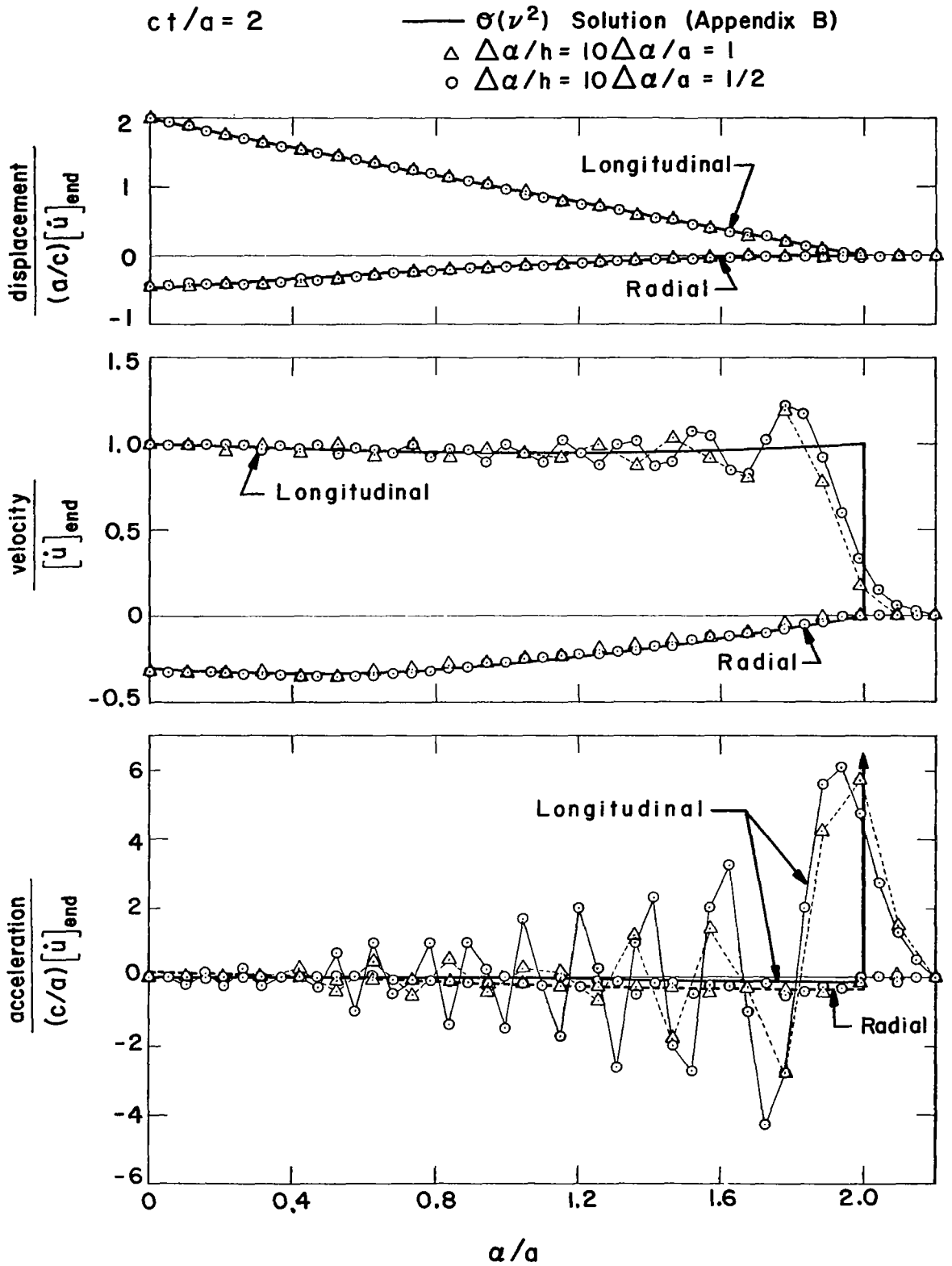

Figure 15. Kinematic Response Snapshots for Example 7

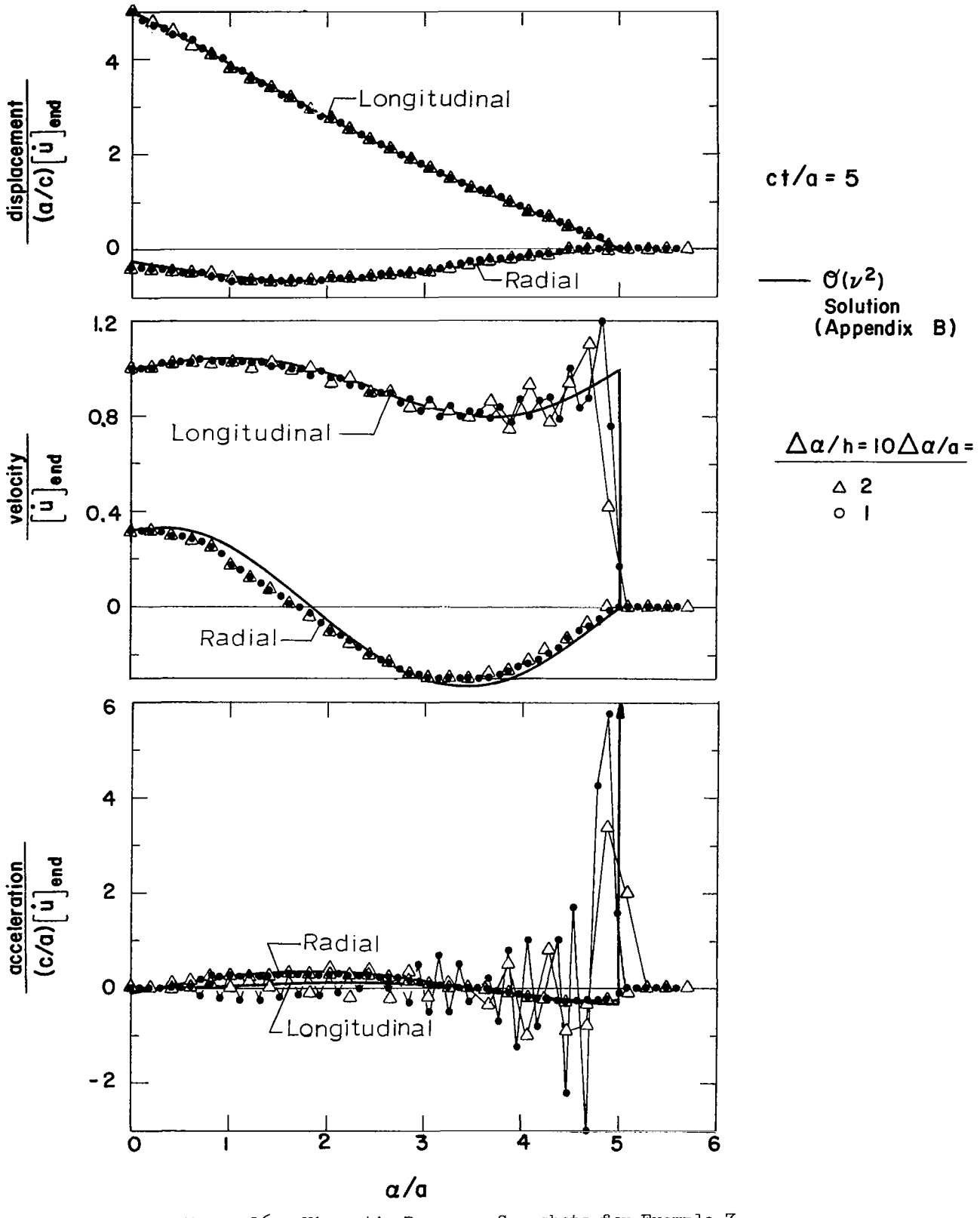

Figure 16. Kinematic Response Snapshots for Example 7

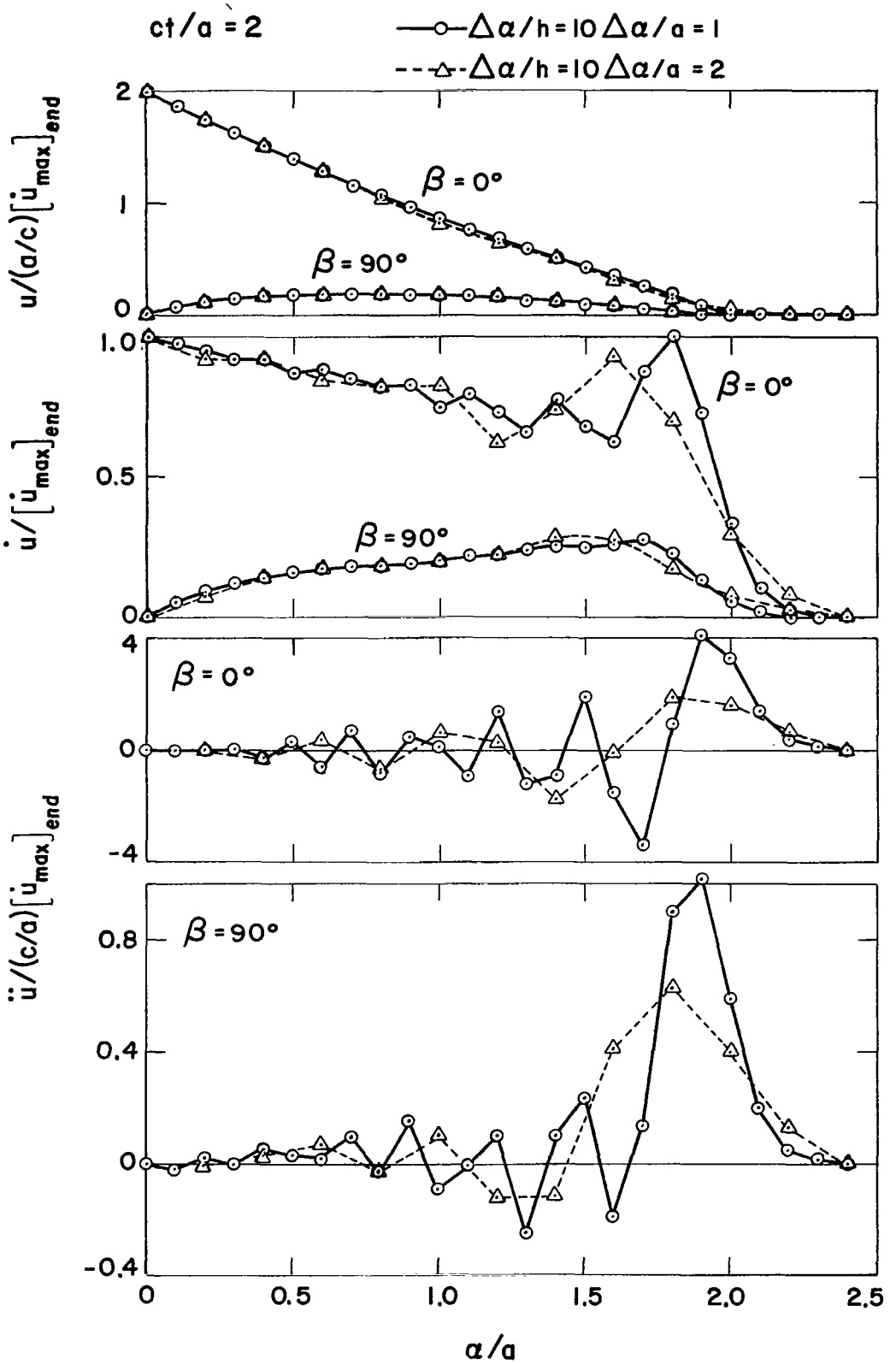

Figure 17. Kinematic Response Snapshots for Example 8

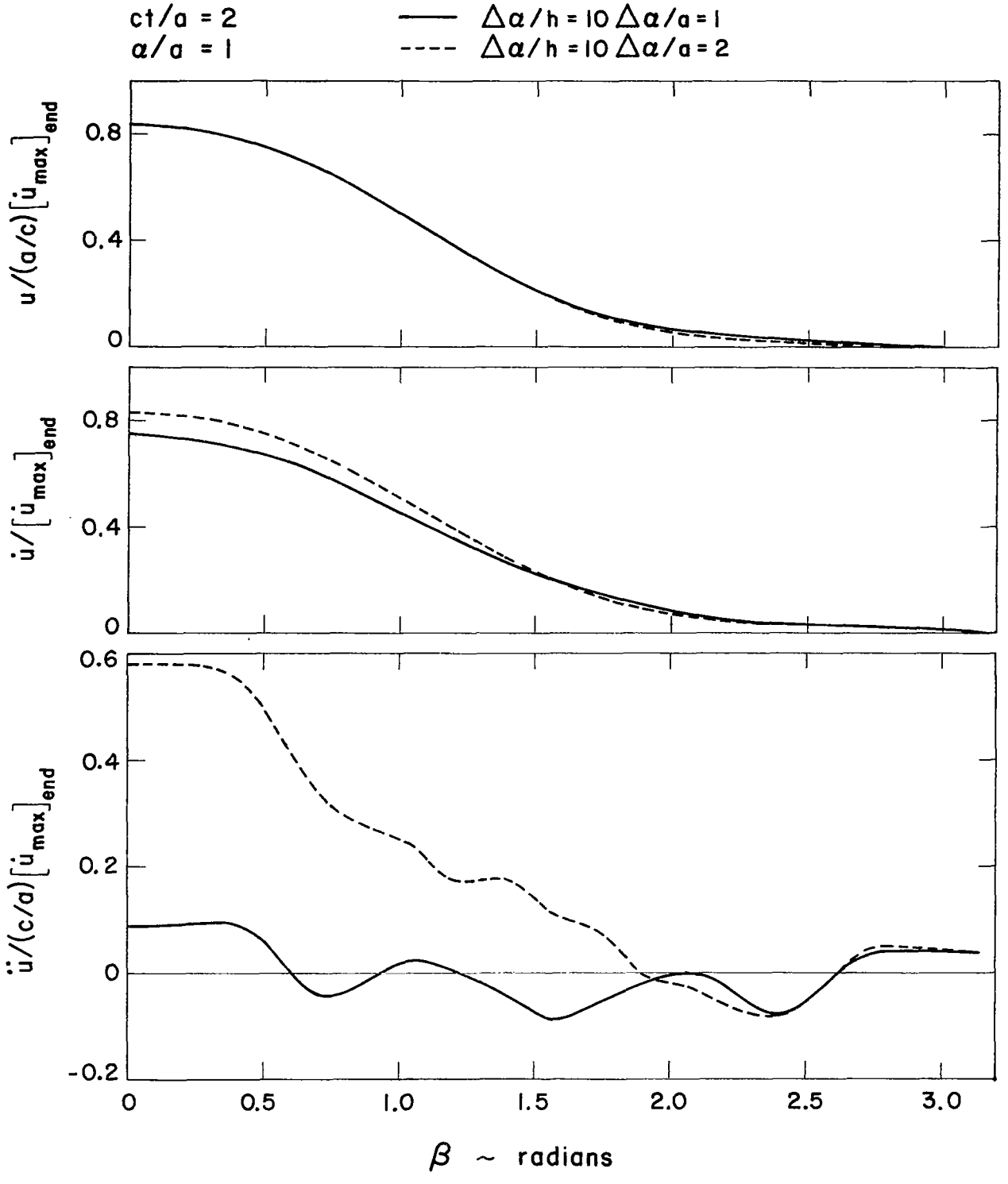

Figure 18. Kinematic Response Snapshots for Example 8

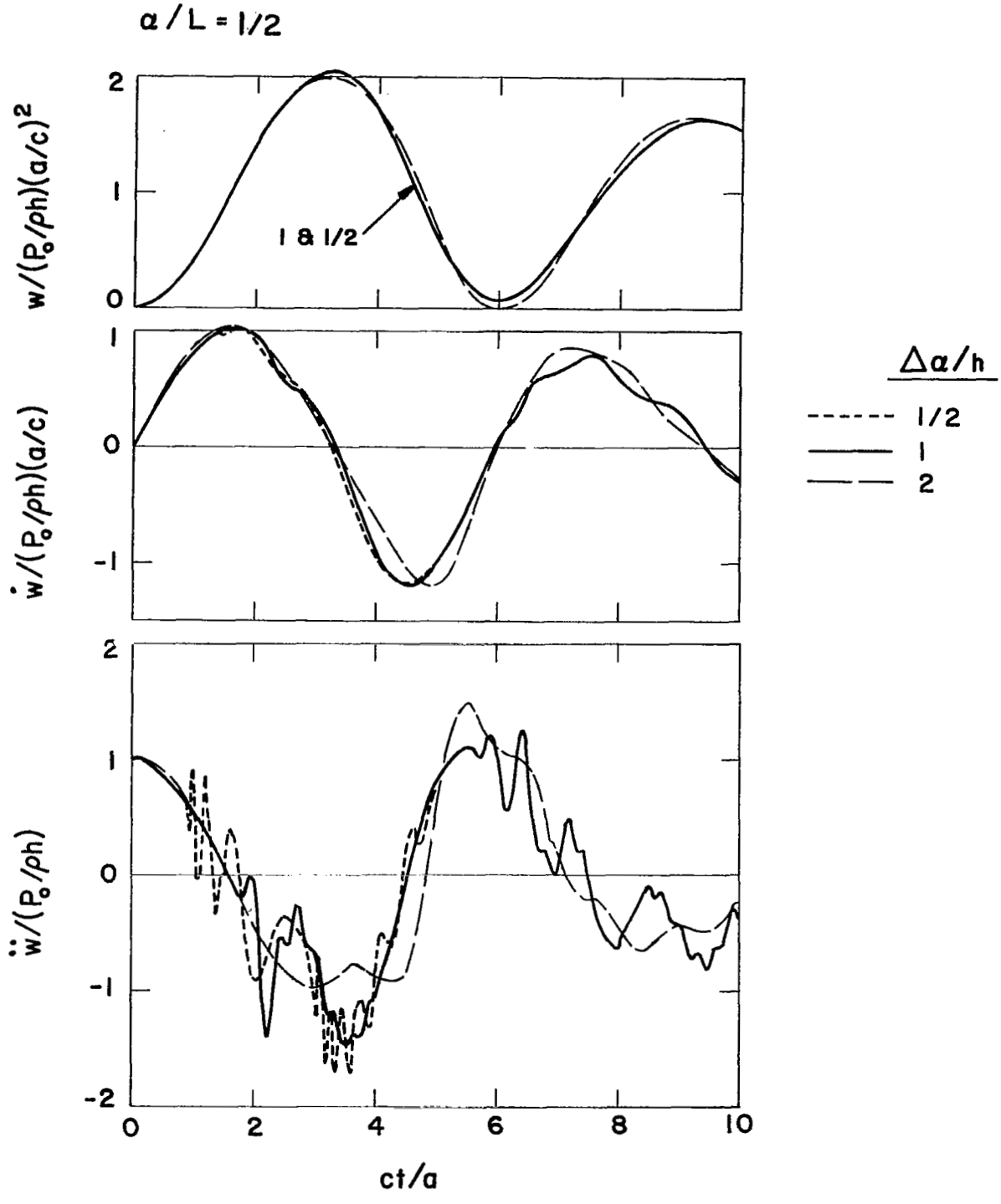

Figure 19. Kinematic Response Histories for Example 9

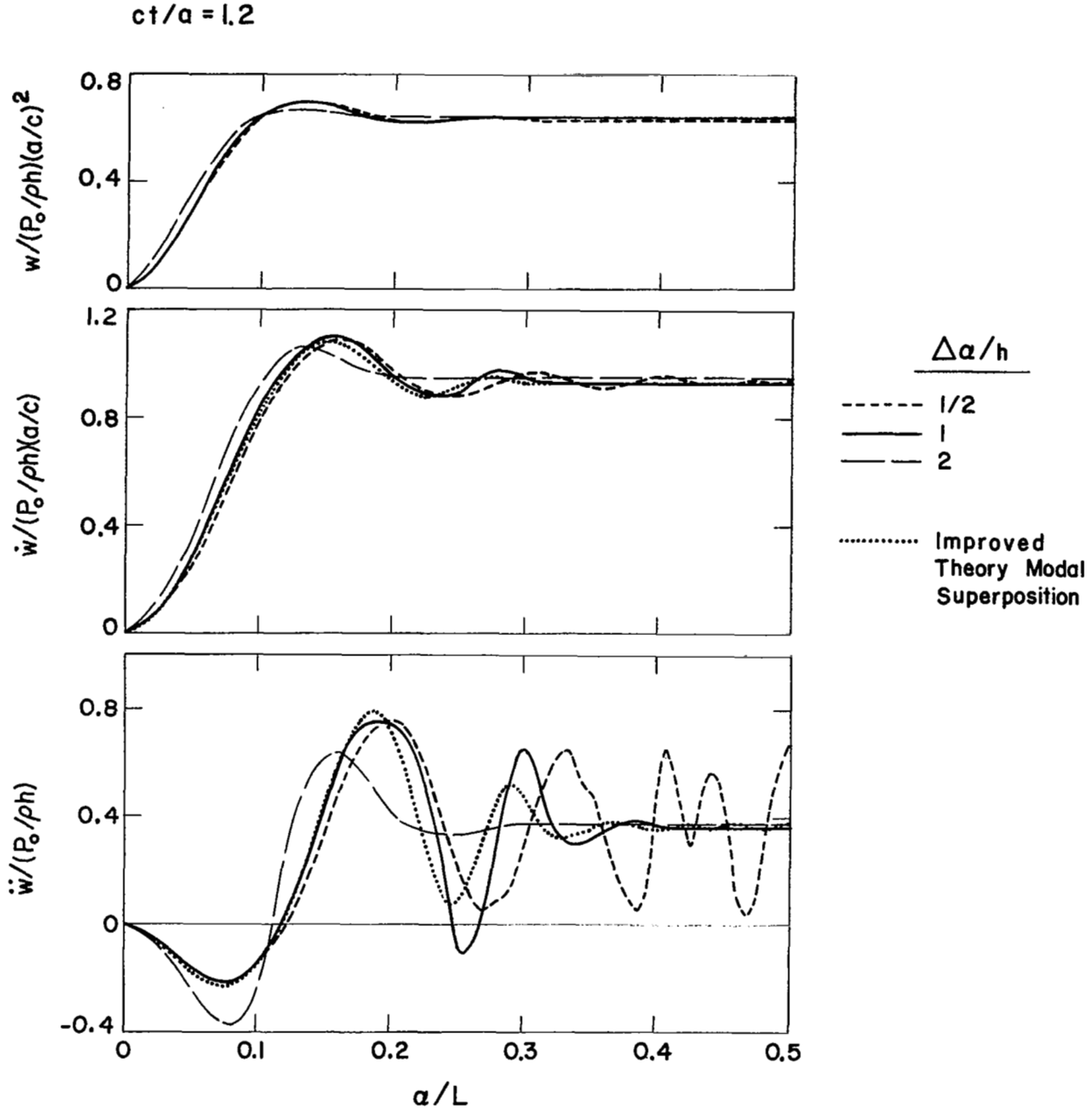

Figure 20. Kinematic Response Snapshots for Example 9

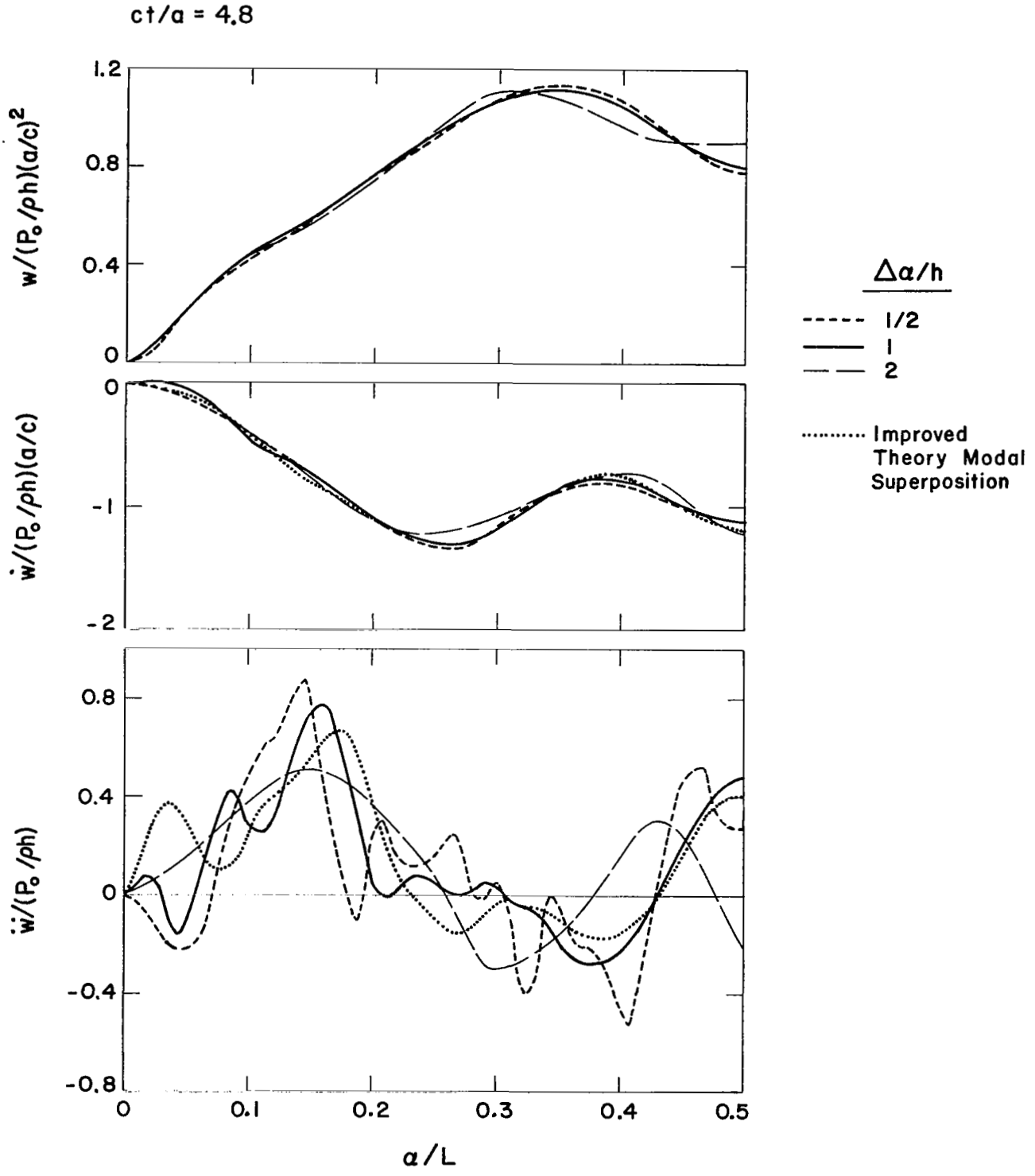

Figure 21. Kinematic Response Snapshots for Example 9

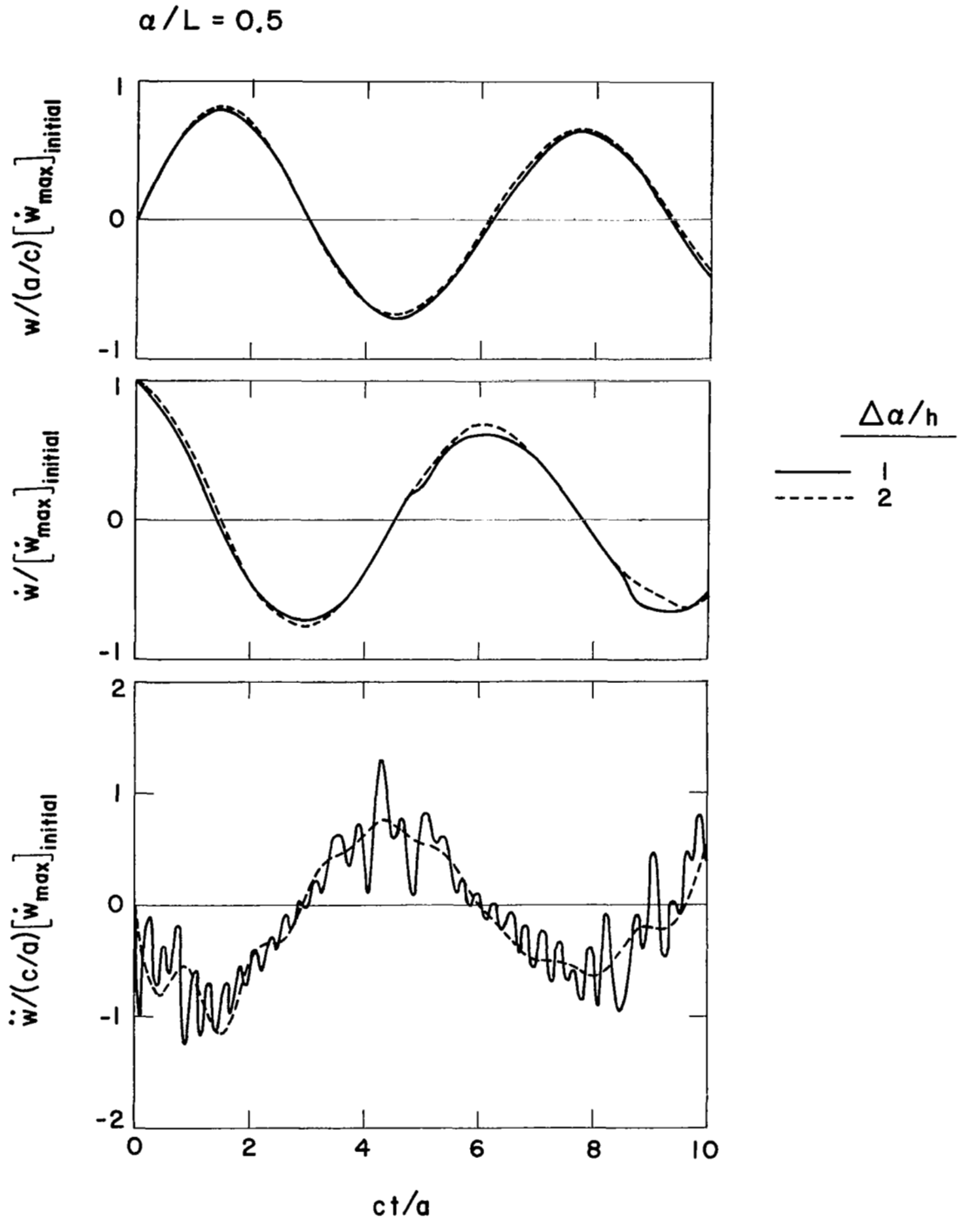

Figure 22. Kinematic Response Histories for Example 10 (α_w = 0.8a)

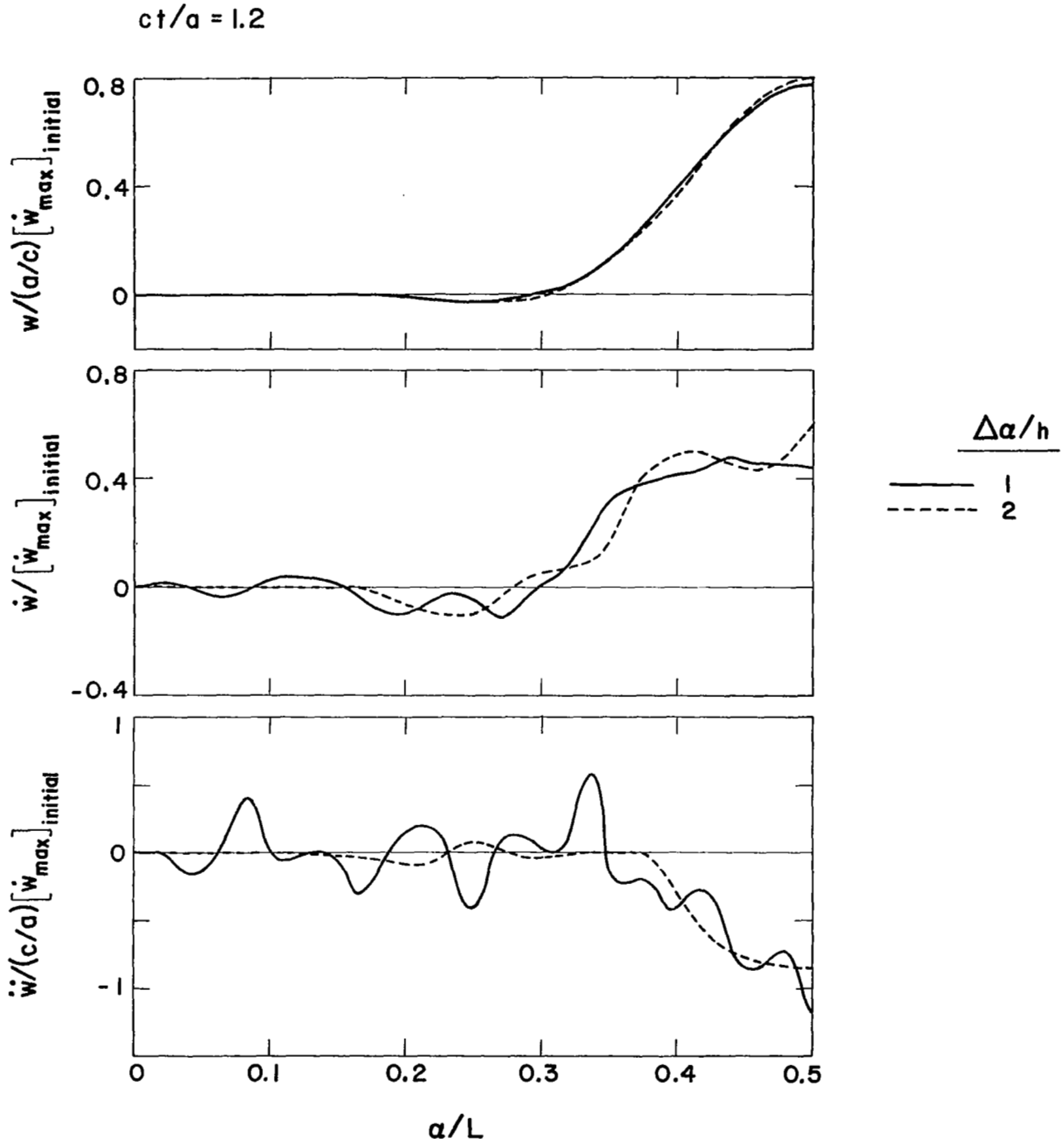

Figure 23. Kinematic Response Snapshots for Example 10 (α_w = 0.8a)

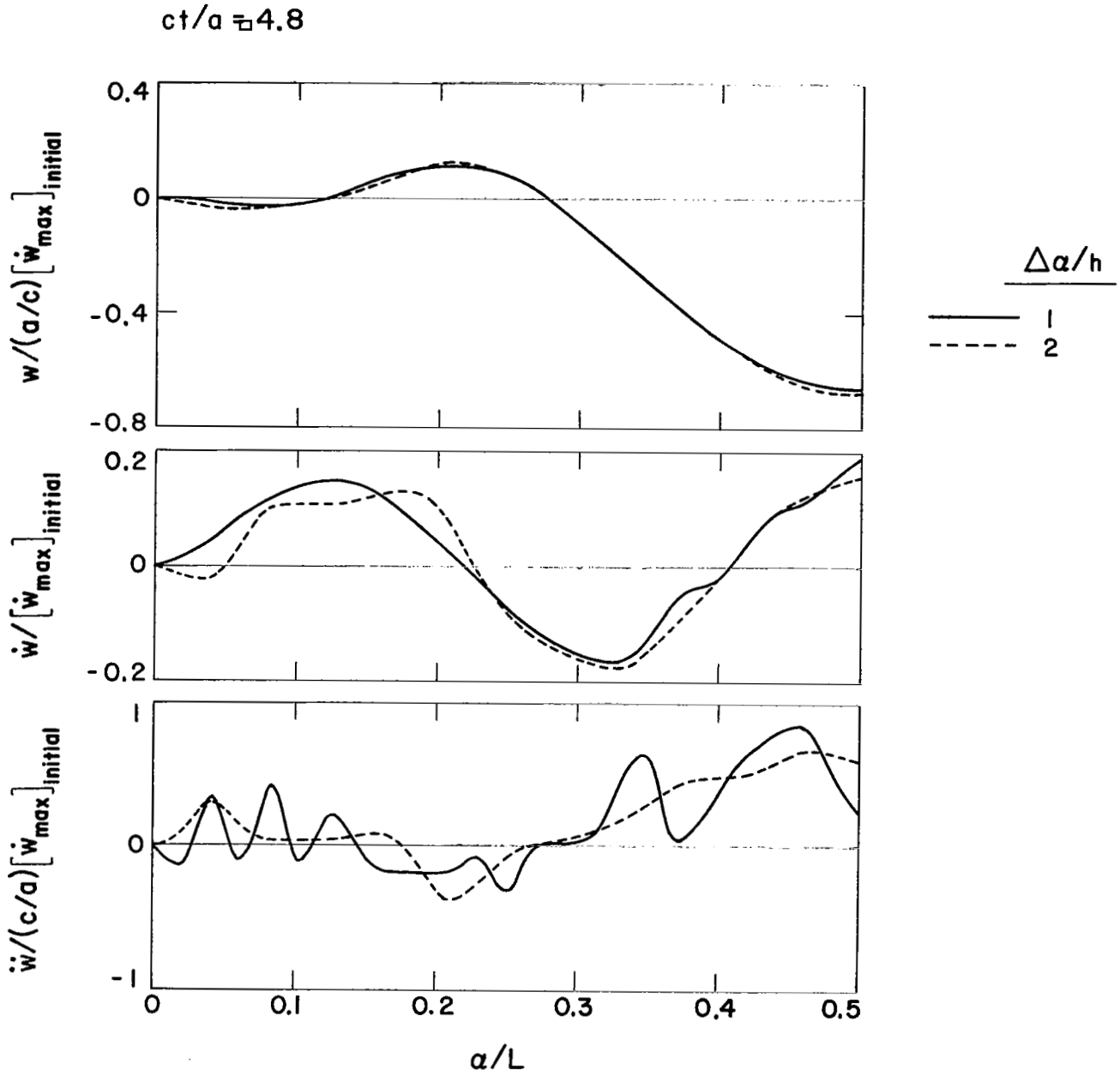

Figure 24. Kinematic Response Snapshots for Example 10 (α_w = 0.8a)

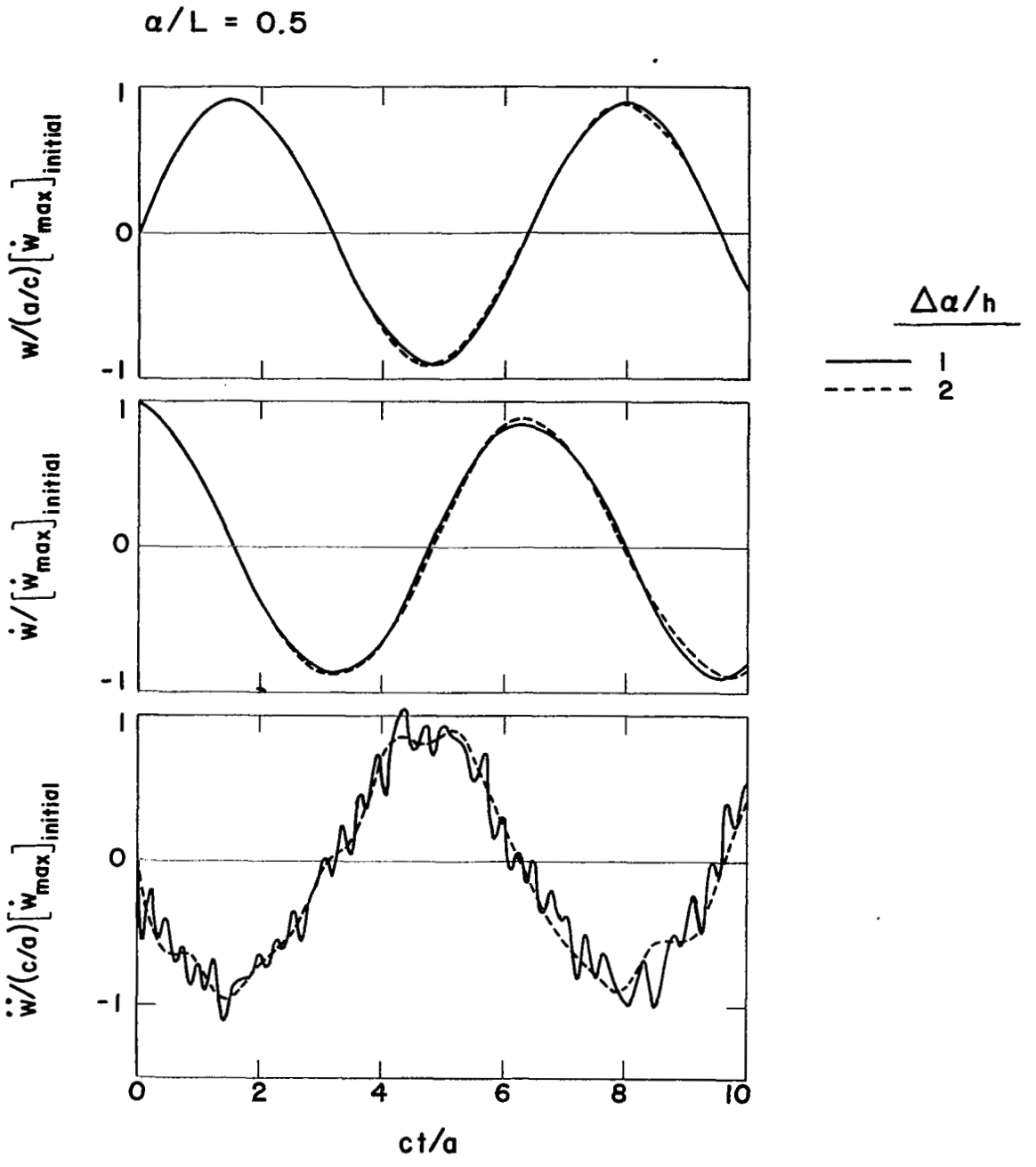

Figure 25. Kinematic Response Histories for Example 10 (α_w = 1.6a)

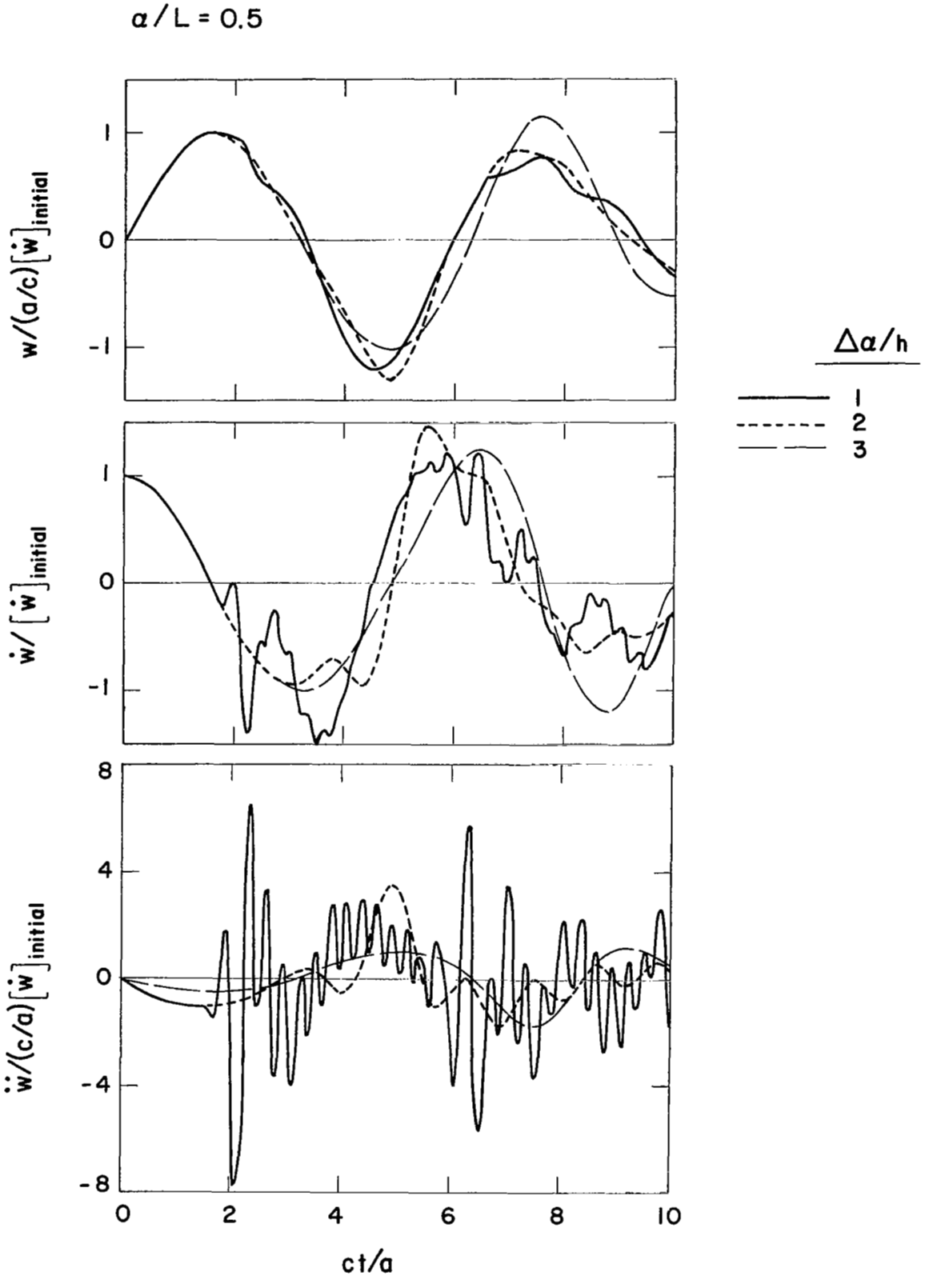

Figure 26. Kinematic Response Histories for Example 11

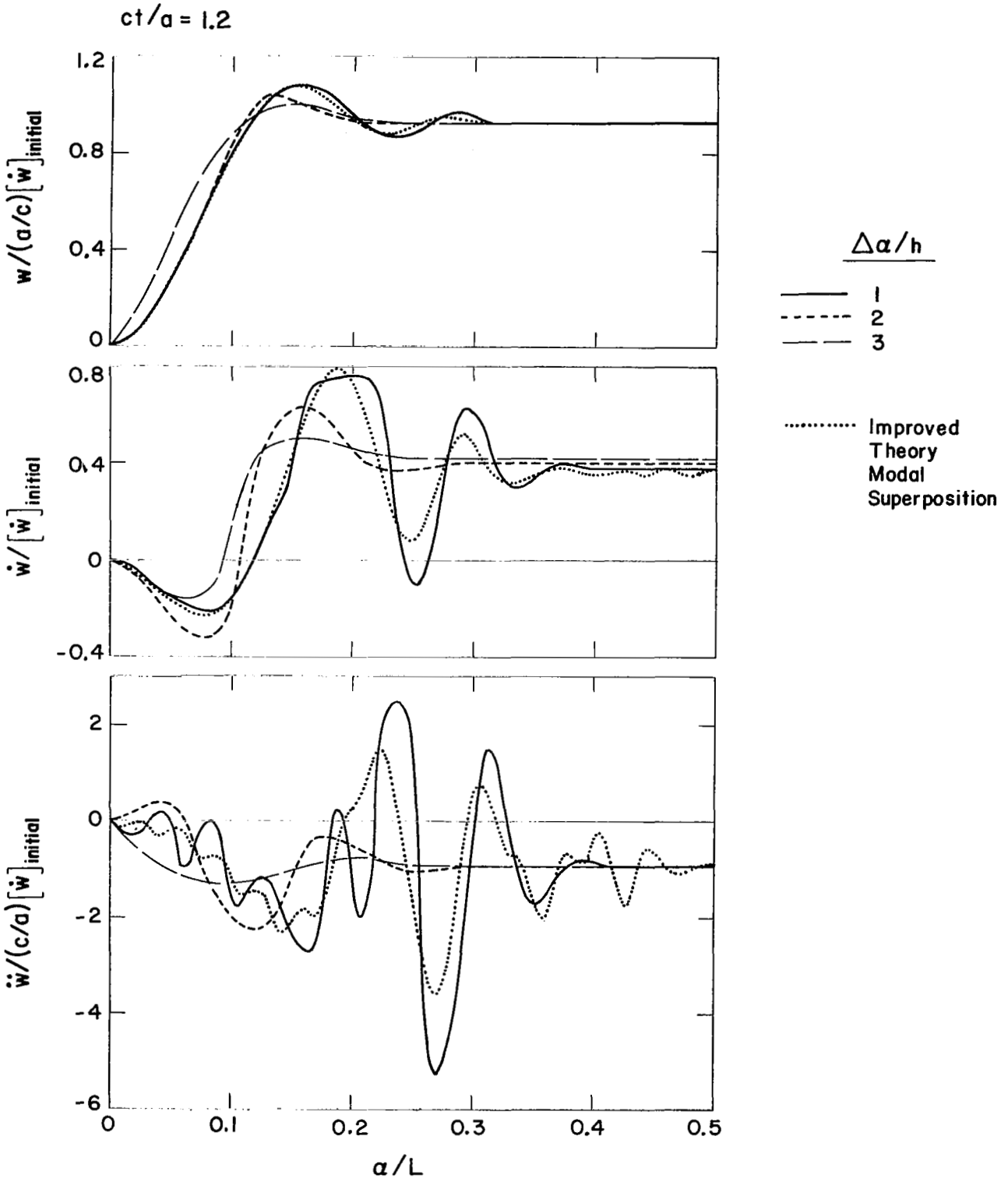

Figure 27. Kinematic Response Snapshots for Example 11

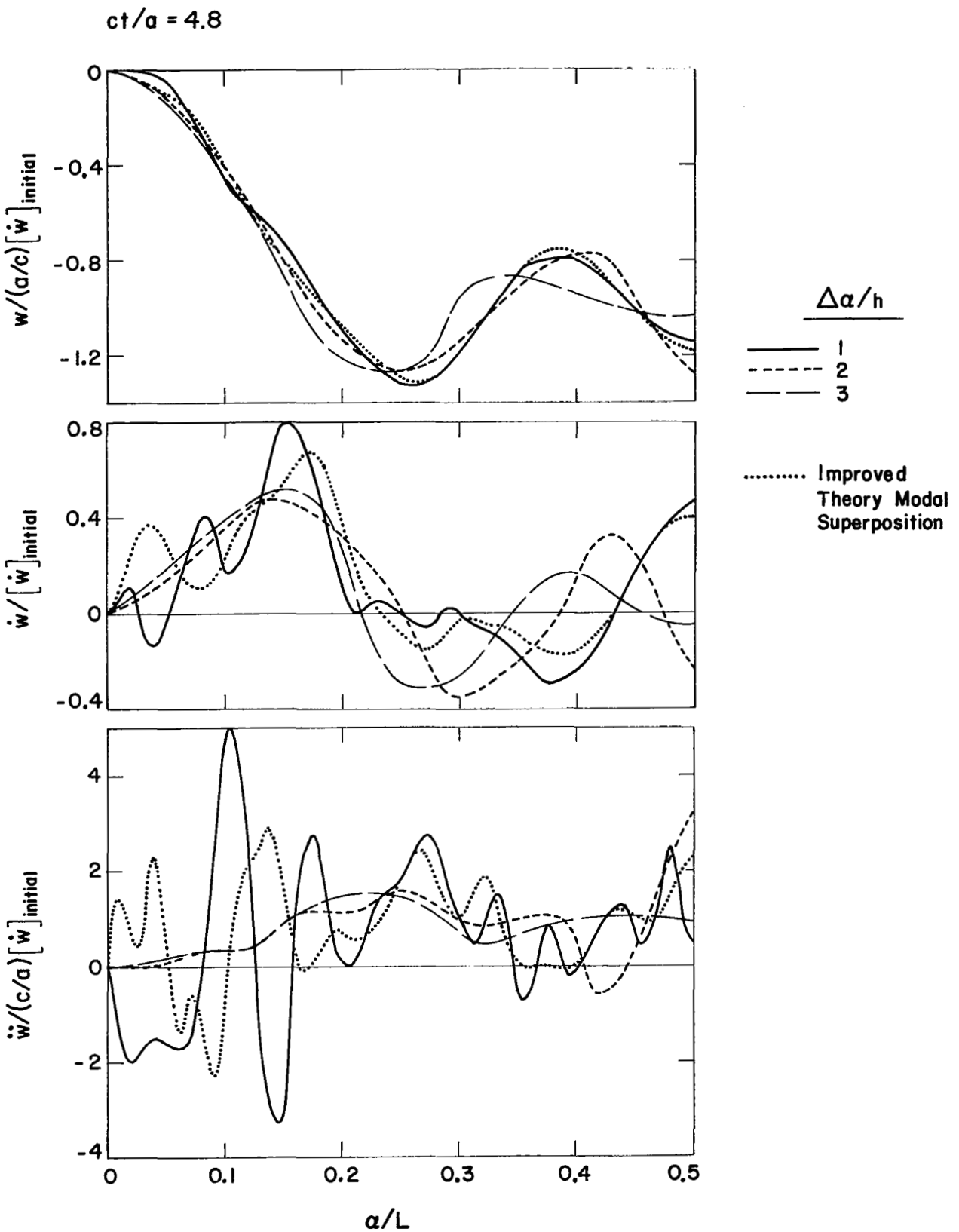

Figure 28. Kinematic Response Snapshots for Example 11

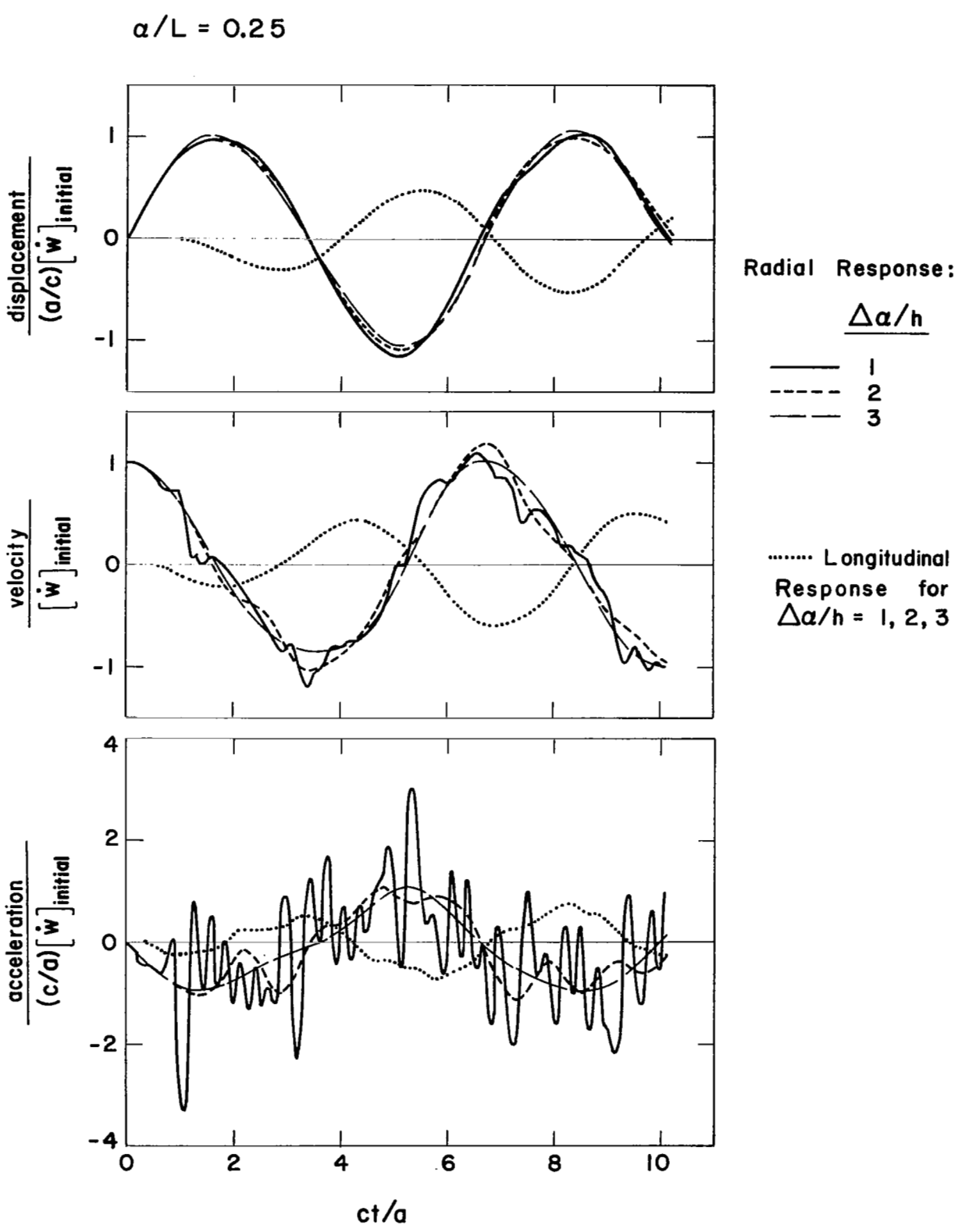

Figure 29. Kinematic Response Histories for Example 12

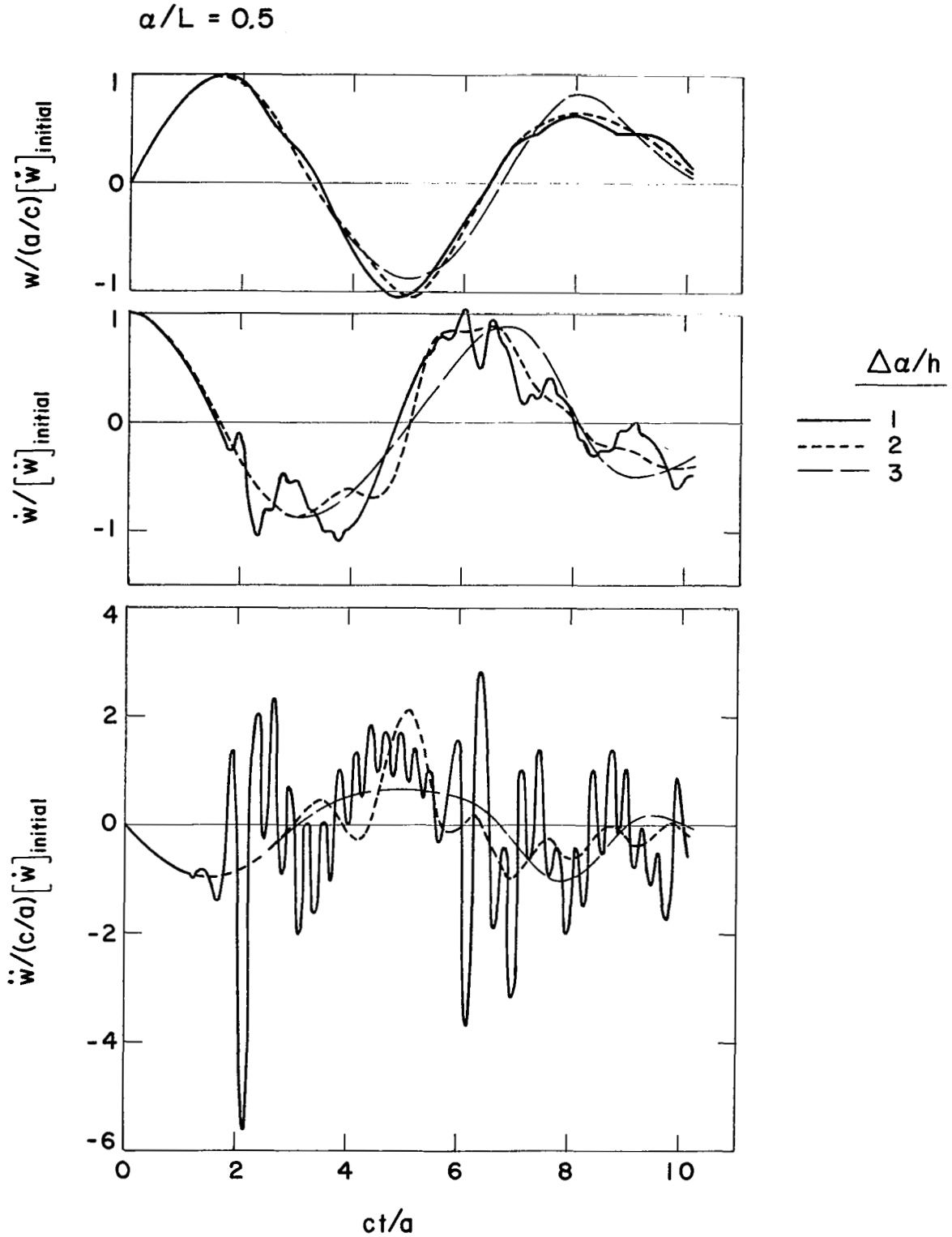

Figure 30. Kinematic Response Histories for Example 12

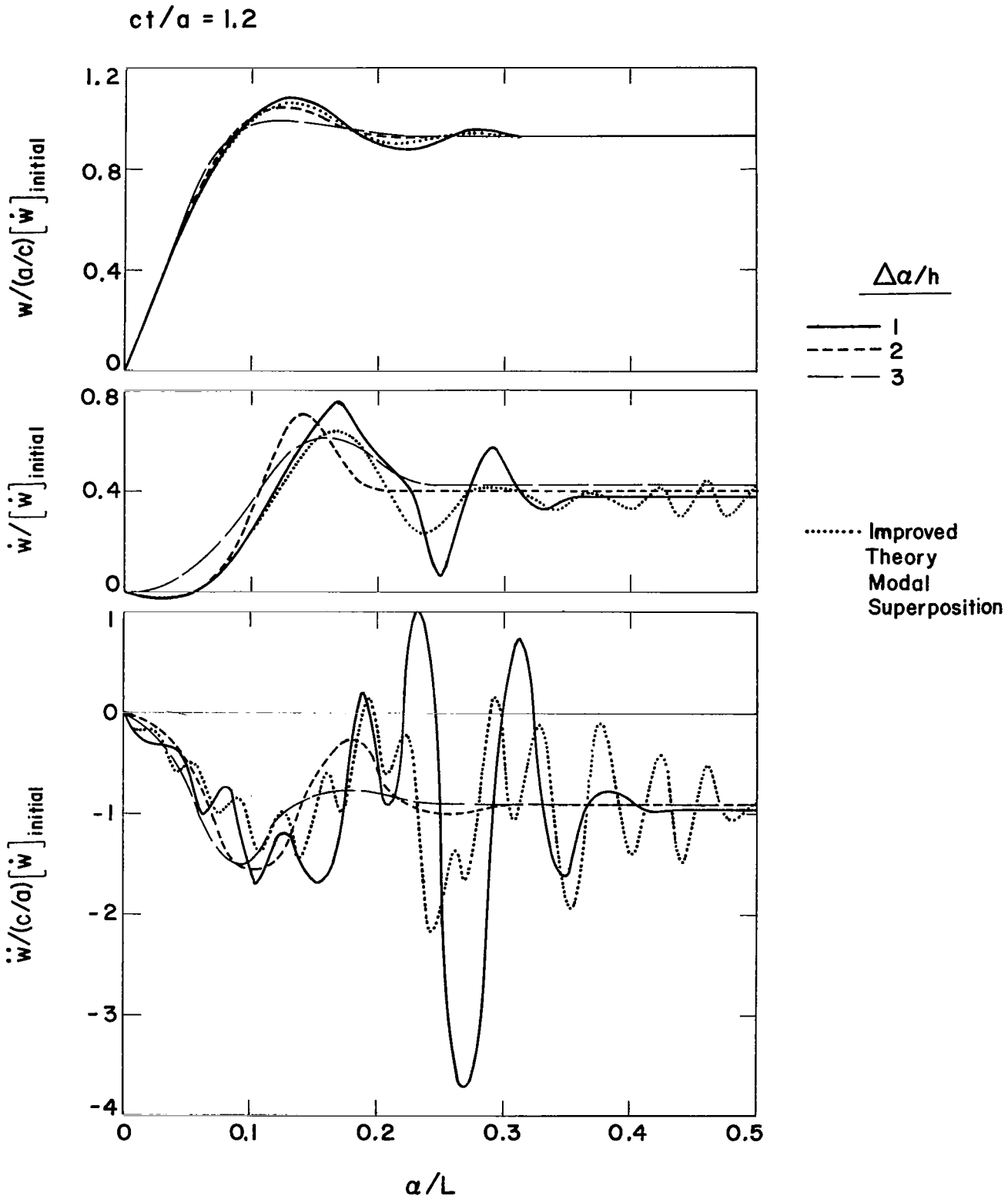

Figure 31. Kinematic Response Snapshots for Example 12

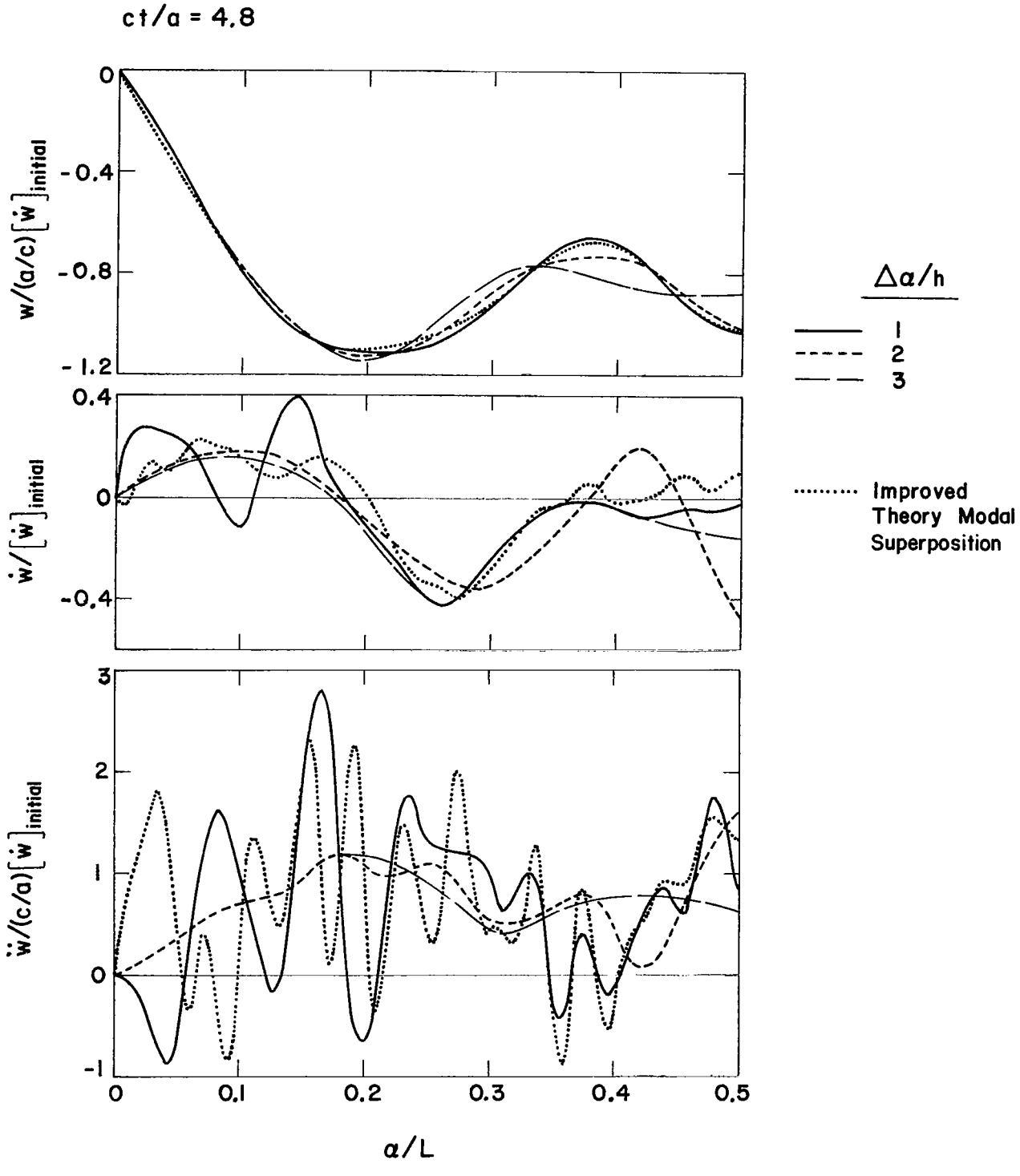

Figure 32. Kinematic Response Snapshots for Example 12

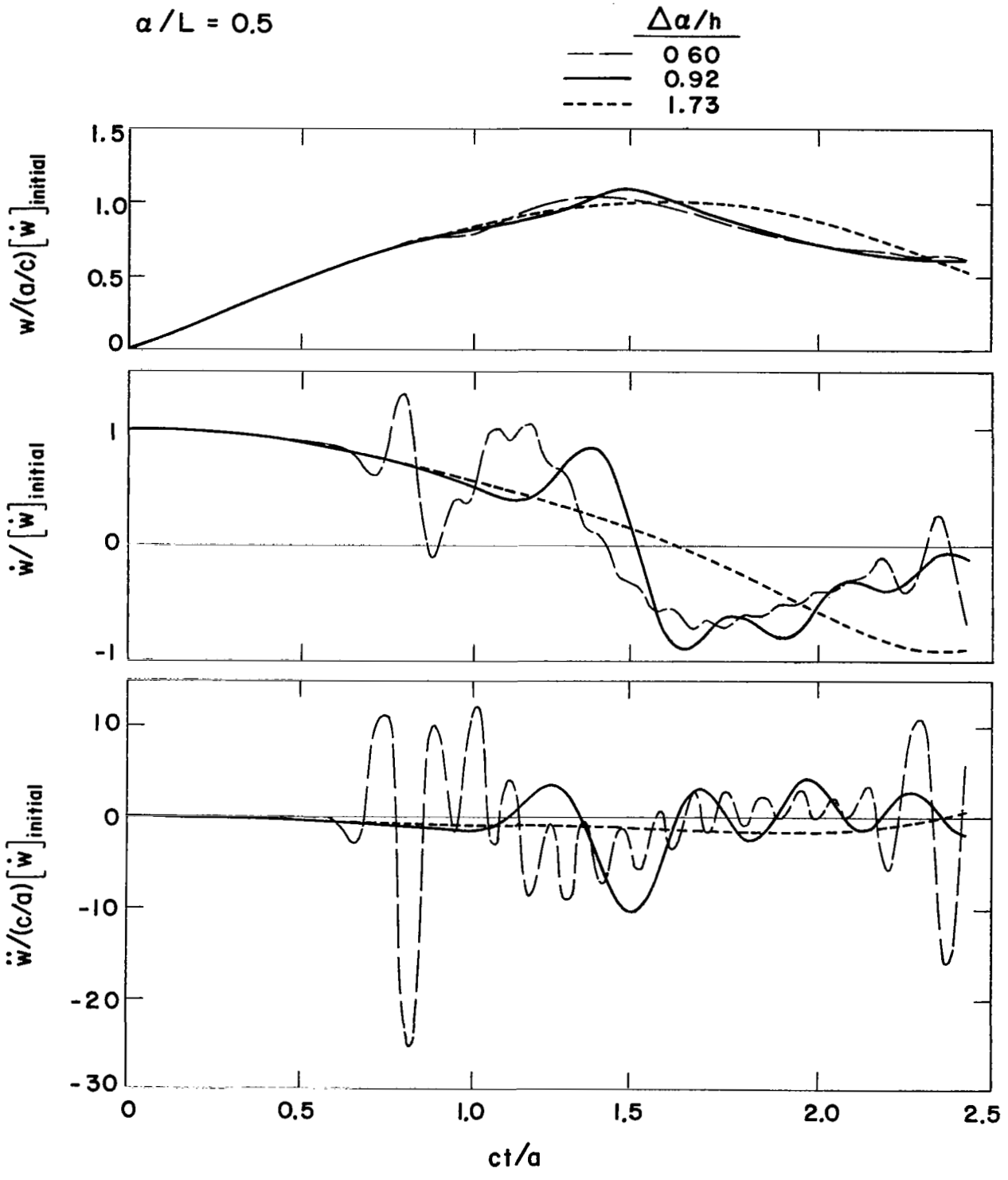

Figure 33. Kinematic Response Histories for Example 13 (Uniform Impulse)

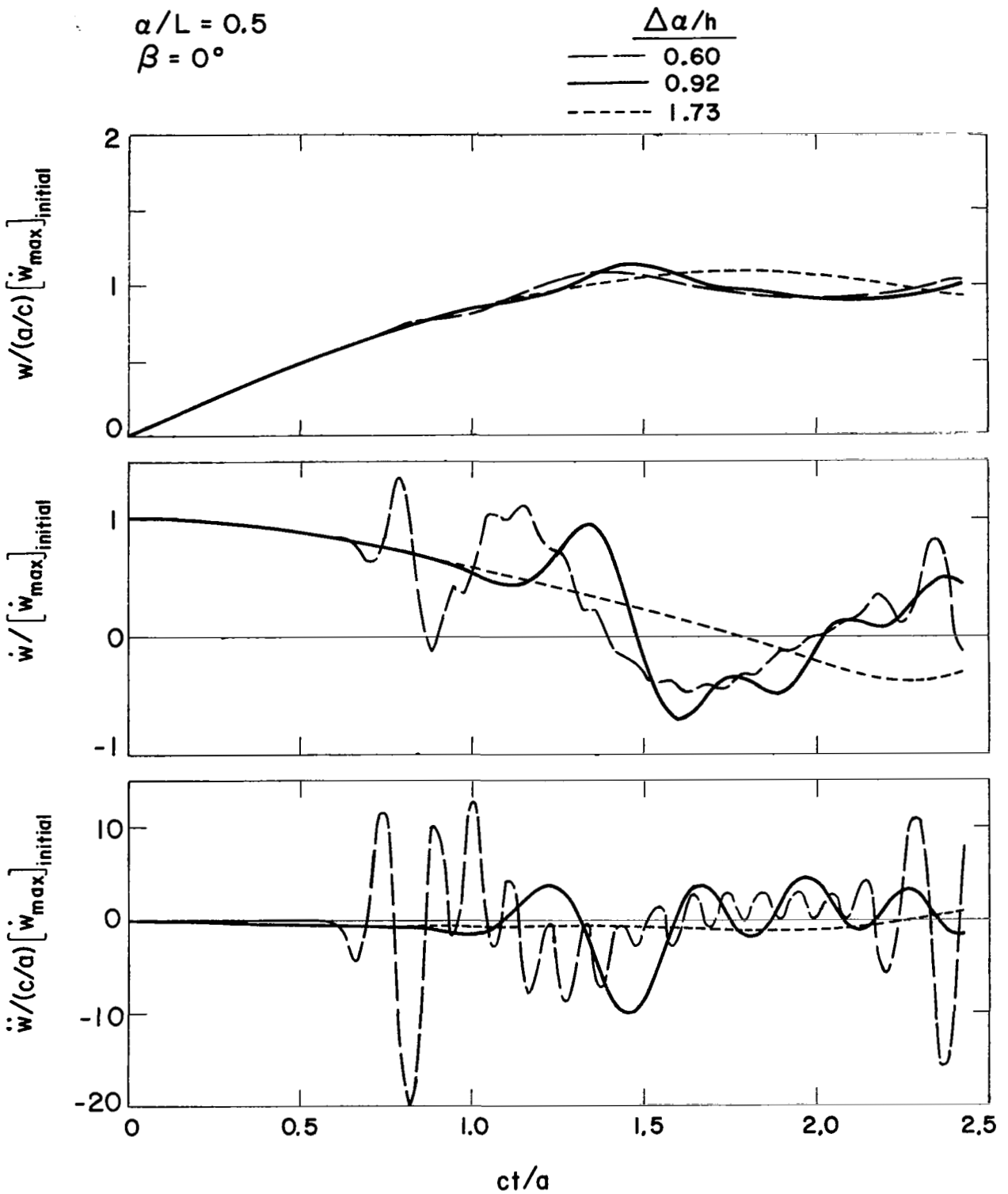

Figure 34. Kinematic Response Histories for Example 13 (Cosine Impulse)

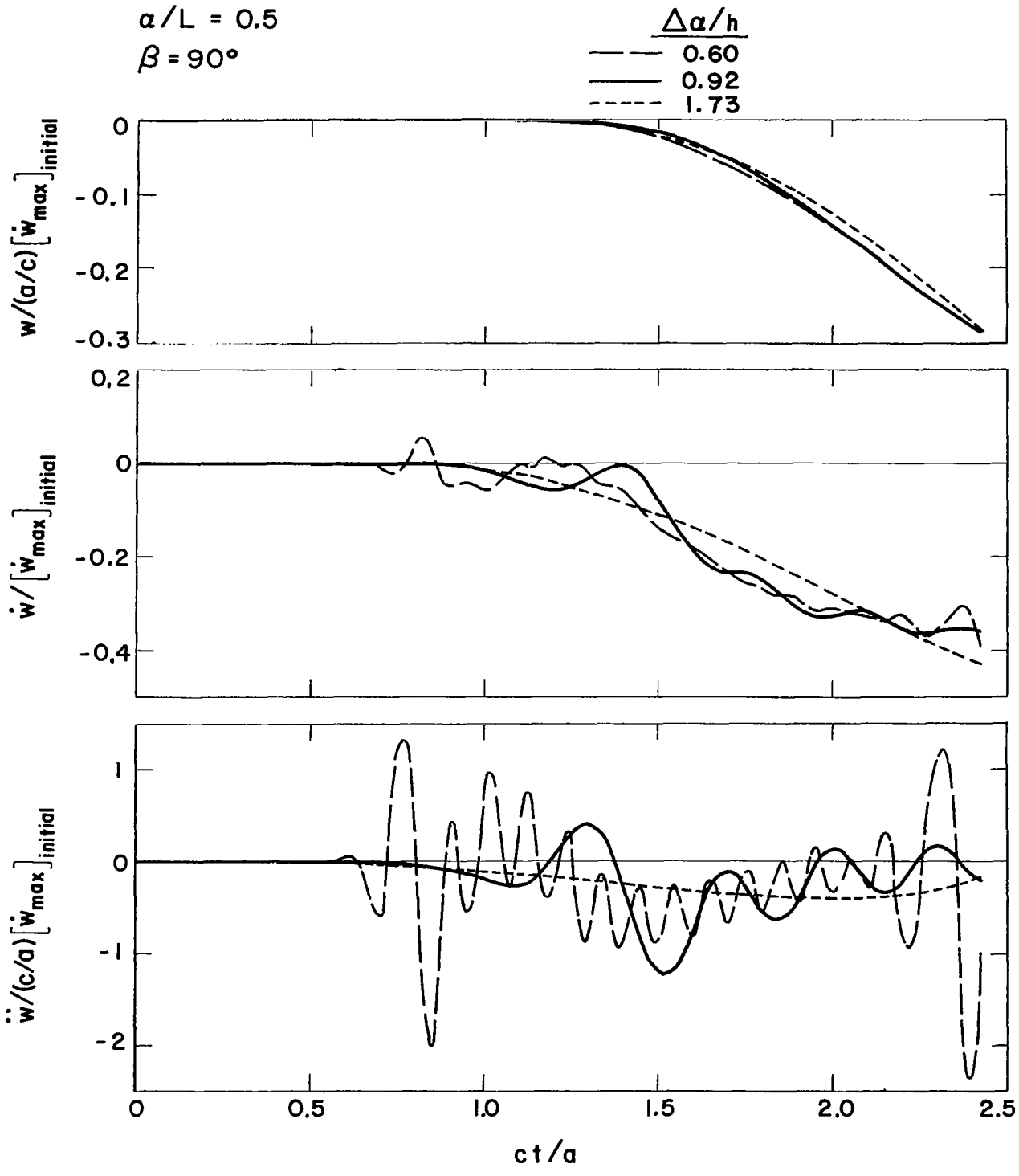

Figure 35. Kinematic Response Histories for Example 13 (Cosine Impulse)

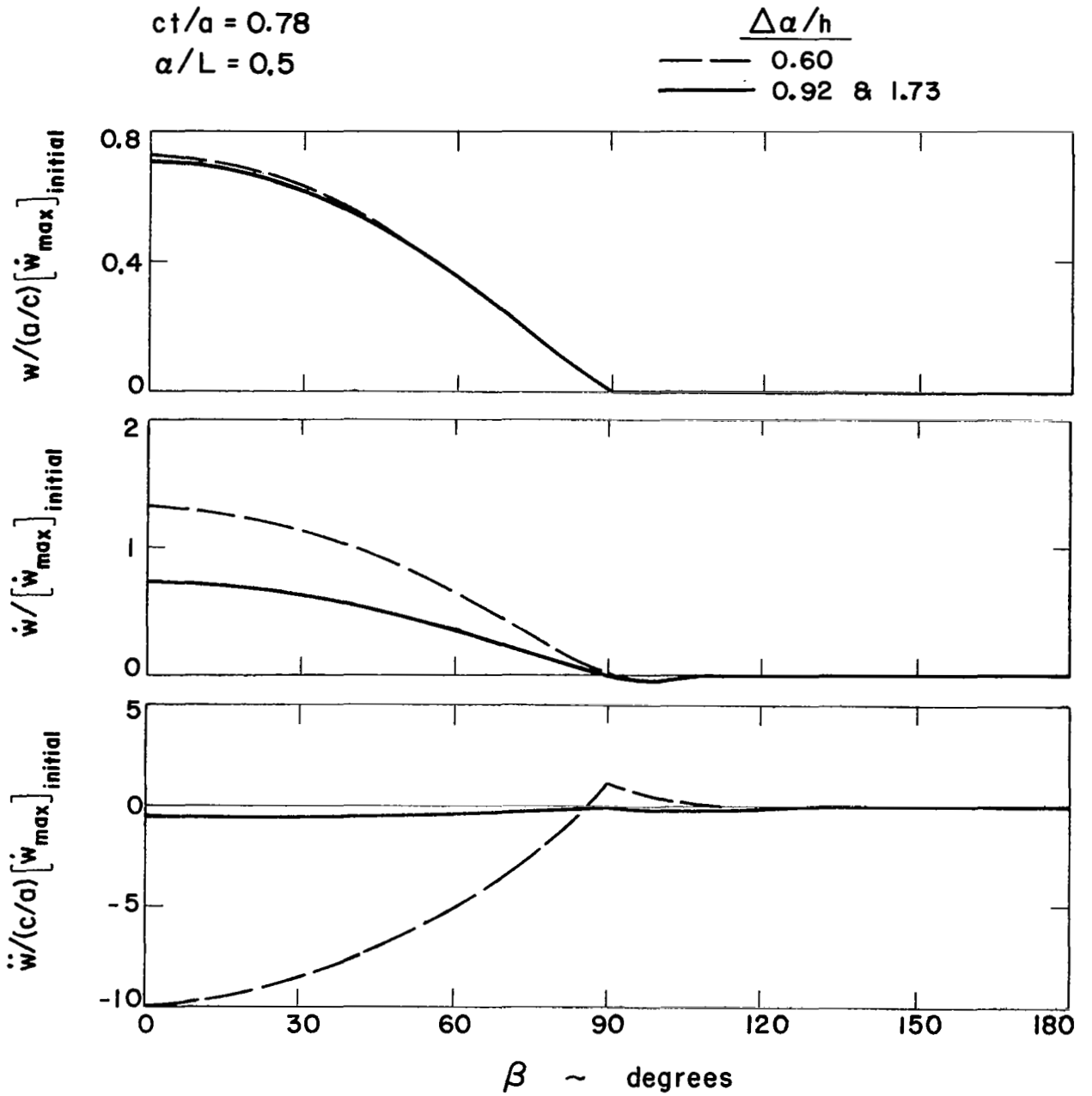

Figure 36. Kinematic Response Snapshots for Example 13 (Cosine Impulse)

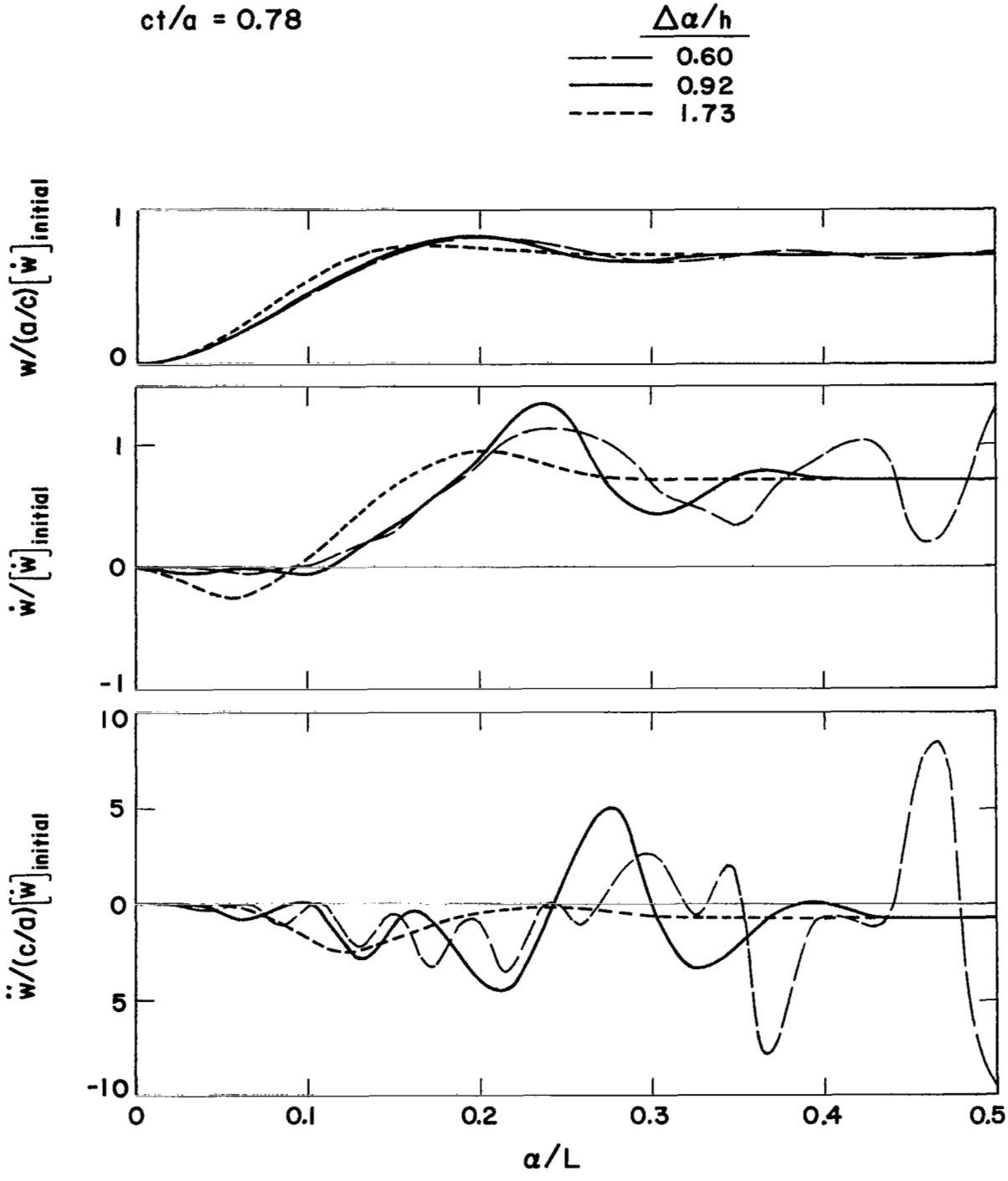

Figure 37. Kinematic Response Snapshots for Example 13 (Uniform Impulse)

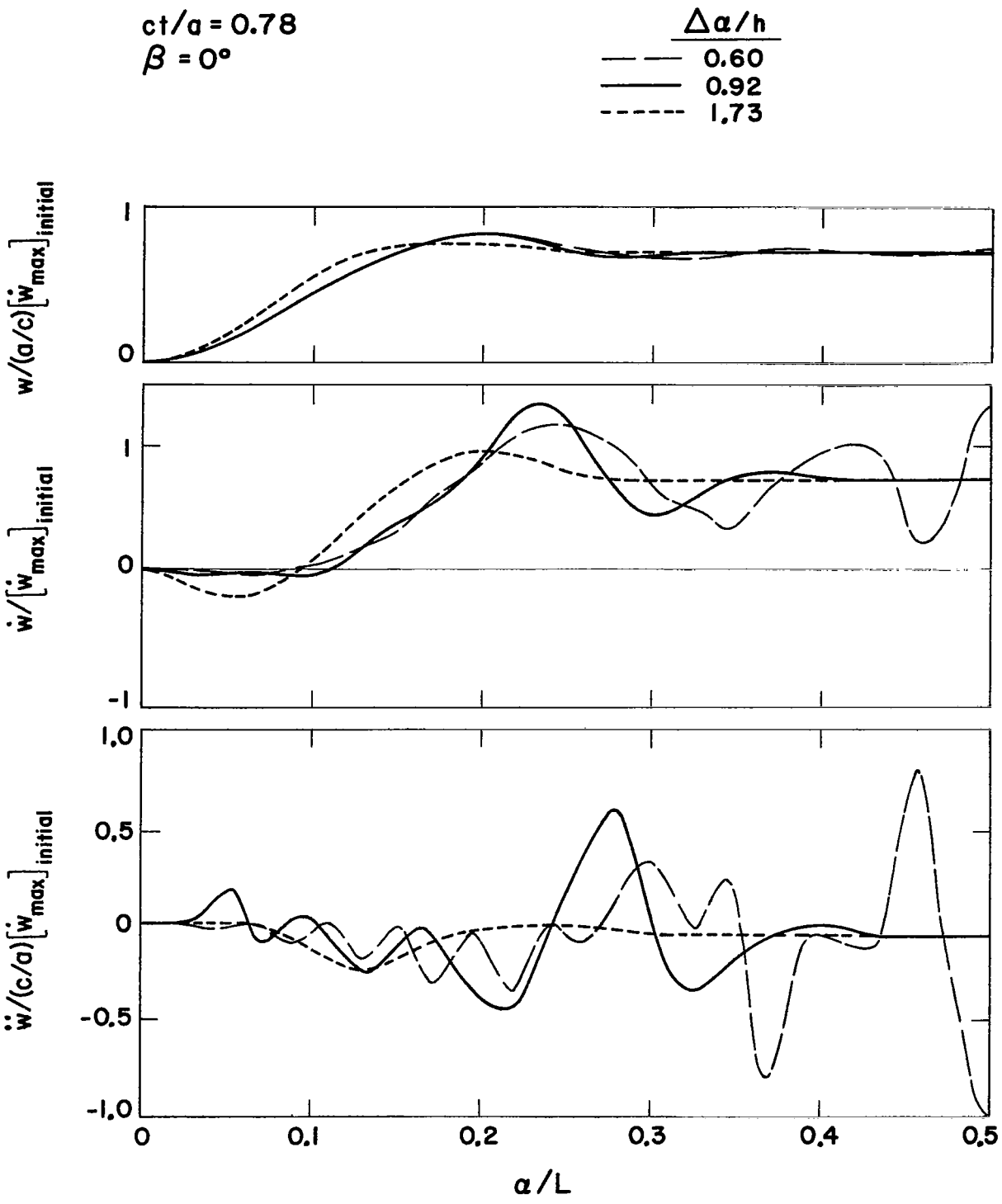

Figure 38. Kinematic Response Snapshots for Example 13 (Cosine Impulse)

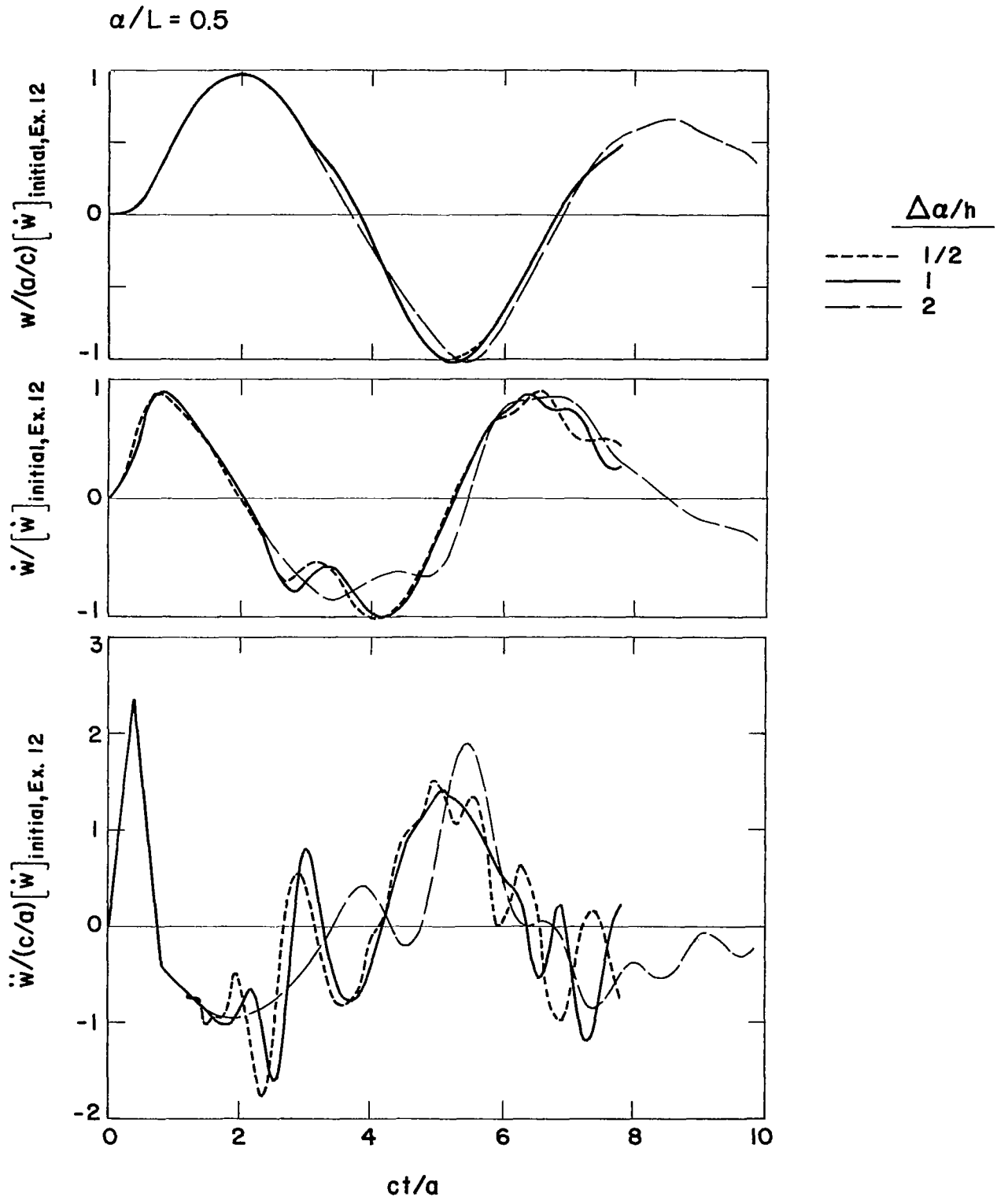

Figure 39. Kinematic Response Histories for Example 14 (t_w = 0.82 a/c)

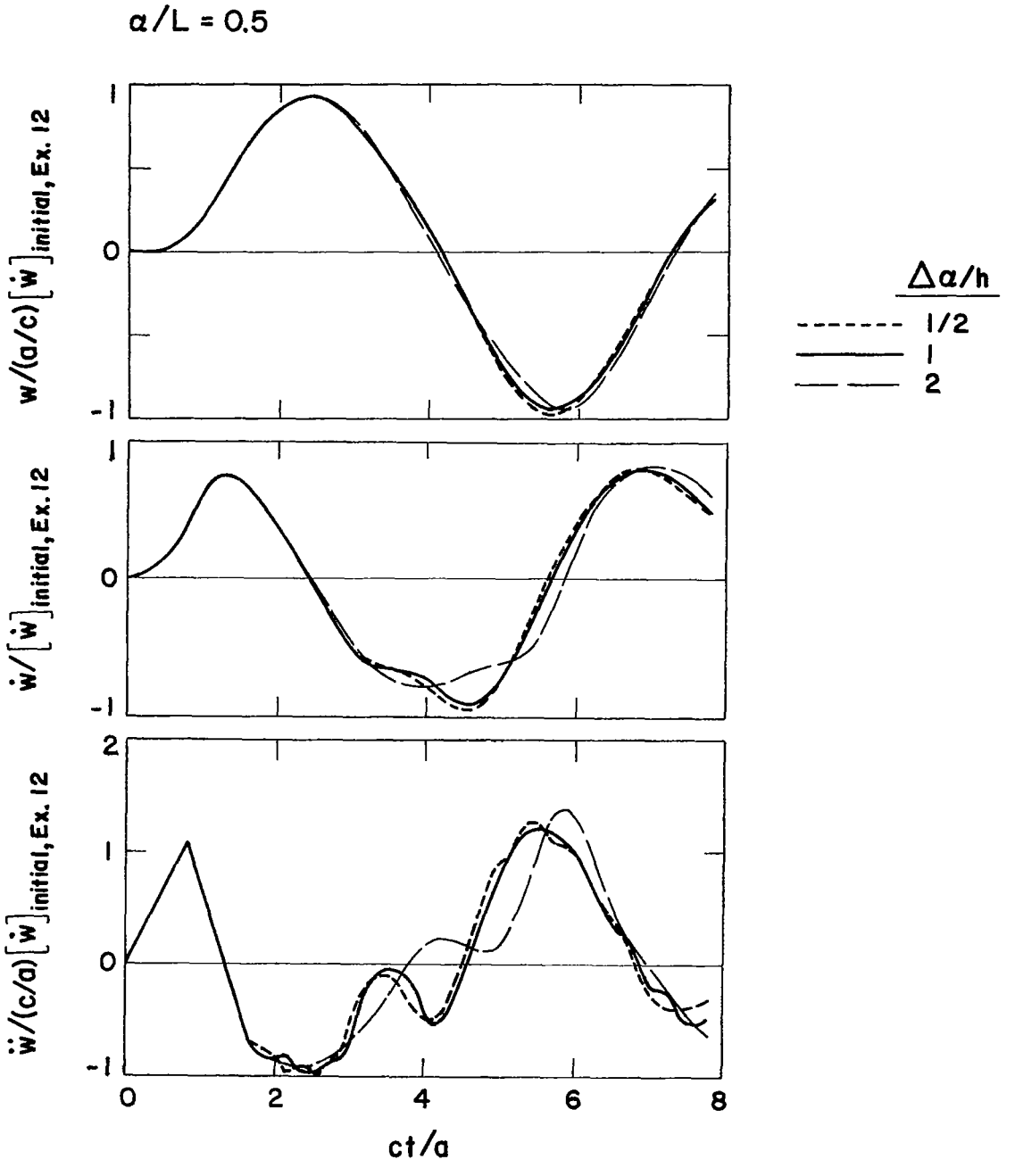

Figure 40. Kinematic Response Histories for Example 14 (t_w = 1.64 a/c)

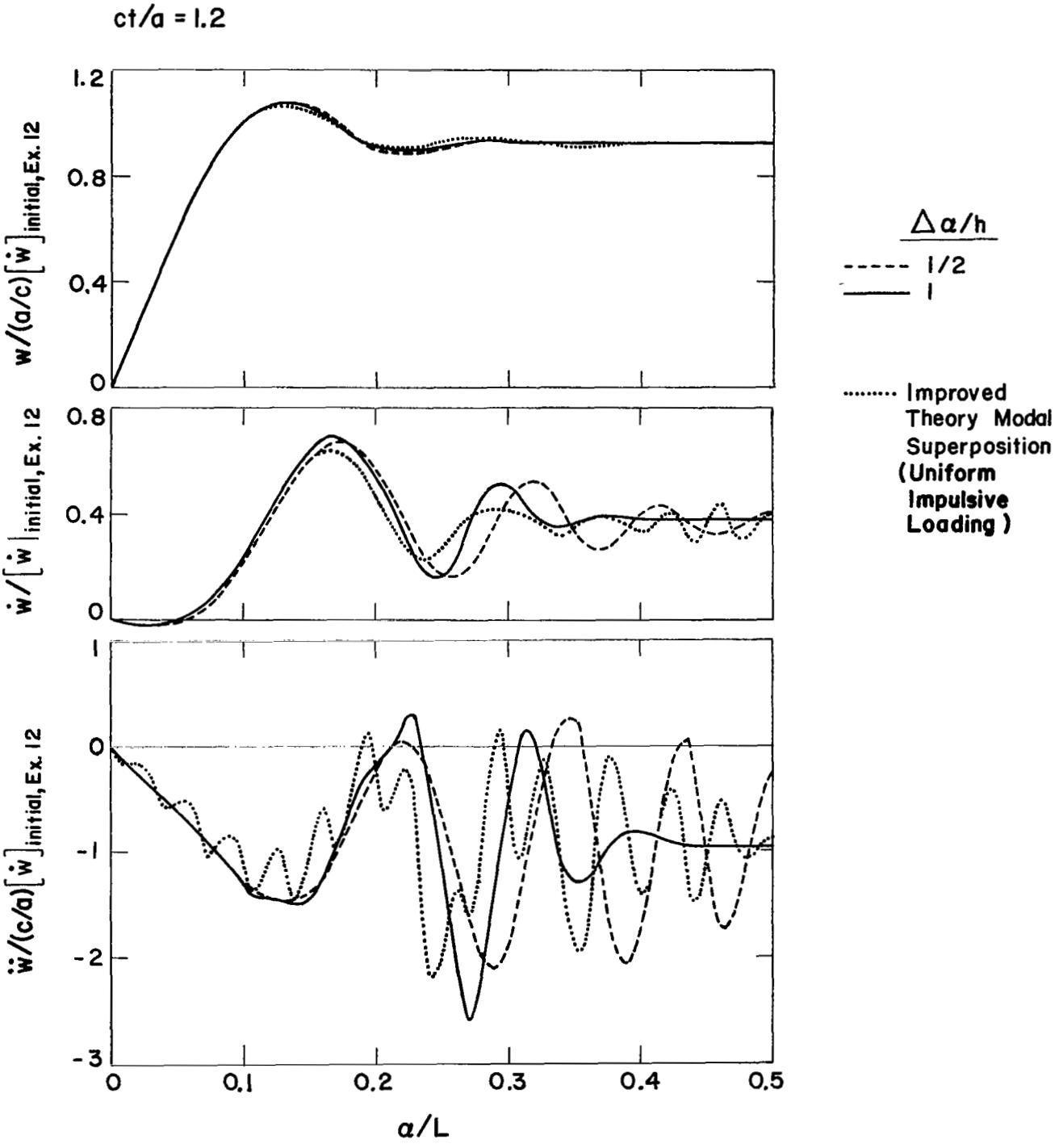

Figure 41. Kinematic Response Snapshots for Example 14 (t_w = 0.40 a/c)

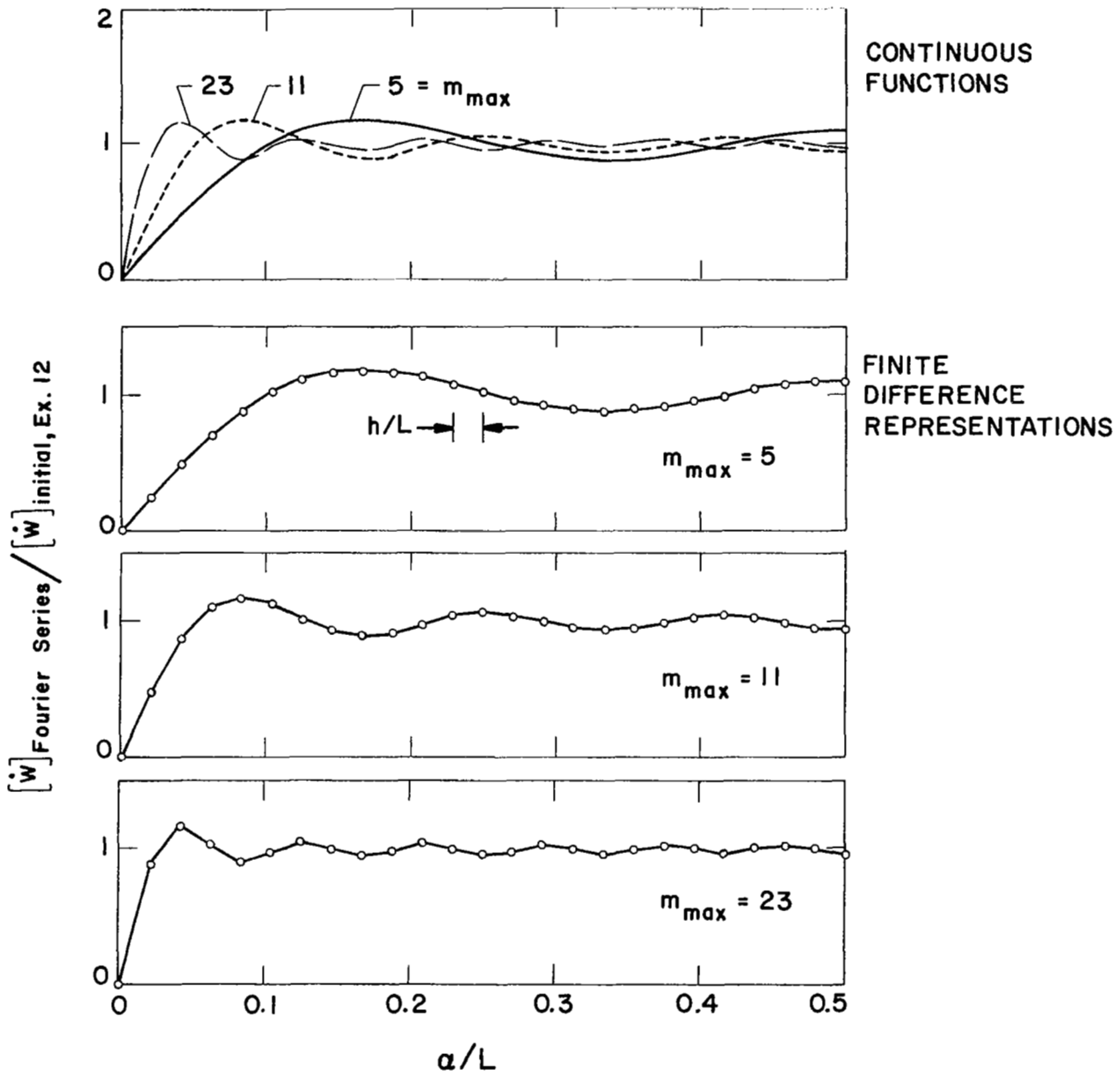

Figure 42. Initial Velocity Conditions for Example 15

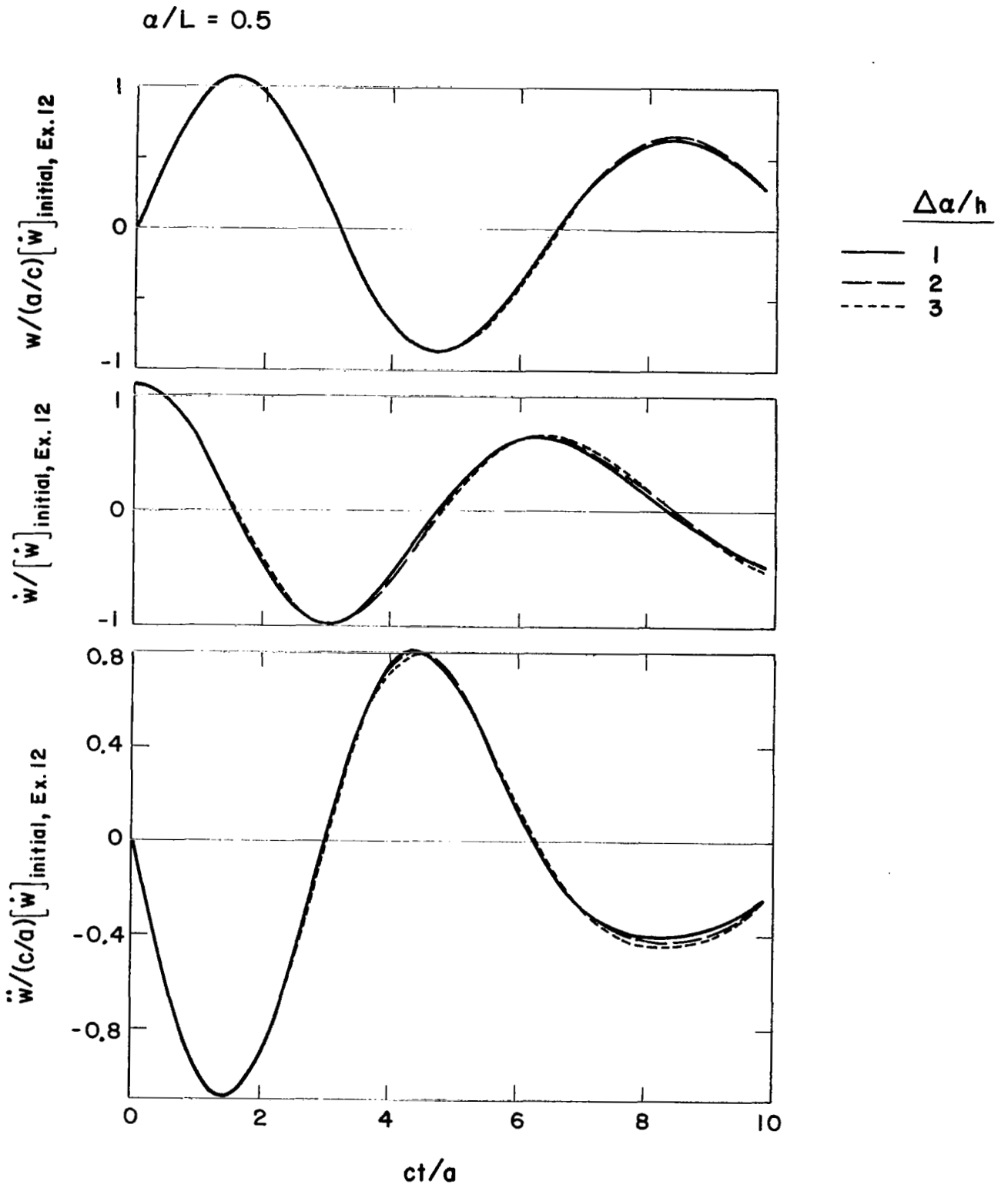

Figure 43. Kinematic Response Histories for Example 15 (m_{max} = 5)

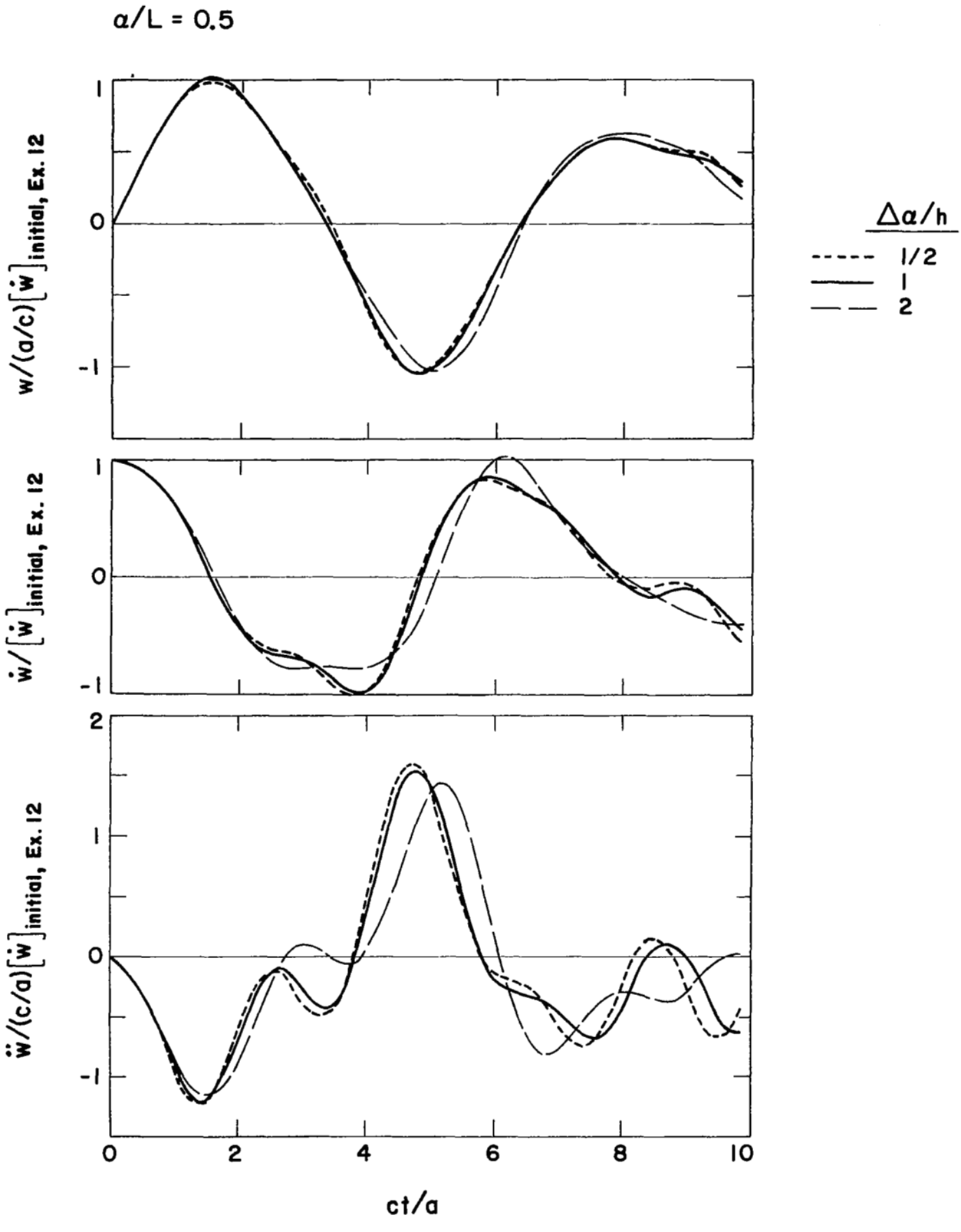

Figure 44. Kinematic Response Histories for Example 15 (m_{max} = 11)

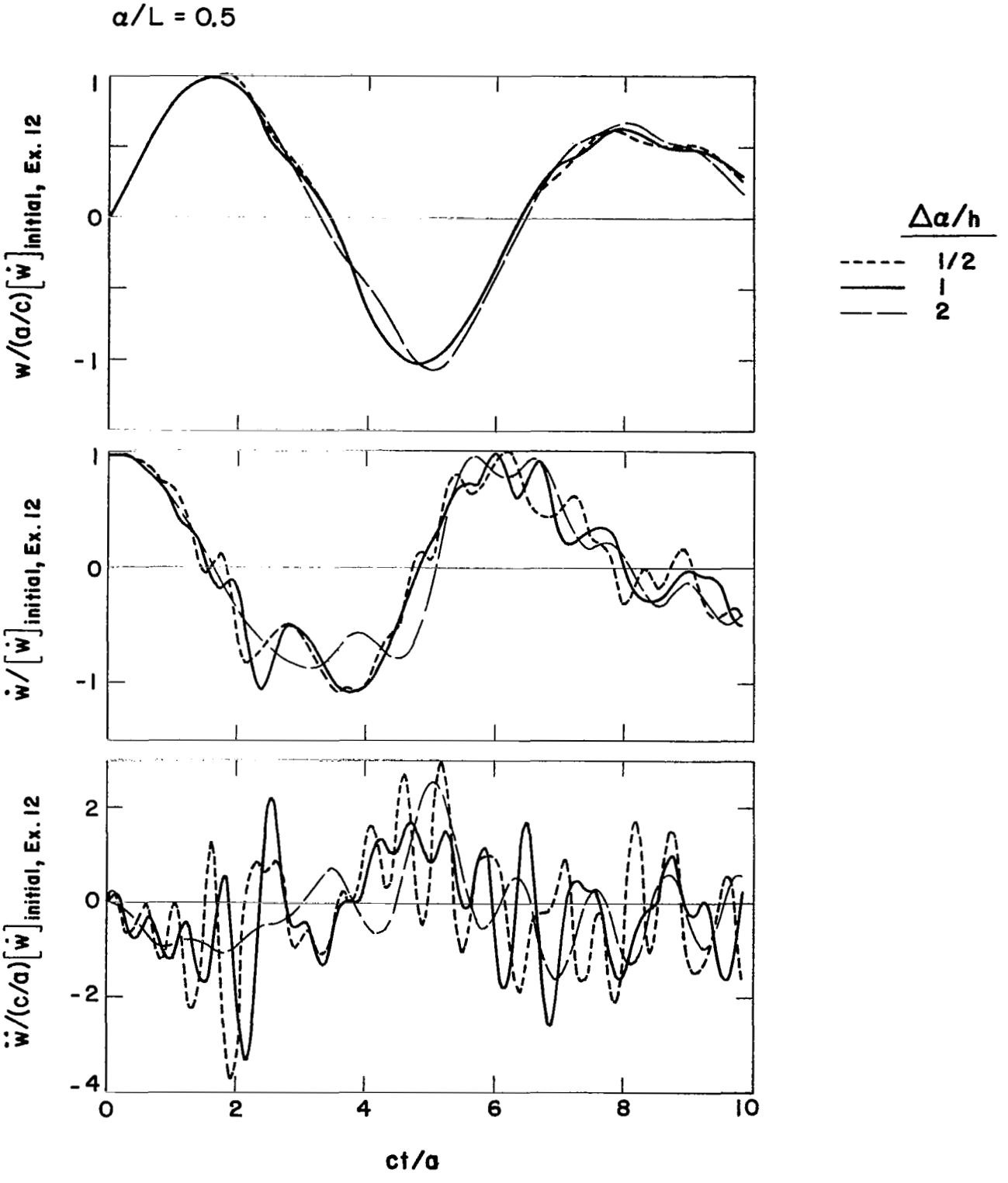

Figure 45. Kinematic Response Histories for Example 15 (m_{max} = 23)

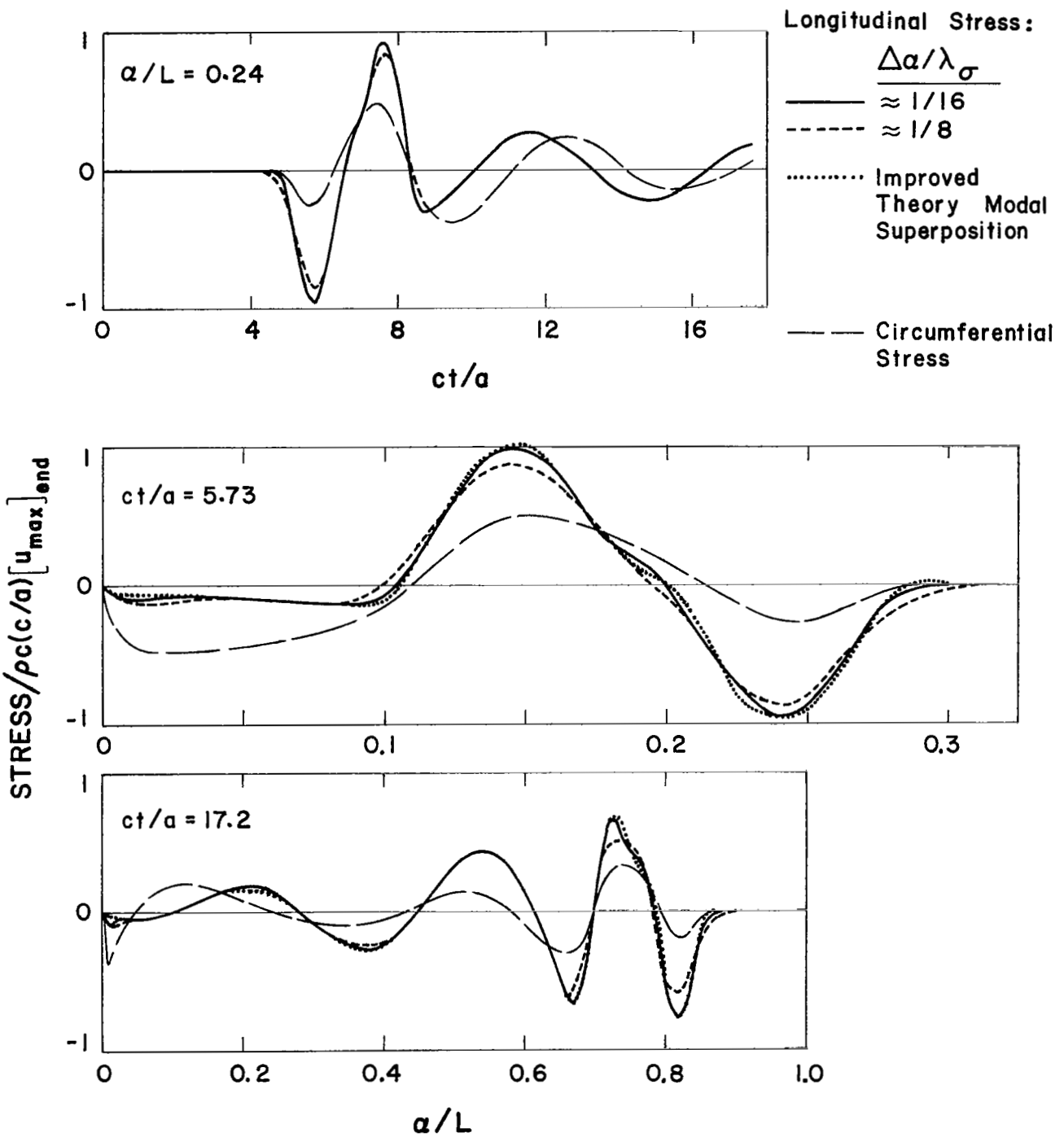

Figure 46. Stress Response History and Snapshots for Example 2

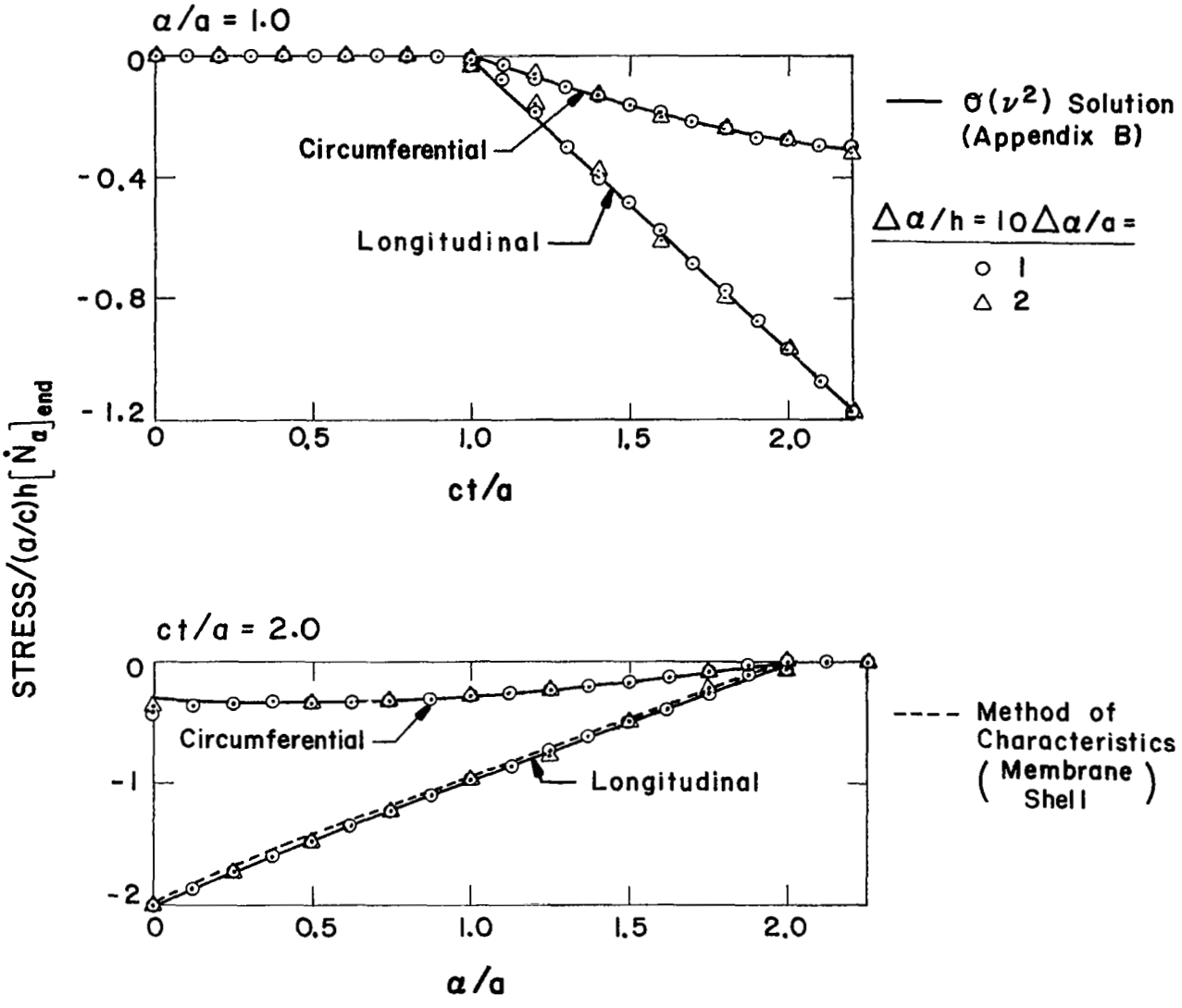

Figure 47. Stress Response History and Snapshot for Example 3

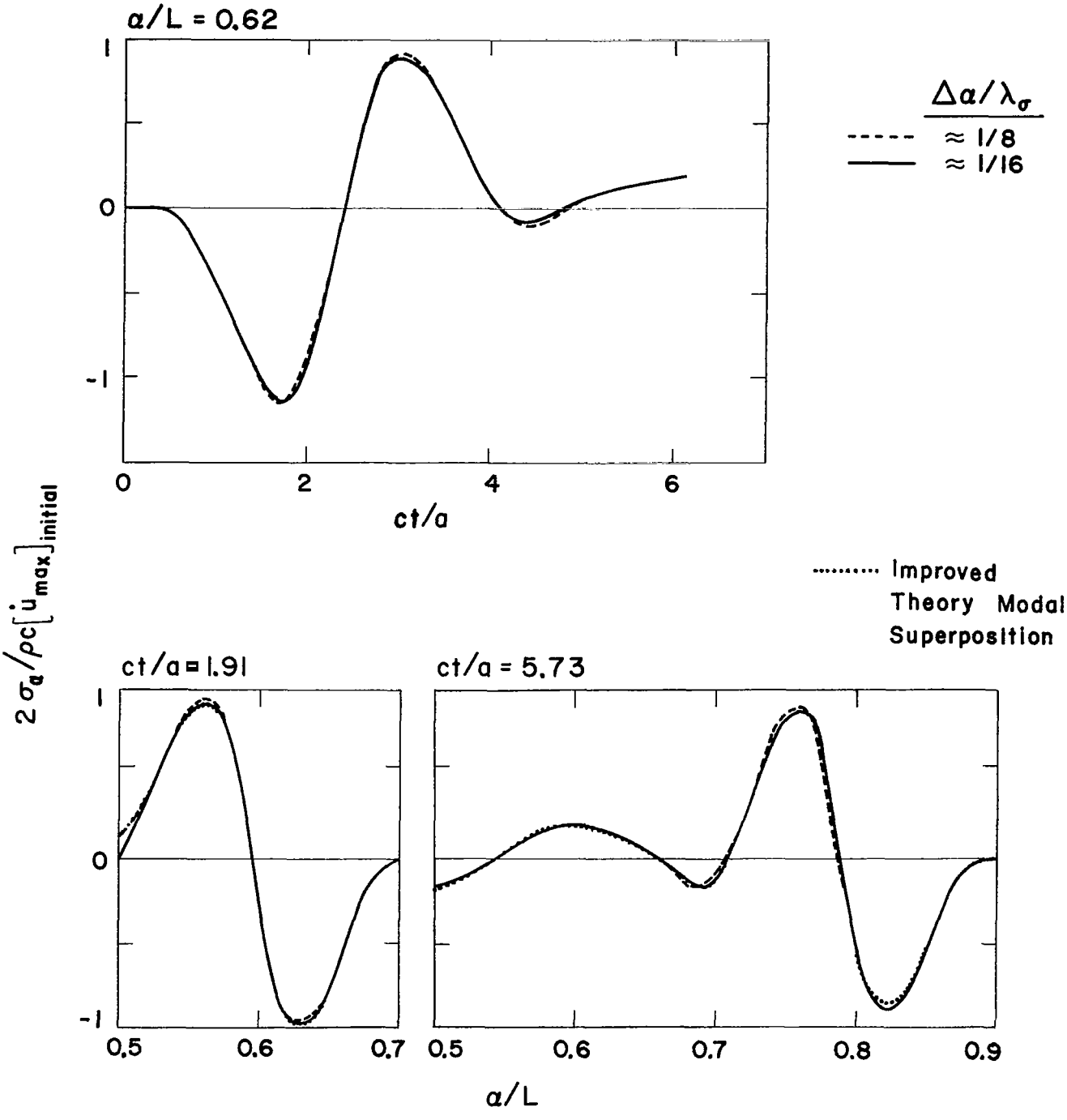

Figure 48. Stress Response History and Snapshots for Example 5

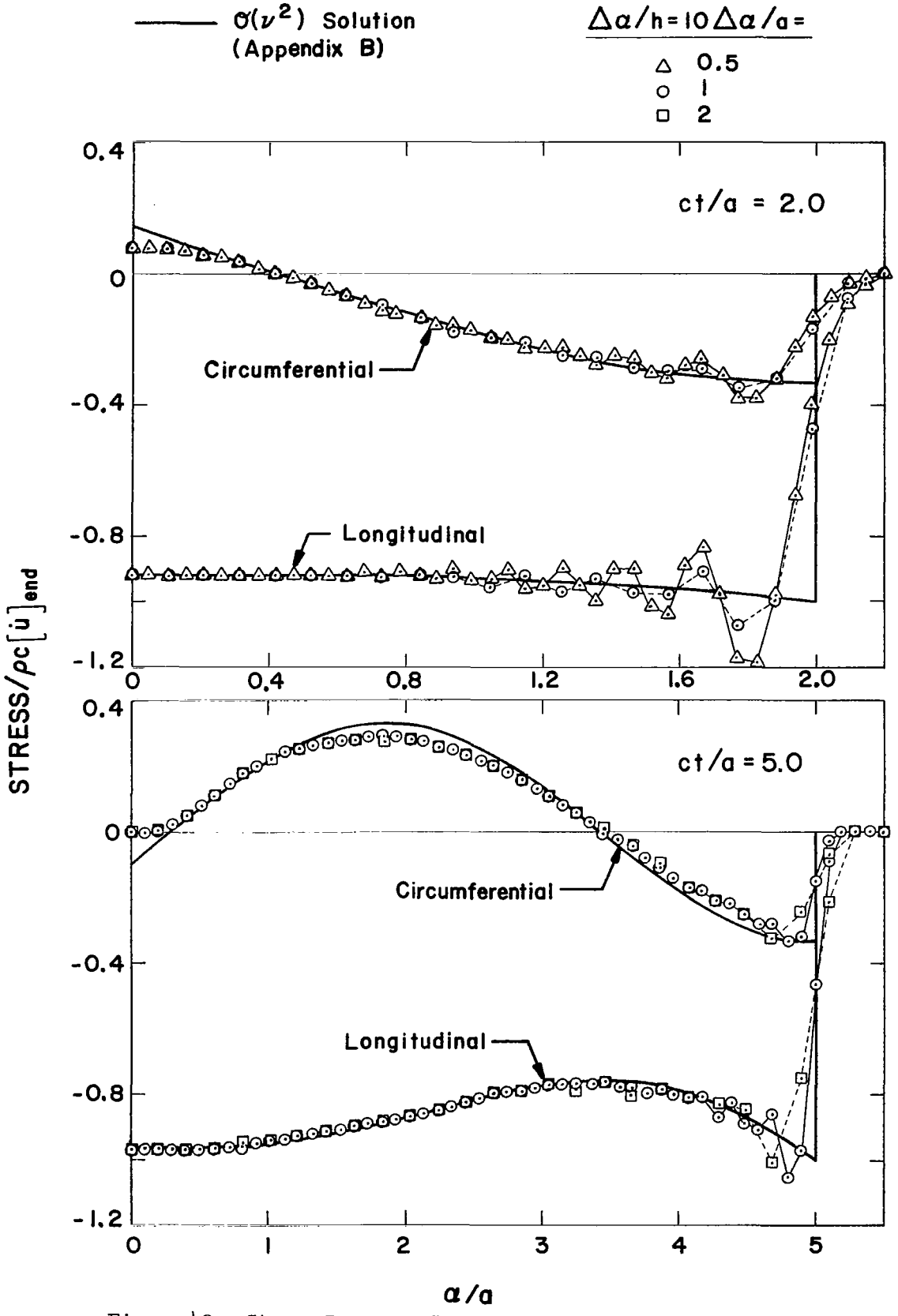

Figure 49. Stress Response Snapshots for Example 7

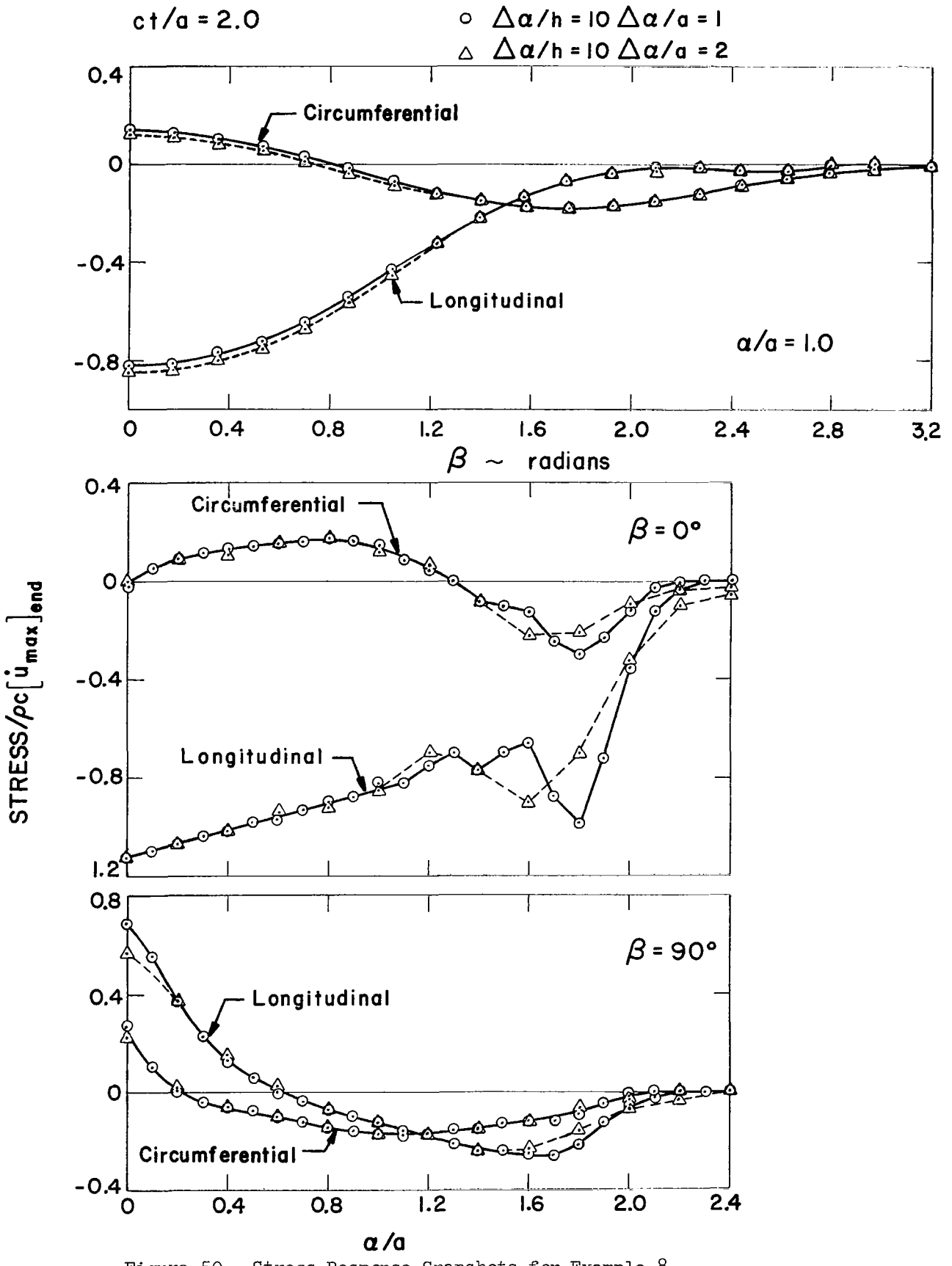

Figure 50. Stress Response Snapshots for Example 8

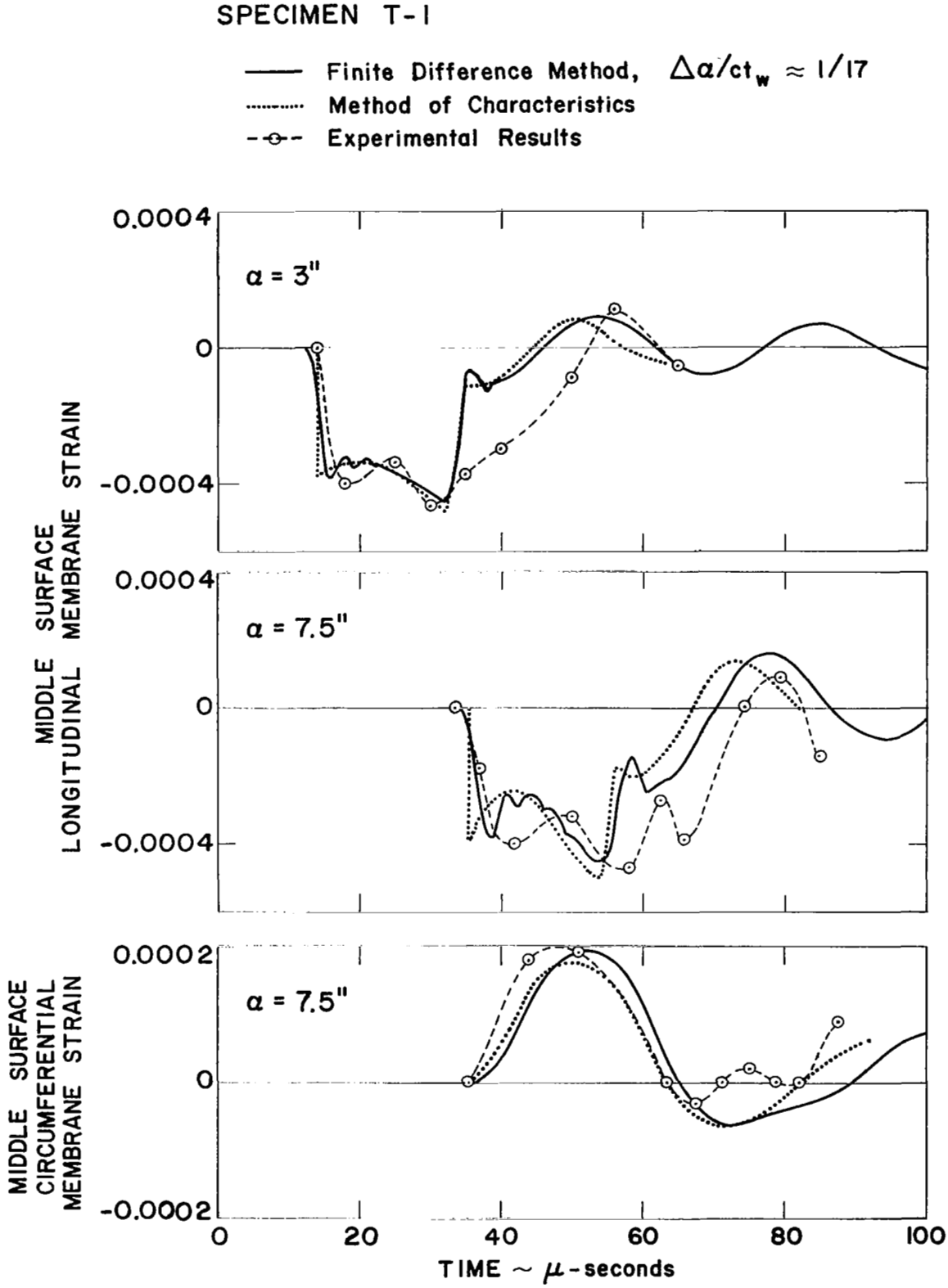

Figure 51. Strain Response Histories for Example 16

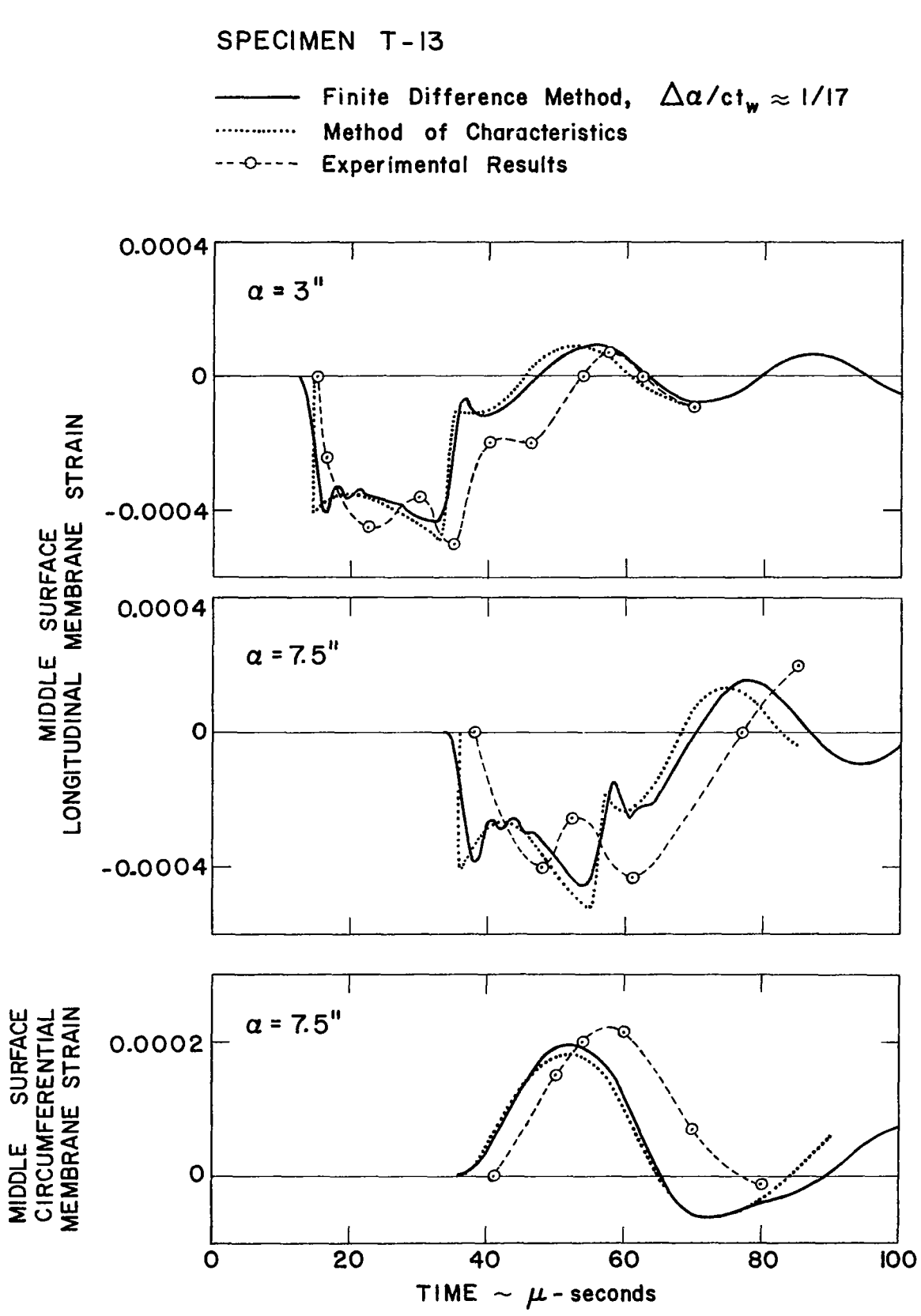

Figure 52. Strain Response Histories for Example 16

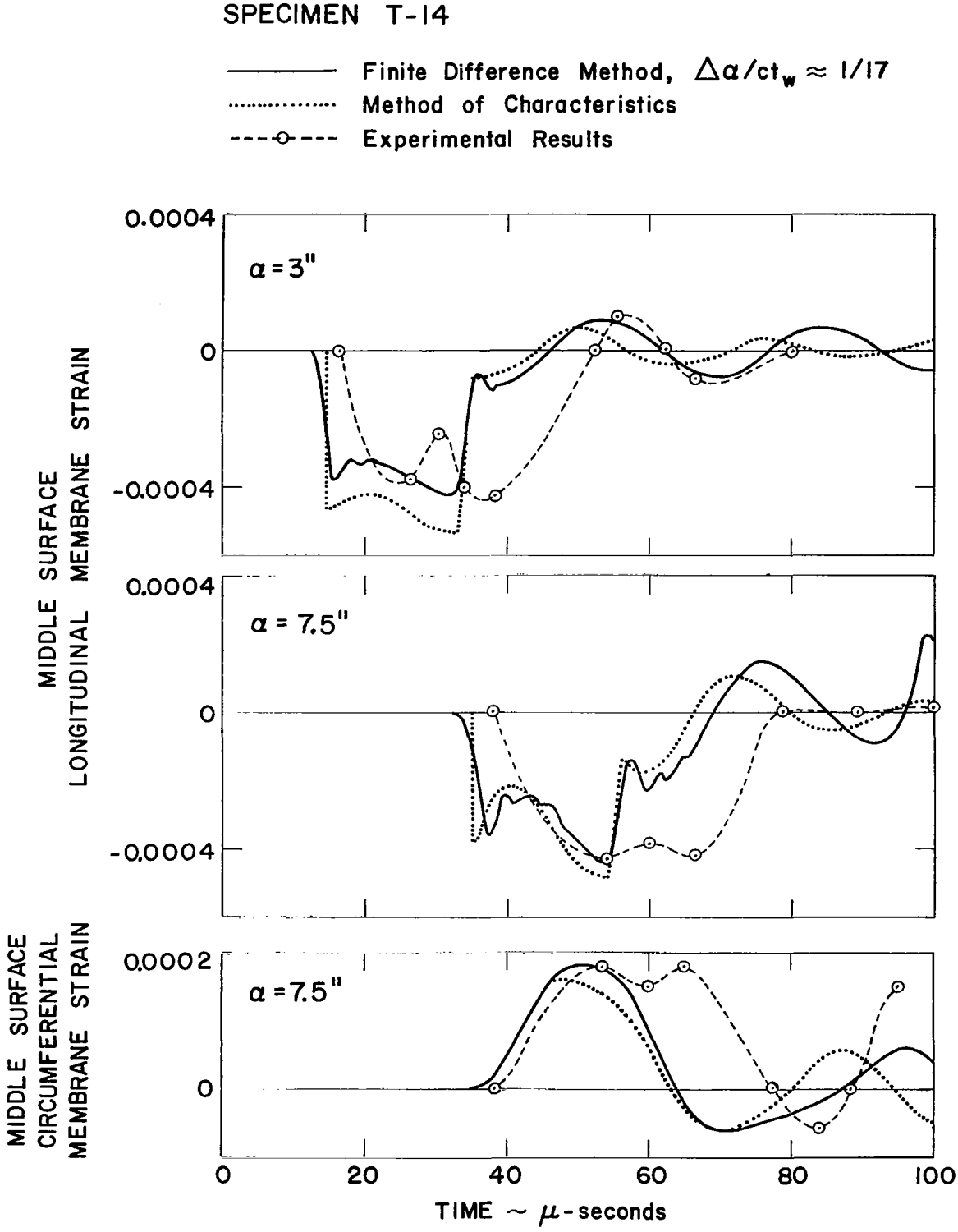

Figure 53. Strain Response Histories for Example 16

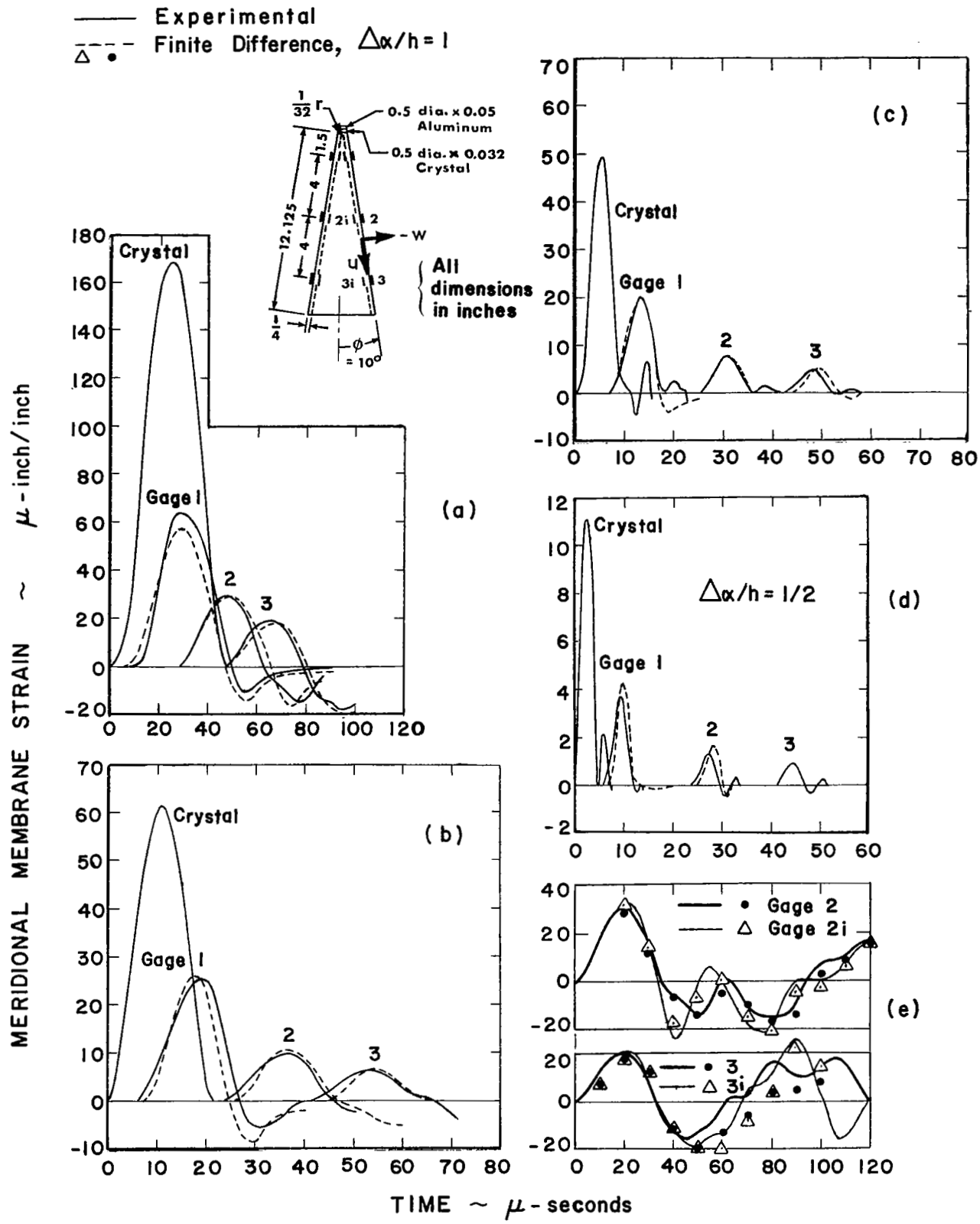

Figure 54. Strain Response Histories for Example 17

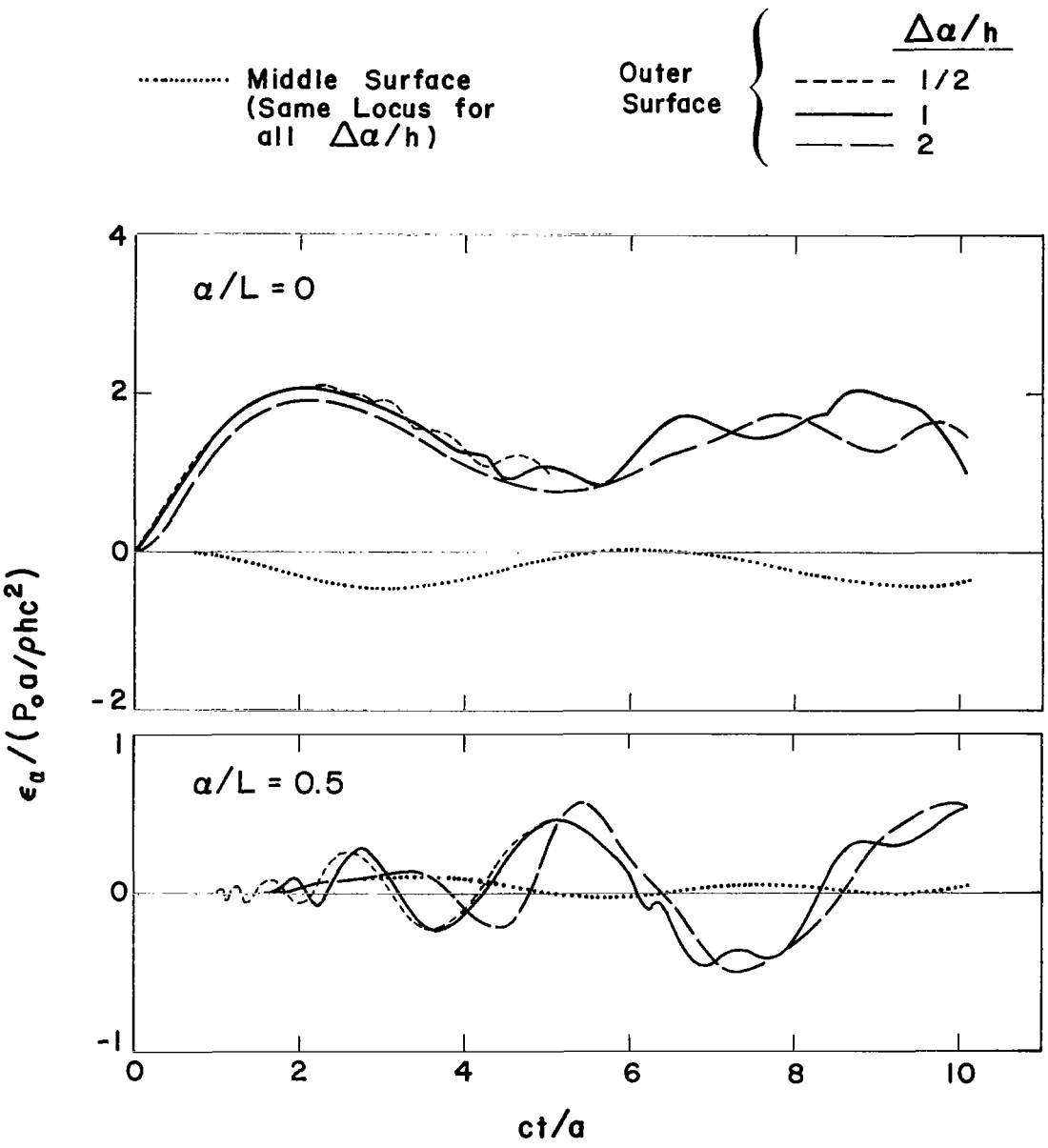

Figure 55. Strain Response Histories for Example 9

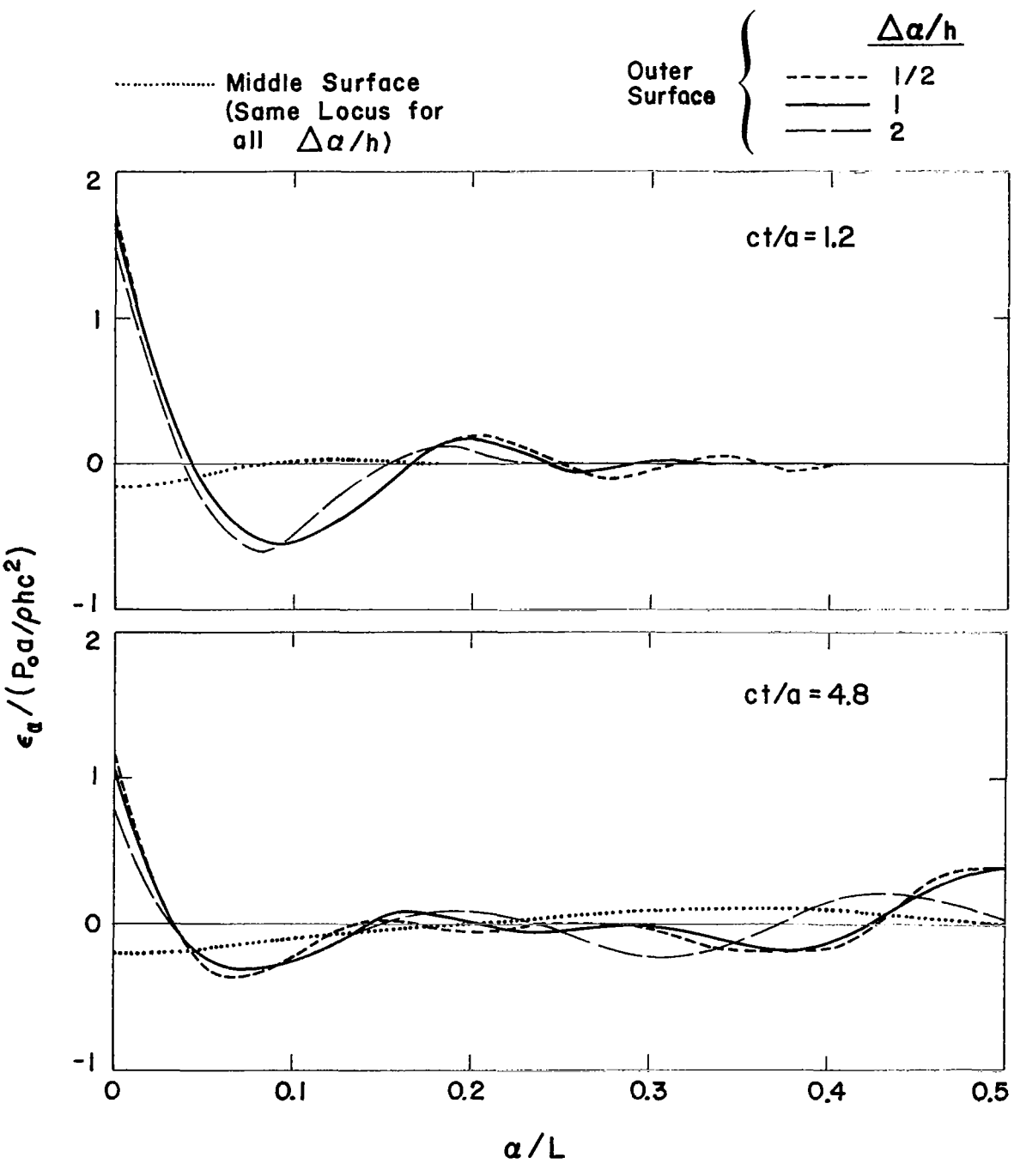

Figure 56. Strain Response Snapshots for Example 9

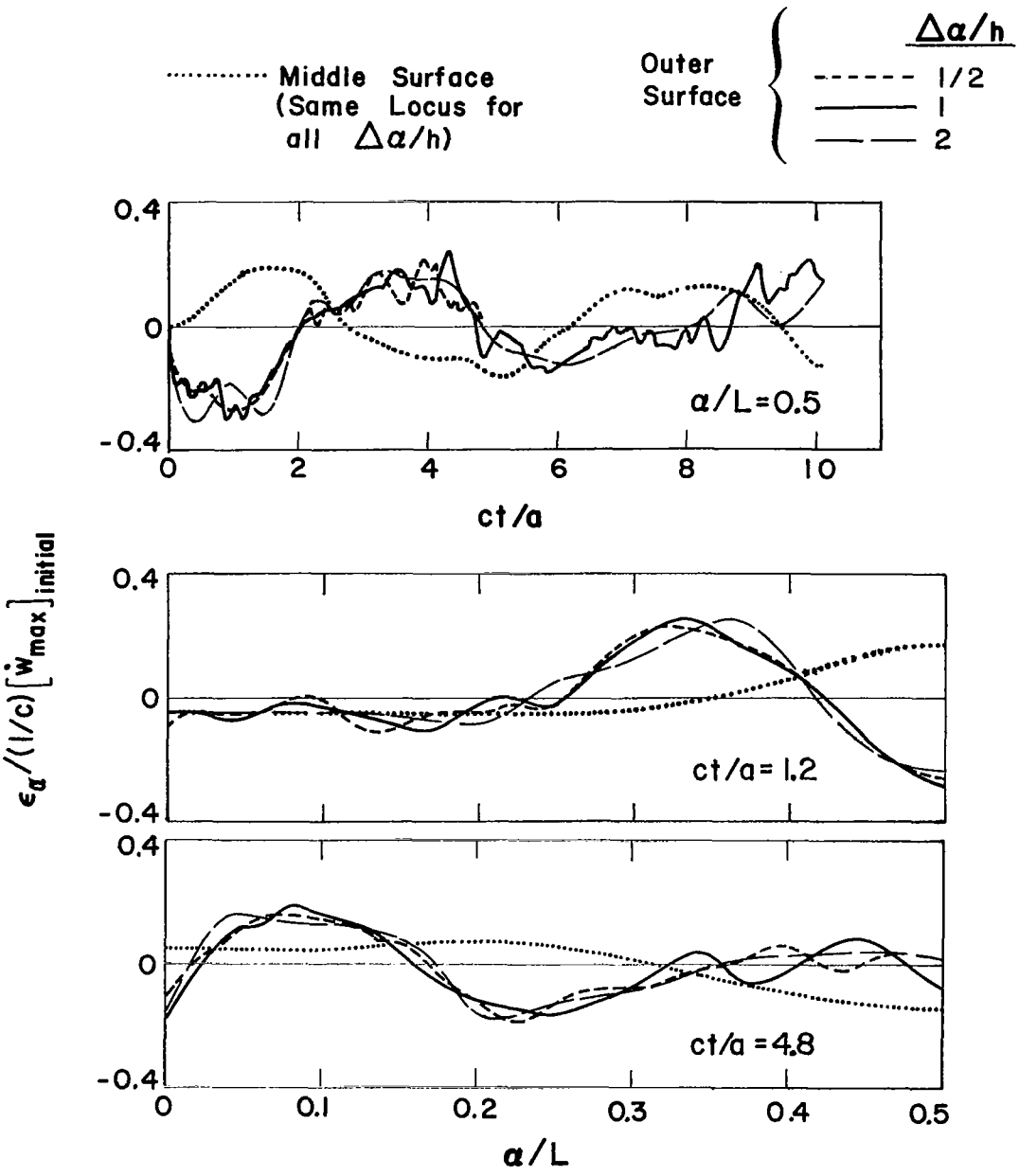

Figure 57. Strain Response History and Snapshots for Example 10 (α_w = 0.8a)

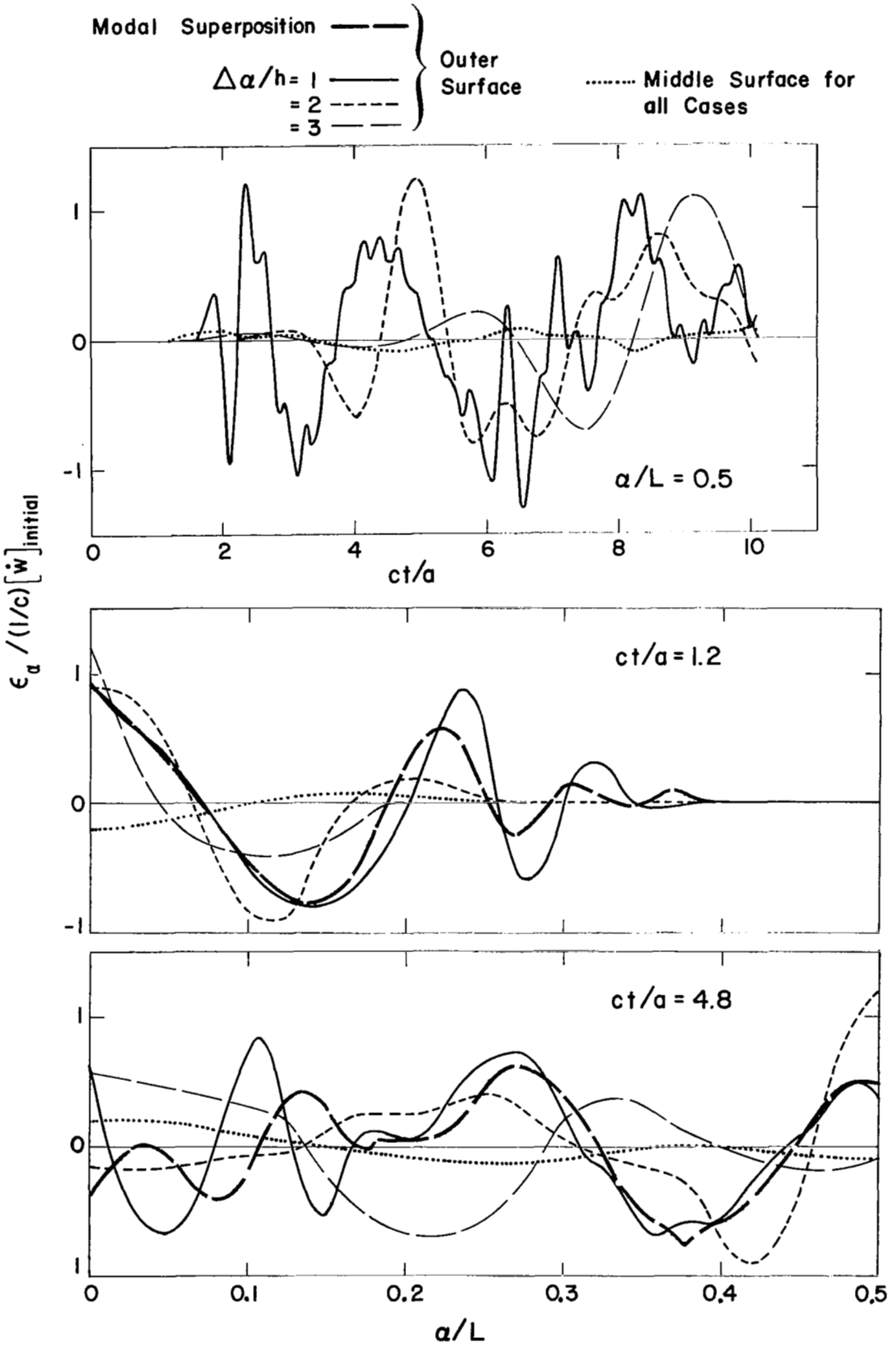

Figure 58. Strain Response History and Snapshots for Example 11

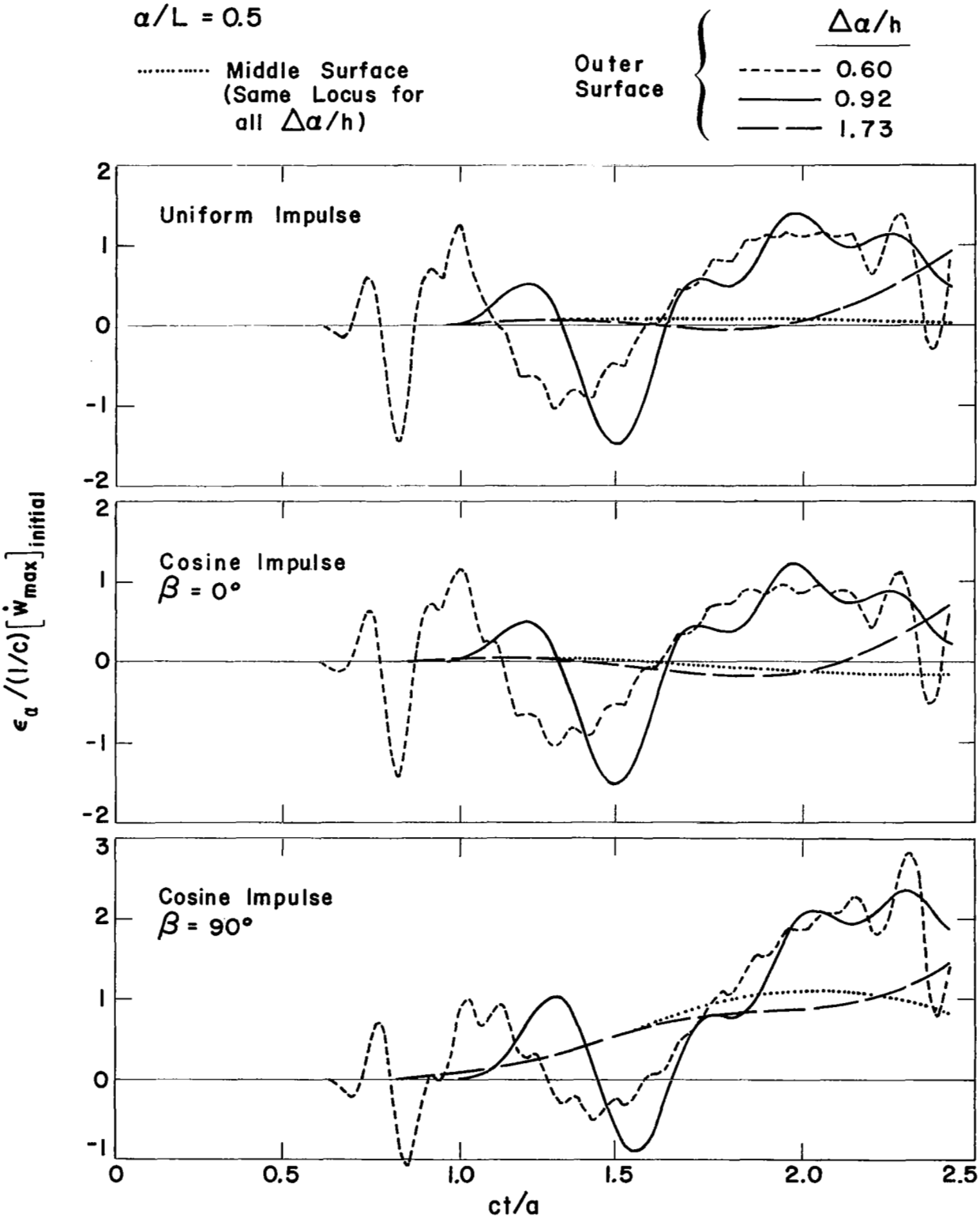

Figure 59. Strain Response Histories for Example 13

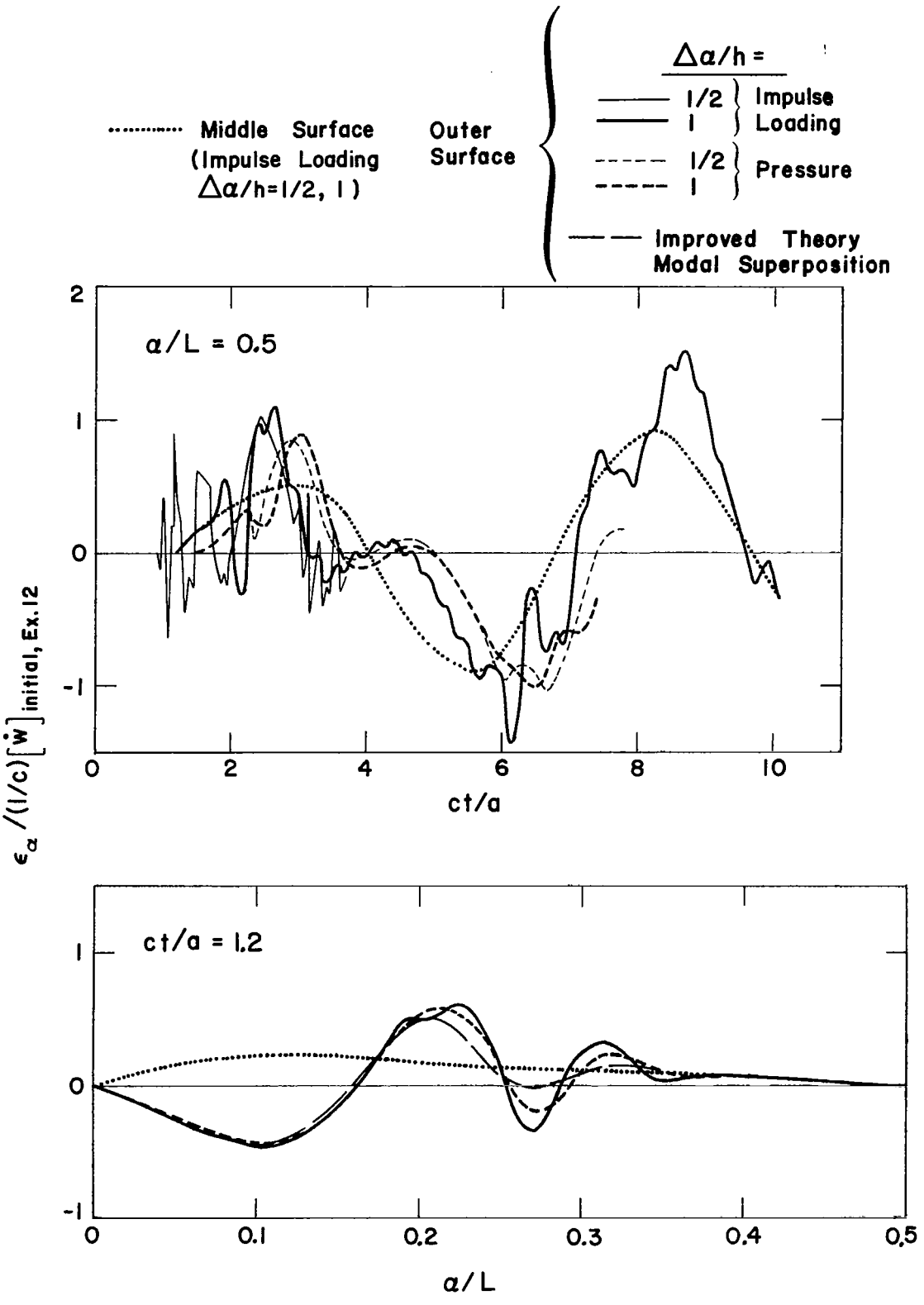

Figure 60. Strain Response History (t_w = 0.82 a/c) and Snapshot (t_w = 0.40 a/c) for Example 14

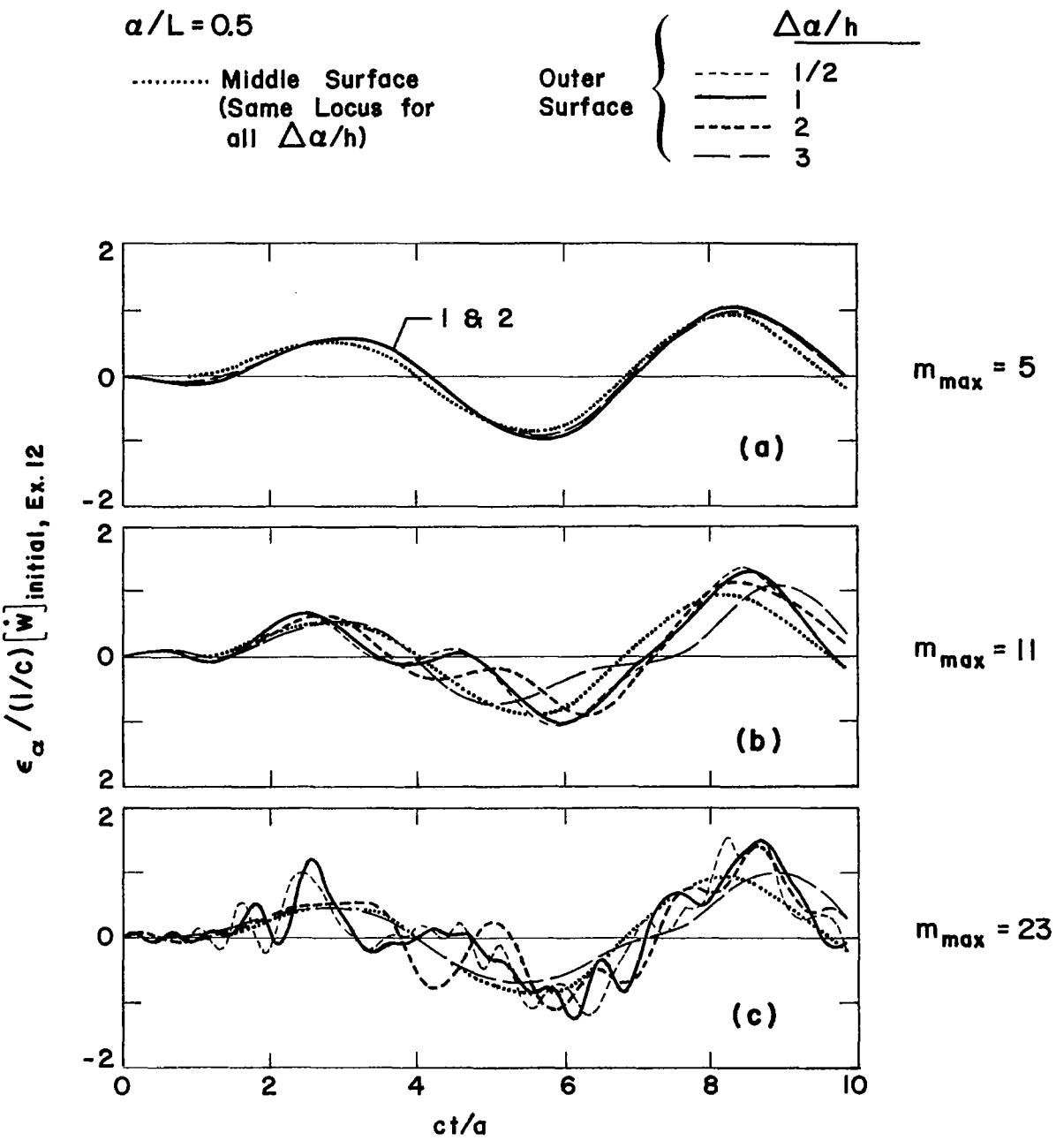

Figure 61. Strain Response Histories for Example 15

Chapter 3

ANALYTICAL STUDY OF CONVERGENCE

The primary objective of this chapter is to study the causes of the convergence problems encountered in Chapter 2. Two causes are possible: limitations inherent in the finite difference method, and limitations of the shell theory employed.

It is clear that in problems characterized by the presence of response discontinuities, there always exists a region near each discontinuity where non-convergent oscillations in the finite difference computations occur. Even though this behavior causes only marginal difficulties, it still represents an inherent limitation of the finite difference method.

We observed in Chapter 2 convergence problems related to flexural response computations that are not caused by the presence of discontinuities in the response of interest. We will see in this chapter that this difficulty is not the result of a limitation in the finite difference method itself, but is instead the result of a limitation of the thin shell (Bernoulli-Euler) theory used.

There is ample evidence in the results of Chapter 2 that the convergence difficulties of finite difference computations are associated with response components with short structural wave lengths. For these components, shell curvature effects are unimportant and it is therefore justifiable to consider the simpler case of a plate instead of a shell. Furthermore, since convergence difficulties in the absence of response discontinuities have not occurred for shells subjected to in-plane excitations, we need only consider transverse motions of the plate.

The principal results of this Chapter are (1) that the finite difference method fails to converge only in regions around discontinuities in the response of interest, (2) that flexural response convergence problems not in regions around response discontinuities are the direct result of the failure of thin shell (Bernoulli-Euler) theory, and (3) that a thin shell finite difference solution may be more accurate than even an exact solution of the corresponding differential equations. In addition, it is pointed out that the method of

modal superposition also suffers from convergence limitations, and that the use of improved shell (Timoshenko) theory instead of thin shell theory will tend to relieve some of the convergence difficulties associated with computations of flexural response, but may also prove to be inadequate for some purposes.

3.1 CONVERGENCE OF FINITE DIFFERENCE COMPUTATIONS OF FLEXURAL RESPONSE

This section examines the dynamic characteristics of a finite difference model of a thin plate. These characteristics are then related to those of the continuous plate and convergence of the finite difference model in the limit of vanishing mesh size is demonstrated.

3.1.1 Frequency Equation for the Finite Difference Plate

A convenient way to characterize the dynamic behavior of a system is to determine the frequency equation for the system. Such an equation relates the (angular) frequency ω to the wave number k. As shown in the subsequent derivation for a plate, and as Ref. 19 shows for simple discrete systems, the frequency equation $\omega = \omega(k)$ for homogeneous discrete systems is independent of the boundary conditions and the number of degrees-of-freedom; different boundary conditions or a different number of degrees-of-freedom merely give different points on the same $\omega = \omega(k)$ curve. It should also be noted that the frequency equation is the same for traveling waves, standing waves due to free oscillations, and forced sinusoidal oscillations (Ref. 19); again the different cases simply give different points on the same frequency curve $\omega = \omega(k)$.

The frequency equation will now be determined for the discrete system that results from a finite difference representation of the flexural motion of a thin, flat plate. A comparison is then made between the frequency equation for the continuous plate and that for the finite difference plate in the limit of vanishing mesh width.

The free transverse motion of a thin plate is governed by the following equation:*

$$\nabla^4 w = \frac{\partial^4 w}{\partial x^4} + 2\frac{\partial^4 w}{\partial x^2 \partial y^2} + \frac{\partial^4 w}{\partial y^4} = \left(\frac{1}{c\gamma}\right)^2 \frac{\partial^2 w}{\partial t^2} \tag{1}$$

where $w(x,y,t)$ is the lateral displacement, x and y are Cartesian coordinates, c is the plate velocity, $\gamma = h/\sqrt{12}$ is the radius of gyration (h = plate thickness) and t is time. This equation will now be converted to a partial difference equation through the use of second order finite difference expressions. The plate domain is replaced by a finite difference mesh with mesh widths Δx and Δy in the x- and y-direction, respectively. The mesh or nodal points are located at the intersections of the lines

$$\begin{aligned} x &= \Delta x,\ 2\Delta x,\ \ldots,\ m\Delta x,\ \cdots \\ y &= \Delta y,\ 2\Delta y,\ \ldots,\ n\Delta y,\ \cdots \end{aligned} \tag{2}$$

where m and n are mesh point indices. The finite difference approximation to the differential operator $\nabla^4 w$ in Eq. 1 is represented at the mesh point m,n by the module shown in Fig. 1. For example, the coefficient of $w_{m,n}$ at point m,n is $6[(\Delta x)^{-4} + (\Delta y)^{-4}] + 8(\Delta x)^{-2}(\Delta y)^{-2}$. In the interest of brevity, we do not explicitly write down the complete difference equation at the point m,n; it can readily be obtained from Eq. 1 and Fig. 1.

For a wave-type solution of the difference equation we take

$$\begin{aligned} w_{m,n} &= A \exp\left[j(\omega t - k_x x - k_y y)\right] \\ &= A \exp\left[j(\omega t - k_x m\Delta x - k_y n\Delta y)\right] \end{aligned} \tag{3}$$

where k_x and k_y are the trace wave numbers relative to the x- and y-axes, respectively, and ω is angular frequency. We can write, therefore,

*This expression can be readily obtained from the last of Eqs. 1.7.

$$w_{m+1,n} = A \exp\{j[\omega t - k_x(m+1)\,\Delta x - k_y n \Delta y]\}$$

$$= w_{m,n} \exp[-jk_x \Delta x] \qquad (4)$$

$$w_{m-1,n-1} = w_{m,n} \exp[j(k_x \Delta x + k_y \Delta y)]$$

.

.

etc.

Proceeding in this way, we can express the lateral displacement at each nodal point of the computational module (Fig. 1) in terms of $w_{m,n}$. Thus the difference equation at the mesh point m,n reduces to an algebraic equation which is homogeneous in $w_{m,n}$. Since $w_{m,n}$ represents the displacement at a general mesh point, the coefficient of $w_{m,n}$ must vanish, so that, after some algebraic manipulations,* we obtain the condition required for the plane wave given by Eq. 3 to be a solution of the finite difference equation for the plate. This condition is the frequency equation for the discrete system, and is given by

$$\omega(k_x, \Delta x, k_y, \Delta y) = 4c\gamma \left[\frac{1}{(\Delta x)^2} \sin^2\left(\frac{k_x \Delta x}{2}\right) + \frac{1}{(\Delta y)^2} \sin^2\left(\frac{k_y \Delta y}{2}\right)\right] \qquad (5)$$

This relation has been obtained without consideration of boundary conditions and is therefore independent of them. Also, $\omega(k_x, \Delta x, k_y, \Delta y)$ is not a function of the indices m and n; hence the frequency curve is independent of the number of degrees-of-freedom.

3.1.2 Cutoff Frequency

The frequency $\omega(k_x, \Delta x, k_y, \Delta y)$ reaches a maximum for

$$k_x \Delta x = k_y \Delta y = \pi, 3\pi, 5\pi, \cdots \qquad (6)$$

*Trigonometric identities for $\sin^4\xi$ and $(\sin^2\xi)(\sin^2\zeta)$ are employed.

which corresponds to wave lengths $\lambda_x = 2\pi/k_x, \lambda_y = 2\pi/k_y$ given by

$$\lambda_x = 2\Delta x, \frac{2}{3}\Delta x, \frac{2}{5}\Delta x, \ldots$$
$$\lambda_y = 2\Delta y, \frac{2}{3}\Delta y, \frac{2}{5}\Delta y, \ldots \tag{7}$$

Since wave lengths smaller than twice the mesh spacing have no meaning (Ref. 20), we conclude that "cutoff" is reached at the following wave numbers

$$k_{xc} = \pi/\Delta x, \; k_{yc} = \pi/\Delta y \tag{8}$$

so that, from Eq. 5, the cutoff frequency is given by

$$\omega_c = 4c\gamma\left(\frac{1}{(\Delta x)^2} + \frac{1}{(\Delta y)^2}\right) \tag{9}$$

The introduction of Eqs. 8 into Eqs. 4 yields the following mode shape appropriate to the frequency ω_c:

$$w_{m+p,n+q} = \begin{cases} +w_{m,n}, & |p| + |q| \quad \text{even} \\ -w_{m,n}, & |p| + |q| \quad \text{odd} \end{cases} \tag{10}$$

Thus, at the cutoff frequency each mesh point moves with equal absolute value and in a direction opposite to that of its immediate neighbors. This "zig-zag" mode is depicted for the basic finite difference module in Fig. 2.

For one-dimensional discrete problems, such as a linear array of oscillators, it has been shown (Ref. 20) that the wave number k is real if the frequency ω is less than the cutoff frequency ω_c. However, for $\omega_c > \omega$, no travelling wave exists and a standing wave develops. This standing wave is characterized by adjacent points oscillating in opposite phase with amplitudes decreasing exponentially in space; k is therefore

complex. At $\omega = \omega_c$, an ambiguity exists and the wave motion can be considered either traveling or standing. Hence the one-dimensional discrete system behaves as a "low pass filter", i.e., it allows propagation of response components with frequencies up to a cutoff frequency ω_c.

If we specialize our plate problem to the one-dimensional discrete case, i.e., the finite difference beam, the above remarks apply and the finite difference beam constitutes a true low pass filter. The two-dimensional case (Eqs. 5 and 9) is more complicated, for it is conceivable that, at certain frequencies, we may have a traveling wave in one direction and a standing wave in the other direction. This possibility has yet to be adequately studied. However, it is clear that for $\omega > \omega_c$, exponentially decaying standing waves will exist in both directions.

Knowledge of the cutoff frequency for a given mesh size is important, since spurious noise will exist in the response computations if the discrete system is significantly excited at frequencies $\omega > \omega_c$ (Ref. 21). In addition, there is a deterioration of accuracy in the computed response appropriate to the region $\omega \to \omega_c$; this will be studied in detail in Section 3.2.

3.1.3 Critical Time Step

The cutoff frequency is also important in the determination of the maximum time step allowed in conjunction with a given spatial mesh for numerically stable computation. In Ref. 11 it is shown that, for a discrete linear system, the critical time step Δt_{cr} can be determined from

$$\Delta t_{cr} = \frac{2}{\omega_{max}} \tag{11}$$

where ω_{max} is the highest frequency of the system. For ω_{max} we use the cutoff frequency ω_c given by Eq. 9 to obtain the second of Eqs. 1.10. For the special case of a square mesh, Eq. 1.10 agrees with the result given in Ref. 22, which is derived through the application of the von Neumann stability method (Ref. 23).

For completeness, we now present an expression for Δt_{cr} appropriate to in-plane motion of a plate. Guided by the results obtained above for

transverse motion, we assume that the cutoff frequency corresponds to a zig-zag mode for adjacent mesh points (Fig. 2). Then, from the governing difference equations for in-plane motion, or through the application of Rayleigh's principle, we can readily show that

$$\omega_c = 2\left[\left(\frac{c}{\Delta x}\right)^2 + \left(\frac{c_s}{\Delta y}\right)^2\right]^{1/2}, \quad (\Delta x < \Delta y) \tag{12}$$

where $c_s = [E/2(1+\nu)\rho]^{1/2}$ is the shear velocity. Introducing this into Eq. 11, we obtain the first of Eqs. 1.10; this result agrees with the result of Ref. 24, which also employs the von Neumann stability criterion. Now it has been stated (Ref. 25) that Eq. 11 is inconvenient in application because of the difficulty of determining ω_{max}; we have just seen that the assumption of zig-zag motion constitutes a very simple means for overcoming this difficulty.

3.1.4 Convergence of the Finite Difference Method

Eq. 5 is the frequency equation for the finite difference plate. We now consider the limiting case when the mesh widths Δx and Δy both approach zero. Thus we have, for fixed structural wave numbers k_x and k_y,

$$\begin{aligned} k_x \Delta x &\to 0 \\ k_y \Delta y &\to 0 \end{aligned} \tag{13}$$

so that the Taylor's series expansion for $\sin \xi$ then yields

$$\lim_{\Delta x, \Delta y \to 0} \{\omega(k_x, \Delta x, k_y, \Delta y)\} = c\gamma(k_x^2 + k_y^2) \tag{14}$$

This is in agreement with the frequency equation for the uniform plate, which may be obtained from Ref. 26. Thus, a finite difference solution does, in fact, converge to the corresponding continuous solution as $\Delta x, \Delta y \to 0$, in the absence of response discontinuities.

3.2 FREQUENCY PARAMETERS

In this section, we give expressions for the characteristic frequency parameters that pertain to the shell theory employed, the given excitation, and the finite difference mesh. These parameters are then used to interpret some of the numerical results presented in Section 2. A finite difference computational procedure based on the use of these parameters is then presented.

3.2.1 Limit Frequencies of Shell Theory

Thin shell theory is limited to the frequency range (Ref. 7)

$$\omega \leq \omega_f \approx 0.1\ \omega_s \tag{15}$$

for flexural motion, and

$$\omega \leq \omega_e \approx \omega_s \tag{16}$$

for extensional motion. In these equations, ω_s is the frequency of the lowest antisymmetric thickness-shear mode of a plate, given by

$$\omega_s = \pi \frac{c_s}{h} = \frac{\pi}{h}\left[\frac{E/\rho}{2(1+\nu)}\right]^{1/2} \tag{17}$$

For comparison, we also write the limit frequency appropriate to improved theory (Ref. 7)

$$\omega \leq \omega_i \approx \omega_s \tag{18}$$

We observe that $\omega_e \approx \omega_i \approx 10\ \omega_f$.

3.2.2 Cutoff Frequency of Excitation

A convenient way to describe a transient excitation is to characterize it in terms of its frequency content, through the use of the Fourier transform (Ref. 2). For example, let us consider a function

with the following triangular temporal variation (Fig. 3)

$$f(t) = \begin{cases} \frac{2t}{t_w} & , \quad 0 \le t \le \frac{1}{2} t_w \\ 2\left(1 - \frac{t}{t_w}\right) & , \quad \frac{1}{2} t_w \le t \le t_w \\ 0 & , \quad \text{otherwise} \end{cases} \tag{19}$$

The Fourier transform of $f(t)$ is then (Eq. 1.2)

$$\bar{f}(\omega) = \frac{t_w}{2} \cdot \frac{\sin^2\left(\frac{\omega t_w}{4}\right)}{\left(\frac{\omega t_w}{4}\right)^2} e^{-\frac{1}{2} j\omega t_w} \tag{20}$$

Figure 3 shows the spectrum $\frac{2}{t_w}\left|\bar{f}(\omega)\right|$ from Eq. 20. This spectrum is clearly a compact function with a reasonably well defined excitation cutoff frequency given by

$$\omega_x \approx \frac{4\pi}{t_w} \tag{21}$$

Not all excitations are blessed with a well defined excitation cutoff frequency. It is often desirable to filter such excitations in order to enforce cutoff. This will be discussed shortly in Sub-section 3.2.5.

3.2.3 Limit Frequency of Mesh

We have observed in the previous section that harmonic waves with frequencies greater than the cutoff frequency will not propagate in the finite difference analog of a continuous system. Furthermore, there is no guarantee that the discrete system will accurately represent all waves propagating in the continuous system with $\omega < \omega_c$. The degree of inaccuracy is, in fact, indicated by the divergence between the frequency equations

for the two systems. Let us now define a limit frequency of the mesh (ω_m) below which the frequency curve for the discrete system diverges by less than a prescribed amount from the frequency curve for the continuous system. That is, let ω_m be the highest value of ω for which the following relationship holds:

$$\left| \frac{\omega(k_x, \Delta x, k_y, \Delta y)}{\omega(k_x, k_y)} - 1 \right| < \epsilon \tag{22}$$

where the numerator of the fraction is given by Eq. 5, the demoninator is the frequency equation for the continuous plate, and $\epsilon \ll 1$. Now we might use any one of three frequency equations for the continuous plate: that appropriate to elementary (Bernoulli-Euler) theory, that appropriate to improved (Timoshenko) theory and, finally, that appropriate to elasticity theory. If we take the shear constant of improved theory equal to $\pi^2/12$, the latter two frequency equations are nearly identical. Thus we consider only the elementary flexural equation (Eq. 14) and an equation that constitutes a very accurate approximation to the one for improved theory (Ref. 27)

$$\frac{h}{c}\,\omega_f(k_x,k_y) = \frac{\pi^2 g}{\sqrt{12}}\,\Gamma$$

$$\frac{h}{c}\,\omega_i(k_x,k_y) = \left[\frac{1+\Gamma}{(1+\Gamma)^2 + \pi^2 g\Gamma/12}\right]^{1/2} \frac{\pi^2 g}{\sqrt{12}}\,\Gamma \tag{23}$$

where $g = \frac{1}{2}(1-\nu)$ and $\Gamma = (h^2/\pi^2 g)(k_x^2 + k_y^2)$.

We first consider flexural waves propagating along the x-axis, so that $k_y = 0$. From Eqs. 5 and 23, then, we have

$$\frac{h}{c}\,\omega(k,\Delta x,0,\Delta y) = \left[\frac{\sin \frac{1}{2} k\Delta x}{\frac{1}{2} k\Delta x}\right]^2 \frac{h}{c}\,\omega_f(k,0) \tag{24}$$

for $\omega(k,\Delta x,0,\Delta y) \leq \omega_c$. Eqs. 23 and 24 are plotted in Fig. 4 for $\nu = 0.3$ and $\Delta x/h = \frac{1}{2}$, 1 and 2. We observe that the $\Delta x/h = 1$ curve deviates less than about 15% from the improved theory curve for $kh \leq \pi$, whereas the elementary flexural theory curve differs from the improved theory curve by more than 100% in this range. If we accept $\varepsilon = 0.15$, then, we can state that for transverse motions the finite difference equations appropriate to thin shell theory possess a significantly higher limit frequency (for $\Delta x/h = 1$) than the corresponding differential equations. This implies that a thin shell finite difference solution (with $\Delta x/h = 1$) may in some cases be more accurate than even an exact solution of the corresponding differential equations. These results, of course, apply equally to waves propagating along the y-axis.

Let us now consider flexural waves propagating in a direction not parallel to either the x- or y-axes. Since, from Eqs. 5 and 23, the discussion of the previous paragraph applies when either $k_x^2 \gg k_y^2$ or $k_y^2 \gg k_x^2$, we turn our attention to the case $k_x^2 = k_y^2 = \frac{1}{2}k^2$. Eqs. 5 and 23 then yield

$$\frac{h}{c}\,\omega\left(\frac{\sqrt{2}}{2}k,\Delta x,\frac{\sqrt{2}}{2}k,\Delta y\right) = \frac{1}{2}\left\{\left[\frac{\sin\frac{\sqrt{2}}{4}k\Delta x}{\frac{\sqrt{2}}{4}k\Delta x}\right]^2 + \left[\frac{\sin\frac{\sqrt{2}}{4}k\Delta y}{\frac{\sqrt{2}}{4}k\Delta y}\right]^2\right\}\frac{h}{c}\,\omega_f\left(\frac{\sqrt{2}}{2}k,\frac{\sqrt{2}}{2}k\right) \qquad (25)$$

This equation and Eqs. 23 are plotted in Fig. 5 for $\nu = 0.3$ and various values of $\Delta x/h$ and $\Delta y/h$. Note that, because of symmetry in the equations, results for $\Delta x = \Delta_1$, $\Delta y = \Delta_2$ are identical to those for $\Delta x = \Delta_2$, $\Delta y = \Delta_1$. We see from the figure that the curve for $\Delta x = \sqrt{2}\,h$, $\Delta y = \sqrt{2}\,h$ lies considerably closer than the curve for $\Delta x = h$, $\Delta y = h$ to the improved theory curve for frequencies below c/h. The curve for $\Delta x = h$, $\Delta y = 2h$ (or vice-versa) lies closer still, but is less desirable for the following reason. Figure 5 pertains to a wave propagating at an angle of 45 degrees with respect to either axis. In order to obtain comparable resolution along each axis (i.e., to have the same number of nodal points per trace wave length), we would wish to set $\Delta x = \Delta y$.

In general, the requirement for comparable resolution is

$$k_x\Delta x = k_y\Delta y \qquad (26)$$

Thus, if we anticipate that the solution to a problem of interest will be characterized by shorter structural wave lengths in one direction than in another, Eq. 26 immediately yields the desired aspect ratio $\Delta y/\Delta x$ for the finite difference mesh. To determine the mesh width magnitude, we note that the finite difference frequency curves of Figures 4 and 5 constitute a nearly optimum fit below $\omega = c/h$ to the improved theory frequency curve if

$$\left(\frac{h}{\Delta x}\right)^2 + \left(\frac{h}{\Delta y}\right)^2 = 1 \tag{27}$$

Combining Eqs. 26 and 27, we find that, for a specified value of k_y/k_x, the optimum mesh widths are given by

$$\begin{aligned} \left(\frac{\Delta x}{h}\right)_{\text{optimum}} &= \left[1 + (k_y/k_x)^2\right]^{1/2} \\ \left(\frac{\Delta y}{h}\right)_{\text{optimum}} &= \left[1 + (k_x/k_y)^2\right]^{1/2} \end{aligned} \tag{28}$$

Often it is all but impossible to anticipate a value for k_y/k_x. It is then advisable to use a square mesh. In this case, Figs. 4 and 5 suggest the use of the compromise mesh widths

$$\left(\frac{\Delta x}{h}\right)_{\text{compromise}} = \left(\frac{\Delta y}{h}\right)_{\text{compromise}} \approx 1.2 \tag{29}$$

Eqs. 28 and 29, in conjunction with Figs. 4 and 5, yield a limit frequency for an optimum or compromise finite difference mesh of $\omega_m \approx \omega_s/2$. However, because the rather large negative curvature of the corresponding frequency curves in this region leads to undesirable inaccuracies in the group velocity $c_g = d\omega/dk$, we reduce the limit frequency to

$$\omega_m \approx \frac{1}{3}\,\omega_s \tag{30}$$

This is considerably above the limit frequency for continuum thin shell theory given by Eq. 15, but is still well below the improved theory limit frequency given by Eq. 18.

Finally, it is interesting to examine the resolution characteristics of finite difference response computations appropriate to the limit frequency of Eq. 30. If, for example, we set $\Delta\alpha/h = 1$ and then take $\Delta t = \Delta t_{cr}$ (see the first of Eqs.1.10) for a one-dimensional transient response problem, we find from Eqs.1.10, 17 and 30 that $\Delta t/T_m \approx c_s/6c \approx 1/10$, where $T_m = 2\pi/\omega_m$. Thus we have ten computation points per period corresponding to the limit frequency, which is satisfactory. In contract, we find from Fig. 4 that the limit wave number k_m (the value of k determined by the $\Delta\alpha/h = 1$ frequency curve for $\omega = \omega_m$) is such that $\Delta\alpha/\lambda_m \approx 1/4$, where $\lambda_m = 2\pi/k_m$. Thus we have only four computation points per spatial wave length corresponding to the limit frequency. We conclude, therefore, that resolution is almost always better in finite difference response histories than in the corresponding snapshots, a conclusion which is supported by numerous response computations in the previous chapter. This flexural result contrasts with the corresponding extensional result, which, because $\omega(k) = ck$ for such motion, states that temporal resolution is identical to spatial resolution.

3.2.4 Interpretation of Previous Numerical Results

Let us now make use of the results of this section to interpret some of the numerical results of Chapter 2. We first consider Example 14 (Subsections 2.2.4 and 2.4.2), which involves the temporal smoothing of a uniform radial impulsive loading on a freely-supported cylindrical shell. From Eq. 30, Eq. 17 and Table 2.2, we find that the limit frequency for $\Delta\alpha/h = 1$ computations is

$$\omega_m \frac{h}{c} \approx 0.64$$

From Subsection 3.2.2, the excitation cutoff frequency for the $ct_w/a = 0.82$ triangular pressure loading is

$$\omega_x \frac{h}{c} \approx 0.77$$

Thus, we are not surprised to see the marginal convergence behavior of the acceleration computations of Fig. 2.39. The satisfactory convergence

behavior of the corresponding displacement, velocity and longitudinal strain computations (Figs. 2.39 and 2.60a) is apparently due to the fact that response components with frequencies above $\omega h/c \approx 0.64$ do not contribute significantly to these responses. Comparison of Figs. 2.39 and 2.60a with Fig. 2.30 demonstrates that filtering the radial impulse loading of Example 12 at $\omega_x h/c \approx 0.77$ improves the convergence of velocity computations from marginal tc satisfactory, the convergence of longitudinal strain computations from unsatisfactory to satisfactory, and the convergence of acceleration computations from unsatisfactory to marginal.

As we would expect, filtering the impulsive loading at a lower frequency improves convergence even more. The excitation cutoff frequency for the $ct_w/a = 1.64$ triangular pressure loading of Example 14 is

$$\omega_x \frac{h}{c} \approx 0.38$$

which is well below the limit frequency $\omega_m h/c = 0.64$. Thus, we would expect to see the uniformly satisfactory convergence exhibited by the $\Delta\alpha/h = \frac{1}{2}$ and 1 response computations of Fig. 2.40. Filtering the excitation at a frequency significantly higher than $\omega_m h/c = 0.64$ yields, of course, less satisfactory convergence behavior. This is demonstrated in Figs. 2.41 and 2.60b, which show results for $ct_w/a = 0.40$, corresponding to

$$\omega_x \frac{h}{c} \approx 1.57$$

Let us now consider Example 15 (Subsections 2.2.4 and 2.4.2), which involves spatial smoothing of a uniform radial impulsive loading on a freely-supported cylindrical shell. The limit frequency is $\omega_m h/c = 0.64$ for this example also; this corresponds, from Fig. 4, to a limit wave number

$$k_m h \approx 1.64$$

Because Fig. 4 pertains to harmonic waves in an infinite plate, the spatial domain over which the truncated Fourier series impulse loading of

Example 15 is defined must be considered infinite in extent. Hence we take the spatial Fourier transform of the loading to find an excitation cutoff wave number $k_x \approx (m_{max} + 2)\pi/\ell$. For $m_{max} = 5$

$$k_x h \approx 0.46$$

which is much smaller than $k_m h$. Thus we would expect to see the uniformly satisfactory convergence exhibited in Figs. 2.43 and 2.61a. For $m_{max} = 11$,

$$k_x h \approx 0.85$$

which is approximately equal to the apparent limit wave number for $\Delta\alpha/h = 2$ computations (Fig. 4). We would therefore expect to see satisfactory convergence behavior for all the $\Delta\alpha/h = 2$ and $\Delta\alpha/h = 1$ computations of Figs. 2.44 and 2.61b. The fact that this is not quite the case means that the true limit wave number for $\Delta\alpha/h = 2$ computations is somewhat less than 0.85. We do find uniformly satisfactory agreement between the $\Delta\alpha/h = 1$ and $\Delta\alpha/h = \frac{1}{2}$ computations, however, which assures us that spatial filtering is effective.

For $m_{max} = 23$,

$$k_x h \approx 1.64$$

which is equal to the limit wave number above. We see, however, that agreement between the $\Delta\alpha/h = 1$ and $\Delta\alpha/h = \frac{1}{2}$ computations of Figs. 2.45 and 2.61c is not uniformly satisfactory. This means that the true limit wave number is somewhat less than 1.64 and suggests that Fig. 4 is more readily applied to temporal filtering than to spatial filtering.

Finally, in view of Eqs. 28 (with $k_y = 0$), it is not surprising that the $\Delta\alpha/h = 1$ acceleration response curve of Fig. 2.19 (as well as the identical velocity response curve of Fig. 2.26) is the most physically meaning- (see the discussion of Subsection 2.2.1). In fact, these figures imply that the $\Delta\alpha/h = 1$ frequency curve lies sufficiently close to the improved theory curve over a sufficiently wide kh-range to predict accurately the gross features of the propagation of response discontinuities.

3.2.5 Finite Difference Computational Procedure

Based on the results of this and the previous chapter, it is possible to construct a recommended procedure for the application of the (thin shell theory) finite difference method in studies of transient, linear wave propagation in shells. This procedure, specialized to the discretization method used herein, is as follows:

Step 1: From Table 2.1, determine whether, for the type of excitation and the responses of interest, convergence can be expected to be satisfactory. If no convergence problems are anticipated, skip to Step 5; if convergence difficulties are expected, proceed to the next step.

Step 2: From information pertaining to the characteristics of the excitation (Sub-section 3.2.2), determine an excitation cutoff frequency ω_x.

Step 3: Using Eqs. 30 and 17, compute ω_m. If $\omega_m \gtrsim \omega_x$, skip to Step 5; if ω_m is appreciably smaller than ω_x, proceed to the next step.

Step 4: Temporally filter the excitation at ω_m; perhaps the best filter to use is the digital filter of Ref. 28, which completely suppresses excitation components with frequencies above the filter cutoff frequency while introducing no amplitude or phase distortion into the excitation components with frequencies below the filter cutoff frequency.

Step 5: If the characteristic structural wave lengths along one axis are expected to be shorter than those along the other axis, determine the mesh widths from Eqs. 28. If there appears to be no preferred direction, determine the mesh widths from Eq. 29.*

Step 6: For temporal step-by-step integration with an explicit numerical scheme, select a time step value slightly less than the critical time step given by the first of Eqs. 1.10. An implicit numerical scheme permits the use of a larger time step.

Step 7: Check the accuracy of the finite difference solution either through an error evaluation procedure incorporated into the numerical scheme or by means of additional runs with smaller mesh dimensions.

Now the above recommended procedure is based upon the short wave length limitations associated with flexural shell response. If the excitation is

---

*For very low frequency excitations, it is possible to use mesh widths larger than those given by Eqs. 28 and 29. The number of nodal points per structural wave length and/or the number of time points per temporal wave length (period) then becomes the deciding factor. (For frequency-wave number relationships, see Figs. 4 and 5).

primarily in-plane, flexural effects play a small role, and the flexural response limitations no longer apply. In this case, Eq. 16 gives a limit frequency of $\omega_e \approx 2c/h$, so that mesh widths smaller than the shell thickness may be profitably used. If the excitation and responses of interest are such that convergence difficulties are anticipated (see Table 2.1), it is advisable to filter the excitation at ω_e in the manner of Step 4 in order not to exceed the limitations of thin shell theory. Convergence of the finite difference computations may then be expected for mesh widths smaller than about $\frac{1}{10}\lambda_e = \frac{1}{10}(2\pi c/\omega_e) \approx h/3$.

3.3 ADDITIONAL CONSIDERATIONS REGARDING THIN SHELL AND IMPROVED THEORIES

This section briefly discusses the solution of flexural response problems by the method of modal superposition and the method of characteristics. The results indicate that, while the modal convergence properties appropriate to improved theory are generally better than those of elementary theory, the ability of improved theory to treat flexural response discontinuities may constitute no real advantage.

3.3.1 Convergence Properties of the Method of Modal Superposition

The previous sections of this chapter have demonstrated that the major limitation on the flexural response computation capabilities of a thin shell finite difference code is the rather long structural wave length limitation of thin shell theory. Here we briefly examine the effect of this structural wave length limitation on the method of modal superposition.

We have observed in Subsection 3.2.3 that limit frequency considerations for finite difference computations of shell response reduce essentially to those for a simple beam. In addition, because convergence behavior is a short structural wave length phenomenon, boundary condition details are unimportant. Hence it is sufficient to focus our attention on the transient response of a simply-supported beam.

Consider a simply-supported Bernoulli-Euler beam that is excited by a uniform impulsive load over a finite part of its length. The pertinent kinetic energy, potential energy and virtual work expressions are (Fig. 6):

$$T = \frac{1}{2}\rho h \int_0^{\ell} \dot{w}^2 dx$$

$$V = \frac{Eh^3}{24(1-\nu^2)} \int_0^{\ell} \left(\frac{\partial^2 w}{\partial x^2}\right)^2 dx \tag{31}$$

$$\delta W = \int_{x_o - \Delta\ell}^{x_o + \Delta\ell} I\delta(t)\cdot\delta w dx$$

where I is the magnitude of the applied impulse. From the known solution of the associated free vibration problem, we write

$$w(x,t) = \sum_{m=1}^{\infty} w_m(t) \sin \frac{m\pi x}{\ell} \tag{32}$$

Introducing Eq. 32 into Eq. 31 and applying Lagrange's equation, we obtain the modal equation of motion; solution of this equation then leads to the series solution for beam displacement

$$w(x,t) = \sum_{m=1}^{\infty} \frac{I_m}{M_m \omega_m} \sin \frac{m\pi x}{\ell} \sin \omega_m t \tag{33}$$

where the generalized mass M_m, natural frequency ω_m, and generalized impulse I_m are given by

$$M_m = \frac{1}{2}\rho h \ell$$

$$\omega_m^2 = \frac{Eh^2}{12\rho(1-\nu^2)} \left(\frac{m\pi}{\ell}\right)^4 \tag{34}$$

$$I_m = \frac{2I\ell}{m\pi} \sin \frac{m\pi x_o}{\ell} \sin \frac{m\pi \Delta x}{\ell}$$

Because flexural stress/strain is proportional to $\partial^2 w/\partial x^2$, we are interested in this quantity as well as the kinematic quantities displacement, velocity and acceleration. Thus, since I_m, ω_m and M_m vary as m^{-1}, m^2 and m^0 (Eq. 34), respectively, i.e., since $I_m \sim m^{-1}$, $\omega_m \sim m^2$ and $M_m \sim m^0$, we find that

$$\begin{aligned} w &\sim m^{-3} & \ddot{w} &\sim m^{1} \\ \dot{w} &\sim m^{-1} & \frac{\partial^2 w}{\partial x^2} &\sim m^{-1} \end{aligned} \tag{35}$$

We observe that the series for displacement response converges quite satisfactorily; in addition, it can be shown by a theorem of Dedekind (Ref. 29) that (for $t > 0$) the series for velocity and stress/strain converge, although they do so slowly. The series for acceleration response clearly diverges.

Let us now consider a simply-supported Timoshenko beam under an identical loading. The pertinent kinetic energy and potential expressions for this beam are (Fig. 6)

$$\begin{aligned} T &= \frac{1}{2}\,\rho h \int_0^{\ell} \left(\dot{w}^2 + \frac{h}{12}\,\dot{\varphi}^2\right) dx \\ V &= \frac{Eh^3}{24(1-\nu^2)} \int_0^{\ell} \left(\frac{\partial \varphi}{\partial x}\right)^2 dx + \frac{Eh\kappa}{4(1+\nu)} \int_0^{\ell} \left(\frac{\partial w}{\partial x} + \varphi\right)^2 dx \end{aligned} \tag{36}$$

From the known solution of the associated free vibration problem, we write

$$\begin{aligned} w(x,t) &= \sum_{m=1}^{\infty} w_m(t) \sin \frac{m\pi x}{\ell} \\ \varphi(x,t) &= \sum_{m=1}^{\infty} \varphi_m(t) \cos \frac{m\pi x}{\ell} \end{aligned} \tag{37}$$

Introducing Eqs. 37 into Eqs. 36 and the last of Eqs. 31, and performing the integrations, we obtain

$$T = \frac{1}{4}\rho h \ell \sum_{m=1}^{\infty} \left(\dot{w}_m^2 + \frac{h^2}{12} \dot{\varphi}_m^2 \right)$$

$$V = \frac{Eh\ell}{4(1-\nu^2)} \sum_{m=1}^{\infty} \left[\frac{h^2}{12} \left(\frac{m\pi}{\ell} \right)^2 \varphi_m^2 + \frac{1}{2} \kappa(1-\nu) \left(\frac{m\pi}{\ell} w_m + \varphi_m \right)^2 \right] \tag{38}$$

$$I = \sum_{m=1}^{\infty} I_m \, \delta(t) \, \delta w_m$$

where I_m is given by the last of Eqs. 34.

Since there are now two modes for each value of m, further investigation of the associated free vibration problem is required. Such an investigation (Ref. 27) yields as an accurate approximation for the first mode

$$\left(\frac{\varphi_m}{w_m} \right)_1 \approx - \left(\frac{m\pi}{\ell} \right) \frac{(1 + \Gamma_m)^2 + \frac{1}{2} \kappa(1-\nu) \Gamma_m}{(1 + \Gamma_m)^3 + \frac{1}{2} \kappa(1-\nu) \Gamma_m (1-\Gamma_m^2)} \tag{39}$$

where $\Gamma_m = \frac{h^2}{6\kappa(1-\nu)} \left(\frac{m\pi}{\ell} \right)^2$. Introducing this into Eqs. 38 and applying Lagrange's equation, we obtain the modal equation of motion whose solution is

$$w_{m1}(t) = \frac{I_m}{M_{m1} \omega_{m1}} \sin \omega_{m1} t \tag{40}$$

in which I_m is given by the last of Eqs. 34 and

$$M_{m1} \approx \frac{1}{2} \rho h \ell \left[1 + \frac{h^2}{12} \left(\frac{\varphi_m}{w_m} \right)_1^2 \right]$$

$$\omega_{m1}^2 \approx \frac{1 + \Gamma_m}{(1 + \Gamma_m)^2 + \frac{1}{2} \kappa(1-\nu) \Gamma_m} \omega_m^2 \tag{41}$$

where $\left(\frac{\varphi_m}{w_m}\right)_1$ is given by Eq. 39 and ω_m^2 is given by the second of Eqs. 34.

The second mode, being orthogonal to $\left(\frac{\varphi_m}{w_m}\right)_1$, is given by

$$\left(\frac{\varphi_m}{w_m}\right)_2 \approx \left(\frac{m\pi}{\ell}\right) \frac{(1+\Gamma_m)^3 + \frac{1}{2}\kappa(1-\nu)\Gamma_m(1-\Gamma_m^2)}{\frac{1}{2}\kappa(1-\nu)\Gamma_m\left[(1+\Gamma_m)^2 + \frac{1}{2}\kappa(1-\nu)\Gamma_m\right]} \tag{42}$$

Introducing this into Eqs. 38 and applying Lagrange's equation, we obtain the modal equation of motion whose solution is

$$w_{m2}(t) = \frac{I_m}{M_{m2}\omega_{m2}} \sin \omega_{m2} t \tag{43}$$

in which I_m is given by the last of Eqs. 34 and

$$M_{m2} \approx \frac{1}{2}\rho h \ell \left[1 + \frac{h^2}{12}\left(\frac{\varphi_m}{w_m}\right)_2^2\right]$$

$$\omega_{m2}^2 \approx \left[1 + \Gamma_m + \frac{1}{2}\kappa(1-\nu)\Gamma_m \frac{1 + \frac{1}{2}\kappa(1-\nu)\Gamma_m/(1+\Gamma_m)}{1 + \Gamma_m + \frac{1}{2}\kappa(1-\nu)\Gamma_m/(1+\Gamma_m)}\right] \frac{\omega_m^2}{\frac{1}{2}\kappa(1-\nu)\Gamma_m^2} \tag{44}$$

where $\left(\frac{\varphi_m}{w_m}\right)_2$ is given by Eq. 42 and ω_m^2 is given by the second of Eqs. 34.

The above results now enable us to write down our response solutions. Since

$$w_m(t) = w_{m1}(t) + w_{m2}(t)$$

$$\varphi_m(t) = \left(\frac{\varphi_m}{w_m}\right)_1 w_{m1}(t) + \left(\frac{\varphi_m}{w_m}\right)_2 w_{m2}(t) \tag{45}$$

we have, from Eqs. 37, 45, 40 and 43

$$w(x,t) = \sum_{m=1}^{\infty} I_m \left[\frac{1}{M_{m1}\omega_{m1}} \sin \omega_{m1} t + \frac{1}{M_{m2}\omega_{m2}} \sin \omega_{m2} t \right] \sin \frac{m\pi x}{\ell}$$

$$\varphi(x,t) = \sum_{m=1}^{\infty} I_m \left[\frac{(\varphi_m/w_m)_1}{M_{m1}\omega_{m1}} \sin \omega_{m1} t + \frac{(\varphi_m/w_m)_2}{M_{m2}\omega_{m2}} \sin \omega_{m2} t \right] \cos \frac{m\pi x}{\ell} \qquad (46)$$

Because flexural stress/strain is proportional to $\partial\varphi/\partial x$, we are interested in this quantity, displacement, velocity and acceleration. Thus, since (for large m) $I_m \sim m^{-1}$, $(\varphi_m/w_m)_1 \sim m^{-1}$, $\omega_{m1} \sim m$, $M_{m1} \sim m^0$, $(\varphi_m/w_m)_2 \sim m$, $\omega_{m2} \sim m$ and $M_{m2} \sim m^2$, we find that for large values of m

$$w \sim m^{-2} \qquad \ddot{w} \sim m^0$$

$$\dot{w} \sim m^{-1} \qquad \frac{\partial\varphi}{\partial x} \sim m^{-2} \qquad (47)$$

Thus, not only is the limit frequency higher for improved theory than for elementary theory, but, from Eqs. 35 and 47, the modal convergence properties of the former are generally superior to those of the latter.

3.3.2 Limitations of Improved Theory

Shell theories in general, and thin shell theory and improved theory in particular, constitute long wave length approximations to elasticity theory. Hence response solutions appropriate to such theories can be considered accurate only by appeal to Saint-Venant's principle, viz., that the inclusion of the effects of neglected, self-equilibrating boundary loads would lead to significant corrections in the stress field only in certain highly localized regions. Novozhilov and Slepian have demonstrated in an excellent paper (Ref. 30) that, for suddenly applied loads, these regions are located at the wave fronts and at the points of load application.

As an example, consider the infinite plate of Figure 7 that is excited uniformly along a straight line by a step shear load of triangular profile through the plate thickness. Treating this excitation as the superposition of a shear load which is uniform through the thickness and

a self-equilibrating shear load that varies linearly through the thickness, we separate the total problem into two component problems. The first has been solved by Boley and Chao (Ref. 18), who used improved plate theory; the second has been solved by Novozhilov and Slepian, who used a plate theory one step "higher" than improved theory (Ref. 30).

Boley and Chao present a snapshot of uniform shear stress only at $t = 5h/2\sqrt{3}\ c = 1.45\ h/c$; the closest comparable result by Novozhilov and Slepian for linearly-varying shear stress is at $t = 3h/c = 1.5\ h/c$. Since the Novozhilov and Slepian results demonstrate only minor dispersion over a time span of 0.05 h/c, their result has been "moved back" and plotted in Figure 8a along with the Boley and Chao result. Because the magnitude of neither spike at the shear wave front decreases as the wave propagates down the beam, this figure demonstrates that the spikes which improved shell theory ignores can be comparable in magnitude to the spike that it predicts. We find, therefore, that consistent application of a shell theory to transient elastic wave propagation problems requires that one keep in mind the limitations appropriate to Saint-Vernant's principle at both the points of load application and at the wave fronts. This means that comparisons between elementary and improved theory solutions can only be made outside of these regions.

Uncertainties at the wave fronts may, in fact, be only a minor problem, in view of Fig. 8b. This figure shows the solution of Ref. 30 for the moment response of a semi-infinite plate to a step moment applied uniformly along its edge. We observe that the "further improved" theory demonstrates a rapid "melting away" of the energy at the wave front which is not indicated by the improved theory. Thus, there is a question whether, at reasonable distances from the region of load application, short wave length pulses predicted by improved (Timoshenko) shell theory are actually present. This is illustrated in Fig. 9, which shows longitudinal moment response

$$M_\alpha(\alpha,t) = \int_{-h/2}^{h/2} \sigma_\alpha(z,\theta,t)\ z\,dz \tag{48}$$

for a semi-infinite cylindrical shell excited by the imposition of an axisymmetric, radial, ramp-step velocity at its end (Ref. 16). The figure

shows moment snapshots at $ct/a = 2$ for various ramp rise times. We observe that, even for a rise time as short as h/c, the ramp-step excitation produces no response comparable to the spike caused by the step excitation ($t_{rise} = 0$).

$$b_x = (\Delta x)^{-2}$$

$$b_y = (\Delta y)^{-2}$$

$$b_{xy} = (\Delta x)^{-2} + (\Delta y)^{-2}$$

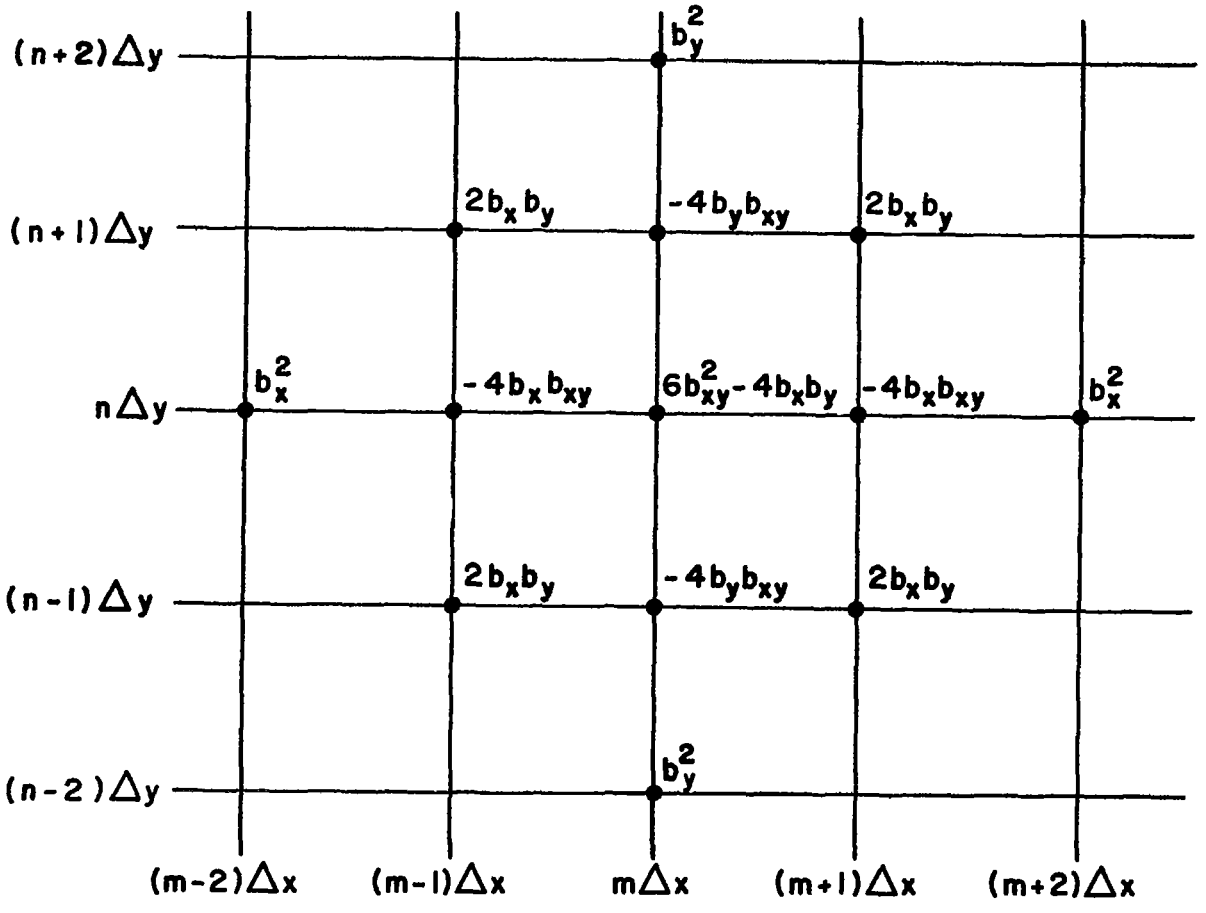

Figure 1. Finite Difference Operator for $\nabla^4 w$ at the point $x = m\Delta x$, $y = n\Delta y$

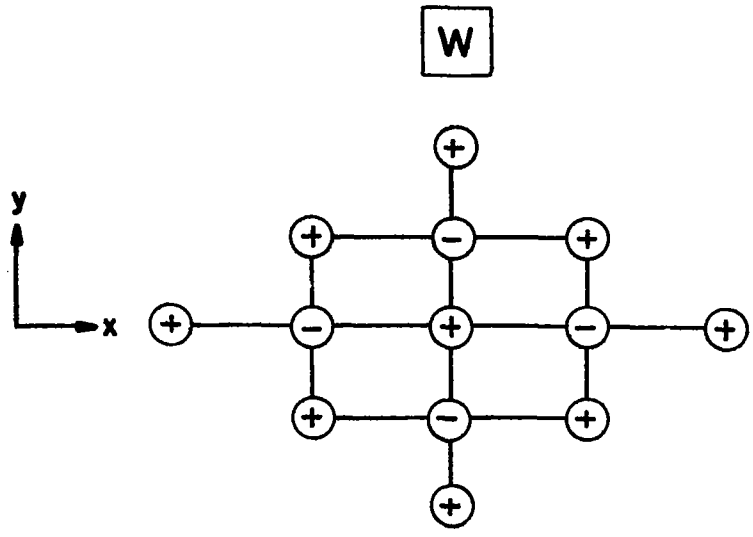

(a) Flexural Motion

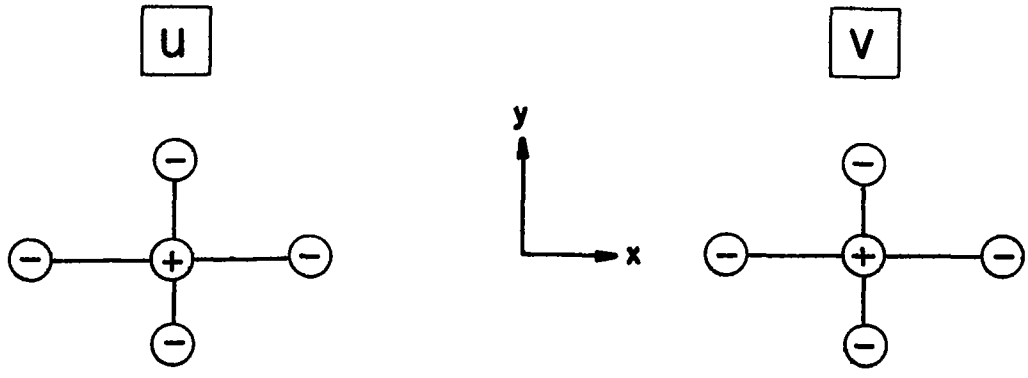

(b) Extensional Motion

Figure 2. Zig-Zag Modes for Cutoff Frequencies

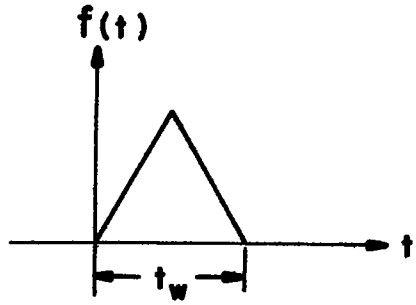

(a) Function

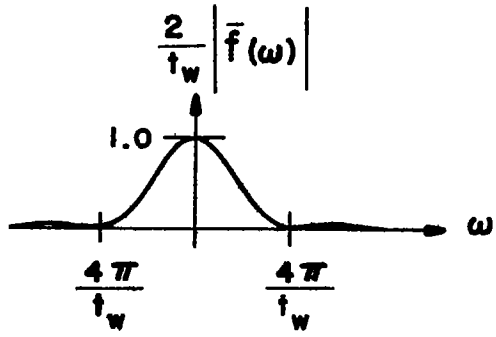

(b) Spectrum

Figure 3. Spectrum of a Triangular Function

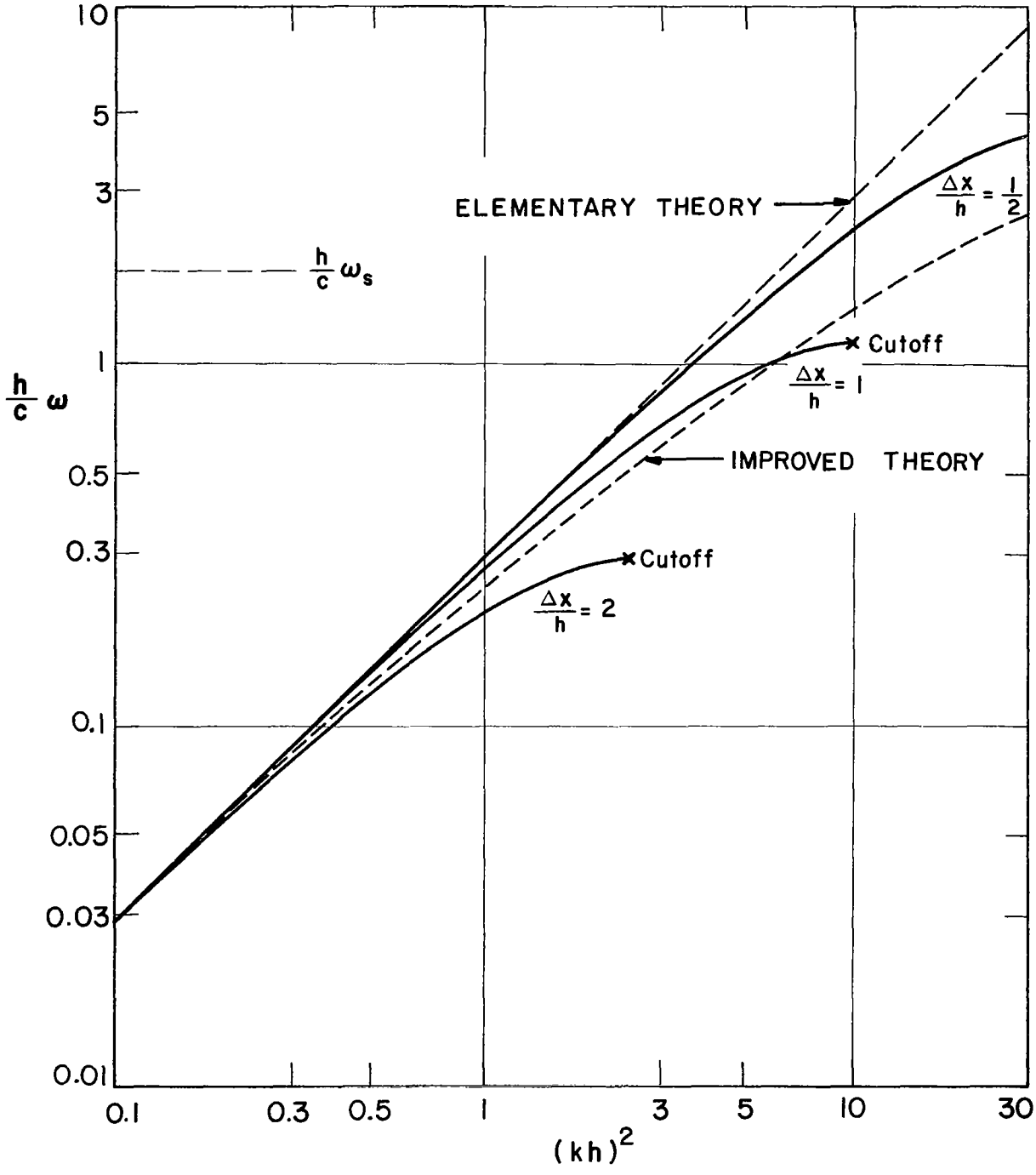

Figure 4. Frequency Curves for Continuous and Finite Difference Plates ($k_x = k$, $k_y = 0$)

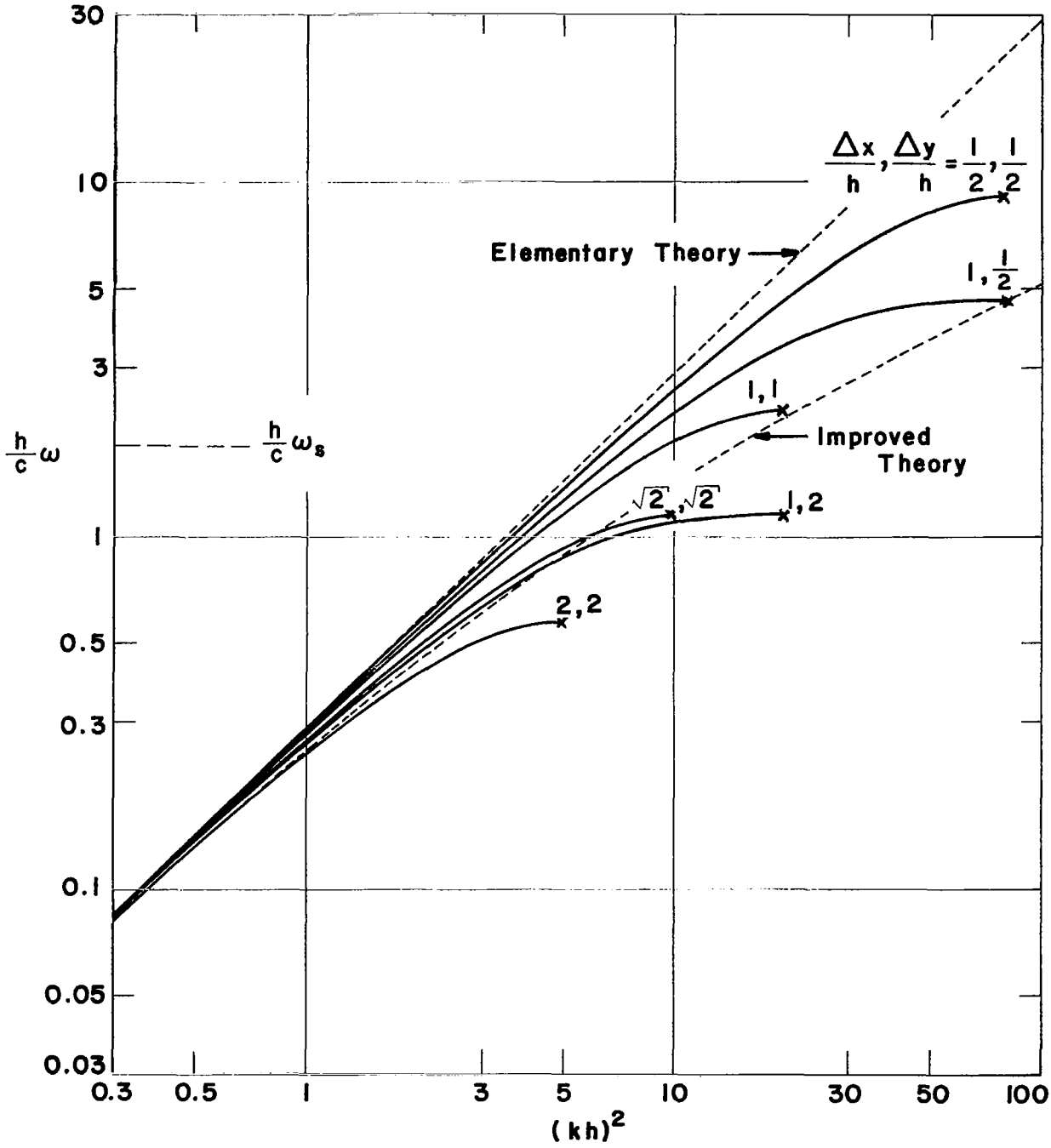

Figure 5. Frequency Curves for Continuous and Finite Difference Plates $\left(k_x = k_y = \frac{\sqrt{2}}{2} k\right)$

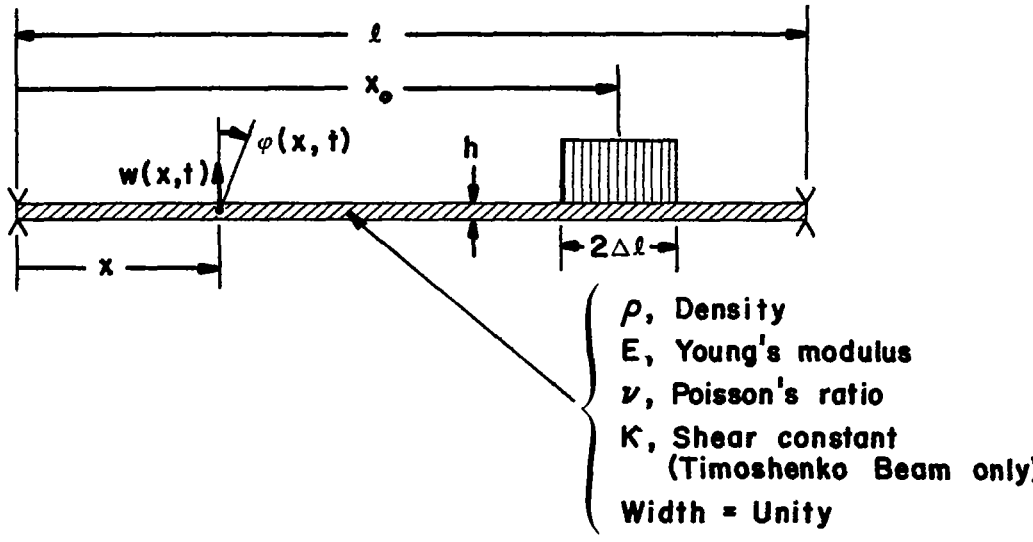

Figure 6. Bernoulli-Euler or Timoshenko Beam

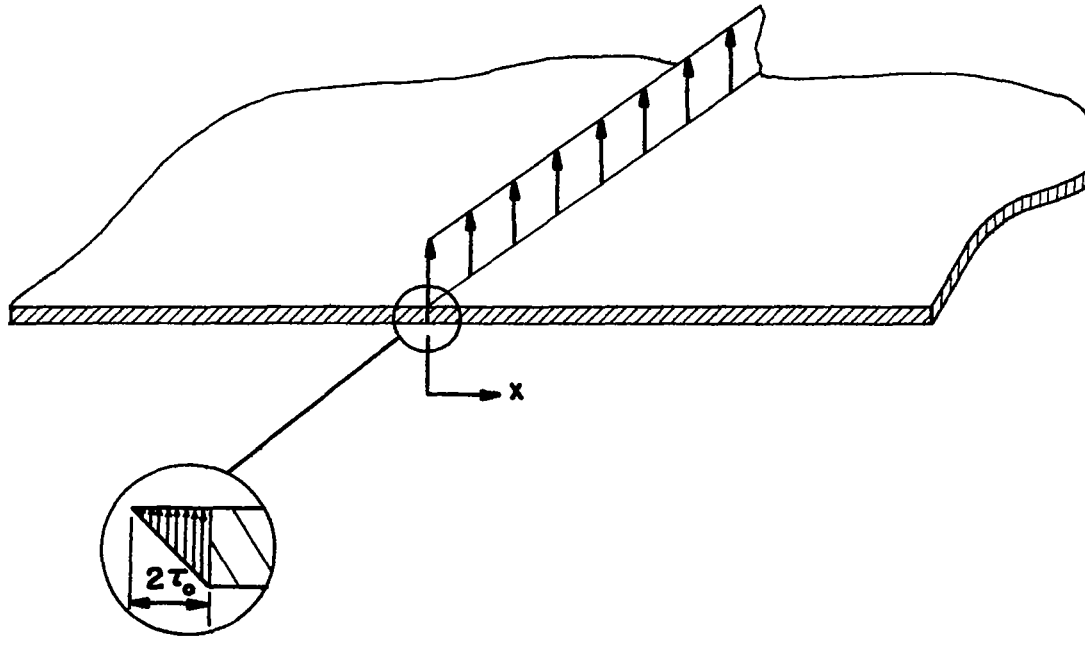

Figure 7. Infinite Plate

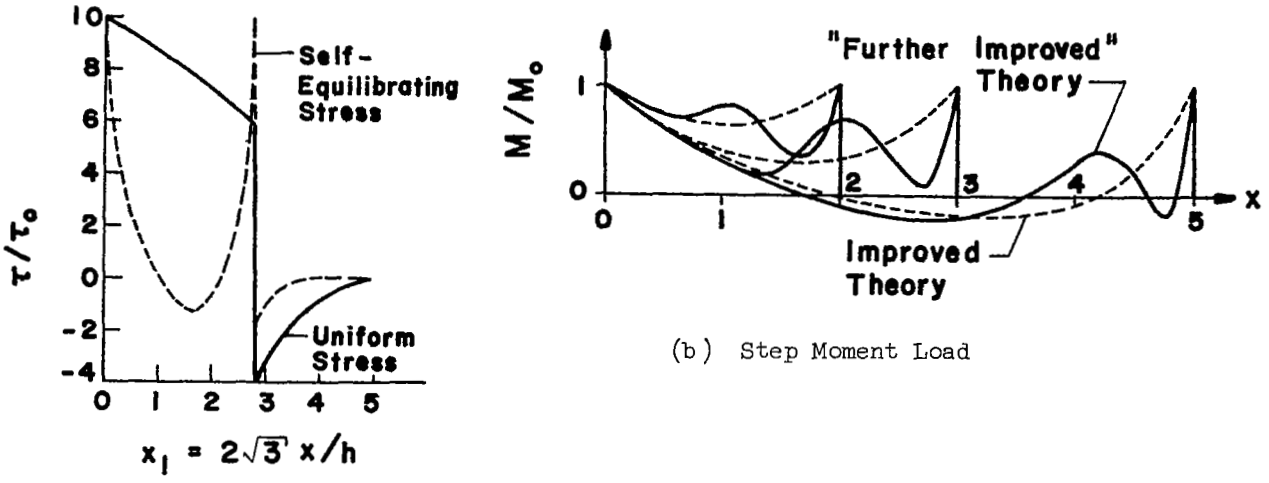

(a) Step Shear Load

(b) Step Moment Load

Figure 8. Response of Infinite Plates to Discontinuous Loads

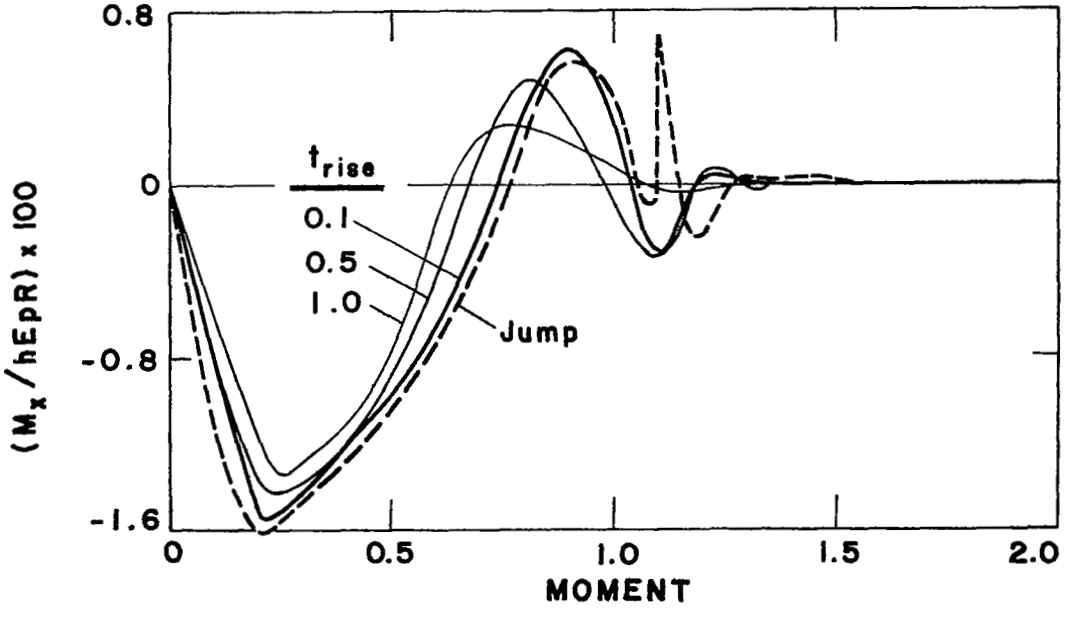

Figure 9. Moment Response of a Cylindrical Shell to an Axisymmetric, Radial, Ramp-Step Velocity Excitation

Chapter 4

EXCITATION OF A SHELL WITH CUTOUTS

This chapter presents numerical results for the response of a circular cylindrical shell with four identical cutouts to unit impulse loads applied at one end. These loads, the first a longitudinal load and the second a radial load, are given by (see Fig. A.2 for notation).

$$\left.\begin{matrix} \frac{1-\nu^2}{Ea} N_\alpha(0,\beta,t) \\ \frac{1-\nu^2}{Ea} Q_\alpha(0,\beta,t) \end{matrix}\right\} = \begin{cases} 5 \sin^2 \frac{\pi ct}{0.4a} & , \quad 0 \le t \le 0.4 \frac{a}{c} \\ 0, & , \quad \text{otherwise} \end{cases} \tag{1}$$

They have been chosen in order to compare computed results for the radial excitation with planned experimental results (Ref. 31).

A diagram of one-eighth of the shell's surface is shown in Fig. 1. Included in the figure is information pertaining to the boundary conditions selected, the points at which response histories are computed, and the α- and β- lines for which response snapshots are obtained. Although the mesh dimensions $\Delta\alpha/h = 1, a\Delta\beta/h = \pi/3$ are not in strict accordance with Eqs. 3.28 or 3.29, they constitute nearly optimum choices that conveniently fit the shell geometry. The time step, selected in accordance with Eqs. 1.10, is $c\Delta t/a = 0.04$. The maximum computation time corresponds to the length of time required for a disturbance travelling at the plate velocity to traverse a distance equal to twice the length of the shell ($ct_{max}/a = 4.8$).

Because the experiments of Ref. 31 rely chiefly on the use of holography to measure shell response, emphasis is placed here on displacement computations. Velocity, longitudinal strain and effective stress responses will also be considered, however. Axisymmetric results for the corresponding virgin shell with $\Delta\alpha/h = 1$ and $\Delta\alpha/h = \frac{1}{2}$ demonstrate satisfactory convergence for the responses to be discussed, except when indicated otherwise.

4.1 LONGITUDINAL EXCITATION

Since the axisymmetric response of the virgin shell is characterized by $(k_\varepsilon a)^2 \approx (2\pi/0.8)^2 \approx 60$, that response constitutes essentially non-dispersive wave propagation in an infinite plate (Appendix B). Hence we expect to observe the "staircase" longitudinal displacement histories for the virgin shell shown in Fig. 2. The corresponding results for the cut shell along the line $\beta = 0$ initially display simple reflection at the left edge of the cutout for $\alpha = 0.4$ and 0.6, as well as significant shielding effects for $\alpha = 1.0$ and 1.2. Well behind the wave front, however, the effects of the cutouts on shell response are not very great, except for an enhancement of radial response in the vicinity of the cutouts. These effects are even less significant at points along the line $\beta = \pi/12$, as shown in Fig. 3. Perhaps the clearest indication of the shielding effects of the cutouts is given in Fig. 4, which shows displacement histories at points along the line $\alpha/a = 1.2$. While shielding effects are clearly discernable in the figure, they cannot be considered dramatic.

Longitudinal strain histories, however, can exhibit rather dramatic effects caused by the cutouts, as demonstrated in Figs. 5 and 6. Whereas the strain responses of the virgin shell contain negligible flexural contributions, significant flexural strain response does occur in the cut shell near the cutouts. Shielding effects of the cutouts are shown in Fig. 7, which presents strain histories at points along the line $\alpha/a = 1.2$. Although the cutouts have a substantial effect on individual strain histories, their impact on values of peak strain is rather minor.

Figures 8-13 show displacement snapshots for the longitudinal lines $\beta = 0$, $\pi/12$, and $\pi/4$ at times $ct/a = 0.8$, 1.2, 2.0, 3.2, 4.0, and 4.4. These results seem to add little new information to that obtained from Figs. 2-4. They are included mainly for comparison with possible future experimental results obtained by holographic techniques. They do illustrate, however, that, although snapshots are very useful for the interpretation of simple wave propagation behavior, they tend to lose their effectiveness, at least for the purposes of these investigations, as the behavior becomes increasingly complicated. For complex response, then, response histories seem to emerge as the more effective interpretive tool.

Figures 14 and 15 are presented to indicate the degree of circumferential non-axisymmetry produced near the wave front of the transient wave by the cutouts. From Fig. 14, we observe that, after the wave front has passed the cutouts, and especially after it has been reflected from the boundary at $\alpha/a = 2.4$, longitudinal displacement response near the wave front tends to become nominally axisymmetric. Much of this is due to the steady growth of rigid body displacement. The tendency toward axisymmetry, however, also characterizes the longitudinal velocity and strain responses near the wave front, except in the vicinity of the cutouts (Fig. 15). Radial displacement and velocity response tends to become increasingly β-dependent as time proceeds (Fig. 14).

A question that remains unanswered by the present computations is whether the presence of the cutouts tends to facilitate the large-scale transfer of energy from extensional (primarily longitudinal) into flexural (primary radial) response. This, in fact, seems to be developing in Figs. 5a, 5b, 5c and 6b; on the other hand, it seems to have been suppressed in Fig. 5d. A satisfactory answer can only be provided by a long-time solution, one that is not efficiently obtained by the present method. It is a problem of considerable interest, however, because such an energy transfer can lead to very large radial responses.

4.2 RADIAL EXCITATION

As implied earlier, the choice of the radial load used here was constrained by the characteristics of an electromagnetic repelling wire excitation mechanism to be used in planned experiments (Ref. 31). In one sense this is unfortunate, since the resulting pulse load possess an excitation cutoff frequency that is about 2-1/2 times the limit frequency given by Eq. 3.30. Hence, from Table 2.1, stress/strain responses computed with the present code are inaccurate. This is illustrated in Fig. 16, which shows longitudinal strain histories for the virgin shell computed with $\Delta\alpha/h = \frac{1}{2}$ and 1. We observe that the peak responses computed with $\Delta\alpha/h = 1$ exceed the corresponding responses computed with $\Delta\alpha/h = \frac{1}{2}$ by as much as 50%.

We also observe that the $\Delta\alpha/h = 1$ responses of Fig. 16, especially for $\alpha/a = 0.4$ and 1.0, contain small amplitude oscillations at the mesh cutoff frequency (Eq. 3.9) that are not present in the corresponding $\Delta\alpha/h = \frac{1}{2}$ responses. This is due to the fact that the excitation cutoff frequency lies above the mesh cutoff frequency for $\Delta\alpha/h = 1$, but below that for $\Delta\alpha/h = \frac{1}{2}$. Hence the $\Delta\alpha/h = 1$ mesh "rings" while the $\Delta\alpha/h = \frac{1}{2}$ mesh does not. This does not necessarily mean that the $\Delta\alpha/h = \frac{1}{2}$ responses are superior to the $\Delta\alpha/h = 1$ responses, however, for the reasons given in Section 3.2.

In another sense, the shortness of the pulse load is only of minor consequence, since we are mainly interested in displacement responses, which do exhibit satisfactory convergence behavior (Table 2.1). Thus we proceed to Fig. 17, which shows displacement histories for the virgin shell; we observe that the flexural wave front travels at about the shear velocity $c_s = [\frac{1}{2}(1-\nu)]^{1/2}c$, while the longitudinal wave front travels slightly faster. Corresponding histories along the line $\beta = 0$ on the cut shell are shown in Fig. 18. We immediately note the dramatic increase in radial displacement response at the front edge of each cutout over the corresponding response of the virgin shell. The opposite occurs (to a lesser degree) at the back edge of each cutout. Only minor differences occur away from the cutouts.

Shielding characteristics of the cutouts are indicated in Fig. 19, which shows displacement histories at points along the line $\alpha/a = 1.2$. The cutouts seem to produce a moderate reduction in radial displacement response in the shadow regions behind them. Figures 20-23 show displacement snapshots of both the virgin and cut shell displacement responses along the longitudinal lines $\beta = 0$, $\pi/12$ and $\pi/4$ at times $ct/a = 0.8$, 1.2, 2.0, 3.2, 4.0, and 4.4. Here too the response histories seem to be less effective as interpretive tools than response snapshots for increasingly complex response. Figures 20-23 are included mainly for comparison with experimental results obtained by holographic techniques.

Let us now examine the degree of non-axisymmetry in the displacement response of a shell. Figure 24 shows displacement snapshots along lines of constant α near and well behind the shear wave front. We see that, while the longitudinal displacement response tends to be β-independent,

radial displacement response tends to become increasingly β-dependent. This behavior is the same as that observed in Fig. 14 for the longitudinal excitation.

We have here too the interesting question as to whether the presence of the cutouts tends to facilitate the large-scale transfer of energy from extensional (primarily axisymmetric radial) into flexural (primarily non-axisymmetric radial) response. Long-time solutions are again required to answer this question.

4.3 SUMMARY

We have examined here the early-time response of a cylindrical shell with cutouts to end pulse-loads whose spatial width appropriate to propagation at the plate velocity is only eight times the thickness of the shell. Computed results indicate that the cutouts introduce no order-of-magnitude changes in the response of the shell. They do point to moderate shielding effects in shadow regions behind the cutouts, however. Furthermore, they suggest that the cutouts may facilitate the transfer of load-injected extensional energy into non-axisymmetric flexural response, a potentially dangerous situation. Definitive conclusions about this phenomenon, however, await long-time solutions.

A broad picture of the effects of the cutouts on the response of the shell is given in Fig. 25. For each point at which a response history was computed, two ratios of peak response in the cut shell to the corresponding peak response in the virgin shell are shown. The responses chosen for these ratio indicators are, for the longitudinal excitation, longitudinal velocity and effective stress and, for the radial excitation, radial velocity and effective stress. Velocity response is chosen because it is often considered to be the most useful indicator of damage potential for attached structural systems (see, e.g., Ref. 32). Effective stress for the Mises yield surface, in the form (Ref. 10)

$$\sigma_{eff} = \left[\sigma_\alpha^{\,2} + \sigma_\beta^{\,2} - \sigma_\alpha\sigma_\beta + 3\tau_{\alpha\beta}^{\,2}\right]^{1/2} \qquad (2)$$

is chosen because it is a useful measure of damage potential for the shell itself. Even though the velocity and strain computations appropriate to the radial loading are not entirely satisfactorily convergent, they are considered adequate for the purposes of Fig. 25.

We observe in Fig. 25 that the cutouts appear to possess significantly greater shielding capability for the radial excitation than for the longitudinal excitation. We also observe that the related tendency toward non-axisymmetry is more prevalent in the case of the radial excitation. The effect of reinforcement of the cutout on these results would be of considerable interest and a worthwhile subject of future studies.

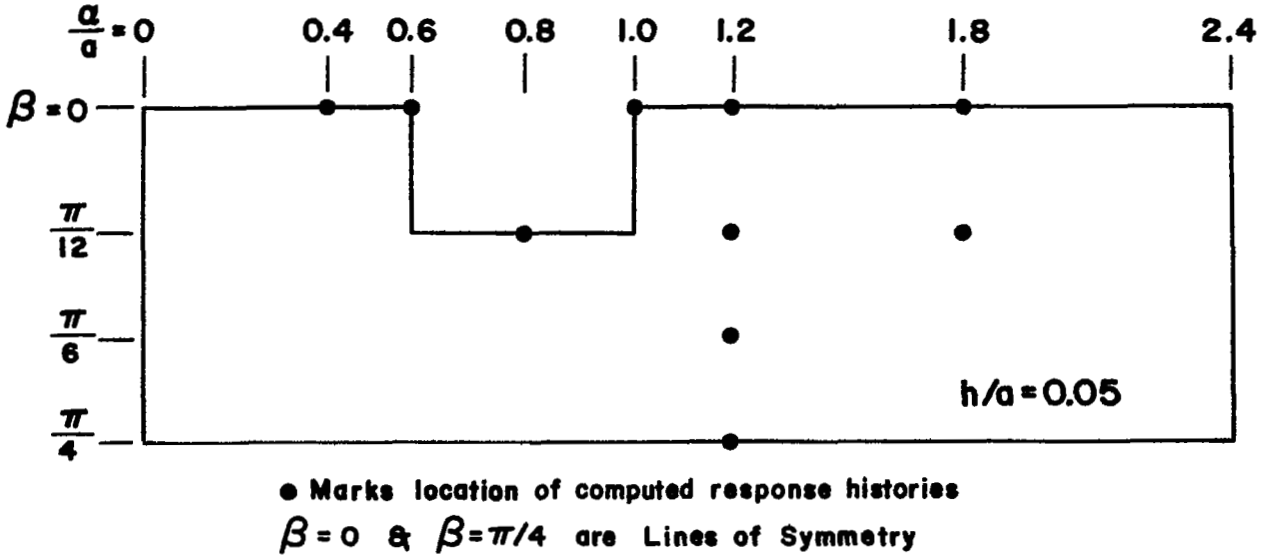

● Marks location of computed response histories

$\beta = 0$ & $\beta = \pi/4$ are Lines of Symmetry

BOUNDARY CONDITIONS

Longitudinal Excitation	Radial Excitation
$N_\alpha(0,\beta,t)$ given, $N_\alpha(2.4a,\beta,t) = 0$	$u(0,\beta,t) = 0$, $N_\alpha(2.4a,\beta,t) = 0$
$v(0,\beta,t) = 0$, $v(2.4a,\beta,t) = 0$	$v(0,\beta,t) = 0$, $v(2.4a,\beta,t) = 0$
$Q(0,\beta,t) = 0$, $w(2.4a,\beta,t) = 0$	$Q_\alpha(0,\beta,t)$ given, $w(2.4a,\beta,t) = 0$
$\omega_\beta(0,\beta,t) = 0$, $M_\beta(2.4a,\beta,t) = 0$	$\omega_\beta(0,\beta,t) = 0$, $M_\beta(2.4a,\beta,t) = 0$

Figure 1. One-Eighth of Surface of Cylindrical Shell with Cutouts

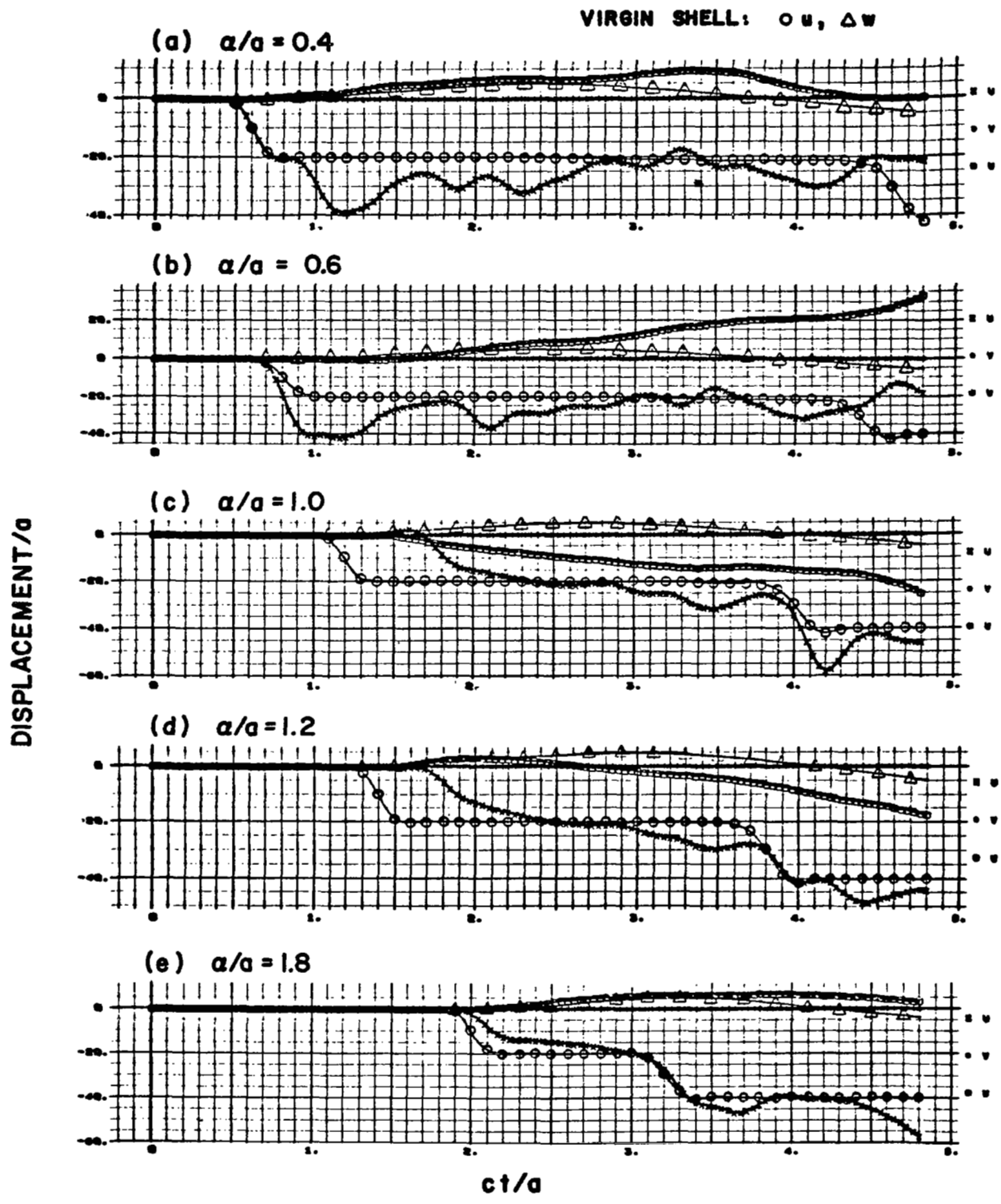

Figure 2. Virgin Shell and (β = 0) Cut Shell Displacement Histories

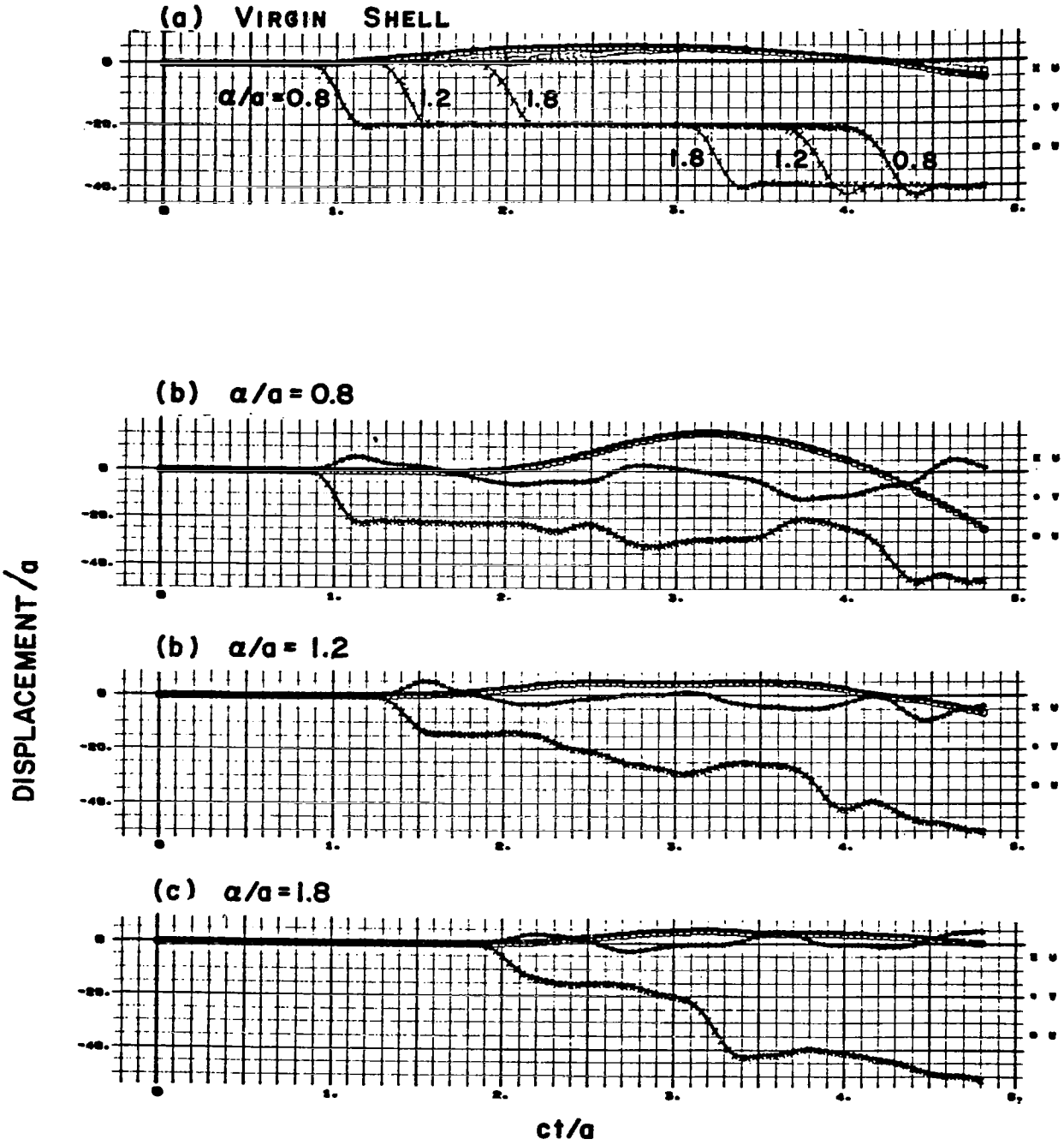

Figure 3. Virgin Shell and ($\beta = \pi/12$) Cut Shell Displacement Histories

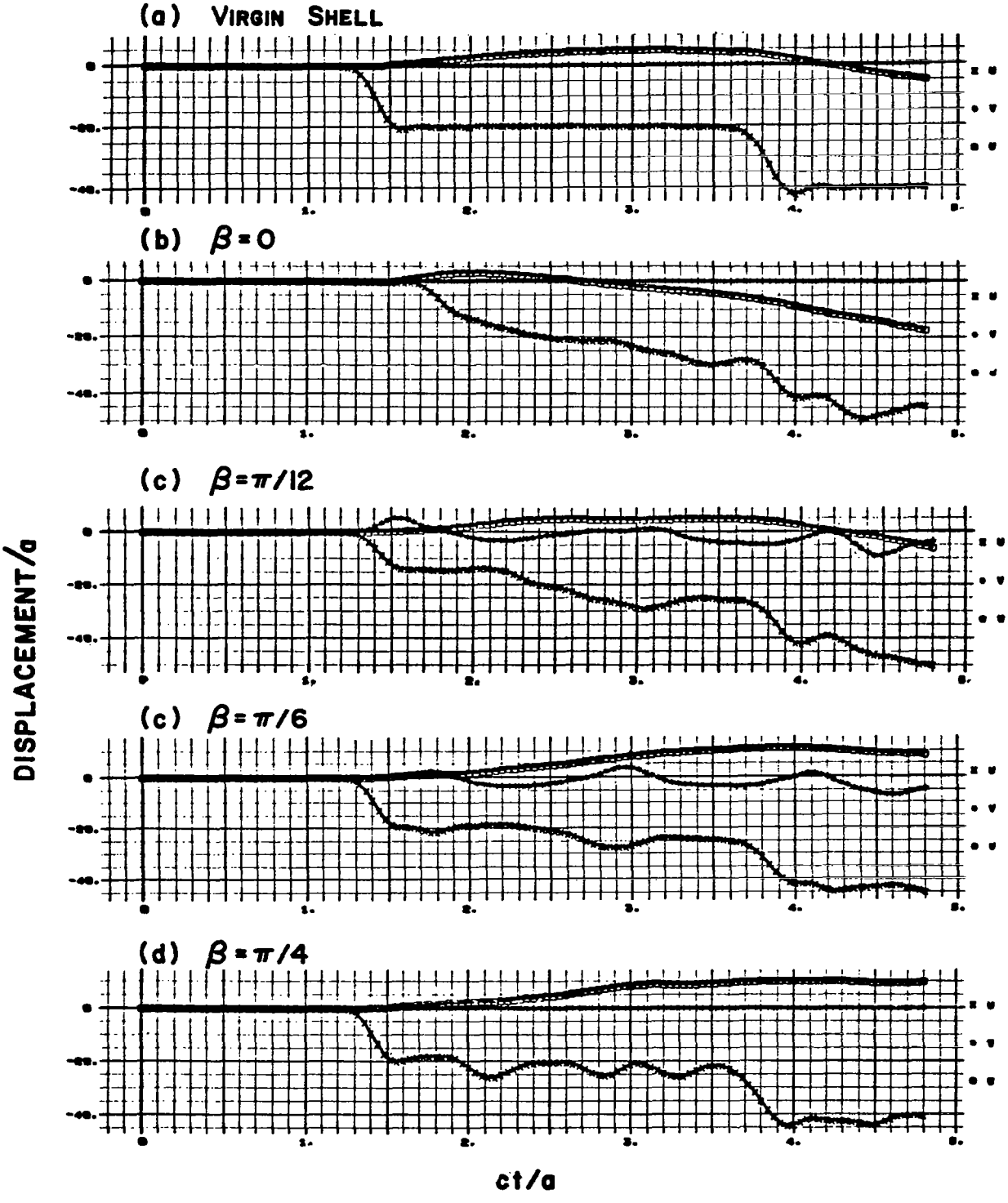

Figure 4. Virgin Shell and Cut Shell Displacement Histories at $\alpha/a = 1.2$

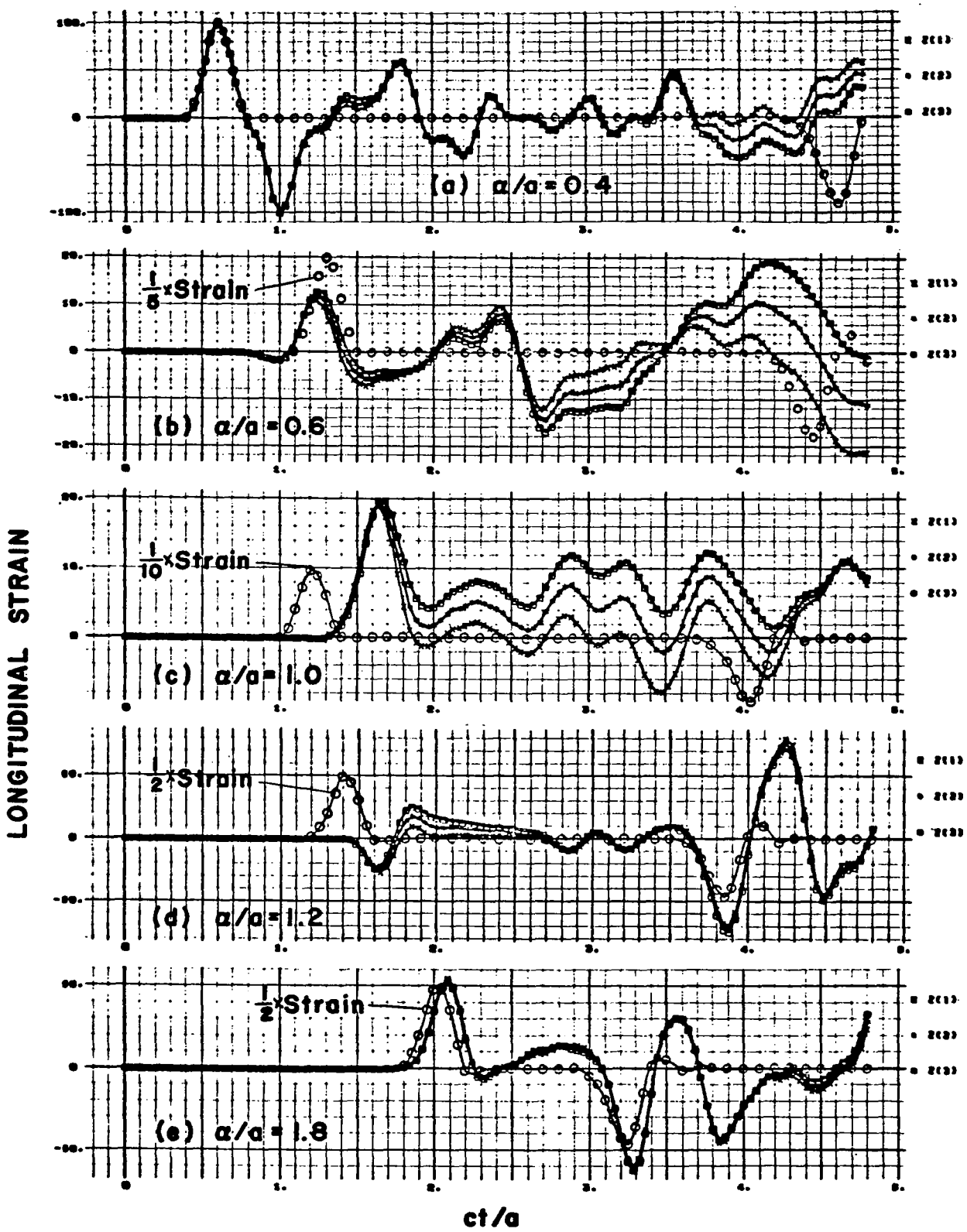

Figure 5. Virgin Shell and (β = 0) Cut Shell Longitudinal Strain Histories [Z(1), Z(2) and Z(3) denote outer, middle and inner surfaces, respectively]

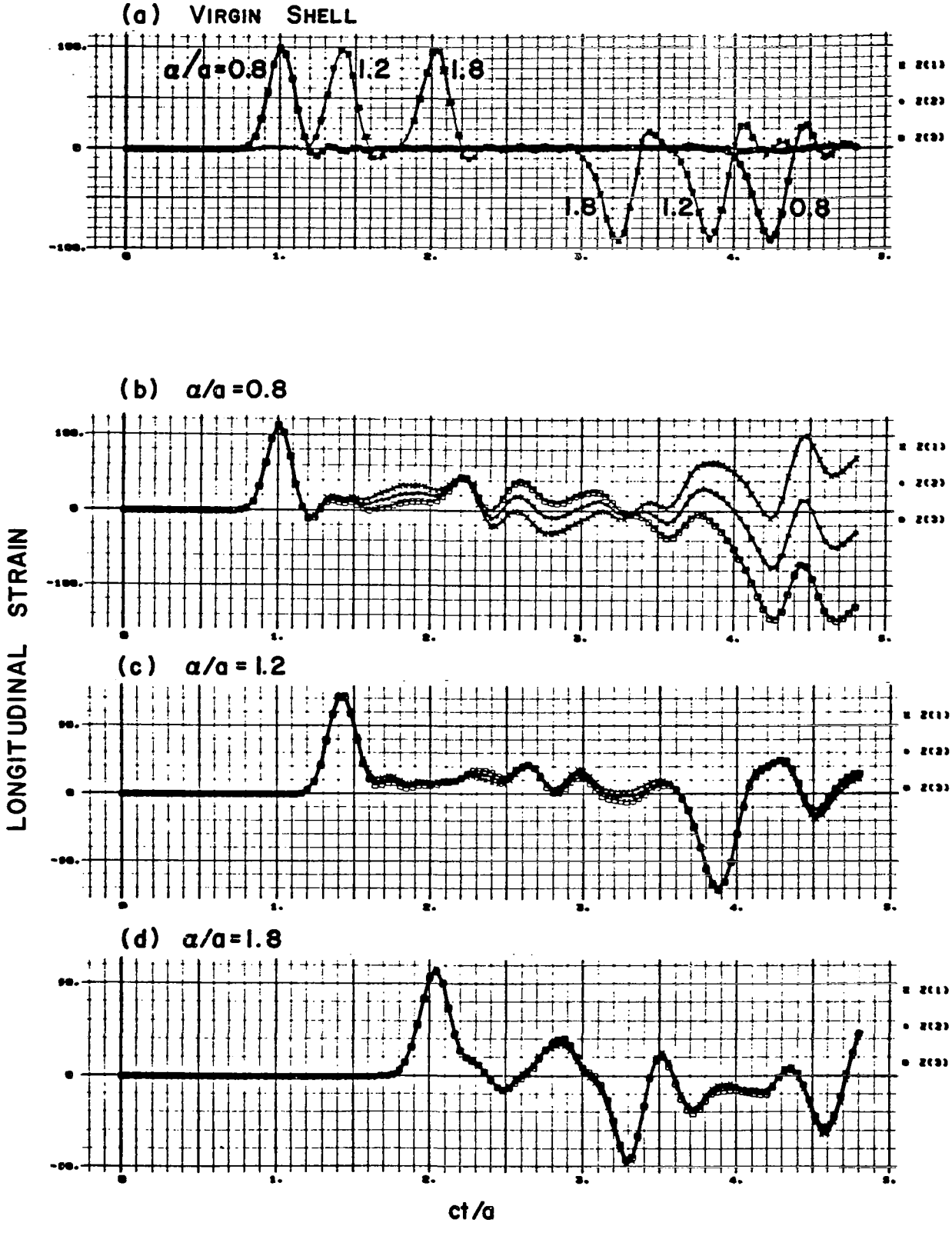

Figure 6. Virgin Shell and ($\beta = \pi/12$) Cut Shell Longitudinal Strain Histories [Z(1), Z(2) and Z(3) denote outer, middle and inner surfaces, respectively]

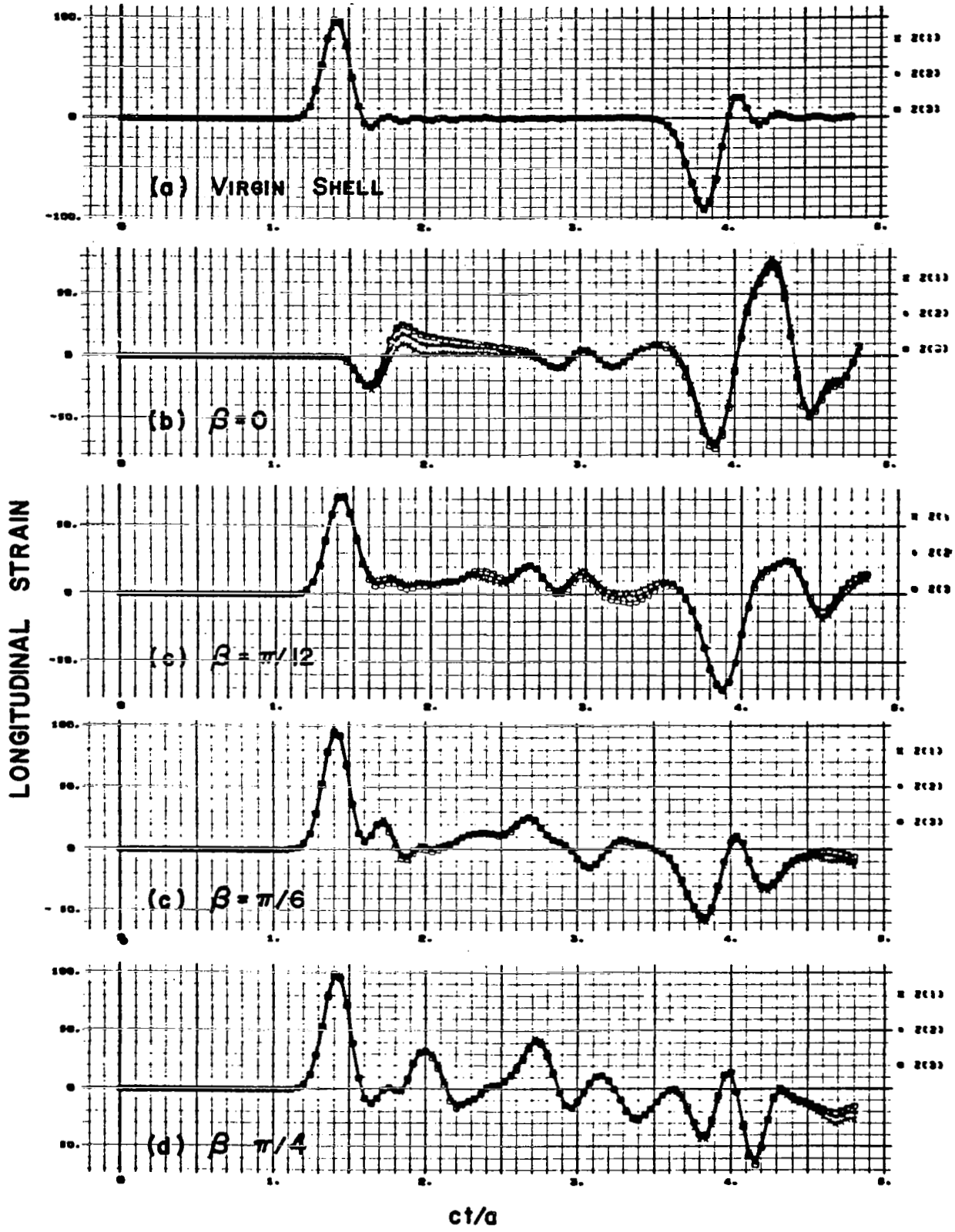

Figure 7. Virgin Shell and Cut Shell Longitudinal Strain Histories at $\alpha/a = 1.2$ [Z(1), Z(2) and Z(3) denote outer, middle and inner surfaces, respectively]

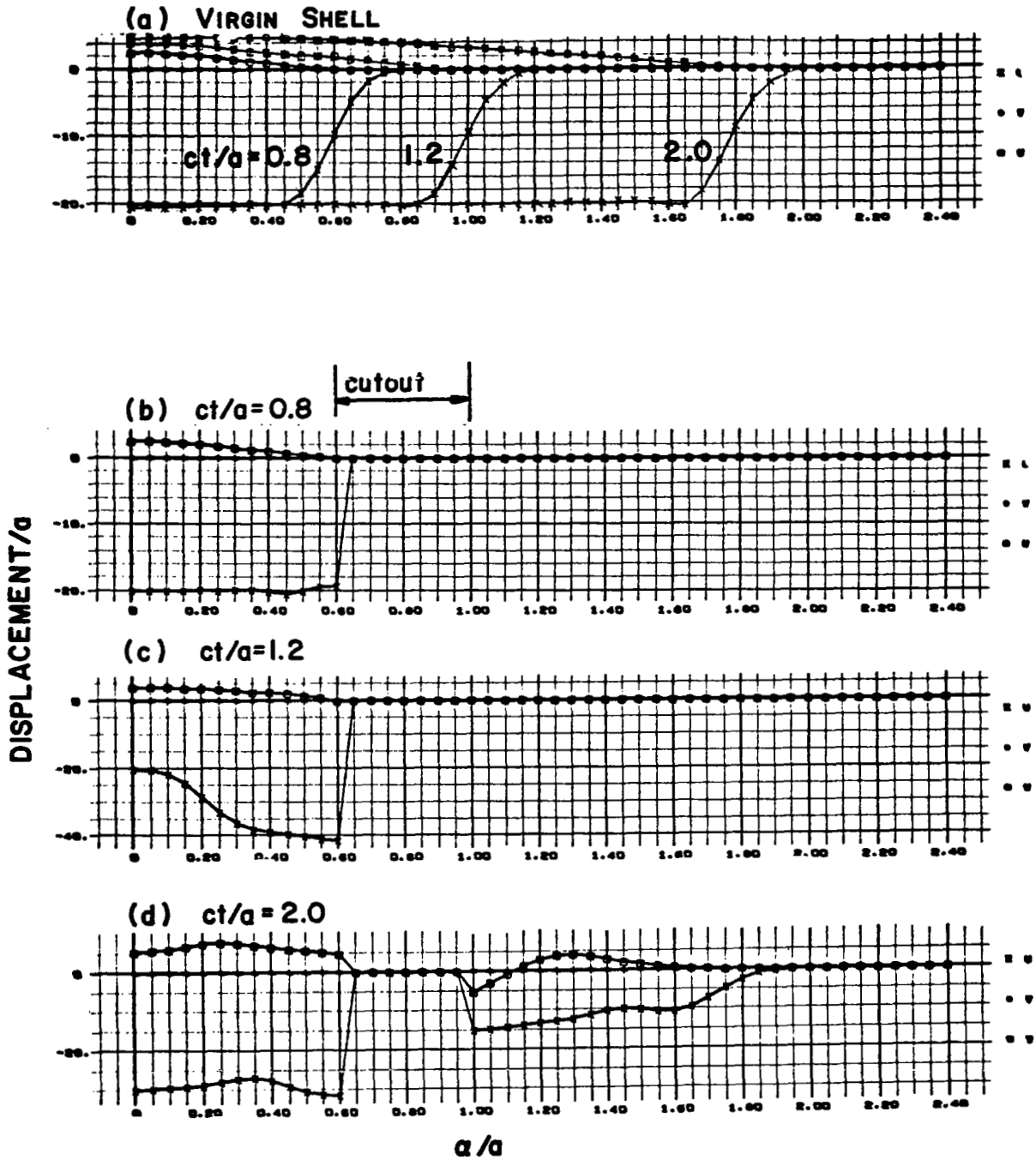

Figure 8. Virgin Shell and (β = 0) Cut Shell Displacement Snapshots

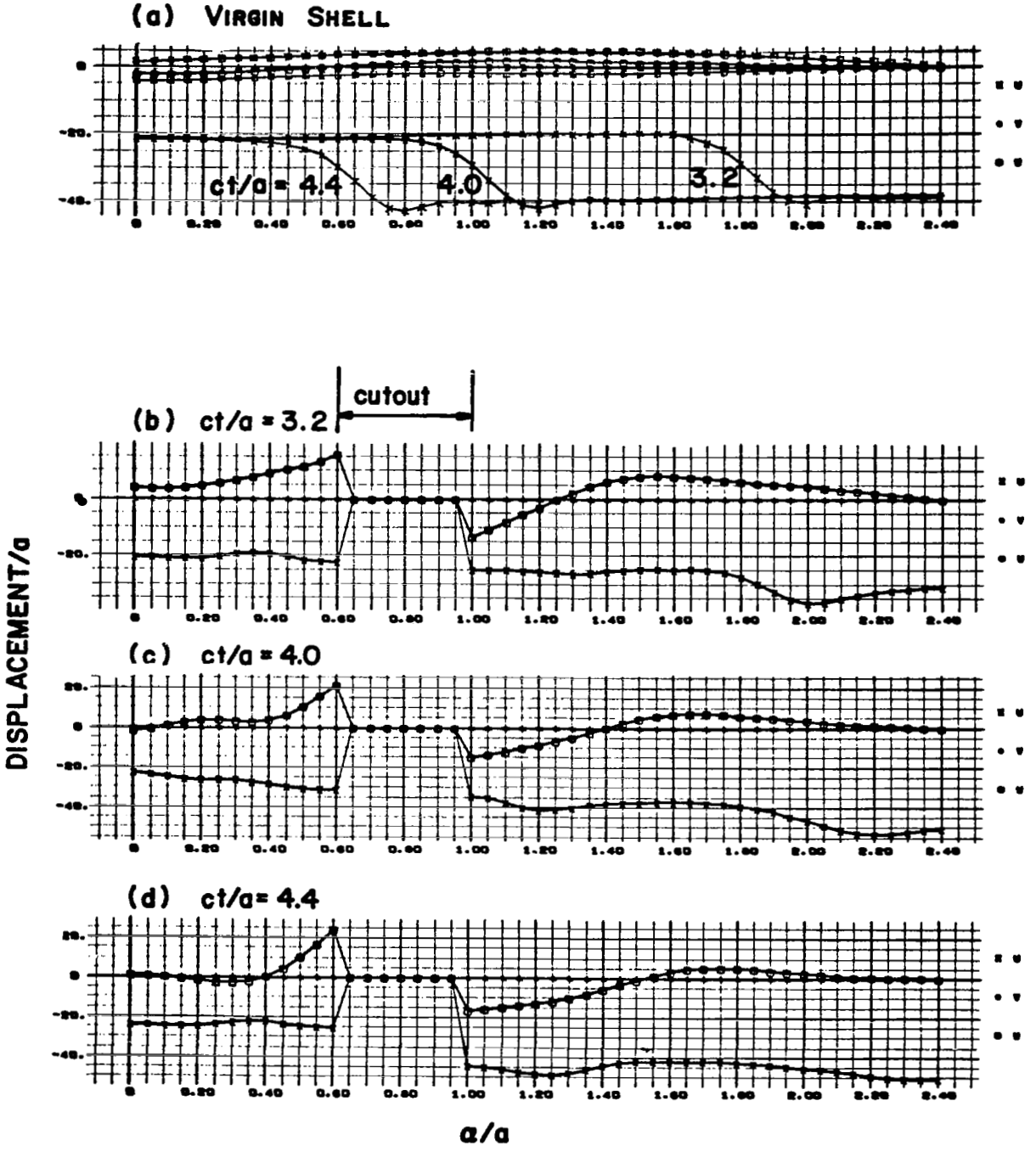

Figure 9. Virgin Shell and (β = 0) Cut Shell Displacement Snapshots

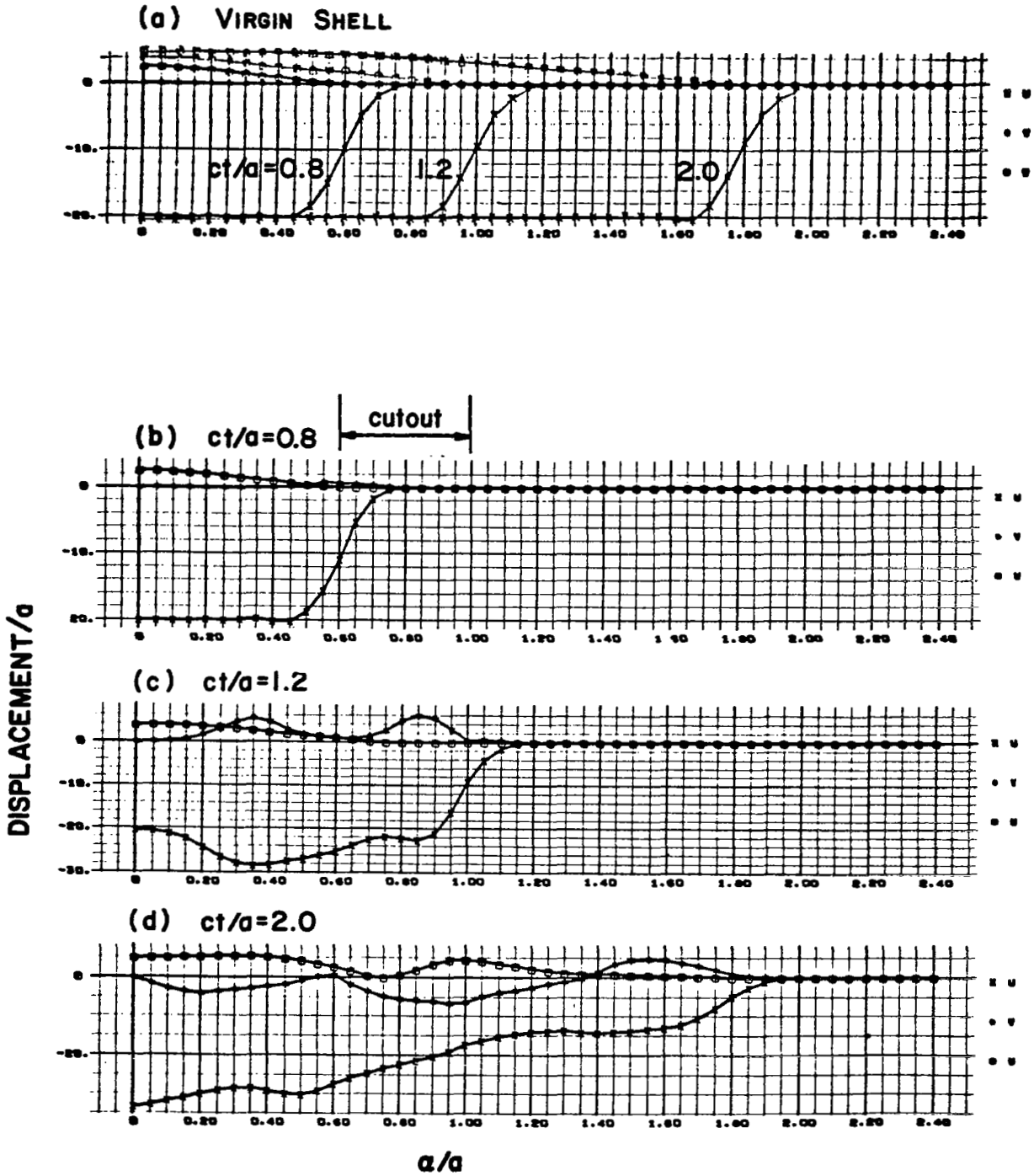

Figure 10. Virgin Shell and ($\beta = \pi/12$) Cut Shell Displacement Snapshots

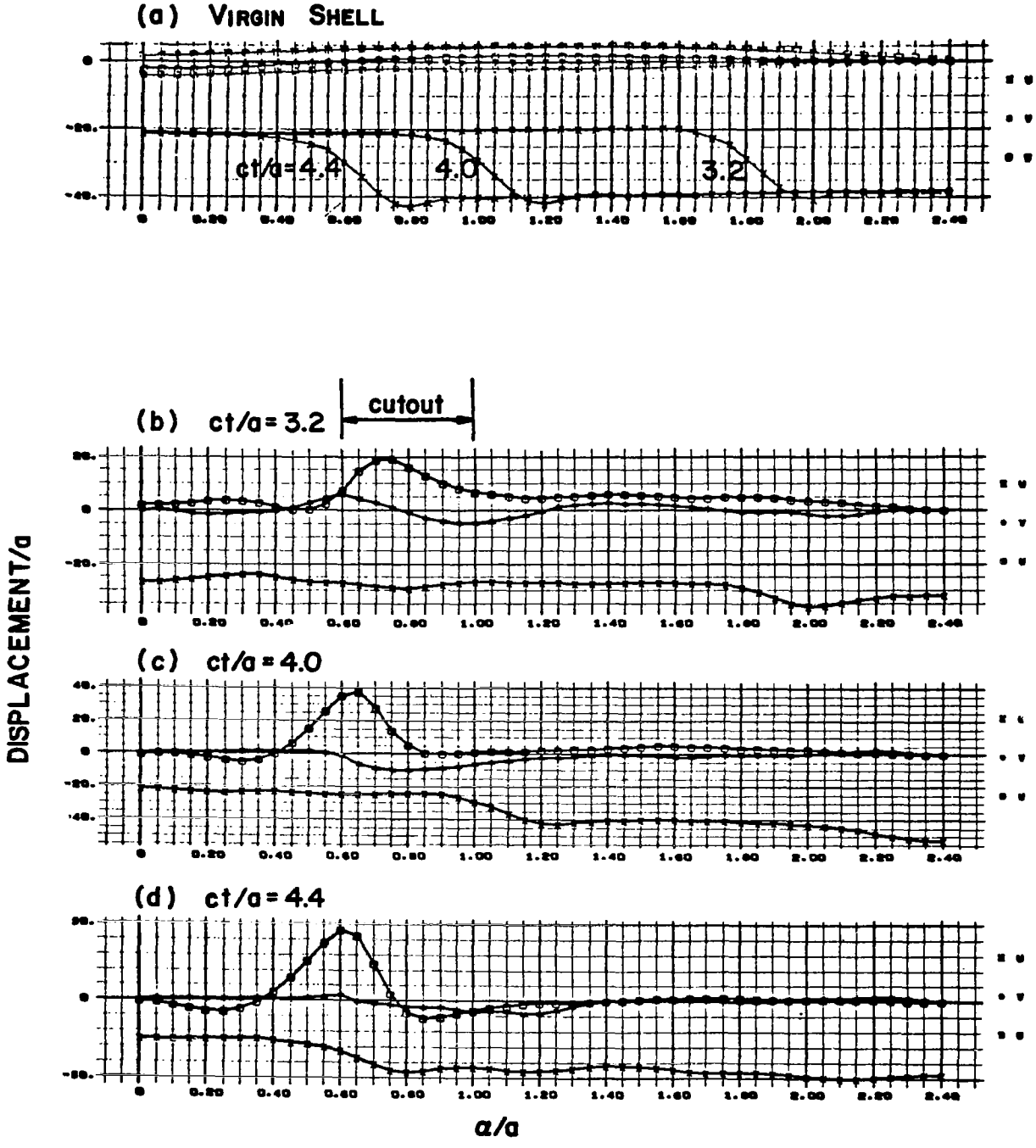

Figure 11. Virgin Shell and ($\beta = \pi/12$) Cut Shell Displacement Snapshots

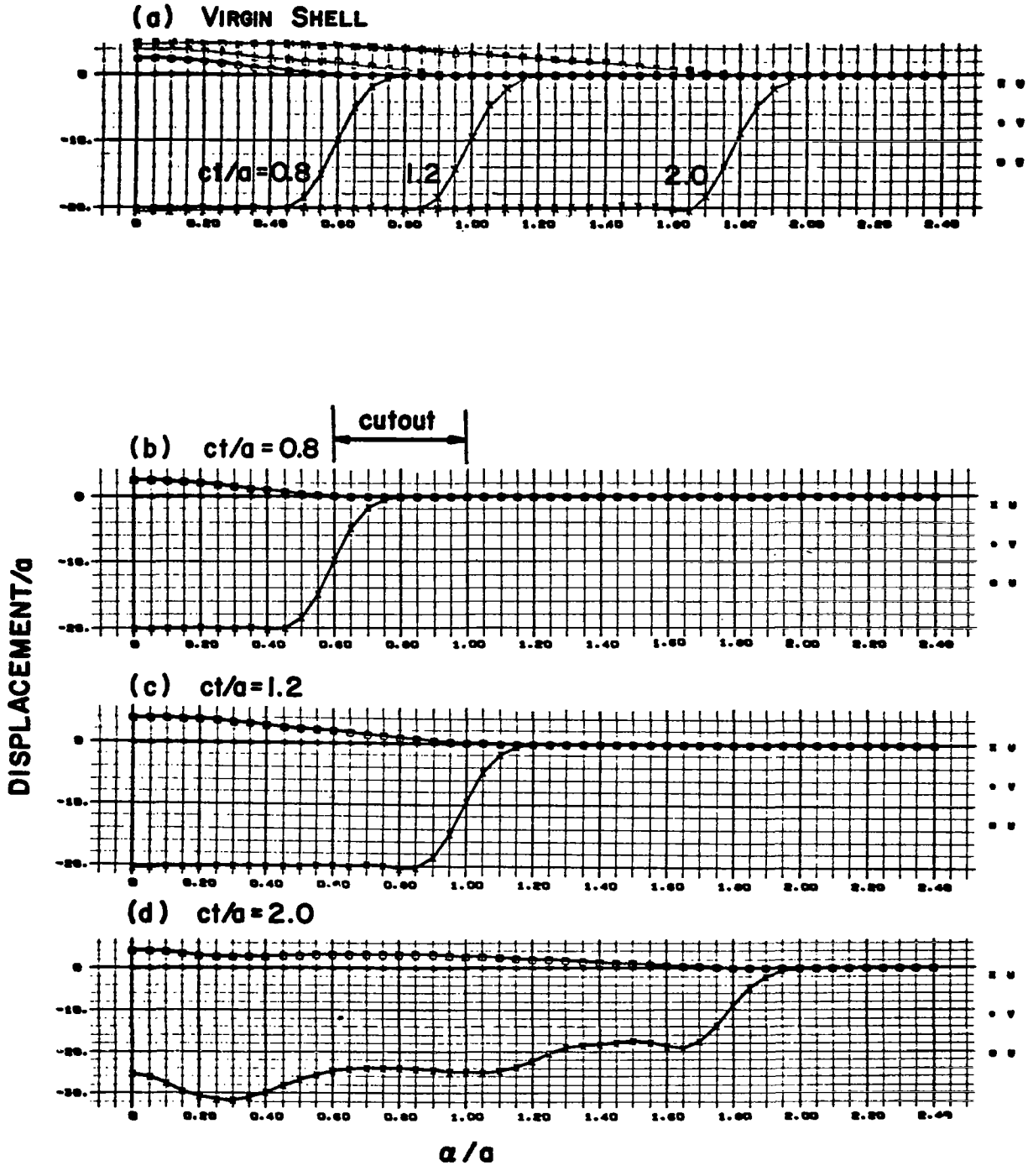

Figure 12. Virgin Shell and ($\beta = \pi/4$) Cut Shell Displacement Snapshots

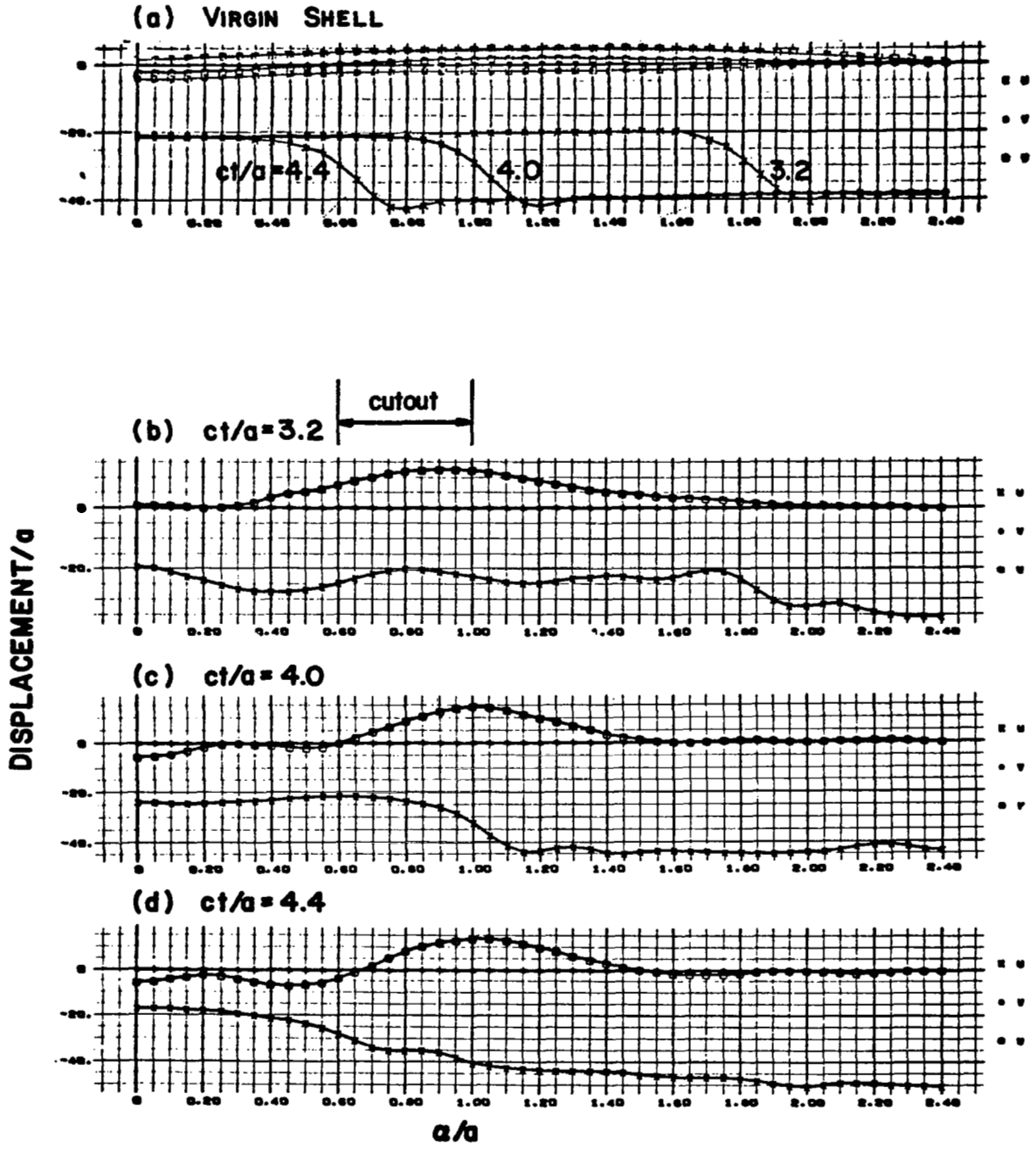

Figure 13. Virgin Shell and ($\beta = \pi/4$) Cut Shell Displacement Snapshots

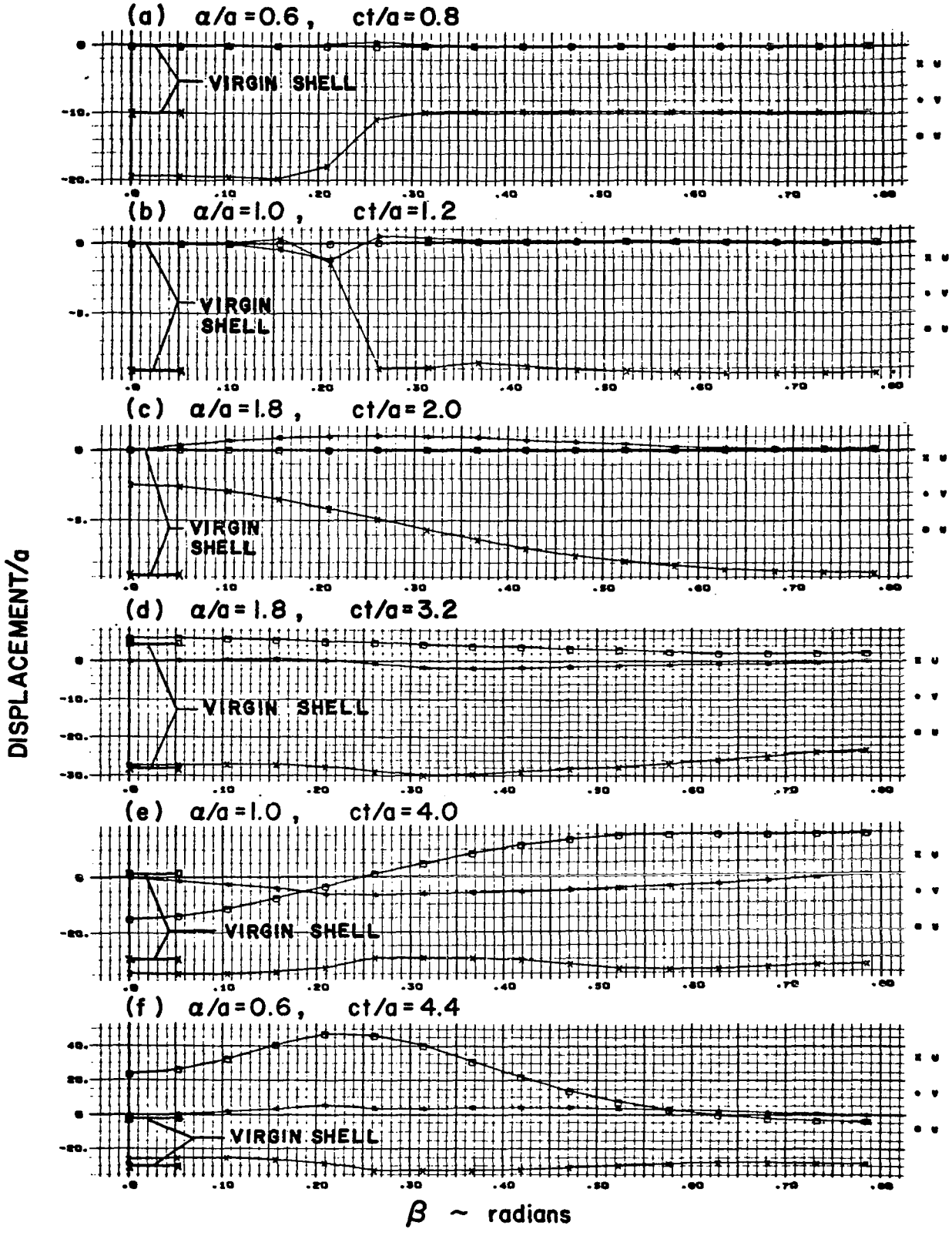

Figure 14. Circumferential Snapshots of Cut Shell Displacement Response Immediately Behind Wave Front

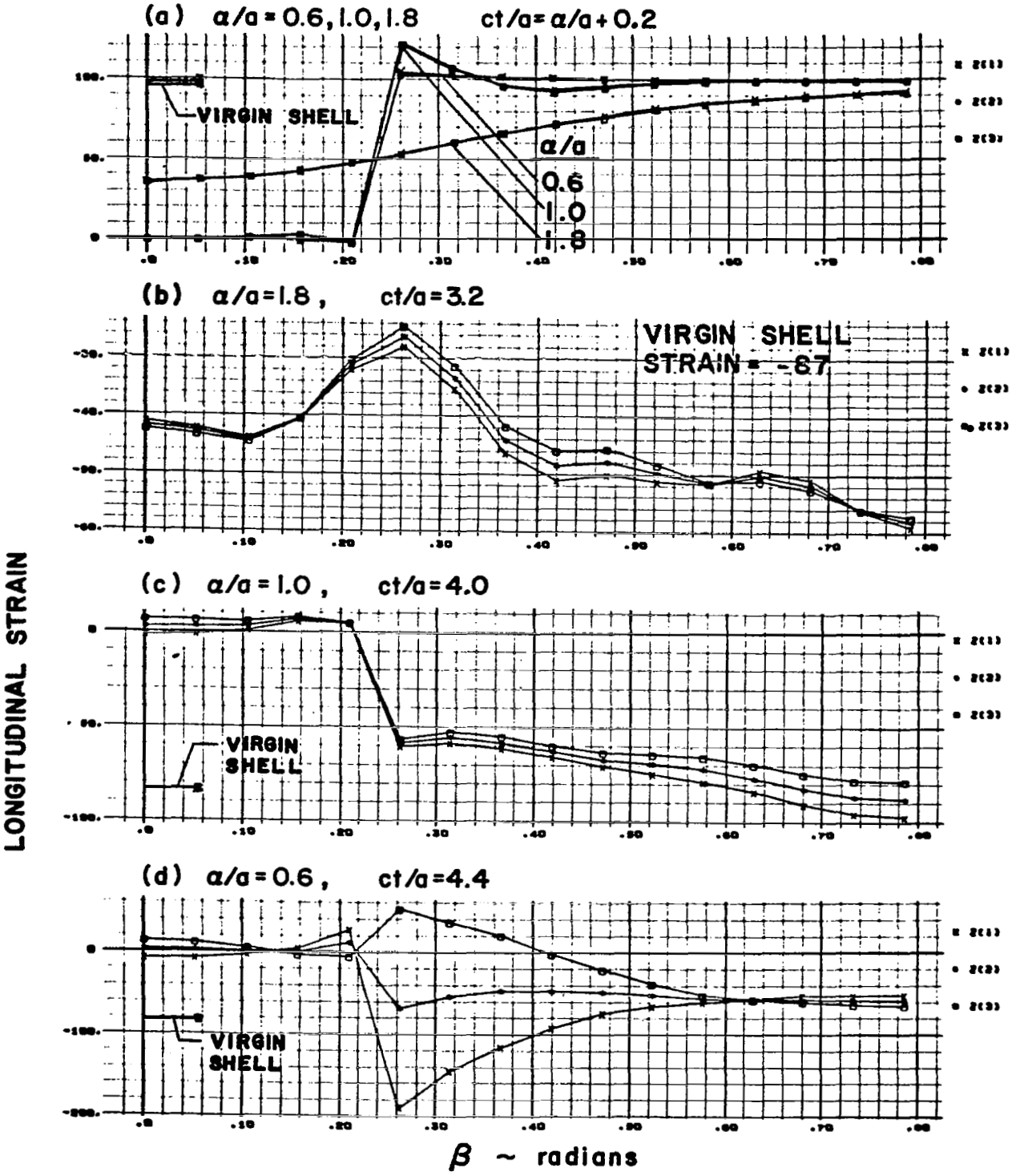

Figure 15. Circumferential Snapshots of Cut Shell Longitudinal Strain Response Immediately Behind Wave Front (Z(1), Z(2) and Z(3) denote outer, middle, and inner surfaces, respectively)

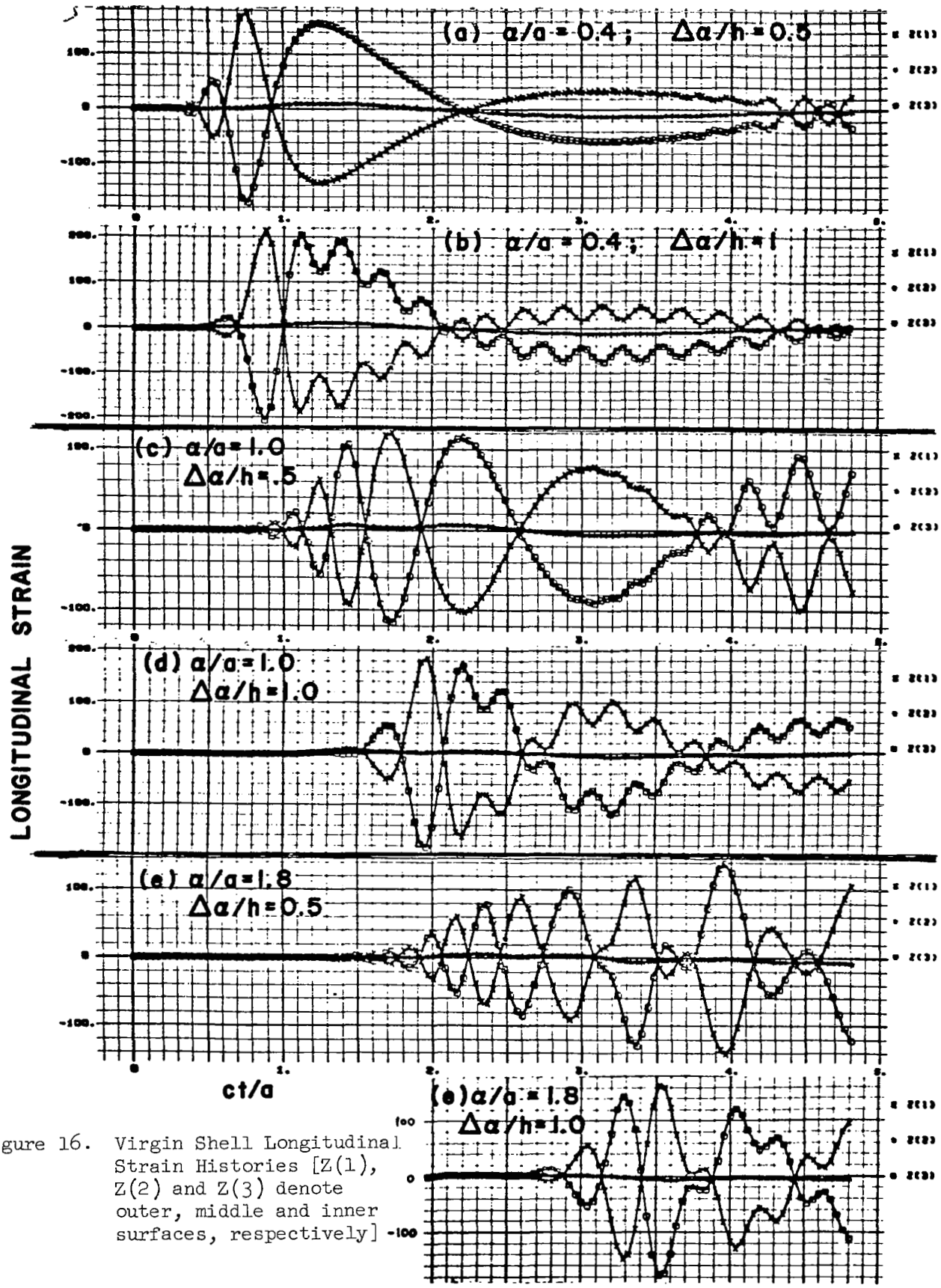

Figure 16. Virgin Shell Longitudinal Strain Histories [Z(1), Z(2) and Z(3) denote outer, middle and inner surfaces, respectively]

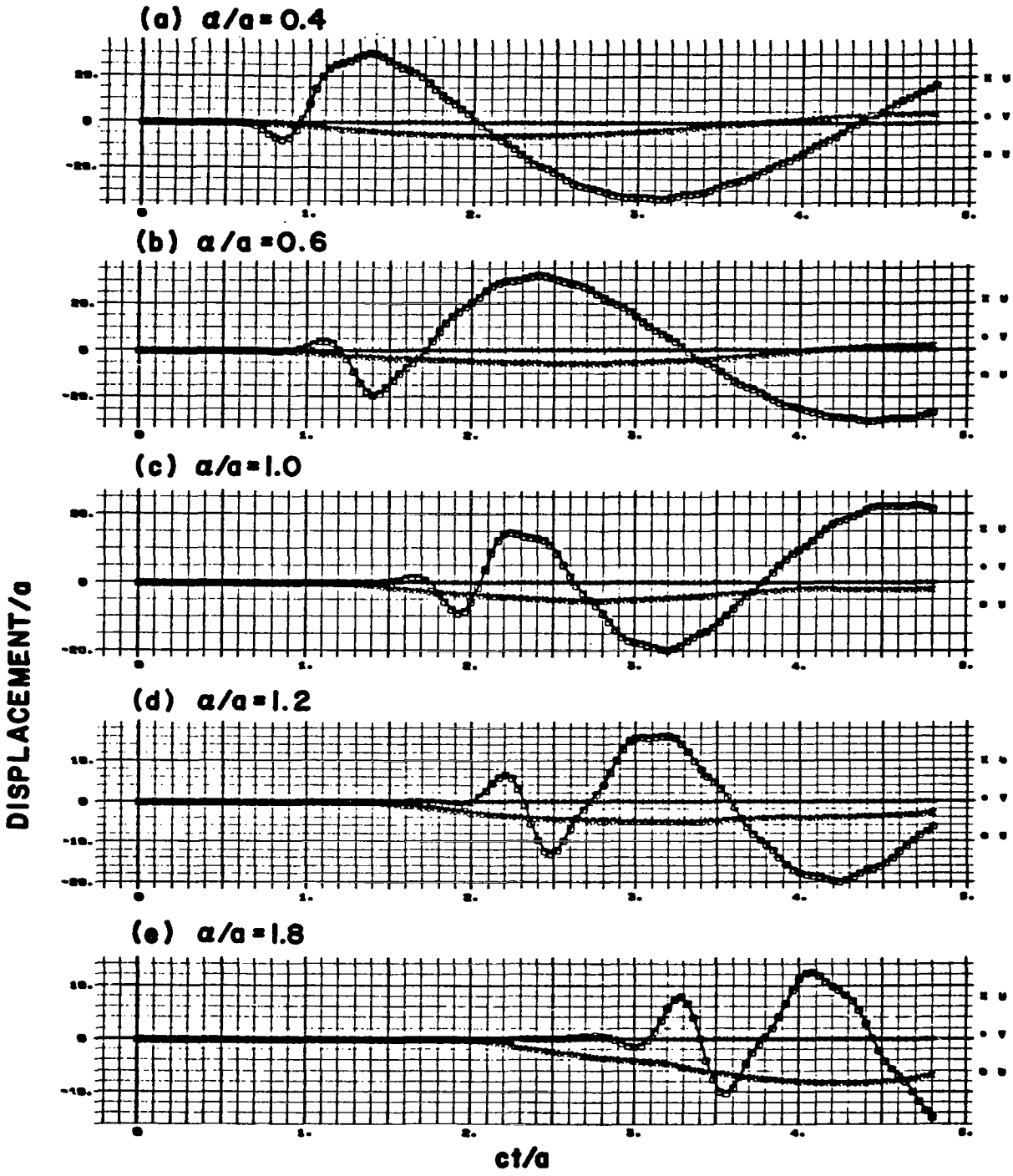

Figure 17. Virgin Shell Displacement Histories

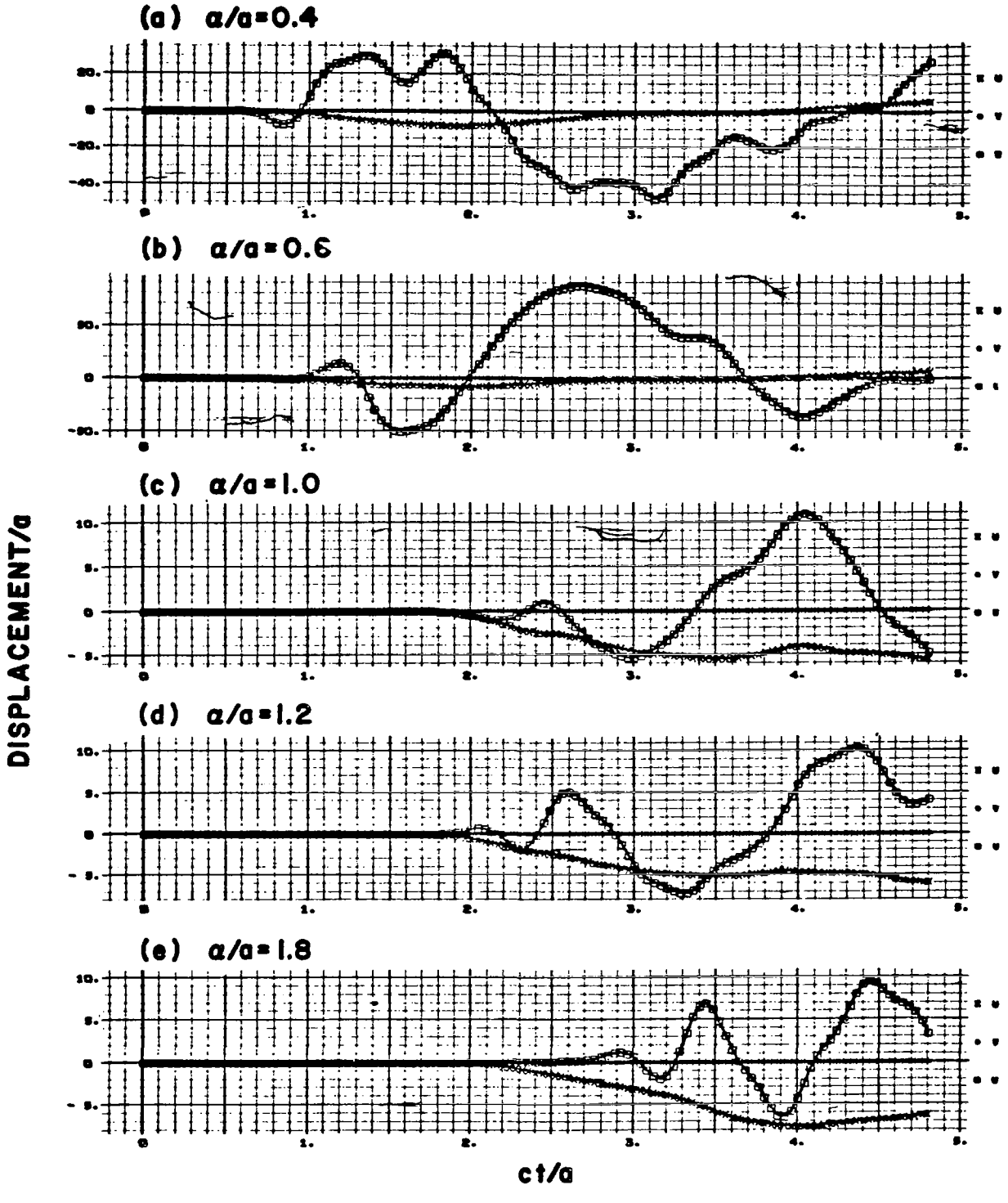

Figure 18. Cut Shell Displacement Histories along the Line $\beta = 0$

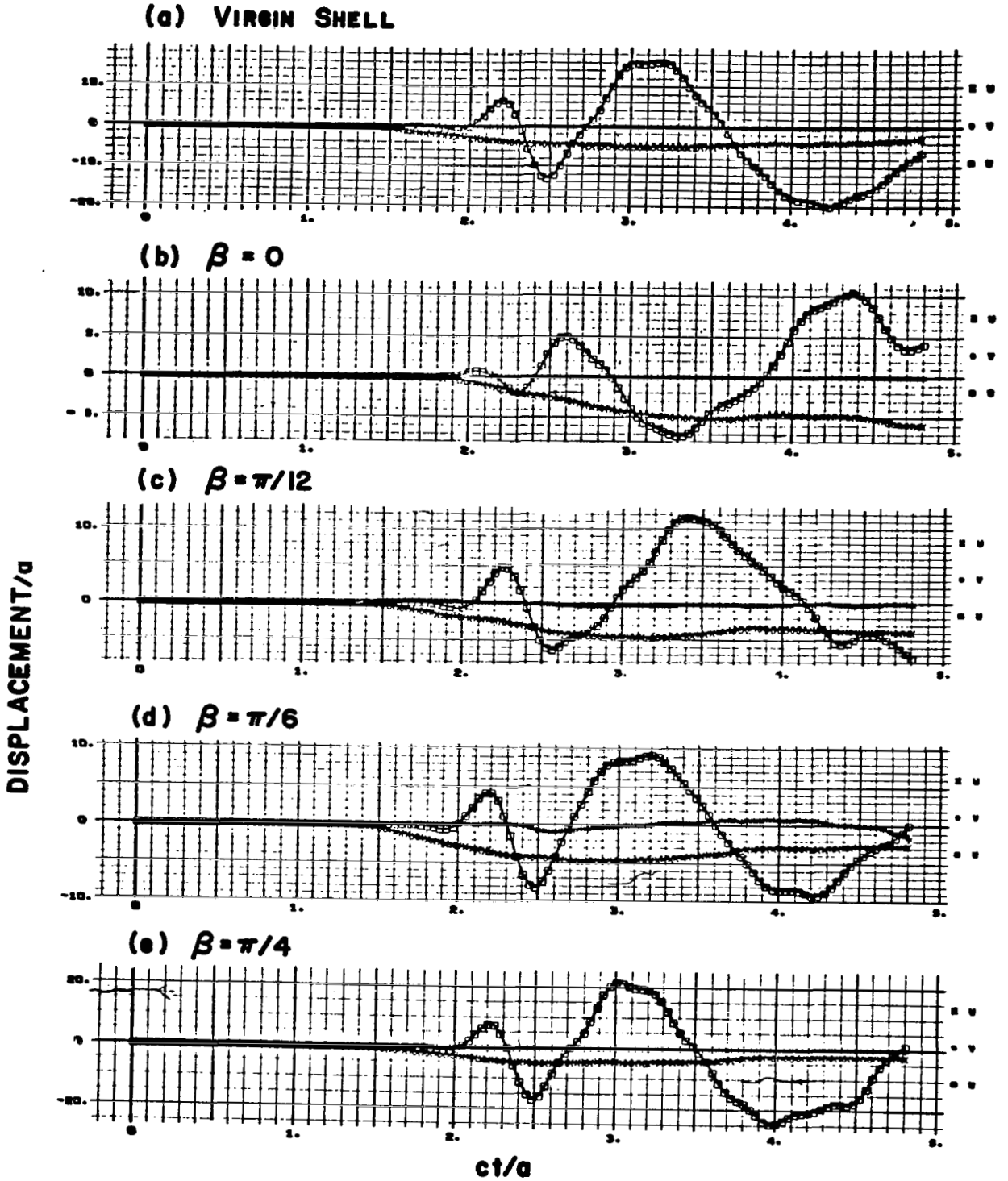

Figure 19. Virgin Shell and Cut Shell Displacement Histories at $\alpha/a = 1.2$

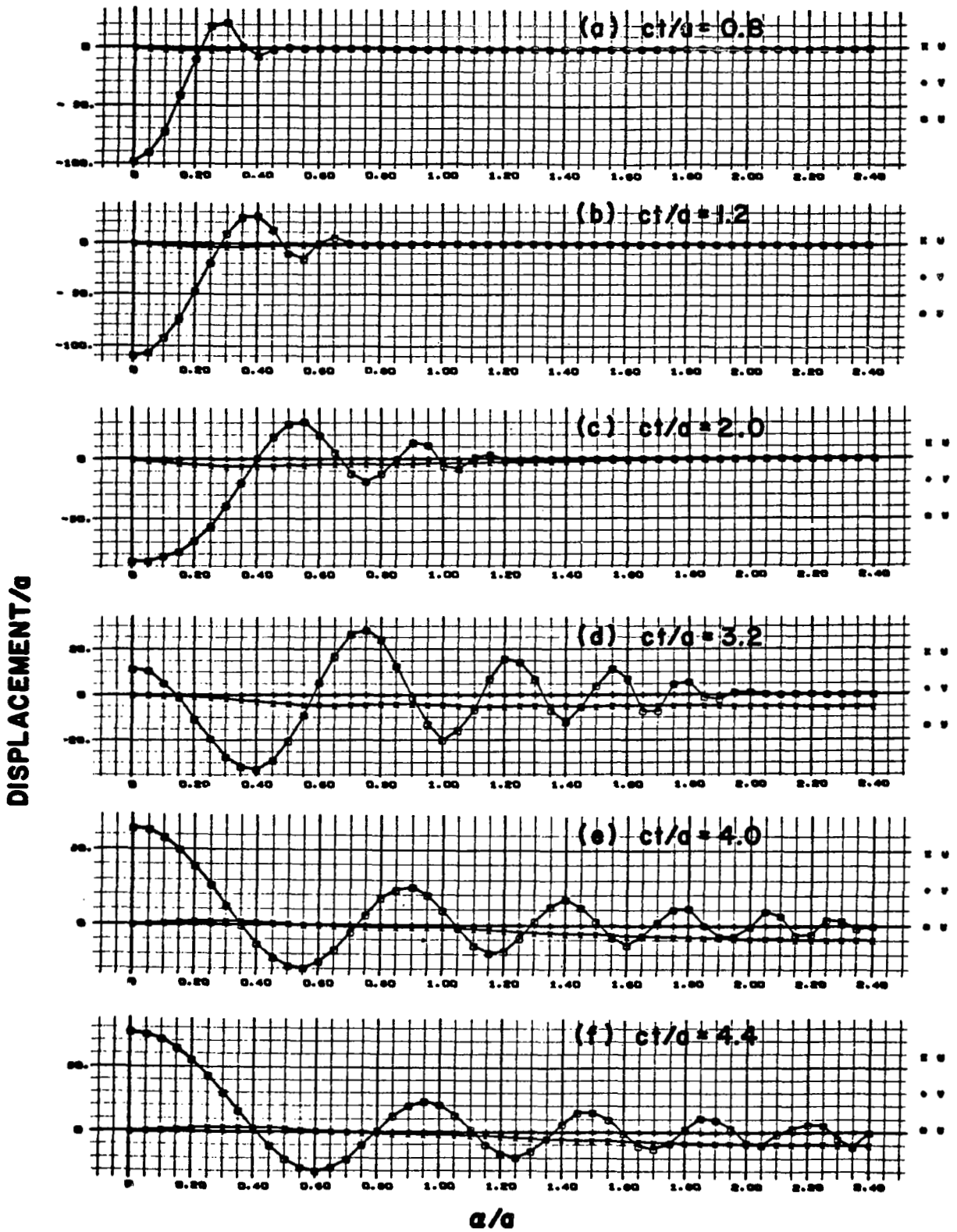

Figure 20. Virgin Shell Displacement Snapshots

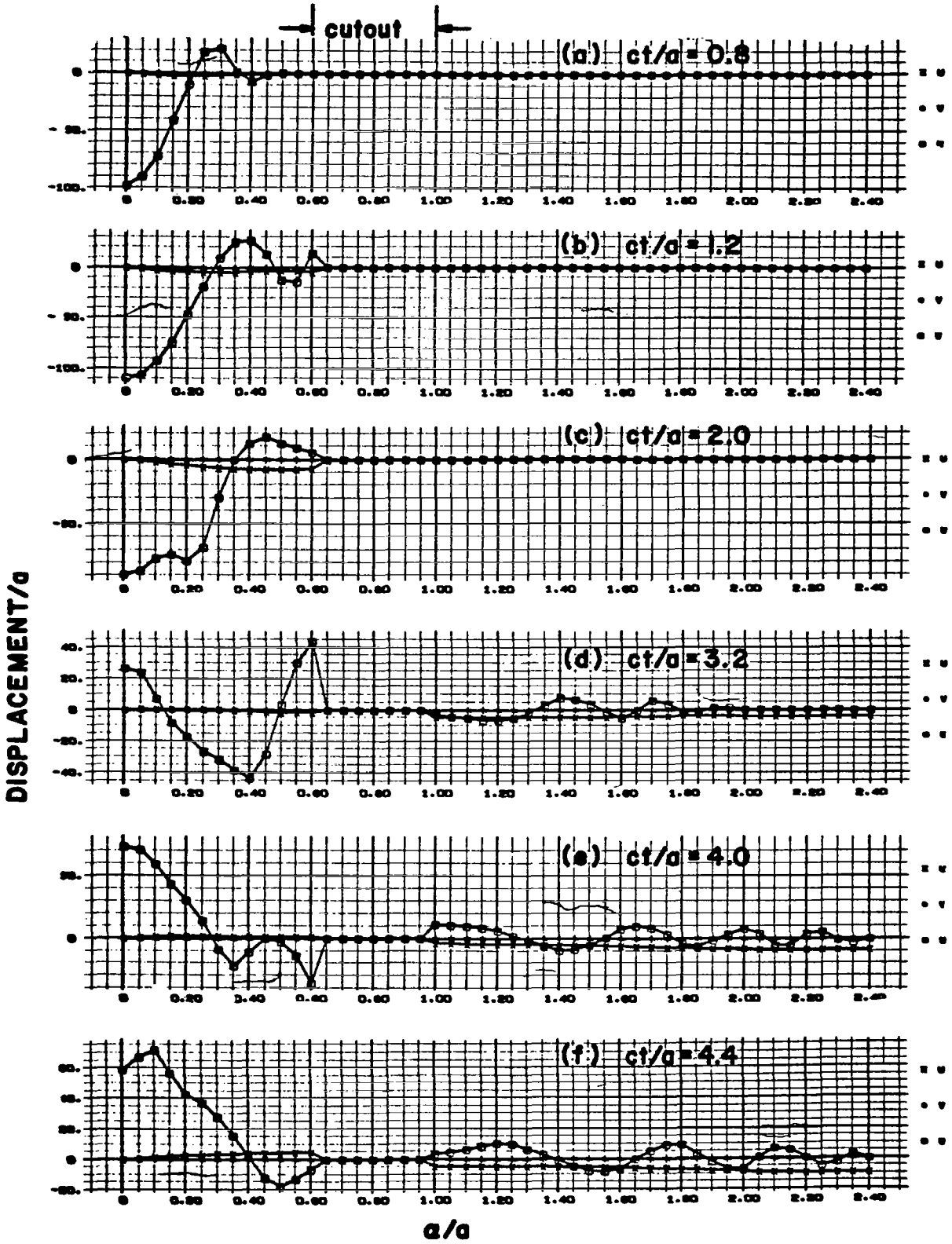

Figure 21. Cut Shell Displacement Snapshots along the Line $\beta = 0$

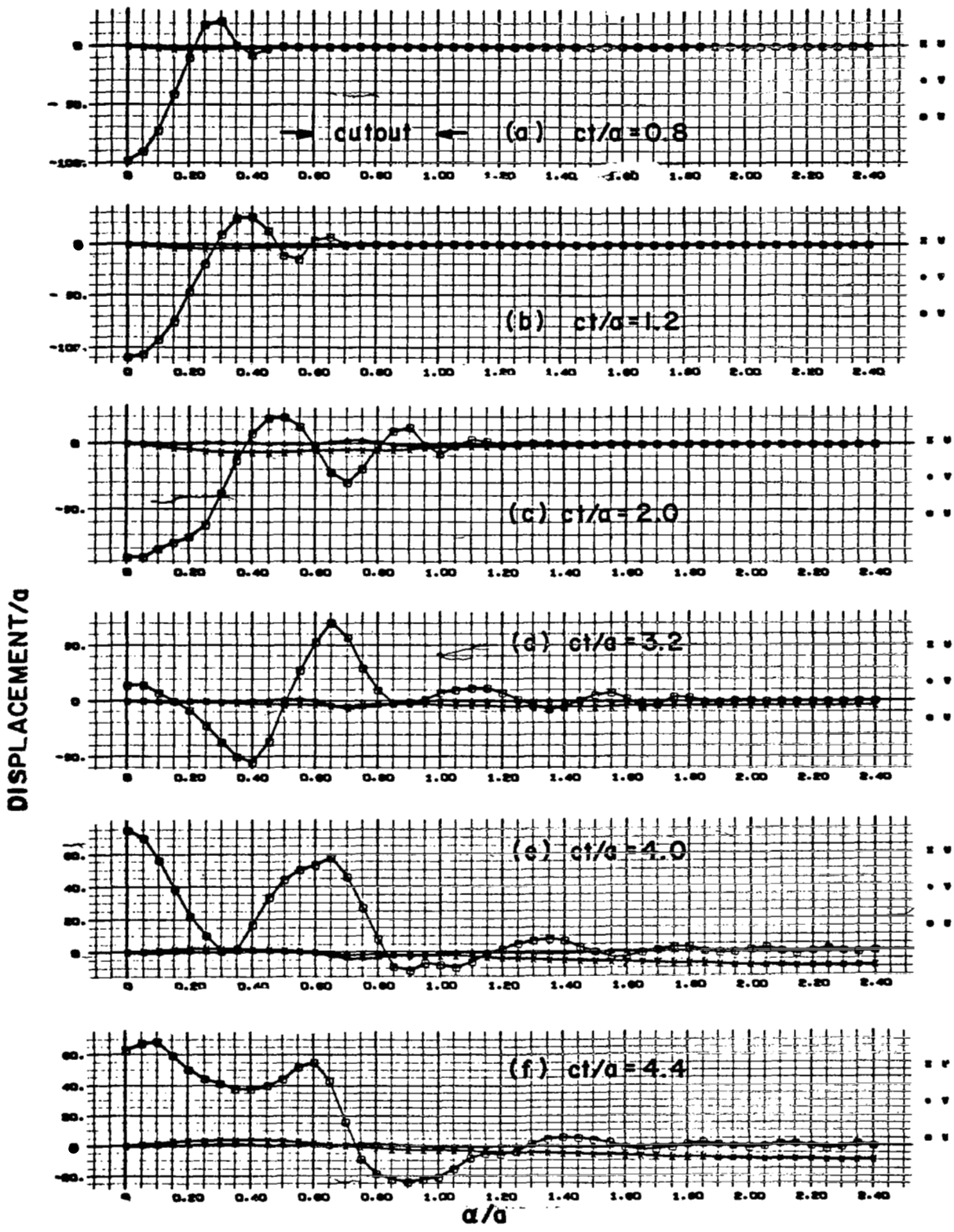

Figure 22. Cut Shell Displacement Snapshots along the Line $\beta = \pi/12$

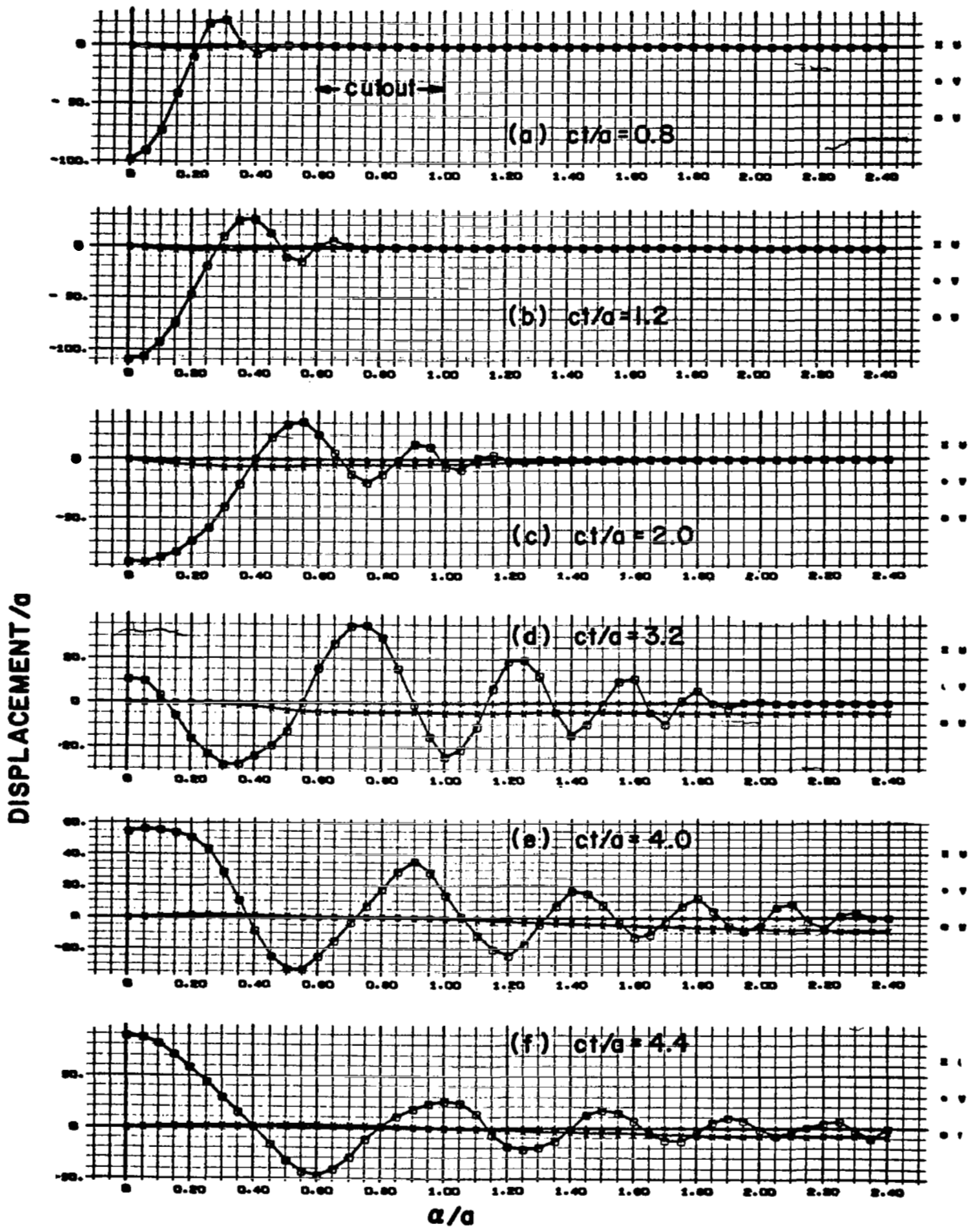

Figure 23. Cut Shell Displacement Snapshots along the Line $\beta = \pi/4$

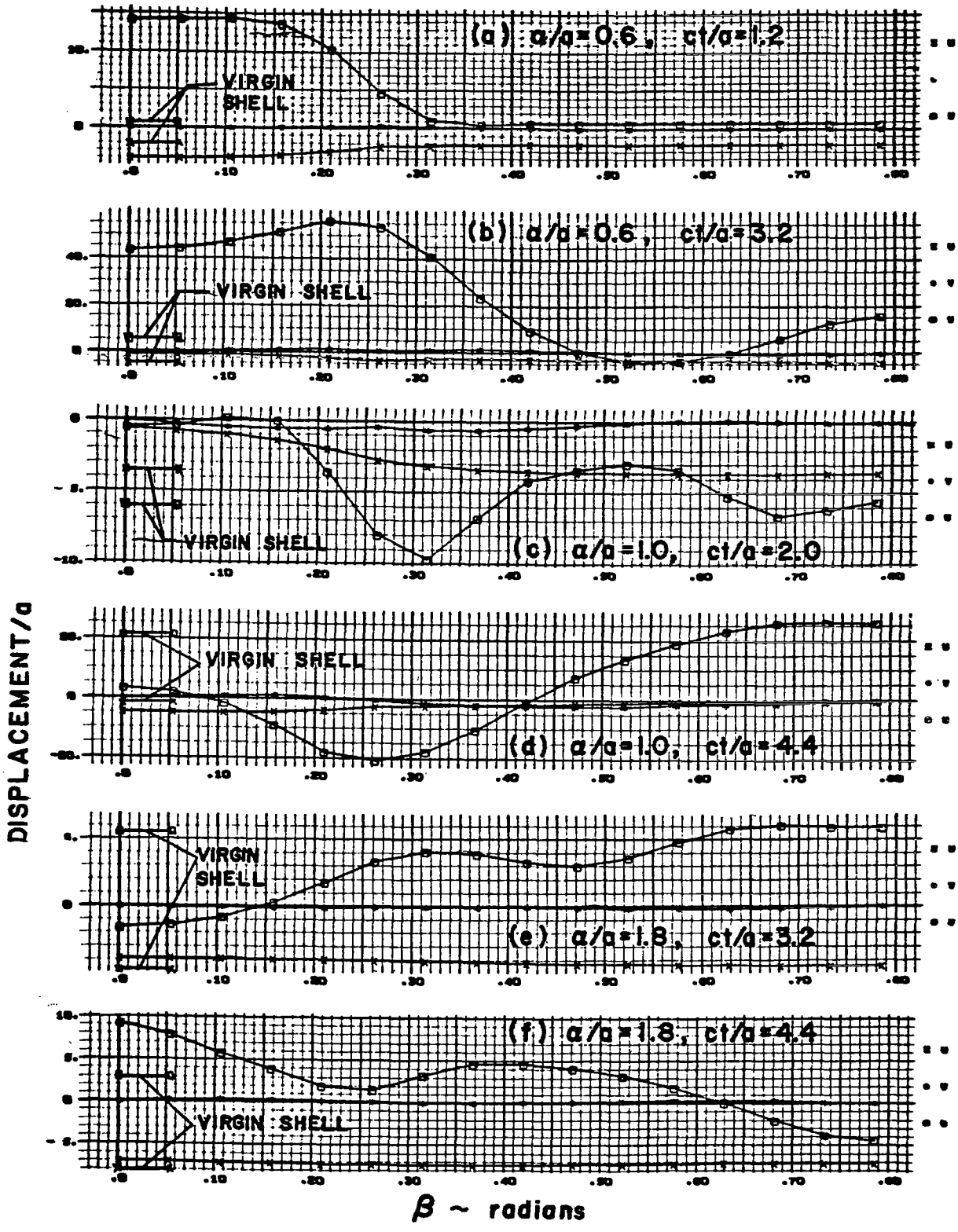

Figure 24. Circumferential Snapshots of Cut Shell Displacement Response

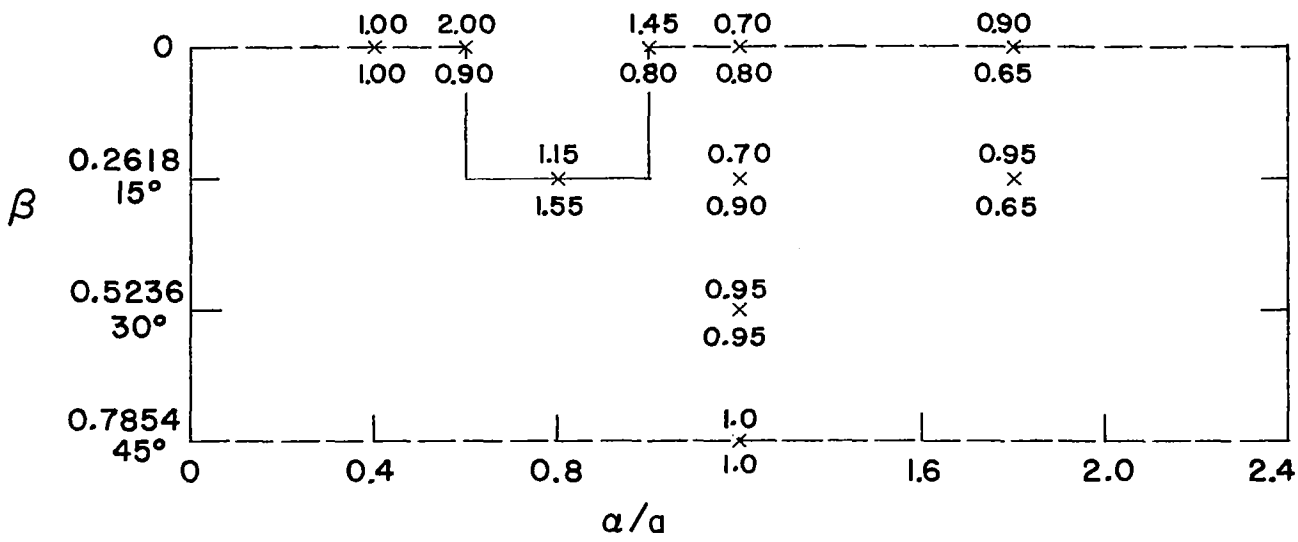

a) Longitudinal Excitation

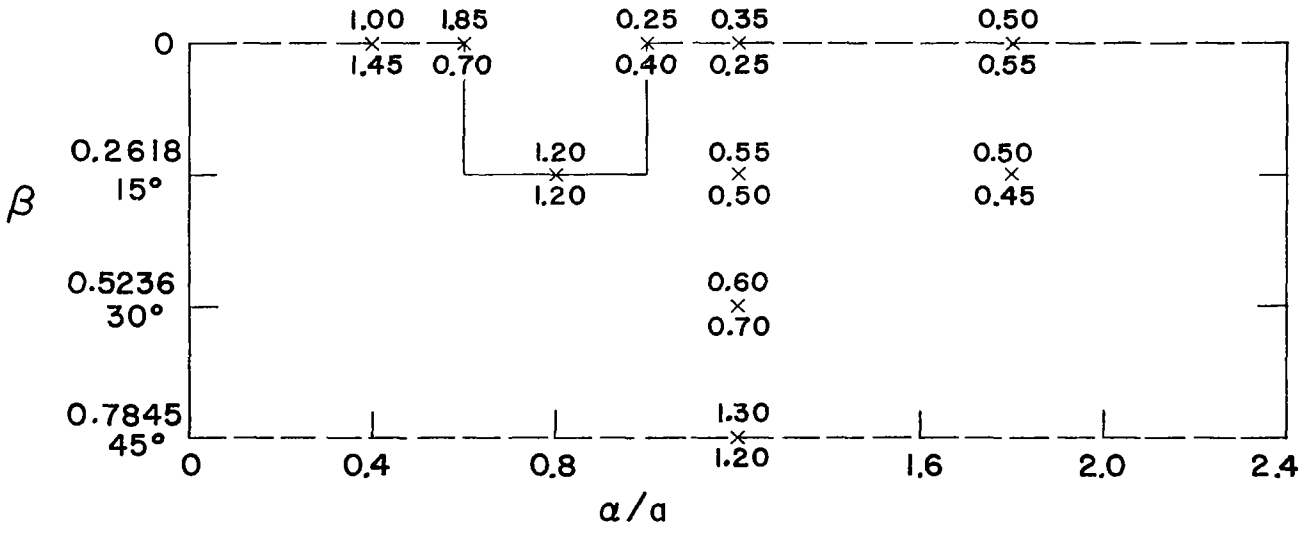

b) Transverse Excitation

Figure 25. Ratios of Peak Cut Shell Responses to Peak Virgin Shell Responses [Velocity × Effective Stress]

Chapter 5

CONCLUSION

This report contains: (1) analytical and numerical studies pertaining to the solution of transient, linear wave propagation problems in thin shells by the finite difference method (Chapters 2 and 3), (2) a recommended computational procedure for the use of the method (Chapter 3), and (3) a numerical investigation of the response of a cylindrical shell with cutouts to both longitudinal and radial transient excitations (Chapter 4). An outline of major conclusions and recommendations for future study follows:

5.1 MAJOR CONCLUSIONS

- The finite difference method accurately reproduces solutions of the partial differential equations of linear thin shell theory if the mesh dimensions are appreciably smaller than the shortest significant structural wave length characterizing the response of interest. (Sections 2.5 and 3.1)

- The only inherent limitation of the finite difference method is its inability to reproduce accurately response discontinuities, a limitation that also applies to the method of modal superposition but does not apply to the method of characteristics. (Sections 2.5 and 3.1)

- The short wave length limitations of thin shell (Bernoulli-Euler) theory create significant convergence difficulties in computed responses to certain types of transverse excitations. (Sections 2.5 and 3.2)

- Proper selection of finite difference mesh dimensions, combined, in some cases, with temporal smoothing of the excitation, increases the frequency range of thin shell (Bernoulli-Euler) theory by a factor of three for transverse excitations. (Section 3.2)

- Convergence difficulties in the case of transverse excitations may be materially alleviated through the use of improved (Timoshenko) theory; the ability of improved theory to treat flexural response discontinuities, however, may constitute no real advantage. (Sections 3.2 and 3.3)

- Cutouts in a cylindrical shell excited at one end by axisymmetric longitudinal and radial pulse-loads produce moderate changes in shell response during early and intermediate times; the cutouts may, however, facilitate the undesirable late-time transfer of load-injected extensional energy into non-axisymmetric flexural response (Section 4.3)

5.2 RECOMMENDATIONS FOR FUTURE STUDY

- The studies of Chapter 2 should be extended to include excitations that are spatially narrow in the circumferential dimension; numerical studies are required.

- The computational procedure recommended in Section 3.2, especially that aspect which deals with temporal filtering of the excitation, should be thoroughly tested; numerical studies are required.

- The advantages and disadvantages associated with the use of improved theory as opposed to the use of thin shell theory should be definitely established; both analytical and numerical studies are required.

- The short wave length limitations of improved theory should be determined with the techniques of Ref. 30; analytical studies are required.

- The degree to which cutouts may facilitate the late-time transfer of load-injected extensional energy into non-axisymmetric flexural response should be determined; solution by the method of modal superposition is suggested for this task.

- The effects of reinforced cutouts, structural (ring and longitudinal) stiffeners, and attached mechanical systems on the propagation of transient waves in shells should be investigated; numerical studies are required.

- The effects of geometric and material nonlinearities on the generation and propagation of transient waves in shells should be examined; numerical studies are required.

- A comprehensive study that compares finite difference, finite element, modal superposition and characteristics methods for the solution of problems involving transient linear wave propagation in shells should be performed.

Appendix A

THE STAR CODE

The finite difference computer program STAR (Shell Transient Asymmetric Response) is capable of computing the two-dimensional, finite-amplitude response of inelastic shells with unreinforced cutouts to mechanical and thermal transient loads. The code is based on the general thin shell equations of Ref. 6 and on constitutive equations for a temperature-dependent, work-hardening material. A detailed description of the code is given in Ref. 10; this appendix merely defines pertinent notation and describes improvements made in the code as part of the present study.

A.1 GEOMETRIC NOTATION

The middle surface of the shell is shown in Fig. 1. The lines of principal curvature, α = constant and β = constant, are selected as the coordinates of the middle surface of the shell. The coordinate in the direction of the inward normal to the middle surface is denoted by z. We see that the coordinates are such that (α, β, z) form a right-handed system. The element of arc length ds on the middle surface is given by

$$ds^2 = A^2 \, d\alpha^2 + B^2 \, d\beta^2 \tag{1}$$

where $A(\alpha, \beta)$ and $B(\alpha, \beta)$ are the Lame' parameters for the middle surface of the undeformed shell. Figure 1 also shows the principal radii of curvature r_α, r_β, the displacement components u, v, w, and the rotation components ω_α, ω_β. The components (u, ω_α), (v, ω_β), and w are taken positive in the direction of increasing α, β, and z, respectively.

If α denotes either the arc length measured along the generator from the apex of a circular cone or the end of a circular cylinder, and if β is the angular coordinate in the circumferential direction, then the Lame' parameters and radii of curvature for these surfaces are as follows:

	A	B	r_α	r_β
Cone	1	$\alpha \sin \varphi$	∞	$\alpha \tan \varphi$
Cylinder	1	a	∞	a

where φ is the half cone angle and a is the radius of the cylinder.

A.2 IMPROVEMENTS IN THE CODE

Improvements to the STAR computer program made during the present study are now summarized.

A.2.1 End Loadings

In many wave propagation problems it is of interest to determine the response of shells excited by end loadings. This is effected through the specification of nonhomogeneous boundary conditions. However, prior to the current study, only homogeneous boundary conditions could be handled by the STAR code. As a result of the present work, this restriction has been removed for cylindrical and conical shells, and various combinations of nonhomogeneous, time-dependent boundary conditions now can be handled through specification of one member of each of the following pairs (Figs. 1 and 2):

- At a boundary α = constant

  $[u(\beta,t),\ \bar{N}_\alpha(\beta,t)]$

  $[v(\beta,t),\ \bar{N}_{\alpha\beta}(\beta,t)]$

  $[w(\beta,t),\ \bar{Q}_\alpha(\beta,t)]$

  $[\omega_\beta(\beta,t),\ \bar{M}_\alpha(\beta,t)]$

- At a boundary β = constant

  $[u(\alpha,t),\ \bar{N}_{\beta\alpha}(\alpha,t)]$

  $[v(\alpha,t),\ \bar{N}_\beta(\alpha,t)]$

  $[w(\alpha,t),\ \bar{Q}_\beta(\alpha,t)]$

  $[\omega_\alpha(\alpha,t),\ \bar{M}_\beta(\alpha,t)]$

A.2.2 One-Dimensional Problems

The STAR code, which was originally developed for the asymmetric response of shells, can, of course, also accommodate one-dimensional problems, such as axisymmetric shells under axisymmetric loads or rings subjected to asymmetric loads. However, prior to the current study, special logic had not been provided for such problems. Thus, to define the finite difference expressions for spatial derivatives in the general equations, it was necessary to specify a minimum of five nodal points along each of the grid lines in the α and β directions. For one-dimensional problems (such as many of the problems considered in Chapter 2), this procedure is obviously quite inefficient and hence, for reasons of economy of computer run time, the code was modified to treat one-dimensional problems more efficiently. As a result of the modification, only one set of grid lines (rather than two) needs to be specified; this leads to a reduction of run time by a factor of approximately five.

A.2.3 More Accurate Computation of Velocity

To describe the explicit numerical technique employed in the computation of the velocity components at each mesh point, it is sufficient to consider the normal component, $\dot{w}(t)$, which had been previously computed from

$$\dot{w}(t) = \dot{w}(t-\Delta t) + \ddot{w}(t-\Delta t)\cdot \Delta t \tag{2}$$

where $(\dot{})$ denotes differentiation with respect to time t, and Δt is the time step. Equation 2 can be derived either from a Taylor series representation of $\dot{w}(t)$, with retention of only linear terms, or from a forward finite difference approximation for $\ddot{w}(t-\Delta t)$. The truncation error $\dot{w}(t)$ as computed from Eq. 2 is $O(\Delta t)^2$.* A truncation error of order $(\Delta t)^3$ is achieved if the velocity is instead computed from

$$\dot{w}(t) = \dot{w}(t-\Delta t) + \frac{1}{2}\,[\ddot{w}(t-\Delta t) + \ddot{w}(t)]\cdot \Delta t \tag{3}$$

*$O(\Delta t)^2$ denotes a term with an error of order $(\Delta t)^2$

This expression may be derived from the central difference representation

$$\ddot{w}(t-\Delta t/2) \cong \frac{1}{\Delta t}\left[\dot{w}(t) - \dot{w}(t-\Delta t)\right] \tag{4}$$

and the approximation

$$w(t-\Delta t/2) \cong \frac{1}{2}\left[w(t-\Delta t) + w(t)\right] \tag{5}$$

The last term in Eq. 3 is computed from the equation of motion in the normal direction, namely,

$$\ddot{w}(t) = F_z(t) - C_z\dot{w}(t) \tag{6}$$

where C_z is a viscous damping coefficient and F_z is a known function of the displacement and the loads. The introduction of Eq. 6 into Eq. 3 yields the following $O(\Delta t)^3$ explicit expression for the velocity that is currently employed in the STAR code:

$$\dot{w}(t) = \frac{1}{1+(\frac{\Delta t}{2})C_z}\left\{\dot{w}(t-\Delta t) + \frac{1}{2}\left[w(t-\Delta t)+F(t)\right]\cdot\Delta t\right\} \tag{7}$$

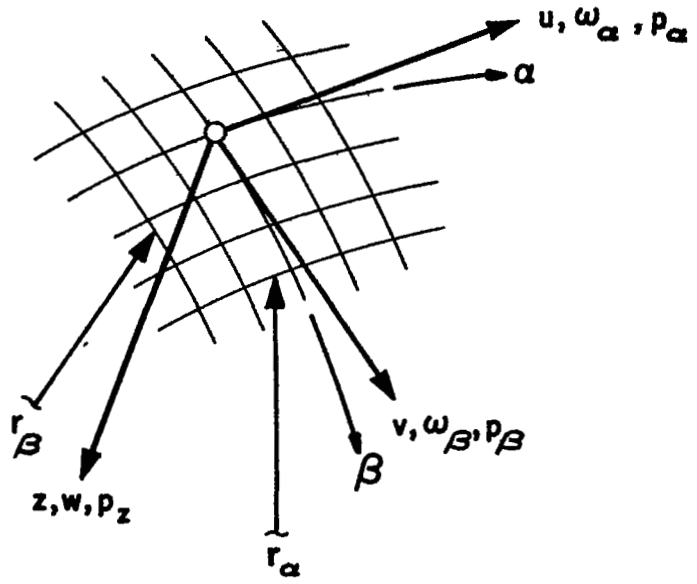

Figure 1. Notation and Coordinate System (Right-Hand Vector System)

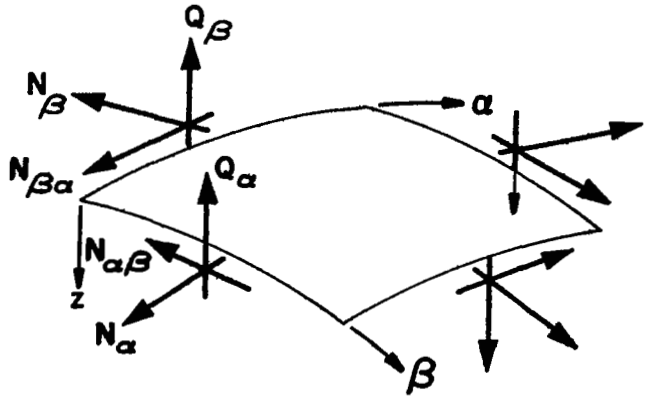

FORCE RESULTANTS

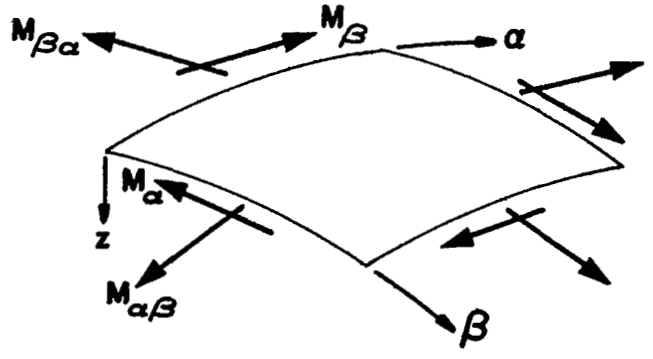

MOMENT RESULTANTS

Figure 2. Sign Convention for Stresses and Stress Resultants (Right-Hand Vector System)

Appendix B

AXISYMMETRIC LONGITUDINAL EXCITATION OF A MEMBRANE CYLINDRICAL SHELL

For axisymmetric, predominantly membrane wave propagation, Eqs. 1.7 for the circular cylindrical shell become

$$\frac{1}{c^2}\frac{\partial^2 u}{\partial t^2} - \frac{\partial^2 u}{\partial \alpha^2} + \left(\frac{\nu}{a}\right)\frac{\partial w}{\partial \alpha} = 0$$

$$\frac{1}{c^2}\frac{\partial^2 w}{\partial t^2} + \frac{w}{a^2} - \left(\frac{\nu}{a}\right)\frac{\partial u}{\partial \alpha} = 0 \qquad (1)$$

If an axial wave propagates down the shell that is characterized by a structural wave number $k(= 2\pi/\lambda)$, we have $u \sim u_o(\alpha)e^{ikc_k t}$, so that the second of Eqs. 1 becomes

$$\frac{\partial^2 w}{\partial t^2} + \left(\frac{c}{a}\right)^2 w \sim \nu \frac{\partial u_o}{\partial \alpha}\frac{c^2}{a} e^{ikc_k t} \qquad (2)$$

This is just the equation for an harmonically excited single-degree-of-freedom oscillator. Now if $(ka)^2 \ll 1$ and $c_k \lesssim c$, $(kc_k)^2 \ll \left(\frac{c}{a}\right)^2$, so that the oscillator is excited well below its natural frequency. For such a quasi-static excitation the inertial term in Eq. 2 is unimportant, and we have

$$w \approx \nu a \frac{\partial u}{\partial \alpha} \qquad (3)$$

Introducing this into the first of Eqs. 1, we obtain

$$\frac{1}{c^2}\frac{\partial^2 u}{\partial t^2} - (1-\nu^2)\frac{\partial^2 u}{\partial \alpha^2} = 0 \qquad (4)$$

so that the (non-dispersive) wave travels with the bar velocity $c_b = \sqrt{1-\nu^2}\, c = (E/\rho)^{1/2}$. If, however, $(ka)^2 \gg 1$ and $c_k \gtrsim c$, then the inertial term in Eq. 2 is dominant, and we have

$$\frac{\partial^2 w}{\partial t^2} \approx \nu \frac{c^2}{a} \frac{\partial u}{\partial \alpha} \tag{5}$$

Introducing this into the first of Eqs. 1, we obtain

$$\frac{1}{c^2} \frac{\partial^4 u}{\partial t^4} - \frac{\partial^4 u}{\partial t^2 \partial \alpha^2} + \nu^2 \left(\frac{c}{a}\right)^2 \frac{\partial^2 u}{\partial \alpha^2} = 0 \tag{6}$$

With $u \sim U_o e^{i(\omega_k t - k\alpha)}$, this yields, since $(ka)^2 \gg 1$,

$$c_k^2 = \left(\frac{\omega_k}{k}\right)^2 = \frac{1}{2} c^2 \left[1 \pm \sqrt{1 + 4\nu^2/(ka)^2}\right] \approx c^2 \tag{7}$$

so that the wave travels essentially without dispersion at the plate velocity c. Finally, if $ka \sim 1$, no simplification is possible and the propagation is characterized by significant dispersion.

We have just observed that, for axially propagating disturbances with pronounced characteristic wave lengths, long wave length disturbances $[(ka)^2 \gg 1]$ propagate as nondispersed waves along a bar and short wave length disturbances $[(ka)^2 \gg 1]$ propagate as nondispersed, straight-crested waves in an infinite plate. For general excitations, however, a more sophisticated analysis is required.

B.1 PERTURBATION TECHNIQUE

Let us write Eqs. 1 in terms of the non-dimensional variables

$$\hat{u} = u/a, \quad \hat{w} = w/a, \quad \tau = ct/a \tag{8}$$

and then omit the circumflex notation to obtain

$$\frac{\partial^2 u}{\partial \tau^2} - \frac{\partial^2 u}{\partial \alpha^2} + v \frac{\partial w}{\partial \alpha} = 0$$

$$\frac{\partial^2 w}{\partial \tau^2} + w + v \frac{\partial u}{\partial \alpha} = 0 \qquad (9)$$

We now expand u and w as follows

$$u = u^{(0)} + v u^{(1)} + v^2 u^{(2)} + \ldots$$

$$w = w^{(0)} + v w^{(1)} + v^2 w^{(2)} + \ldots \qquad (10)$$

substitute into Eqs. 9, and equate the coefficients of like powers of v to obtain the displacement recursion formulas

$$\frac{\partial^2 u^{(i)}}{\partial \tau^2} - \frac{\partial^2 u^{(i)}}{\partial \alpha^2} = - \frac{\partial w^{(i-1)}}{\partial \alpha}$$

$$\frac{\partial^2 w^{(i)}}{\partial \tau^2} + w^{(i)} = \frac{\partial u^{(i-1)}}{\partial \alpha} \qquad , \; i = 0,1,2, \ldots \qquad (11)$$

Considering the right side of each of these equations as known, we see that the equations are particularly easy to solve, the first being the wave equation and the second the equation of motion for a simple oscillator. Furthermore, satisfaction of the applicable boundary conditions at the zeroth level yields $w^{(0)} = u^{(1)} = w^{(2)} = u^{(3)} = \ldots = 0$. Thus, since v^2 is generally much smaller than unity, convergence of the series of Eqs. 10 is rapid. We now illustrate the application of the perturbation technique by treating two simple impact problems for a semi-infinite shell.

B.2 PRESCRIBED END MOTION

Consider an initially quiescent semi-infinite shell that is subjected to a prescribed longitudinal end displacement $u(0,t) = f(\tau)H(\tau)$, where $H(\tau)$ is the Heaviside step-function. From Eqs. 11, then,

$$u^{(0)}(\alpha,\tau) = f(\tau - \alpha)\, H(\tau - \alpha)$$
$$w^{(1)}(\alpha,\tau) = -\int_0^{\tau-\alpha} f'(\tau - \alpha - \xi) \sin \xi d\xi \tag{12}$$

where f' is the derivative of f with respect to its argument.*

We now seek $u^{(2)}$ ($u^{(1)}$ being zero), which, from Eqs. 11 and 12, is given by

$$\frac{\partial^2 u^{(2)}}{\partial \tau^2} - \frac{\partial^2 u^{(2)}}{\partial \alpha^2} = -\int_0^{\tau-\alpha} f''(\tau-\alpha-\xi) \sin \xi d\xi \tag{13}$$

The desired particular solution to this equation is of the form

$$u_p^{(2)}(\alpha,\tau) = (\tau + \alpha)\, g(\tau - \alpha) \tag{14}$$

Thus, Eqs. 13 and 14 yield

$$g'(\tau-\alpha) = -\frac{1}{4}\int_0^{\tau-\alpha} f''(\tau-\alpha-\xi) \sin \xi d\xi \tag{15}$$

The homogeneous solution to Eq. 13 is of the form

$$u_h^{(2)}(\alpha,\tau) = h(\tau-\alpha) \tag{16}$$

---

*Response discontinuities are most conveniently handled through the use of generalized functions.

Finally, since $u^{(0)}$ satisfies our boundary condition at $\alpha = 0$, we have $u^{(2)}(0,\tau) = 0$, which, from Eqs. 14 and 15, yields

$$u_h^{(2)}(\alpha,\tau) = -(\tau-\alpha)\, g(\tau-\alpha) \tag{17}$$

Thus, from Eqs. 14, 15 and 17, we obtain

$$u^{(2)}(\alpha,\tau) = -\frac{1}{2}\,\alpha \int_0^{\tau-\alpha}\int_0^{\eta} f''(\eta-\xi)\sin\xi\, d\xi\, d\eta \tag{18}$$

so that, from Eqs. 10, 12 and 18,

$$\begin{aligned} u(\alpha,\tau) &= f(\tau-\alpha)H(\tau-\alpha) - \frac{1}{2}\,v^2\alpha \int_0^{\tau-\alpha}\int_0^{\eta} f''(\eta-\xi)\sin\xi\, d\xi\, d\eta + O(v^4) \\ w(\alpha,\tau) &= -v\int_0^{\tau-\alpha} f'(\tau-\alpha-\xi)\sin\xi\, d\xi + O(v^3) \end{aligned} \tag{19}$$

As τ increases, additional terms are required; for example, we will require below the addition of the $O(v^3)$ term to the second of Eq. 19. From Eq. 18 and the second of Eqs. 11, this term is given by

$$w^{(3)}(\alpha,\tau) = -\frac{1}{2}\int_0^{\tau-\alpha}\left[\int_0^{\tau-\alpha-\xi} F(\eta)\, d\eta - \alpha F(\tau-\alpha-\xi)\right]\sin\xi\, d\xi \tag{20}$$

where

$$F(\eta) = \int_0^{\eta} f''(\eta-\xi)\sin\xi\, d\xi \tag{21}$$

Let us now, as an example, consider the case of a step end-velocity, i.e., $f(\tau) = \tau$. From Eqs. 19, then,

$$\begin{aligned} u(\alpha,\tau) &= \{(\tau-\alpha) - \frac{1}{2}\,v^2\alpha[1 - \cos(\tau-\alpha)]\}\, H(\tau-\alpha) + O(v^4) \\ w(\alpha,\tau) &= -v[1 - \cos(\tau-\alpha)]\, H(\tau-\alpha) + O(v^3) \end{aligned} \tag{22}$$

and from Eq. 20,

$$w^{(3)}(\alpha,\tau) = \left\{\frac{1}{4}\,\tau \sin(\tau-\alpha) - \frac{1}{4}\,\alpha(\tau-\alpha)\cos(\tau-\alpha) - \frac{1}{2}[1-\cos(\tau-\alpha)]\right\}H(\tau-\alpha) \quad (23)$$

Figure 1 presents longitudinal and radial velocity snapshots from Eqs. 22 and from Refs. 13 and 14 for $\tau = 2$ and 5. The results from Ref. 14 were obtained by application of the method of characteristics to the membrane shell equations; the results from Ref. 13 were obtained by application of the method of characteristics to equations appropriate to improved (Timoshenko) shell theory. Figure 2 shows longitudinal and radial velocity snapshots from Eqs. 22 and 23 and from Ref. 14 for the rather late time $\tau = 10$. We observe the significant improvement in the solution for $\dot{w}(\alpha,10)$ through the addition of the $O(\nu^3)$ term.

Longitudinal and circumferential membrane stress in the cylindrical shell are given by

$$\sigma_\alpha = \frac{\partial u}{\partial \alpha} - \nu w$$

$$\sigma_\theta = -w + \nu\,\frac{\partial u}{\partial \alpha} \quad (24)$$

where σ_α and σ_θ are normalized to $E/(1-\nu^2)$. Results for these quantities in the form of snapshots at $\tau = 2$ and 5 appear in Figure 3. The σ_α - results from Eqs. 22 and 24 include terms up to and including those of order ν^2, while the σ_θ - results from those equations pertain to a single $O(\nu)$ term. The results from Ref. 14 pertain to a modal superposition solution of membrane theory shell equations, while those from Ref. 13 pertain to a method of characteristics solution of improved theory shell equations. Figure 4 shows longitudinal and circumferential membrane stress snapshots at $\tau = 10$. A σ_θ - result with terms up to and including those of order ν^3 is shown in this figures; we notice here too the significant improvement in the solution through the addition of the $O(\nu^3)$ term to the second of Eqs. 19.

We observe in Figures 1-4 that a perturbation solution of given order begins to fail as τ increases. This comes as no surprise, since we expect the cumulative effects of coupling through Poisson's ratio eventually to produce such failure. It is, in fact, rather surprising

that the $\tau = 5$ and 10 solutions of Figures 1-4 are as accurate as they are, since we also expect to encounter convergence problems as $\nu^2\tau$ approaches unity. Even when $\nu^2\tau \gtrsim 1$, however, the perturbation solution is convergent in the vicinity of the wave front. Furthermore, when $\tau \gg 1$, asymptotic methods may be used to obtain solutions, as in Ref. 33.

B.3 PRESCRIBED END LOAD

We now consider an initially quiescent semi-infinite shell that is excited by a prescribed longitudinal end load $\sigma_\alpha(0,\tau) = f(\tau)\, H(\tau)$. To treat this problem, we use Eqs. 24 to transform Eqs. 9 into the set

$$\frac{\partial^2 \sigma_\alpha}{\partial \tau^2} - (1-\nu^2)\frac{\partial^2 \sigma_\alpha}{\partial \alpha^2} - \nu \frac{\partial^2 \sigma_\theta}{\partial \tau^2} = 0$$

$$\frac{\partial^2 \sigma_\theta}{\partial \tau^2} + (1-\nu^2)\sigma_\theta - \nu \frac{\partial^2 \sigma_\alpha}{\partial \tau^2} = 0 \qquad (25)$$

Now it is clear that these equations lead to perturbation solutions which predict that the wavefront travels at the bar velocity $c_b = (1-\nu^2)^{1/2} c$. Hence, we recombine these equations to obtain the equivalent set

$$\frac{\partial^2 \sigma_\alpha}{\partial \tau^2} - \frac{\partial^2 \sigma_\alpha}{\partial \alpha^2} + \nu\sigma_\theta = 0$$

$$\frac{\partial^2 \sigma_\theta}{\partial \tau^2} + \sigma_\theta - \nu \frac{\partial^2 \sigma_\alpha}{\partial \alpha^2} = 0 \qquad (26)$$

Following the same procedure used to obtain Eqs. 11, we obtain the stress recursion formulas

$$\frac{\partial^2 \sigma_\alpha^{(i)}}{\partial \tau^2} - \frac{\partial^2 \sigma_\alpha^{(i)}}{\partial \alpha^2} = -\sigma_\theta^{(i-1)}$$

$$\frac{\partial^2 \sigma_\theta^{(i)}}{\partial \tau^2} + \sigma_\theta^{(i)} = \frac{\partial^2 \sigma_\alpha^{(i-1)}}{\partial \alpha^2} \qquad , \; i = 0,1,2, \ldots \tag{27}$$

Satisfaction of the boundary conditions appropriate to these equations at the zeroth level yields $\sigma_\theta^{(0)} = \sigma_\alpha^{(1)} = \sigma_\theta^{(2)} = \sigma_\alpha^{(3)} = \ldots = 0$.

For the prescribed end load $\sigma_\alpha(0,\tau) = f(\tau)\, H(\tau)$, we obtain from Eqs. 27

$$\sigma_\alpha^{(0)}(\alpha,\tau) = f(\tau-\alpha)\, H(\tau-\alpha)$$

$$\sigma_\theta^{(1)}(\alpha,\tau) = \int_0^{\tau-\alpha} f''(\tau-\alpha-\xi) \sin \xi \, d\xi \tag{28}$$

Next we seek $\sigma_\alpha^{(2)}$, which, from Eqs. 27 and 28, is given by

$$\frac{\partial^2 \sigma_\alpha^{(2)}}{\partial \tau^2} - \frac{\partial^2 \sigma_\alpha^{(2)}}{\partial \alpha^2} = -\int_0^{\tau-\alpha} f''(\tau-\alpha-\xi) \sin \xi \, d\xi \tag{29}$$

Proceeding as before, we find

$$\sigma_\alpha^{(2)}(\alpha,\tau) = -\frac{1}{2}\, \alpha \int_0^{\tau-\alpha} \int_0^{\eta} f''(\eta-\xi) \sin \xi \, d\xi \, d\eta \tag{30}$$

so that, from Eqs. 28 and 30

$$\sigma_\alpha(\alpha,\tau) = f(\tau-\alpha)\,H(\tau-\alpha) - \tfrac{1}{2}\nu^2\alpha\int_0^{\tau-\alpha}\int_0^{\eta} f''(\eta-\xi)\sin\xi\,d\xi\,d\eta + O(\nu^4)$$

$$\sigma_\theta(\alpha,\tau) = \nu\int_0^{\tau-\alpha} f''(\tau-\alpha-\xi)\sin\xi\,d\xi + O(\nu^3) \tag{31}$$

As τ increases, additional terms are again required; for example, from Eq. 30 and the second of Eqs. 27, the $O(\nu^3)$ term for $\sigma_\theta(\alpha,\tau)$ is given by

$$\sigma_\theta^{(3)}(\alpha,\tau) = \int_0^{\tau-\alpha}\left[F(\tau-\alpha-\xi) - \tfrac{1}{2}\,\alpha\,F'(\tau-\alpha-\xi)\right]\sin\xi\,d\xi \tag{32}$$

where $F(\eta)$ is given by Eq. 21 and $F'(\eta)$ is the derivative of $F(\eta)$ with respect to argument.

As an example, we consider the case of a ramp end-load; i.e., $f(\tau) = \tau$. From Eqs. 31, then,

$$\sigma_\alpha(\alpha,\tau) = \{(\tau-\alpha) - \tfrac{1}{2}\nu^2\alpha[1 - \cos(\tau-\alpha)]\}\,H(\tau-\alpha) + O(\nu^4)$$

$$\sigma_\theta(\alpha,\tau) = \nu\sin(\tau-\alpha)\,H(\tau-\alpha) + O(\nu^3) \tag{33}$$

Figure 5 shows snapshots of longitudinal and circumferential stress response at $\tau = 2$. The results from Ref. 14 were obtained by application of the method of characteristics to the membrane shell equations; we see that they are very closely approximated by the perturbation solutions at this rather early time.

Before concluding this discussion, let us briefly examine the argument behind the transformation of Eqs. 25 into Eqs. 26, viz., that perturbation solutions obtained from Eq. 26 give c instead of c_b as the wave front velocity. This is clearly desirable if one is interested in information near the wave front, but is less desirable if the excitation $f(\tau)$ varies so slowly that the shell behaves much like a bar. In the latter case, it is better to use Eqs. 25 or, in the case of prescribed end motions, the equations

$$\frac{\partial^2 u}{\partial \tau^2} - (1-\nu^2)\frac{\partial^2 u}{\partial \alpha^2} - \nu \frac{\partial^3 w}{\partial \alpha \partial \tau^2} = 0$$

$$\frac{\partial^3 w}{\partial \alpha \partial \tau^2} + (1-\nu^2)\frac{\partial w}{\partial \alpha} - \nu \frac{\partial^2 u}{\partial \tau^2} = 0 \tag{34}$$

The solutions to these equations that correspond to Eqs. 19 are

$$u(\alpha,\tau^*) = f(\tau^*-\alpha)\, H(\tau^*-\alpha) + \frac{1}{2}\nu^2\alpha\int_0^{\tau^*-\alpha}\int_0^{\eta} f^{iv}(\eta-\xi)\sin\xi\, d\xi\, d\eta + O(\nu^4)$$

$$w(\alpha,\tau^*) = -\nu\int_0^{\tau^*-\alpha} f'(\tau^*-\alpha-\xi)\sin\xi\, d\xi + O(\nu^3) \tag{35}$$

and the solutions to Eqs. 25 that correspond to Eqs. 31 are

$$\sigma_\alpha(\alpha,\tau^*) = f(\tau^*-\alpha)\, H(\tau^*-\alpha) + \frac{1}{2}\nu^2\alpha\int_0^{\tau^*-\alpha}\int_0^{\eta} f^{iv}(\eta-\xi)\sin\xi\, d\xi\, d\eta + O(\nu^4)$$

$$\sigma_\theta(\alpha,\tau^*) = \nu\int_0^{\tau^*-\alpha} f''(\tau^*-\alpha-\xi)\sin\xi\, d\xi + O(\nu^3) \tag{36}$$

where $\tau^* = (1-\nu^2)^{1/2}\cdot\tau = c_b t/a$ and f^{iv} is the fourth derivative of f with respect to argument. For the examples considered above, Eqs. 35 and 36 yield responses which differ from those produced by Eqs. 19 and 31 only in that τ is replaced by τ^*. For slowly-varying excitations, however, Eqs. 35 and 36 should yield better solutions than Eqs. 19 and 31.

B.4 CONCLUDING REMARKS

We have seen that the perturbation method can provide remarkably accurate solutions for problems involving the propagation of transient, axisymmetric stress waves in elastic cylindrical shells. In addition, the technique may be applied to a variety of related problems, such as the propagation of compressional waves in elastic rods. To illustrate this application, we consider the Mindlin-Herrmann equations (Ref. 34)

$$\rho a^2 \frac{\partial^2 \tilde{u}}{\partial t^2} - (\lambda + 2\mu)\, a^2 \frac{\partial^2 \tilde{u}}{\partial x^2} - 2\varkappa_1 \lambda a \frac{\partial \tilde{w}}{\partial x} = 0$$

$$\rho a^2 \frac{\partial^2 \tilde{w}}{\partial t^2} + 8\varkappa_1^2 (\lambda + \mu)\, \tilde{w} - \varkappa^2 a^2 \mu \frac{\partial^2 \tilde{w}}{\partial x^2} + 4\varkappa_1 \lambda a \frac{\partial \tilde{u}}{\partial x} = 0 \qquad (37)$$

where $\tilde{u}$ and $\tilde{w}$ are longitudinal and radial displacements, respectively, ρ and a are the rod density and radius, respectively, λ and μ are the Lame' constants, and $\varkappa$ and $\varkappa_1$ are correction factors on the order of unity. For motions with spatial wave lengths on the order of and larger than the rod radius, the third term on the left side of the second of Eqs. 37 may be neglected in favor of the term immediately preceding it. This yields a set of equations that are of the same form as Eqs. 9, which permits direct application of the perturbation technique applied to Eqs. 9.

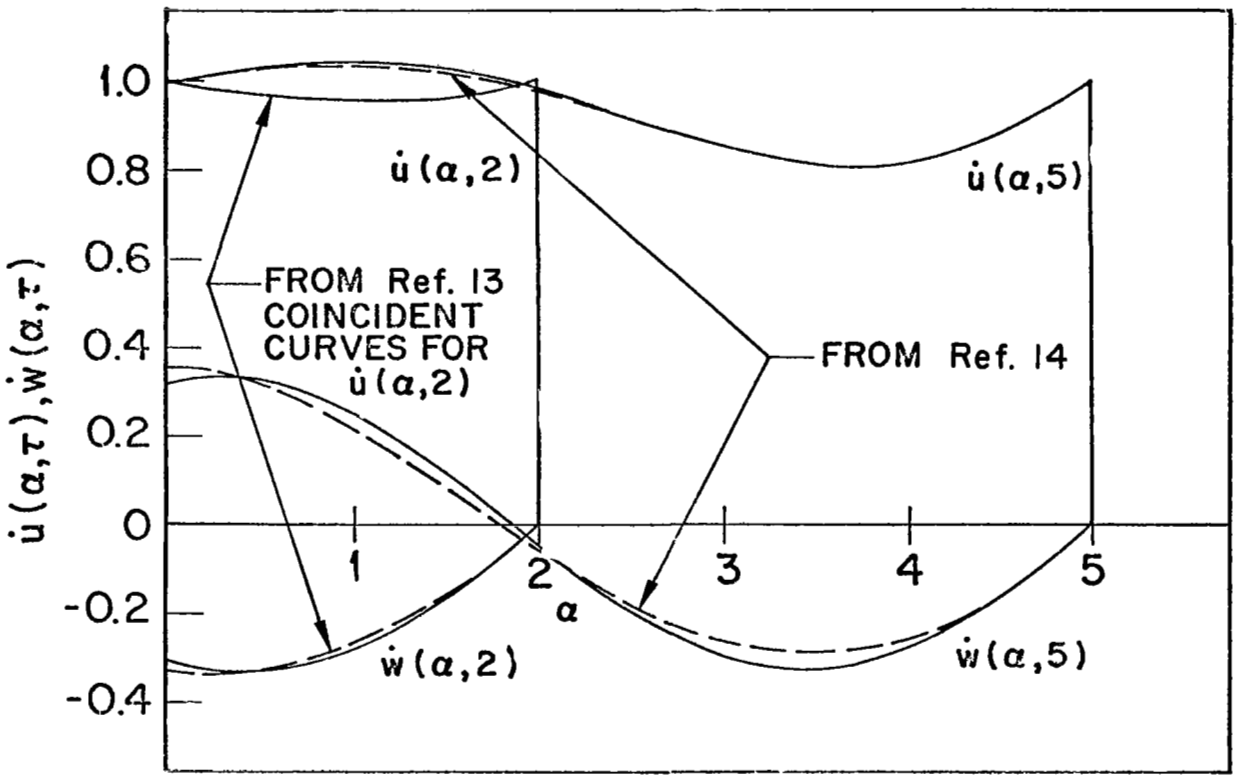

Figure 1. Velocity Snapshots at $\tau = 2$ and 5 (Step-Velocity Excitation)

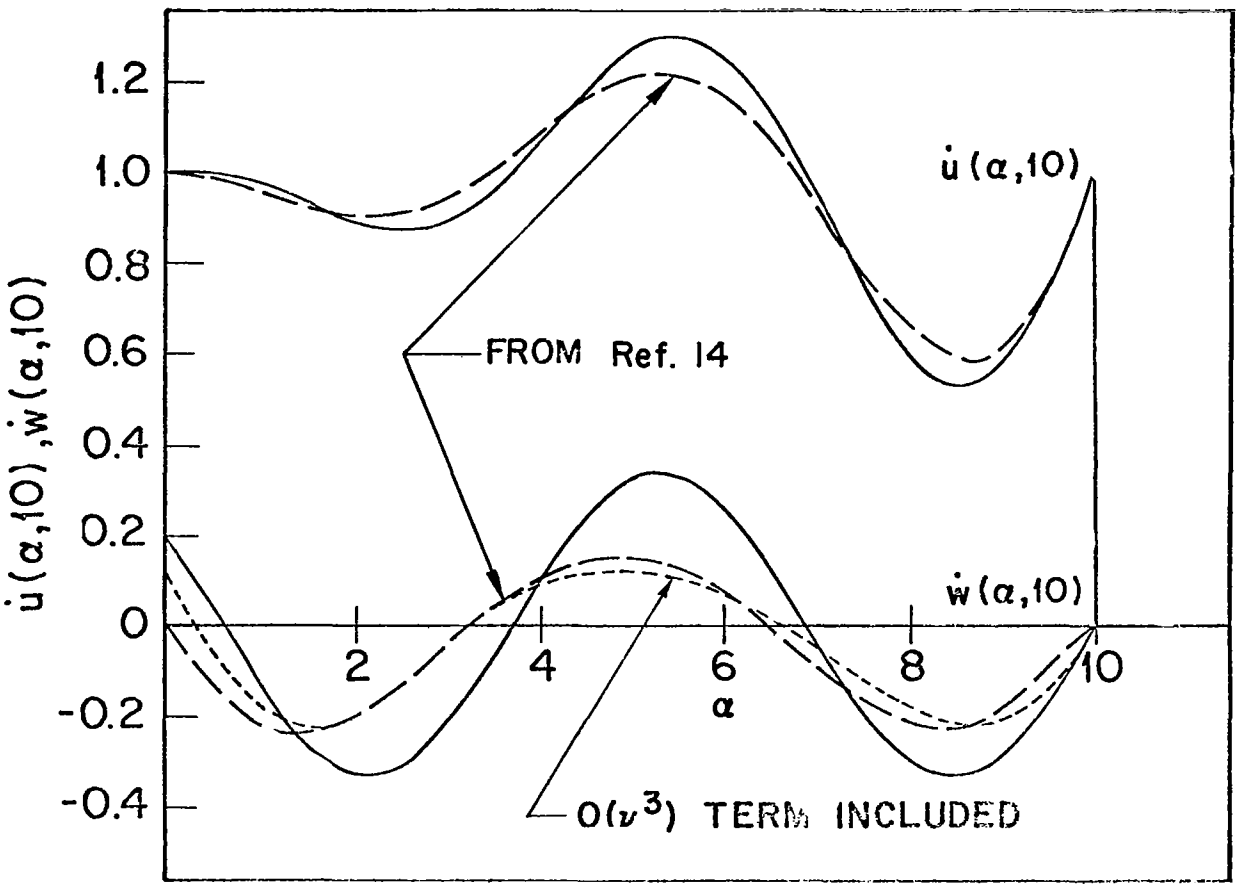

Figure 2. Velocity Snapshot at $\tau = 10$ (Step-Velocity Excitation)

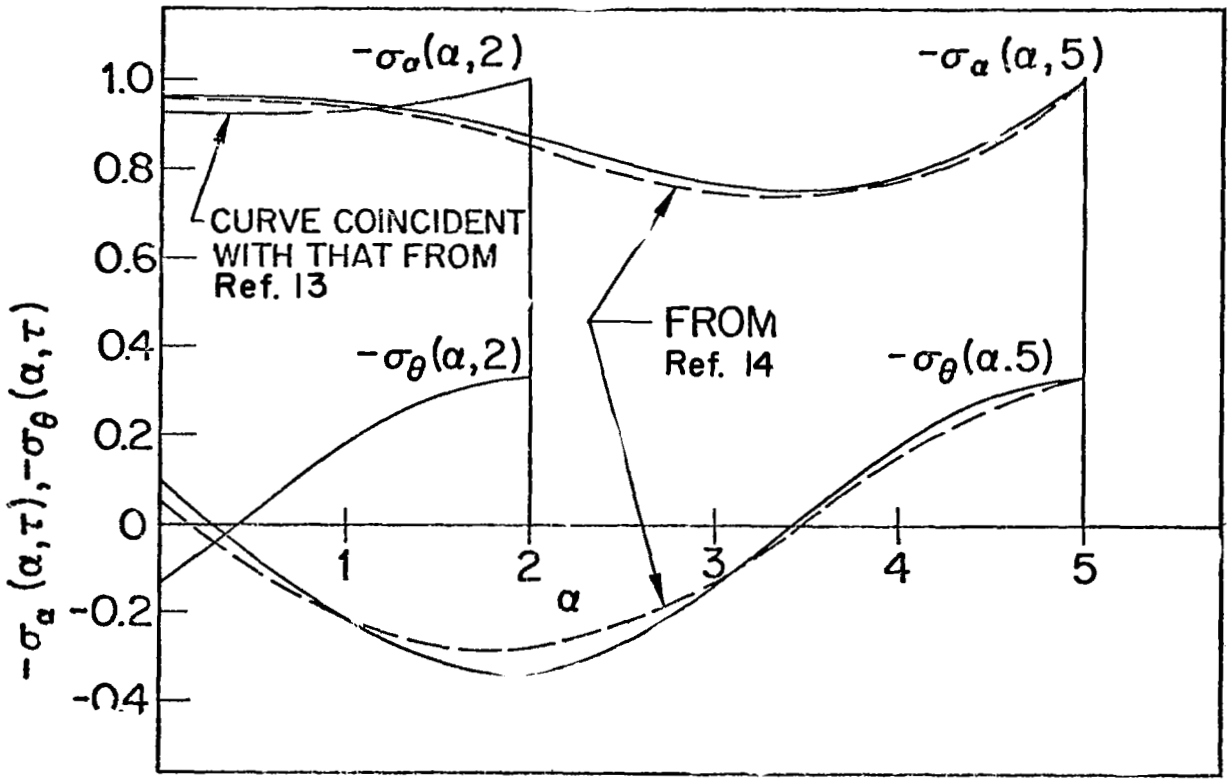

Figure 3. Stress Snapshots at $\tau = 2$ and 5 (Step-Velocity Excitation)

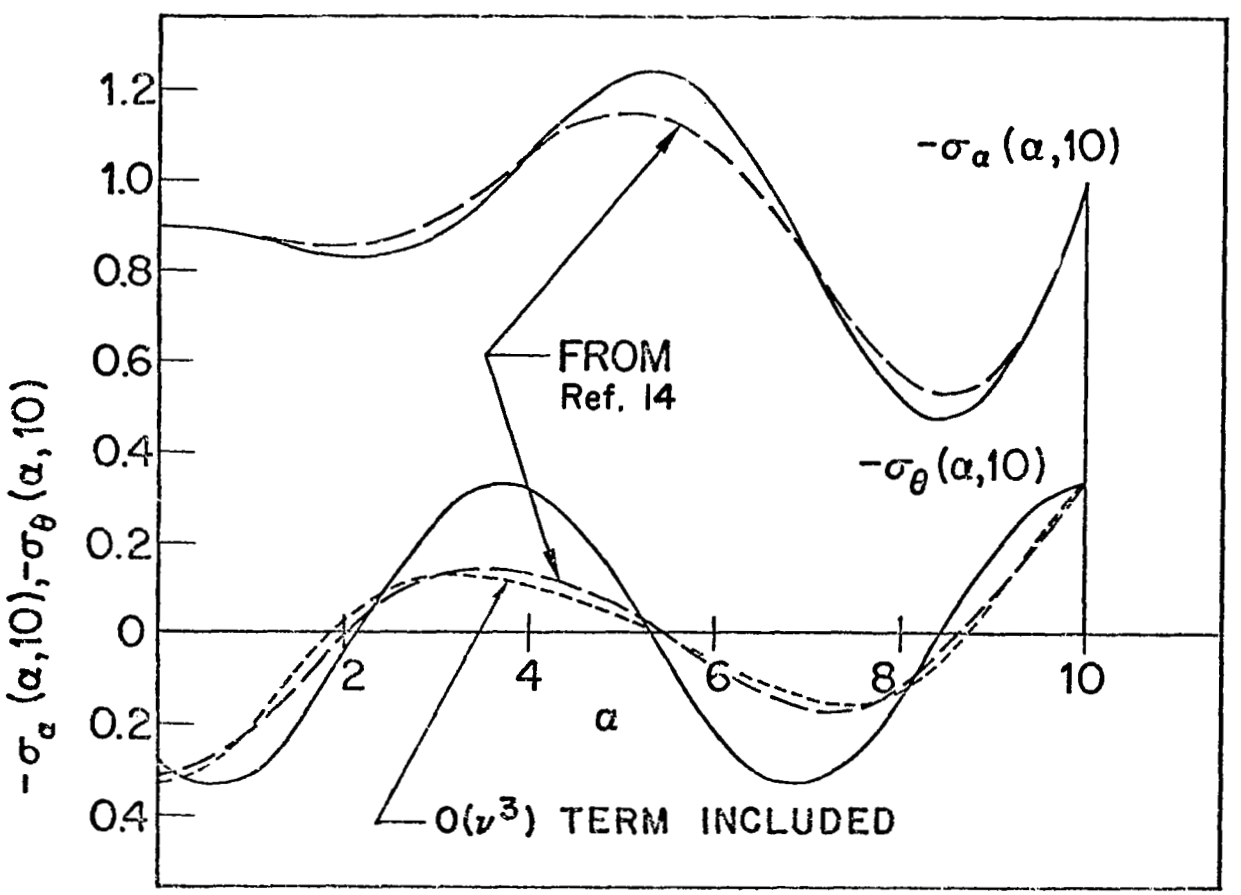

Figure 4. Stress Snapshot at $\tau = 10$ (Step-Velocity Excitation)

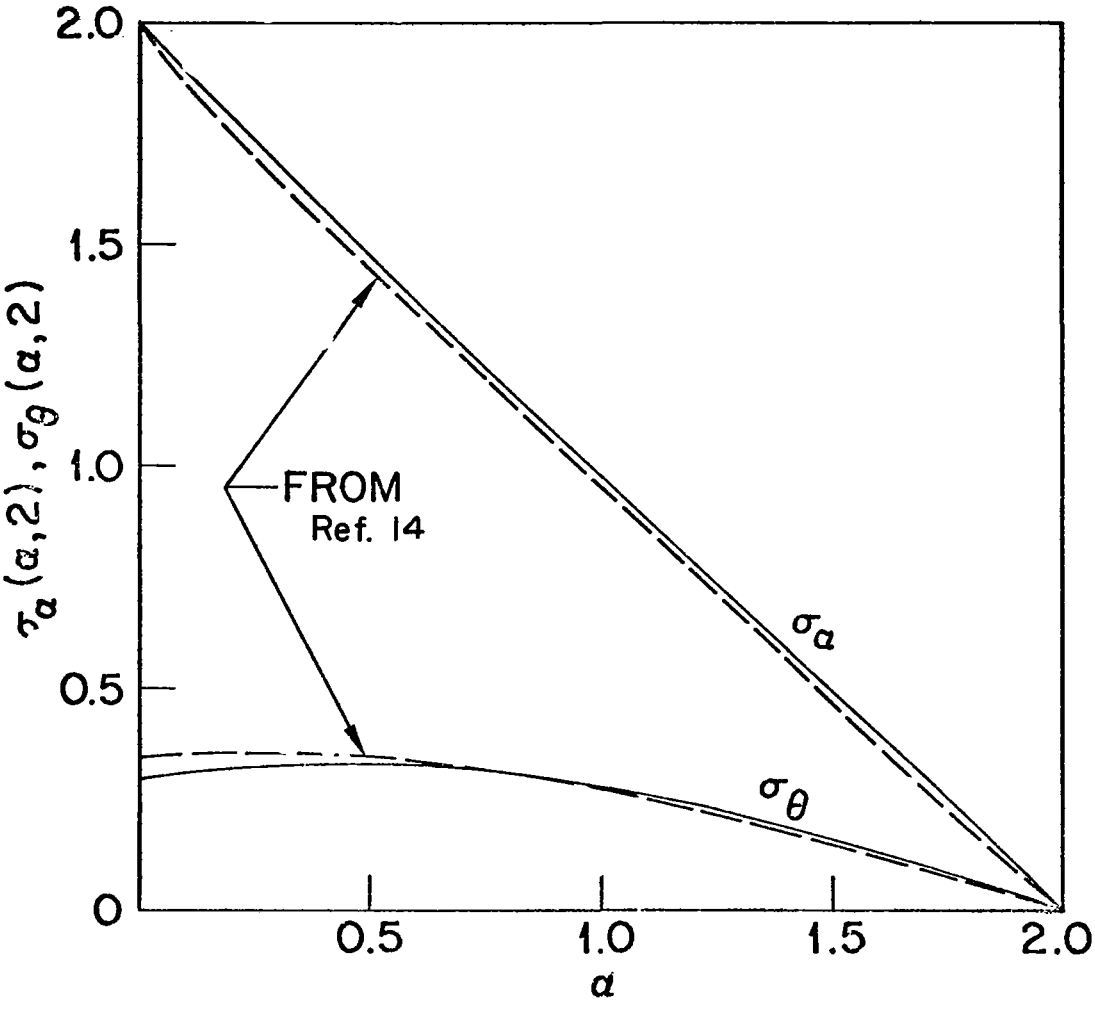

Figure 5. Stress Snapshot at $\tau = 10$ (Ramp-Stress Excitation)

REFERENCES

1. S. Timoshenko and D. H. Young, Vibration Problems in Engineering, Van Nostrand Company, Inc., (3rd Ed.), 1955.

2. J. A. Aseltine, Transform Methods in Linear System Analysis, McGraw-Hill Book Company, Inc., 1958.

3. A.E.H. Love, A Treatise on the Mathematical Theory of Elasticity, Dover Publications, New York, 1926.

4. W. Flügge, Stresses in Shells, Springer-Verlag, New York, 1967.

5. V. V. Novozhilov, The Theory of Thin Shells, P. Nordhoff, Ltd., Groningen, The Netherlands, 1959.

6. J. Kempner, "Unified Thin Shell Theory," Polytechnical Institute of Brooklyn, PIBAL Report No. 566, March 1960.

7. H. Kraus, Thin Elastic Shells, John Wiley & Sons, Inc., New York, 1967.

8. I. Mirsky and G. Herrmann, "Nonaxially Symmetric Motions of Cylindrical Shells," J. Acoustical Soc. Am., Vol. 29, pp 1116-1123 (1957) see also J. Acoustical Soc. Am., Vol. 31, p 250 (1959)

9. R. F. Hartung, "An Assessment of Current Capability for Computer Analysis of Shell Structures," Jl. Computers & Structures, Vol. 1, 1971.

10. L. H. Sobel, W. Silsby, B. G. Wrenn, "Computer User's Manual for the STAR (Shell Transient Asymmetric Response) Code," SAMSO-TR-70-240, LMSC-D006673, April 1970.

11. J. W. Leech, P. T. Hsu, E. W. Mack, "Stability of a Finite Difference Method for Solving Matrix Equations," AIAA J., Vol. 3, No. 11, Nov. 1965, pp 2172-2173.

12. J. P. Raney and J. T. Howlett, "A Modal Solution for Wave Propagation in Finite Shells of Revolution," presented at the AIAA/ASME 11th Structures, Structural Dynamics and Materials Conference, Denver, Colo., April 1970.

13. P. C. Chou, "Analysis of Axisymmetrical Motions of Cylindrical Shells by the Method of Characteristics," AIAA J., Vol. 6, No. 8, Aug. 1968, pp 1492-1497

14. S. Adham, "Wave Propagation in Elastic and Elastic-Plastic Cylindrical Shells," Ph.D. Dissertation, Univ. of Southern California, 1967.

15. J. P. Raney, Private Communication, August 1970.

16. R. W. Mortimer, P. C. Chou, J. L. Rose, "Annual Report in Stepped and Joined Shells," NASA Grant NGR 30-004-013, October 1969.

17. V. H. Kenner, W. Goldsmith, and J. L. Sackman, "Longitudinal Impact on a Hollow Cone," J. of Appl. Mech., Vol. 36, Sept. 1969, pp 445-450.

18. B. A. Boley and C. C. Chao, "Some Solutions of the Timoshenko Beam Equations," J. of Appl. Mech., Vol. 22, Dec. 1955, pp 579-586.

19. F. S. Crawford, Jr., Waves, McGraw-Hill Book Company, New York, 1965.

20. T. von Karman and M. A. Biot, Mathematical Methods in Engineering, McGraw-Hill Book Company, New York, 1940.

21. R. S. Dunham, R. E. Nickell and D. C. Stickler, "Integration Operators for a Transient Structural Response," proceedings of Conference on Computer Oriented Analysis of Shell Structures, Lockheed Missiles & Space Company, Palo Alto, Calif., August 1970.

22. J. W. Leech, "Stability of Finite Difference Equation for the Transient Response of a Flat Plate," AIAA J., Vol. 3, No. 9, Sept. 1965, pp 1772-1773.

23. G. G. O'Brien, M. A. Hyman, and S. Kaplan, "A Study of the Numerical Solution of Partial Differential Equations," J. Math & Physics, Vol. 29, 1951, pp 223-251.

24. B. G. Wrenn, L. H. Sobel and W. Silsby, "Nonsymmetric and Nonlinear Response of Thin Shells," Lockheed Missiles & Space Company Report No. B-72-67-3, Dec. 1967.

25. L. Morino, J. W. Leech, and E. A. Witmer, "PETROS 2: A New Finite Difference Method and Program for the Calculation of Large Elastic-Plastic Dynamically Induced Deformations of General Thin Shells," BRL CR 12, Dec. 1969.

26. R. D. Mindlin, "An Introduction to the Mathematical Theory of Vibrations of Elastic Plates," U.S. Army Signal Corps Engineering Laboratories, Fort Monmouth, N.J., 1955.

27. T. L. Geers, "An Approximate Method for Analyzing the Vibrations of Stiffened Plates and Shells," Cambridge Acoustical Associates, Inc., Cambridge, Mass., Final Report (II) U-238-165, under contract NObs-90438, Nov. 1966.

28. T. L. Geers and S. A. Denenberg, "A Digital Filter for Separating High- and Low-Frequency Components of a Transient Signal," David Taylor Model Basin Report 1795, Jan. 1964.

29. K. Knopp, Infinite Sequences and Series (Trans. by F. Bagemihl), Dover Publications, New York, 1956.

30. V. V. Novozhilov and L. I. Slepian, "On Saint-Venant's Principle in the Dynamics of Beams," PMM, Vol. 29, No. 2, 1965, pp 261-281.

31. D. A. Evensen, Monthly Progress Report No. 10, NASA/Langley Contract NAS 1-9876, March 1971.

32. R. H. Chalmers and H. A. Gaberson, "Modal Velocity as a Criterion of Shock Severity," Naval Electronics Laboratory Report NEL 1682, Jan. 1970.

33. H. M. Berkowitz, "Longitudinal Impact of a Semi-Infinite Elastic Cylindrical Shell," J. of Appl. Mech., Vol. 30, Sept. 1963, pp 347-355.

34. R. D. Mindlin and G. Herrmann, Proc. 1st U.S. Nat'l Cong. Appl. Mech., June 1951, ASME, New York, N.Y., 1952, pp 187-191.